CRAFTING ORDERED STRUCTURES OF NANOMATERIALS VIA FLOW-ENABLED SELF-ASSEMBLY (FESA) AND CONTROLLED EVAPORATIVE SELF-ASSEMBLY (CESA)

A Dissertation
Presented to
The Academic Faculty

by

Bo Li

In Partial Fulfillment
of the Requirements for the Degree
Doctor of Philosophy in the
School of Materials Science and Engineering

Georgia Institute of Technology
May 2015

CRAFTING ORDERED STRUCTURES OF NANOMATERIALS VIA FLOW-ENABLED SELF-ASSEMBLY (FESA) AND CONTROLLED EVAPORATIVE SELF-ASSEMBLY (CESA)

Approved by:

Dr. Zhiqun Lin, Advisor
School of Materials Science and Engineering
Georgia Institute of Technology

Dr. John Reynolds
School of Chemistry and Biochemistry & Materials Science and Engineering
Georgia Institute of Technology

Dr. Suman Das
School of Mechanical Engineering & Materials Science and Engineering
Georgia Institute of Technology

Dr. Vladimir Tsukruk
School of Materials Science and Engineering
Georgia Institute of Technology

Dr. Daniel Goldman
School of Physics
Georgia Institute of Technology

Date Approved: March 18th, 2015

Dedicated to my loving family

ACKNOWLEDGEMENTS

I would like to thank Prof. Zhiqun Lin for offering me the opportunity to join his research group at Georgia Institute of Technology, for his constant support and motivation and the trust in me, and for his knowledge, inspiring guidance and encouragement throughout my research during my PhD. I will appreciate all this important experience for the rest of my life and implement what I have learned to improve the quality of living of people in society. I would also like to thank all my PhD dissertation committee members, Prof. Suman Das, Prof. Daniel Goldman, Prof. John Reynolds and Prof. Vladimir Tsukruk for their helpful feedback, suggestions and kind willingness to take part in my dissertation committee.

I am also thankful to former and current members in NanoFM group. Particularly, I would like to thank Dr. Xinchang Pang, Dr. Ming He, Dr Xukai Xin, Dr. Wei Han, Prof. Shunhua Li, Prof. Yingkui Yang for their helpful discussion on current progress of today's science in general. I would also like to thank Chaowei Feng, Yanjie He, Chuchu Zhang and all the other group members for their support and help.

Finally, I am very grateful to my wife and my family for their unconditional love and support. Without them all my achievements means nothing to me.

TABLE OF CONTENTS

LIST OF TABLES

LIST OF FIGURES

Figure 1.11. (a) Schematic illustration of the wedge-on-flat geometry on a silicon surface. The height of the wedge, H was 1000 μm. (b) Stepwise representation of the morphological evolution of CBCP stripes as a function of solvent vapor annealing: first panel, as-prepared; second panel, annealed for 5 h; third panel, annealed for 10 h; last panel, annealed for 15 h. (c) Schematic illustration of the wedge-on-Si geometry with H of 500 μm. (d) Stepwise representation of the morphological evolution of CBCP stripes as a function of solvent vapor annealing time: left panel, as-prepared; central panel, annealed for 12 h; right panel, annealed for 16 h.

Figure 1.12. Representative AFM height images of conjugated polymer stripes taken in the three different regions (X_1-X_3). (a–c) P3HT; (d–f) P3BT; (g–i) P3BHT. X_1 is the outermost region, X_2 is an intermediate region, and X_3 is the innermost region, where X is the distance away from the cylinder/flat substrate contact. Image size=80×80 μm^2. Z range=400 nm for (a, d, g); 300 nm for (b, e, h); and 200 nm for (c, f, i).

Figure 3.1. (a) Chemical structure of amphiphilic diblock copolymer PS-*b*-P4VP, and scheme of the formation of PS-*b*-P4VP micelles in toluene. (b) Schematic illustration of the formation of periodic threads composed of PS-*b*-P4VP micelles (represented as red chains and red bars).

Figure 3.2. (a) Optical micrograph of parallel threads composed of PS-*b*-P4VP micelles with the spacing between two adjacent threads of 50 μm (i.e., λ_{50} = 50 μm). The scale bar = 200 μm. (b-g) AFM height images of a thread containing a monolayer and a coexisted monolayer/bilayer PS-*b*-P4VP micelles obtained at the stop times of (b) 0.5s, (c) 1.0s, (d) 1.5s, (e) 2s, (f) 2.5s, and (g) 3s, respectively.

Figure 3.3. (a) Programed movement of the Si substrate mounted on the translational stage, in which the velocity is plotted as function of time. The shaded areas represent each moving distance of 20 μm after the alternative stop of the Si substrate for 0.3s and 5s. (b) Optical micrographs of periodic threads of PS-*b*-P4VP micelles formed on the Si substrate by flow-enabled self-assembly (FESA), in which the Si substrate moved 20 μm, followed by an alternative stop for 0.3s and 5s to yield monolayer- and monolayer/bilayer-thick threads, respectively. The scale bar = 500 μm. (c-e) Representative AFM images of (c) 4 threads (i.e., 2 monolayers and 2 coexisted monolayers/bilayers), (d) single thread containing a monolayer of PS-*b*-P4VP micelles, and (e) single thread containing a coexisted monolayer/bilayer of PS-*b*-P4VP micelles (i.e., monolayers at both edges with and bilayer in the center). (f-g) Corresponding height profiles of (f) the monolayer-thick thread in (d), and of (g) the monolayer/bilayer-thick thread in (e). (h) The encoded thread pattern on the substrate represented the first sentence of the traditional Chinese song *Jasmine*. The image sizes are 80 μm x 80 μm in (c), 800 nm x 800 nm in (d), and 3 μm x 3 μm in (e), respectively.

Figure 3.4. Musical score of the traditional Chinese song *Jasmine.*

Figure 3.5. Optical micrographs of (a) relatively irregular, and (b) highly regular parallel threads of PS-*b*-P4VP micelles. The scale bar = 100 μm in both (a) and (b). (c) Relationship between λ_{min} (blue symbols) and the thread width W_{thread} (red symbols) and the stop time of the Si substrate. (d) Relationship between λ_{min} and $W_{thread.}$

Figure 3.6. (a) Schematic illustration of the flow-enabled self-assembly (side view). (b) The close-up of the meniscus stretched to a new position due to the movement of the Si substrate.

Figure 3.7. (a-b) Representative (a) TEM image of a monolayer-thick thread composed of an array of PS-*b*-P4VP/$HAuCl_4$ micelles (Au^{3+} : P4VP = 110:1) before exposure to oxygen plasma, and (b) corresponding AFM height image after exposure to oxygen plasma. (c) Schematic illustration of the formation of PS-*b*-P4VP micelles surrounded by a ring of PS-capped CdSe nanoparticles. (d-e) AFM height images of a thread composed of (d) plain PS-*b*-P4VP micelles, and (e) hybrid micelles comprising PS-*b*-P4VP micelles decorated with an outer ring of CdSe nanoparticles. A close-up of an individual hybrid micelle is shown as an inset in (e). The image sizes are 600 nm x 600 nm in (b), 1.2 μm x 1.2 μm in (d), and 1.2 μm x 1.2 μm in (e).

Figure 3.8. TEM images of PS-*b*-P4VP micelles incorporated with Au^{3+} ions within the thread at the Au^{3+} /P4VP ratios of (a) 0:1 (*i.e.*, plain PS-*b*-P4VP micelles), (b) 10:1, (c) 30:1, and (d) 110:1. (e-h) Corresponding TEM images of one single PS-*b*-P4VP micelle with the incorporation of Au^{3+} ions.

Figure 3.9. (a) and (d) TEM images of PS-*b*-P4VP micelles before the exposure to oxygen plasma. (b) and (e) Corresponding AFM height images, and (c) and (f) corresponding cross sectional analysis of Au nanoparticles obtained from the samples at the Au^{3+} /P4VP ratios of 10:1 and 110:1, respectively, after the exposure to oxygen plasma. The image sizes are 600 nm x 600 nm in (b), and 400 nm x 400 nm in (e).

Figure 3.10. TEM image of PS-*b*-P4VP micelles with the incorporation of Au^{3+} at Au^{3+} /P4VP ratio of 10:1. The sample was prepared by spin-coating PS-*b*-P4VP/$HAuCl_4$ micelles at 3000 rpm/min.

Figure 3.11. TEM image of a thread composed of PS-*b*-P4VP/$HAuCl_4$ micelles at the Au^{3+} /P4VP ratio of 110:1.

Figure 3.12. (a-b) AFM height images, and (c-d) the corresponding cross sectional analysis of threads composed of plain PS-*b*-P4VP micelles (a and c) and hybrid micelles of PS-*b*-P4VP/CdSe (b and d). (e) Schematic illustration of the formation of PS-*b*-P4VP micelles surrounded by a ring of CdSe nanoparticles with the presence of one vacancy. The image sizes 1.2 μm x 1.2 μm in (a) and (b).

Figure 4.1. (a) Schematic illustration of a home-made apparatus for FESA. (b) One typical result of uniform PMMA parallel stripes formed on Si substrate prepared by FESA of the PMMA toluene solution.

Figure 4.2. Schematic illustration of the stripe formation induced by evaporation.

Figure 4.3. Schematic illustration of the stripe formation induced by the movement of lower substrate.

Figure 4.4. Relationships between a) λ_{jump} and velocity of substrate and b) λ_{jump} and stopping time of substrate.

Figure 5.4. The fluctuations in height along two DNA spokes obtained at pH = 6.2, T = 65°C, and the concentration of DNA solution = 8 μg/ml, that is, Line 1 and Line 2, marked in AFM image in Figure 5.1.2, over a distance of 1.6 mm (i.e., the total length of a DNA spoke). We note that the height from the outermost region X_1 (h = 80 nm), to intermediate region X_2 (h = 50 nm), and to innermost region X_3 (h = 20 nm) in Figure 5.4 was slightly different from those in Figure 5.1.4 (i.e., 60 nm, 40 nm, and 20 nm from X_1, to X_2, and to X_3, respectively). This is because that the results in Figure 5.1.4 and Figure 5.1.5 were obtained from two different samples, but under the same experimental condition (pH = 6.2, T = 65°C, and the concentration of DNA solution = 8 μg/ml). It is possible that there may be a slight variation in height between two different samples. However, the trend that there was a decrease in height from the outermost region X_1 to the innermost region X_3 (evidenced in Figure 5.1.4g-i) with the height fluctuation (demonstrated in Figure 5.1.5) was real for all the samples.

Figure 5.5. Representative fluorescence micrographs of DNA spokes formed in sphere-on-PMMA-coated-Si geometry at the concentration of DNA solution = 8 μg/ml: (a-c) increasing temperature from 55 °C, 65 °C, to 71 °C, respectively, at the constant pH = 6.2; (d-f) increasing pH from 5.5, 6.2, to 7.1, respectively, at constant temperature, T = 65 °C. The white arrows marked the movement of drying front. Scale bar = 200 μm.

Figure 5.6. Summary of experimental results on the formation of DNA spokes at various pH and temperature T. The red area represented the optimum experimental conditions, within which highly aligned DNA spokes can be achieved.

Figure 5.7. (a) Schematic illustration of cylinder-on-flat geometry composed of a cylindrical lens situated on a PDMS substrate (side view). (b) Schematic illustration of formation of parallel DNA stripes on two sides of the cylinder/PDMS contact (marked as "cylinder/PDMS contact center"); similar illustrations are shown in Figure 5.1.8a. (c) A small zone of parallel DNA stripes (marked as white dashed box in (b)) yielded at pH = 6.2, T = 65°C, and the concentration of DNA solution = 8 μg/ml, emitting green fluorescence. Scale bar = 200 μm.

Figure 5.8. (a) Schematic representation of preparation of 2D arrays of DNA nanowires by two consecutive orthogonal transfer-printing using PDMS substrate. The parallel DNA stripes (i.e., a set of lines on the left and right sides in the 2nd and 5th upper panels) were formed on two sides of the cylinder/PDMS contact center. (b) Representative fluorescence micrograph of 2D arrays of DNA nanowires; scale bar = 40 μm. (c) AFM height image of a selected area in (b); image size = 20 μm × 20 μm. (d) The close-up of an overlapped area in (c); image size = 20 μm × 20 μm. (e) The corresponding height profiles of stripe 1, stripe 2, and overlapped area in (d).

Figure 6.1 a) Schematic illustration of crafting an array of high-density continuous DNA nanowires by flow-enabled self-assembly (FESA). The DNA solution was constrained between two nearly parallel plates with the lower PDMS substrate placed on a translation stage programmably moved against the upper fixed glass plate. b) Schematic representation of swelling-induced transfer printing (SIT-Printing) of DNA nanowires and the subsequent metallization of DNA nanowires by exposing them preloaded with metal salts to O_2 plasma.

Figure 6.2. Representative fluorescence micrographs of self-assembled YOYO-1-labeled DNA molecules. a) branched DNA bundles, b) continuous DNA nanowires, c) short DNA lines. d) 3D map of the DNA concentration, moving speed of PDMS substrate, and temperature for DNA pattern formation. The label a, b and c correspond to the range. of experimental conditions for yielding DNA nanostructures shown in a), b) and c), respectively. e) 2D map of the moving speed of lower PDMS substrate as a function of temperature for DNA pattern formation at the fixed concentration of 8 μg/ml. Scale bar = 500 μm in a) and c), and 100 μm in b).

Figure 6.3. Two-dimensional map of the moving speed of lower PDMS substrate as a function of temperature for DNA pattern formation at the concentrations of 6 μg/ml, 7 μg/ml, 8 μg/ml and 10 μg/ml, respectively.

Figure 6.4. Schematic representation of swelling-induced transfer printing (SIT-Printing) of DNA nanowires.

Figure 6.5. Representative fluorescence micrograph of disordered DNA nanowires yielded by casting a drop of toluene on the PDMS substrate.

Figure 6.6. Representative SEM images of Ag nanowire formed by (a) chemical reduction with Ag nanoparticles deposited all over the surface, and (b) the reduction induced by oxygen plasma. The morphologies of Ag nanowires with the increased concentrations of $AgNO_3$ (from top to bottom are 0.5mg/ml, 1mg/ml, 10mg/ml, and 50mg/ml, respectively) are shown in (b). (c) Current-voltage (*I*-*V*) characteristics of the resulting Ag nanowires from DNA nanowires preloaded with 50 mg/ml $AgNO_3$ precursors (blue: continuous nanowire; red: discontinued nanowire). Scale bar = 400 nm in both (a) and (b).

Figure 6.7. Representative SEM image of Ag nanowires and its corresponding EDS spectrum.

Figure 6.8. SEM image of Au nanoparticles produced by using the DNA nanowire as template.

Figure 6.9. Representative SEM image of sea-urchin-like Au nanoparticles using the DNA nanowire as template. The 0.004 M $AgNO_3$ and 0.08 M ascorbic acid (reducer) were added in the Au precursor solution.

Figure 6.10. AFM height and phase images of corroded DNA nanowire when applying sodium borohydride as the reducer, instead of sodium citrate. Image size = 2 μm × 2 μm.

Figure 6.11. AFM height and phase images of Au flakes grown along DNA nanowire when using borane morpholine complex as the reducer, instead of sodium citrate. Image size = 2 μm × 2 μm.

Figure 6.12. (a) Representative TEM image, and (b) 2D AFM height image of direct assembly of premade Au nanoparticles (~16 nm) by employing the DNA nanowire as scaffold.

Figure 7.10. TEM image of Au nanorods formed at CTAB concentration of 0.05M with the addition of 100-μl toluene to the Au growth solution prior to the addition of the Au seed solution.

Figure 7.11. TEM image of Au nanostructures with irregular shapes formed at low Ag^+ ion concentration (i.e., 0.04 mM by adding 40-μl 0.01M Ag^+ solution to a 10-ml Au growth solution) with the addition of 100-μl toluene. The concentration of CTAB was 0.1M.

Figure 7.12. TEM image of Au nanostructures with irregular shapes formed at low Ag^+ ion concentration (i.e., 0.04 mM by adding 40-μl 0.01M Ag^+ solution to a 10-ml Au growth solution) with the addition of 100-μl toluene. The concentration of CTAB was 0.1M.

Figure 7.13. TEM image of short Au nanorods formed at the low Ag^+ concentration (i.e., 0.04 mM) without the addition of toluene.

Figure 7.14. Prepared solution with layered structures by mixing either (a) toluene or (b) chloroform with the Au growth solution after adding the Au seed solution and gently shaking the mixed solution. (c) The proposed mechanism for the formation of ultrathin Au nanowires. Hydrophobic molecules (toluene or chloroform) preferably incorporate with the inner hydrophobic chains of the CTAB double layer, thereby leading to a decrease in the inner diameter of self-assembled cylindrical CTAB micelles, which in turn template the growth of ultrathin Au nanowires.

Figure 7.15. TEM image of Au nanorods formed on the bottom layer of solution with the addition of 100 μl toluene to the Au growth solution after adding the Au seed solution. The mixed solution was only gently shaken by hands without stirring. The growth solution was prepared by mixing 10 ml 0.1M CTAB aqueous solution with 0.5 ml 10 mM $HAuCl_4$, 40 μl 0.1 M $AgNO_3$ and 0.5 ml 0.1 M hydroquinone aqueous solution.

Figure 7.16. TEM image of Au nanorods formed on the upper layer of solution with the addition of 100-μl toluene to the Au growth solution after adding the Au seed solution. The mixed solution was only gently shaken by hands without stirring. The growth solution was prepared by mixing 10 ml 0.1M CTAB aqueous solution with 0.5 ml 10 mM $HAuCl_4$, 40 μl 0.1 M $AgNO_3$ and 0.5 ml 0.1 M hydroquinone aqueous solution.

Figure 7.17. TEM image of ultrathin Au nanowires formed by adding a 80-μl chloroform to the Au growth solution after adding the Au seed solution. The growth solution was prepared by mixing 10 ml 0.1M CTAB aqueous solution with 0.5 ml 10 mM $HAuCl_4$, 40 μl 0.1 M $AgNO_3$ and 0.5 ml 0.1 M hydroquinone aqueous solution.

Figure 8.1. a) Schematic illustration of the formation of uniform microchannels all over the colloidal thin films by FESA and b) the optical microscope image and c) SEM image of the microchannels. For figure 1, the temperature, moving velocity of lower substrate and concentration was 50℃, 13μm/s and 0.5wt% respectively.

Figure 8.2 SEM image of uniform colloidal microchannels formed by FESA at 50℃, moving velocity of lower substrate of 13μm/s and concentration of 0.5wt%..

Figure 8.3. Optical microscope images of colloidal microchannels with various spacing, which are crafted by different moving velocity of lower substrate of a) 10 μm/s, b) 8 μm/s, c) 5 μm/s and d) 3 μm/s. All scale bars are 100 μm.

Figure 8.4. Experimental data and theoretical prediction of the relationship of a) the spacing between adjacent microchannels λ_{c-c} and the moving velocity of the lower substrate v, b) λ_{c-c} and the thickness of the colloidal thin film with microchannels all over the surface H and c) H and $\frac{1}{v}$. d) optical microscope image of colloidal thin film of thickness lower than a critical value, in which the microchannels discontinued and microchannel-free region appeared.

Figure 8.5. discontinuous microchannels formed at a) lower temperature (e.g. 45℃), concentration of 0.5wt% and moving velocity of lower substrate of 13 μm/s; b) at lower concentration (e.g., 0.2wt%,), temperature of 50℃ and moving velocity of lower substrate of 13 μm/s.

Figure 8.6. a) optical microscope image and b)-c) SEM images at different magnifications of microchannels formed on chemically patterned substrate by controlled drying of PS latex particle suspension in the direct perpendicular to the PS stripes. The microchannels were formed all over the substrate except on top of PS stripes. The spacing between PS stripes is 100 μm. d) SEM image of the crack in a PS stripe induced by a formed microchannel.

Figure 8.7. a) optical microscope image and b)-c) SEM images at different magnifications of colloidal ribbons formed on chemically patterned substrate by controlled drying of PS latex particle suspension in the direct perpendicular to the PS stripes. The colloidal ribbons were only formed in the middle region between two PS stripes, due to the stick-slip motion of the contact line. The microchannels were formed inside the colloidal ribbons and the direction of the microchannels was parallel to the moving direction of the lower substrate. The spacing between PS stripes is 50 μm.

Figure 8.8. optical microscope image of microchannels formed on chemically patterned substrate by controlled drying of PS latex particle in the direct parallel to the PS stripes at 50℃, moving velocity of lower substrate of 13 μm/s and concentration of 0.5wt%. It is noteworthy that the three-phase contact line at the liquid front was strongly curved due to the hydrophobicity of PS stripes, thereby yielding the formation of curved microchannel patterns in between PS stripes.

Figure 8.9. a) optical microscope image and b)-c) SEM images at different magnifications of microchannels formed on chemically patterned substrate by controlled drying of PS latex particle in the direct parallel to the PS stripes. Curved microchannels were formed all over the substrate except on top of PS stripes due to the curved liquid water during drying of PS latex particle suspension. The spacing between PS stripes is 100 μm.

Figure 8.10. a) schematic illustration and optical microscope images of colloidal microchannels formed by the guidance of an angled upper blade of b) 60 ° and b) 30 ° at 50℃, moving velocity of lower substrate of 13 μm/s and concentration of 0.5wt%.

Figure 8.11. a) schematic illustration and b) optical microscope images of colloidal microchannels formed by the guidance of a round-shape upper blade at 50℃, moving velocity of lower substrate of 13μm/s and concentration of 0.5wt%.

Figure 8.12. a) SEM image of threads of Au NPs aligned by using prepared colloidal microchannels as template. The scale bar is 10 μm. b) schematic illustration of the formation mechanism of two threads of Au NPs in one microchannels.

LIST OF SCHEMES

SUMMARY

The use of spontaneous self-assembly as a lithography free means to construct well-ordered, often intriguing structures has received much attention for its ease of producing complex, centimeter-scale structures with small feature sizes. These self-organized structures promise new opportunities for developing miniaturized optical, electronic, optoelectronic, and magnetic devices. One extremely simple route to intriguing structures is the evaporative self-assembly of nonvolatile solutes from a sessile droplet on a solid substrate. However, flow instabilities during the evaporation process often result in non-equilibrium and irregular dissipative structures (e.g., randomly organized convection patterns, stochastically distributed multi-rings, etc.). Therefore, in order to fully control the evaporative self-assembly of solutes, two strategies, namely, controlled evaporative self-assembly (CESA) and flow-enabled evaporative-induced self-assembly (FESA) were developed to create ordered structures of various nanomaterials.

First, hierarchical assemblies of amphiphilic diblock copolymer (i.e., polystyrene-*block*-poly(4-vinylpyridine) (PS-*b*-P4VP)) micelles were crafted by FESA. The periodic threads comprising a monolayer or a bilayer of PS-*b*-P4VP micelles were precisely positioned and patterned over large areas. Second, highly aligned parallel DNA nanowires in the forms of nanostructured spokes over a macroscopic area were created via evaporative self-assembly (CESA) by subjecting DNA aqueous solution to evaporate in a curve-on-flat geometry composed of a spherical on a flat substrate. Third, large-scale aligned metallic nanowires templated by highly oriented DNA were produced by flow-enabled self-assembly (FESA). A simple yet robust swelling-induced transfer printing (SIT-Printing) technique was developed to transfer ultralong DNA nanowires onto the desirable substrate. Subsequently, the resulting DNA nanowires were exploited as templates to form metallic nanowires by exposing DNA nanowires preloaded with metal

salts under oxygen plasma. Moreover, DNA nanowires were also employed as scaffold for aligning metal nanoparticles and nanorods. Fourth, colloidal microchannels (i.e., cracks) on a large scale were yielded by fully controlling the drying process of colloidal suspensions via flow-enabled self-assembly (FESA). The influence of chemically patterned substrate (i.e., hydrophobic stripes on a hydrophilic substrate) on the formation of colloidal microchannels was explored. In addition, such colloidal microchannels with tunable center-to-center distance between the adjacent cracks, λ_{c-c} was exploited as template for aligning inorganic nanoparticles.

Importantly, theoretical study of the formation mechanism of parallel stripes of solutes by FESA was conducted. The relationship between the characteristic spacing of adjacent stripes λ_{c-c} and other experimental parameters such as the stripe width, the stop time and the moving speed of lower substrate were scrutinized. Such theoretical modeling would provide guidance for the precise design and crafting of ordered structures composed of nanomaterials by FESA in the future study.

Interestingly, during the preparation of Au nanorods, the formation of ultrathin gold nanowires were unexpectedly observed. Based on conventional synthetic route to Au nanorods using CTAB as soft-templates, we discovered that the addition of a small amount of hydrophobic solvent (e.g., toluene or chloroform) to the Au growth solution entailed the formation of ultrathin Au nanowire, rather than Au nanorods. The growth mechanism of such intriguing water-soluble ultrathin Au nanowires, differed from those formed by using oleylamine (i.e., non-water-soluble Au nanowires), was explored.

In general, the ability to craft ordered structures comprising nanomaterials by FESA and CESA provides new opportunities for organizing nanomaterials for use in electronics, optics, optoelectronics, sensors, nanotechnology and biotechnology.

CHAPTER 1

INTRODUCTION

B. Li, J. Iocozzia and Z. Lin, "Directing Convection to Pattern Thin Polymer Films: Coffee Rings" chapter in "Instability-Based Methods for Patterning Polymer Surfaces", J. Rodriguez-Hernandez and C. Drummond., Springer Press, in press, 2015 (**book chapter**)

1.1 Ordered Structure of Nanomaterials

Self-assembly of nanoscale materials to form hierarchically ordered structures has received considerable attention[1-6] as it enables high-density integration of controlled and tunable functionalities of nanoscopic building blocks into optical, electronic, optoelectronic, and magnetic materials and devices.[7-9] The ability to position and pattern nanomaterials at desired positions underpins the realization of these applications and enables the construction of hierarchical device structures.[10] To date, many work has focused on creating hierarchically assembled nanomaterials using lithographically prepared templates.[11] However, the use of lithographic methods often requires costly, complex and multistep procedures. Clearly, a low-cost strategy for achieving hierarchically structured nanomaterials over large scales is highly desirable. The use of spontaneous self-assembly as a lithography free means to construct well-ordered, often intriguing structures has received much attention for its ease of producing complex, centimeter-scale structures with small feature sizes. These self-organized structures promise new opportunities for developing miniaturized optical, electronic, optoelectronic, and magnetic devices.[12-15] To this end, evaporative self-assembly of nonvolatile solutes (*e.g.*, polymers, nanoparticles, and biomaterials, among others) from a sessile drop is widely recognized as an extremely simple and non-lithographic route to creating intriguing one- or two-dimensional structures.[16-20]

1.2 Evaporative Induced Self-Assembly

In daily life, coffee-rings are commonly seen after a droplet of coffee has dried on a table or dish. The mechanism of this phenomenon was first proposed by Deegan in 1997[16] It was found that the "coffee-ring" of solute (e.g., colloidal particles) was formed because the suspended solutes were carried by radial flow towards the edge due to larger evaporative flux at the contact line with the surface. For application such as surface coating, it is generally desirable to have a uniform deposition of material across the entire surface. Consequently, the coffee ring effect is a problematic issue for many applications such as inkjet printing. Thus, numerous studies on evaporation-induced patterning of a droplet composed of volatile solvent and non- volatile solutes have been performed in an attempt to eliminate the coffee ring effect entirely and thus enhance inkjet printing efficiency and quality. Though it seems such a phenomenon would always be considered a nuisance, research into the coffee ring effect has since redeemed it as both an interesting and useful property.

Drying droplets containing nonvolatile solutes (polymers, nanospheres, nanoparticles, DNA, etc.) on a solid substrate have been utilized to yield self-assembled structures (e.g., "coffee rings",[16] fingering instabilities,[21] cellular structures,[22] etc.), possessing dimensions from a few hundred nanometers and larger. One simple route to such interesting structures, based on the coffee ring effect, is the evaporative self-assembly of nonvolatile solutes from a sessile droplet on a solid substrate.[23] However, these dissipative structures created by evaporation are often irregular and not in equilibrium (e.g., randomly organized convection patterns within the drop, and stochastically distributed multi-rings, etc.). Yet for applications in microelectronics, data storage devices and biotechnology,[12-15] it is prerequisite to achieve surface patterns with a highly ordered spatial arrangement at large scale (square centimeters or larger). Therefore, fully controlling evaporative self-assembly as a simple route to creating

regular structures for various applications strongly depends on precise control over several factors, such as evaporative flux, radial and Marangoni flow and interactions between substrate and solutes.

To date, several studies have focusing on establishing a means of controlling the drying process of an evaporating droplet to produce highly regular structures. For example, controlled evaporative self-assembly (CESA) in a restricted geometry is a simple, rational preparation route for the creation of microscopic structures having high fidelity and regularity.[24-25] In addition, flow-enabled evaporative-induced self-assembly (FESA) stands out as an extremely simple route to creating intriguing one- or two-dimensional structures. In this strategy, the evaporation flux and the interfacial interaction between the solute and substrate are precisely controlled by programmable motion of the substrate on a motorized linear translation stage, thereby producing well-ordered structures with high fidelity and regularity.

In the following, recent progress on the theoretical study of a drying droplet both with and without solutes will be first reviewed. Then, the advances in highly ordered structures crafted by controlled evaporative self-assembly will be discussed. In particular, the focus will be on controlled evaporative self-assembly in a "curve-on-flat" geometry and flow-enabled evaporative-induced self-assembly (FESA).

1.3. Understanding "Coffee Rings": mechanism and theoretical models

A ring-like deposition can be commonly noticed after the evaporation of a solution composed of volatile solvent and non-volatile solutes. In general, the formation of coffee-ring structures of non-volatile solutes at the contact line requires the completion of four steps:

a. A capillary flow is generated towards the contact line by an evaporation rate gradient at the air-solvent interface close to the contact line. It is noteworthy that the first step is often referred to as the "coffee-ring" effect proposed by Deegan in 1997.[16] However the entire four step process is more accurately described as such with this merely being the first part in an essentially iterative process throughout the duration of evaporation.

b. The solute is effectively transported by the radial flows to the contact line[17, 23]

c. Due to the attraction between substrate and solute, the solute deposits and forms a continuous line along the contact line. Simultaneously, the contact line of the solvent is pinned at the deposition of the solute. This is known as the "pinning" process.

d. Due to the continuous evaporation of the droplet, the force induced by surface tension of the extracted liquid surface overcomes the pinning force. As a result, the contact line depins from the ring of deposited solute and jumps inward. This is known as the "depinning" process. As this process proceeds, a concentric ring-like deposition pattern is left behind with each retreating depinned contact line.

The formation of ring-like deposition pattern requires fulfillment of all the four steps in sequence. Thus the "coffee ring" cannot form if any of the four steps is not satisfied, thereby resulting in suppression of coffee-ring formation. The following sections will review the theoretical principles underlying each step as well as the related experimental studies employing them.

In addition to a requisite series of steps, there are also three essential components for the successful formation of "coffee-ring" structures. These include the volatile solvent, non-volatile solutes and the substrate (**Scheme 1**). The influence of both the non-volatile solute and substrate on the flow inside a volatile solvent drop is related to steps ***a***

and ***b***, while the influence of volatile solvents and substrates to the deposition of non-volatile solutes is related to steps ***c*** and ***d***.

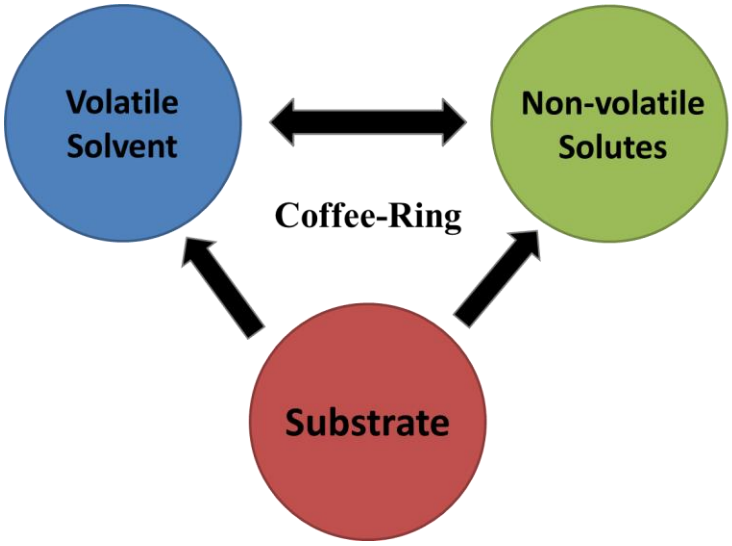

Scheme 1.1. The three essential components for the formation of "coffee-ring" structures: volatile solvent, non-volatile solutes and substrate.

1.3.1 The evaporation flux of a droplet evaporating on a substrate (i.e. step *a*, the evaporation rate difference along the meniscus)

The evaporation of droplets has been studied for a long time,[26] particularly, the evaporation of an aerosol droplet in air.[27] Intuitively, one expects that the evaporation rate of a spherical droplet, which is proportional to the surface area and thus the radius of the droplet, decreases linearly with time. However, this is only the case for evaporation of a spherical droplet in a vacuum.[28] From experiments, it is found that the squared radius of a macroscopic droplet decrease linearly with time.[29] The reason is that the evaporation is determined by the diffusion of the solvent molecules into its quiescent gas phase, rather than the vacuum.[27, 30] Notably, the evaporation flux of an aerosol droplet in air is uniform all over its surface, which is given by the Hertz- Knudsen relation[30-31]:

$$j = \alpha\sqrt{\frac{k_B T_s}{2\pi M}}\frac{\rho_s - \rho_v}{\rho_l} \qquad (1.1)$$

where k_B is the Boltzmann constant, T_s is the surface temperature, M is the mass of a liquid molecule, ρ_s is the vapor density at the surface ρ_v is the homogeneous vapor density, ρ_l is the vapor density of the liquid and α is the accommodation coefficient describing the possibility of phase change, which normally has a value between 0.1 and 1.[32-34] If the diffusion process is quasi-stationary and the temperature T is homogeneous, then the density ρ_V of the vapour obeys $\Delta\rho_V = 0$ with a fixed boundary conditions $\rho_V = \rho_\infty$ far from the drop and $\rho_V(R) = \rho_s$ just above the interface.[31] To this end, the evaporative flux can be given by the simplified equation[31]:

$$j = \frac{j_0}{R} \qquad (1.2)$$

where R is the radius of the droplet and j_0 is the evaporation parameter defined as

$$j_0 = D_m \frac{\rho_s - \rho_\infty}{\rho_L} \qquad (1.3)$$

where D_m is the diffusion coefficient of the vapor molecules in the atmosphere. From eq. (1.2), it can be seen that the evaporation flux for a spherical droplet is related to the droplet size.[35] Furthermore, the evaporative flux of a hemispherical droplet on a substrate can also be assumed to be $j = \frac{j_0}{R}$. When the contact angle θ is smaller than 90°, the evaporation flux was calculated by an analogous electrostatic problem of a charged lens at fixed potential by Deegan[16]

$$j(r) \propto (R - r)^{-\lambda} \qquad (1.4)$$

where $= \frac{\pi-\theta}{2\pi-\theta}$, R is the radius of the pinned droplet and r is the distance to the center of a droplet. From eq. (1.4), it can be seen that the evaporative flux increase nonlinearly from the center of the droplet to the edge (i.e., the contact line). Notably, when the contact angle is sufficiently small, λ will be ~0.5. Hence, the evaporation of a thin droplet (i.e., with small contact angle) is analogous to the evaporation of a thin film. This point will be discussed later. Hu & Larson achieved better fit for eq. (1.4), given by[36]

$$j = j_0 \frac{J_0(\theta)}{R}\left(1 - \left(\frac{r}{R}\right)^2\right)^{-\lambda} \qquad (1.5)$$

where

$$J_0(\theta) = (0.27\theta^2 + 1.30)\left(0.6381 - 0.2239\left(\theta - \frac{\pi}{4}\right)^2\right) \qquad (1.6)$$

Importantly, for a droplet with contact angle larger than 90° (i.e., evaporation of a droplet on a hydrophobic surface), the evaporative flux will be much different (as shown in **Figure 1.1**).[37] When the contact angle is smaller than 90°, the evaporative flux increase towards the contact line; when the contact angle is equal to 90°, the evaporative flux is constant all over the surface; when the contact angle is larger than 90°, the evaporative flux deceases when close to the contact line. A more detailed study with similar results was also reported elsewhere.[38]

It is noteworthy that the radius and volume change of a droplet,[35, 39-42] and the dynamics of the moving contact line[43-45] are of particular physical interests, however they will not be discussed in this review. Discussion will focus only on the evaporative flux along the surface of the droplet, which results in the radial flow inside the droplet.

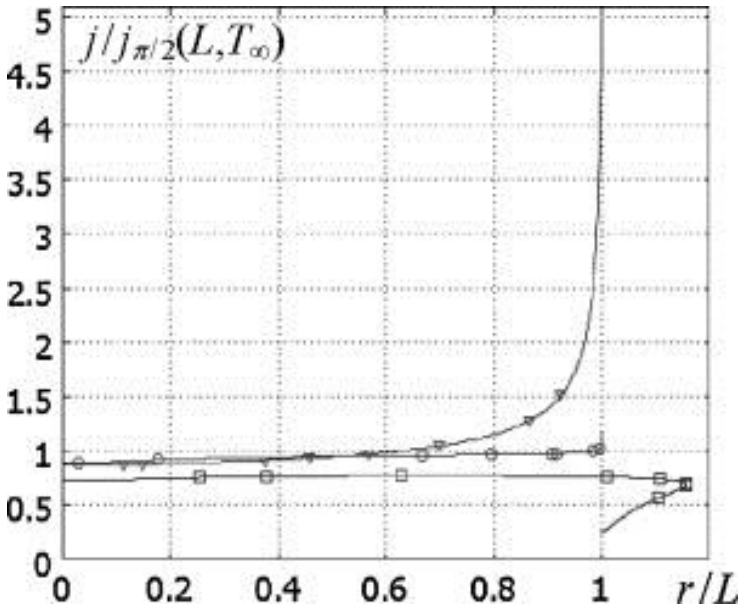

Figure 1.1 Calculated distributions of local normal evaporative flux over the droplet surface, L = 1mm. circles: $\theta = \pi/2$; squares: $\theta = 2\pi/3$; triangles: $\theta = 2\pi/9$.[38]

It is reported that thermal conductivity of the substrate can strongly influence the evaporative flux throughout (**Figure 1.2**).[46]

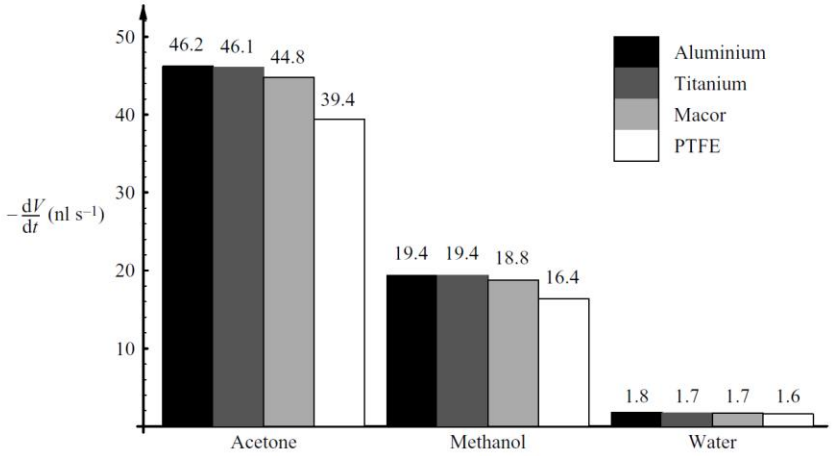

Figure 1.2 Summary of theoretically predicted values for the total evaporation rate of a droplet of acetone, methanol and water of radius R =1.35 mm on substrates of Al, Ti, Macor and PTFE.[46]

A distinct approach for describing the evaporation of volatile thin films can also be employed for calculating the evaporation flux of a thin droplet (or a thin disc).[47] The difference between thin film and thin droplet is that the height (i.e., thickness) of a droplet changes with the distance to the center, however the thickness of thin film is uniform. In this approach, the influence of the gas phase on the evaporative flux is neglected. Thus, the liquid phase and vapor phase are decoupled in calculation. Such a model is referred to as a non-equilibrium one-sided (NEOS) model while the abovementioned model developed by Deegan is referred to as the lens model. Based on the Clausis–Clapeyron law,[48] which is used to relate the temperature and the pressure, the boundary condition at the liquid–gas interface is given as[33]

$$j(h) = \frac{1}{h+K+W} \qquad (1.7)$$

where K is the non-equilibrium parameter[49], W is the thermal effect given by $W = \frac{kd_s}{k_s d_0}$, where k is the liquid thermal conductivity, k_s is the thermal conductivity of substrate, d_0 is the liquid thickness and d_s is the thickness of substrate. By assuming that the shape of a droplet is still a spherical cap, the thickness h can therefore be determined by r, the distance to the droplet center. Furthermore, the evaporative flux is also dependent on the distance to the droplet center. According to the lens model (i.e., eq. (1.4) and eq. (1.5)), the evaporative flux diverges at the contact line. However, based on the NEOS model, for $h = 0$ at the contact line, the evaporative flux is still a finite number. The difference of evaporative flux predicted by two models is shown in **Figure 1.3**.[49] It can be seen that, in the lens model the evaporative flux is significantly larger close to the contact line, compared to NEOS model. In addition, for the evaporation of a water droplet on Si wafer, it was found that the volume change with time predicted by NEOS model fitted the experimental results well, while the lens model overestimated the volumes because of the singularity of evaporation flux at the contact line.[49]

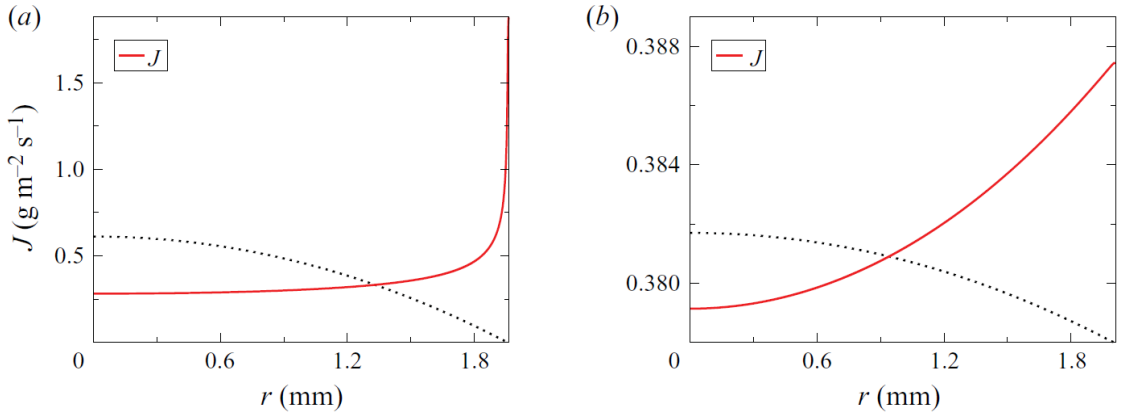

Figure 1.3 Evaporative flux j of a water droplet as a function of the radial coordinate r predicted by (a) The lens model. (b) The NEOS model. The solid red lines represent j, and the dotted lines represent the corresponding drop profile.[49]

Clearly, even though the lens model allows the prediction of evaporative flux with contact angle ranging from 0° to 90°, the divergence of the evaporative flux at the contact is not physically true and needs to be corrected.[50] One way to solve this problem is to assume the formation of a thin film at the contact line region. Therefore the evaporation flux at the contact line can be calculated using the NEOS model (i.e., eq. (1.7)). [51-52] It is noteworthy that the assumption of the presence of a thin liquid film formed upon receding of contact line has been indirectly shown to exist by using a grafted substrate.[53]

The theoretical models of the evaporation of a droplet on a substrate have been intensively studied during the past years.[54-64] However, the evaporative flux along the droplet surface has been rarely measured experimentally. Typically, the global evaporation rate over the entire surface of a droplet was provided in experimental data. To this end, the singularity of evaporative flux at the contact line remains a question. Thanks to the development of digital holographic interferometry, the local evaporative flux of an evaporating droplet can now be determined (**Figure 1.4**).[65] It is clear shown that the evaporative flux did not significantly increase close to the contact line and the

evaporative flux at the contact line region predicted by a modified lens model failed to show good agreement with experimental results.[65]

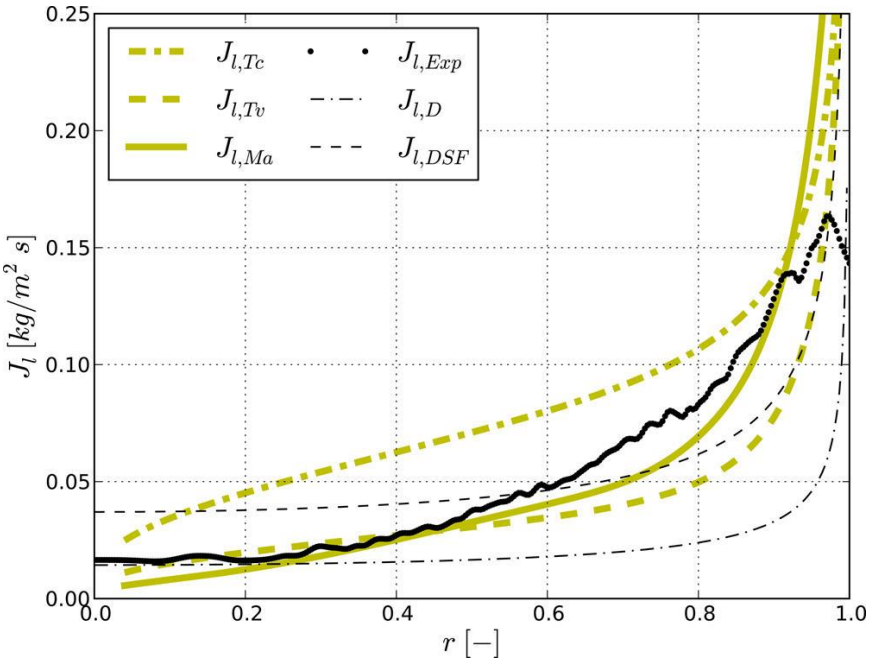

Figure 1.4 Local evaporation rates versus *r*, the dimensionless radial distance to the center of a droplet. The black dotted line shows experimental results while the others are calculated results from models.[65]

1.3.2 The flow inside of the droplet (i.e. step b)

It is straightforward that the evaporative flux at the contact line will result in radial flow inside of a droplet to compensate the liquid loss at the contact line. However, the flow inside of an evaporating droplet turns out to be more complicated. It was found that radial flow, which facilitates coffee-ring formation, and Marangoni flow, which reverses coffee-ring formation, could occur during evaporation and ultimately lead to entirely different deposition patterns.

1.3.2.1 Radial flow

During the drying of a sessile droplet, the mass loss of liquid evaporating from the contact line is replenished by the migration of liquid from the interior, thereby causing a radial flow which carries solutes towards the contact line in the process. This is the reason for coffee-ring formation first noticed by Deegan in 1997.[16] In this work, the mass of solute accumulated at the contact line, $M(R,t)$ was found to follow the expression $M(R,t) \sim t^{1.37}$,[16] where t is the time of evaporation.Furthermore, the expression of evaporative flux allows for the prediction of the solute transport to the contact line $v(r,t)$ (i.e., the velocity of the radial flow at time t), which was given by the following equation[17]

$$v(r,t) = \frac{-1}{\rho r h}\int_0^r r\left(j(r)\sqrt{1+\left(\frac{\partial h}{\partial r}\right)^2} + \rho\frac{\partial h}{\partial t}\right)dr \qquad (1.8)$$

where ρ is the density of the liquid and h is the position of the air-liquid interface. However, as the velocity of radial flow is obtained by the expression of evaporative flux, the singularity at the contact line remains problematic. To this end, Fisher employed the NEOS approximation to determine the radial flow at the contact line.[66] Notably, the evaporative flux was assumed to decrease exponentially near the contact line due to the effect of solute deposition at the contact line, and the evaporative flux expression was thus modified to[66]:

$$j(h) = \frac{1}{h+K}\left[1 - e^{-A(r-1)^2}\right] \qquad (1.9)$$

By assuming the contact line was always pinned during evaporation, the velocity of radial flow was given by

$$v = -\frac{1}{Ca}\frac{\partial}{\partial r}\left[\frac{1}{r}\frac{\partial}{\partial r}\left(r\frac{\partial h}{\partial r}\right)\right]\left(\frac{1}{2}z^2 - hz\right) \qquad (1.10)$$

where Ca is the capillary number, and z is the vertical distance to the substrate. Thus, the velocity vectors can be obtained (**Figure 1.5**).[66] In general, as the evaporative flux was higher at the contact line, the capillary force created a radial flow towards the contact line.[16] Moreover, Popov also proposed an analytical solution to the evaporation of volatile solvent with low solute concentrations by assuming that solute occupied finite volume.[67] In addition, both the height and width of the deposition ring as a function of time were evaluated. By taking into account the convection, diffusion and adsorption of the solute, an extended model for predicting the radial flow was developed with improved accuracy.[50] Notably, the deposition pattern left by the evaporation of a droplet with an unpinned contact line was also provided.

Recently the radial flow was measured experimentally using particle image velocimetry (PIV) analysis.[68] Interestingly, the velocity of a radial flow increased from zero at the center to its maximum at around 70% of the radius of the droplet, which remained pinned during evaporation (**Figure 1.6**).[68] Interestingly, the intermediate radial position of maximum velocity within the droplet is not considered in all the previously mentioned models. All previous models predicted a maximum velocity at the contact line. Moreover, the maximum velocity increased by an order of magnitude in the final moments of the pinned evaporating droplet. According to experimental results, at the early stage of the evaporation of a droplet the velocity can be well predicted by models that assumed evaporation occurs only at the contact line.; In contrast, in the final stage of droplet evaporation (at approximately 70% of the entire evaporation time) models that assumed evaporation occurred uniformly over the entire droplet agreed well with experimental data.[68] To this end, it can be concluded that the theoretical models proposed by Deegan,[16-17, 23] Fischer[66] and Popov[67] still provide good predictions of the velocity of the radial flow at the early stage of evaporation. Furthermore, a similar study also observed that the velocity of radial flow reached its maximum at an inner radial position

(at around 80% of the radius of the droplet) from the contact line, instead at the contact line.[69] The concentration of solute was found to strongly influence the velocity of the radial flow as it affects the viscosity of solution.[69-70]

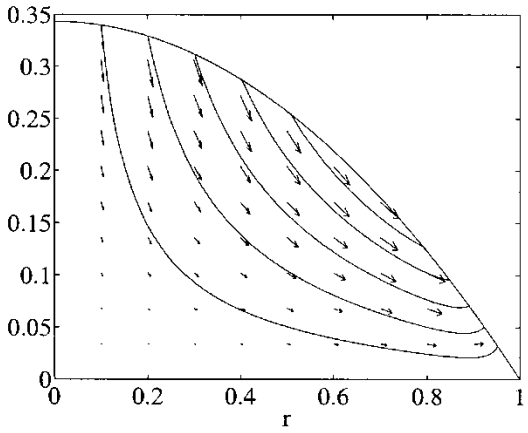

Figure 1.5 Representative streamlines and velocity vectors for a pinned droplet in which the evaporative mass flux is given by eq. 9. Fluid flows from the center of the droplet toward the contact line.[66]

1.3.2.2 Marangoni flow

Marangoni flow was first described in the early 1900s.[71] The effect has been observed for centuries and is the cause of the "tears of wine" phenomenon. The effect is induced by a surface tension gradient resulting from a concentration or temperature gradient along the liquid surface.[72] Different from the radial flow induced by evaporative flux at the contact line, Maragoni flow is circular in nature and carries solutes near the liquid surface inward toward the top of the droplet and then plunges them downward to the bottom-center of the droplet where they are carried along the substrate to the edge where they are recirculated back to the top (**Figure 1.7**).[73] This surface tension- induced circular flow has been intensively studied in interesting "self-organized" flat liquid structures called Bernard cells.[74-77]

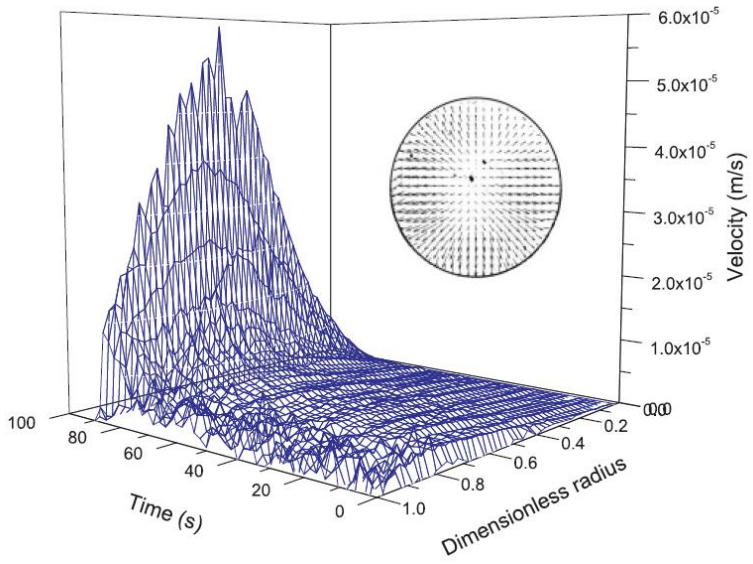

Figure 1.6 Three-dimensional Spatiotemporal evolution of the flow field, measured just above substrate, in an evaporating water droplet. Inset shows that the velocity vectors are those of a radially outward flow.[68]

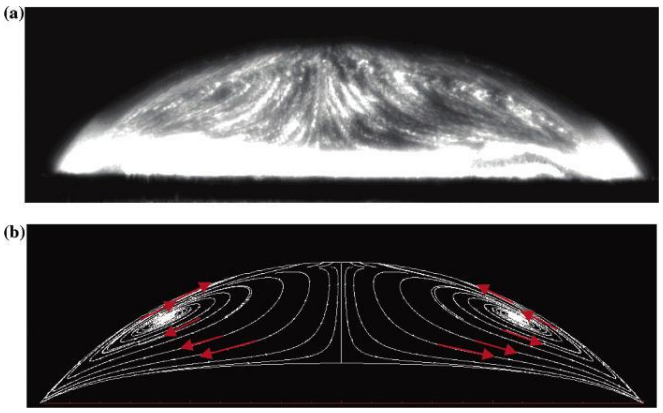

Figure 1.7 Flow field in a drying octane droplet: (a) imaged experimentally, and (b) predicted. To observe a clear Marangoni vortex, the illumination plane was moved forward about 0.66 mm from the symmetrical axis of the droplet.[73]

In an evaporating droplet, the nonuniform evaporation flux will produce a temperature gradient, thereby generating a surface tension gradient along the surface and inducing a Marangoni flow. To date, Marangoni flow has been observed in various liquid

droplets (e.g., ethanol, methanol, acetone). [78-80] The theoretical study of Marangoni flow was proposed by Pearson and Nield.[81-82] The Marangoni number (i.e., Ma) was introduced to characterize the importance of surface tension forces caused by the temperature gradient. If the Marangoni number exceeds a critical value, a Marangoni flow will be induced.[83] The Marangoni number is defined as[84-85]

$$Ma = \frac{\Delta\gamma L}{\eta D} \qquad (1.11)$$

where $\Delta\gamma$ is the surface tension gradient, L is the size of the system where $\Delta\gamma$ (i.e., surface tension gradient) exists, η is the viscosity of solution and D is the diffusion coefficient of solvent. It is important to note that Marangoni flow can be strongly influenced by the contact angle of a droplet and that this is not considered in eq. (1.11).[86]

However, it remains questionable as to whether the Pearson-Nield model can be accurately applied to volatile liquid systems.[87] This is because experimental results show that energy is transported from the vapor phase to the liquid-vapor interface which is opposite to the assumption made in the Pearson-Nield model. Moreover, it was predicted that thermally driven Marangoni flow would exist in an evaporating water droplet, which was not observed in experiments.[72, 88] The suppression of Marangoni flow in a water droplet may be attributed to the surfactant contaminants.[89] In addition, whether the temperature at the contact line is cooler than the top of the droplet is also unclear.[17, 90]

Almost all the circular flow observed in evaporating droplets can be attributed to Marangoni flow. However, it was found recently that Rayleigh convection can also induce circular flow inside of a water droplet on a hydrophobic substrate (**Figure 1.8**).[91] Rayleigh convection is generated by the concentration gradient of solutes (e.g., NaCl) induced by the evaporation of water droplet.[91]

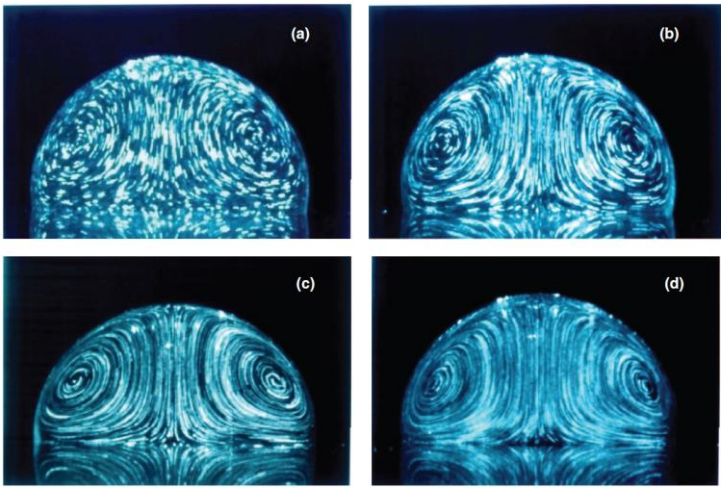

Figure 1.8 Flow inside evaporating droplets with different NaCl concentrations: (a) 0.01 wt.% (evaporation time (ET) ~ 39 min); (b) 0.1 wt.% (ET ~ 45.7 min); (c) 1 wt.% (ET ~ 50.5 min); and (d) 10 wt.% (ET ~ 63 min). Exposure time was 20 s for (a), (b), and (c) and 2 s for (d). The substrate was placed on a glass substrate coated with the amorphous fluoropolymer Teflon.[91]

1.3.3 The pinning and depinning of the contact line (i.e. step c and step d)

Due to radial flow carrying solutes towards the contact line, the solutes deposit and form a coffee ring-like pattern resulting in the pinning of the contact line and preventing its recession inwards during evaporation. In some circumstance, even though solutes are successfully transported to the contact line by radial flow and negligible Marangoni flow, the solutes may still not be able to deposit onto the substrate. This in turn fails to pin the contact. As discussed in **Scheme 1.1**, either the interaction between the solutes or the interaction between the solutes and substrate will affect the deposition of solutes on the substrate, thereby determining the pinning of the contact line. For example, if the spherical colloidal particles are replaced by elongated ones, a uniform deposition will be left after evaporation of the droplet, because of the jamming of a monolayer of elongated colloids at the surface of the droplet suppressing the "coffee-ring" formation.[92] Moreover, by changing the colloidal particle surface charges or van de Waals interactions between particles, the coffee-ring formation can also be suppressed.[93]

If there is a repulsion between substrate and solutes (i.e., negative Hamaker constant), the solute transported to the edge will move with the receding contact line and no deposition is observed. In contrast, rather than coffee-ring pattern, strong attractions between solutes and substrate (i.e., DLVO interactions) yielded uniform deposition of solutes on substrate. [94-95]

Depinning is the process whereby the liquid phase detaches from the deposited solute ring. However, detailed theoretical studies of the depinning process have not yet been reported.[67] The mechanism of the depinning process is straightforward. The depinning force is determined by the surface tension of the liquid meniscus at the contact line. During the evaporation process, the depinning force gradually increases while the contact angle continues to decrease until a critical contact angle is reached. Upon further decreasing of the contact angle, the pinning force at the contact line cannot compensate the depinning force, and as a result, the droplet edge depins from the contact line and moves back.[96] Recently, by programmably crafting solute (i.e., diblock copolymer micelle) stripes with a series of different widths, it was found that the pinning force is proportional to the width of the deposited ring.[97] The increase of the width of the deposition ring (i.e., stripe) leads to the decrease of the critical contact angle and an increase in the depinning force.

1.4. Controlling "Coffee Rings": highly ordered structures by controlled evaporation

Pinned drying droplets containing nonvolatile solutes (e.g., polymers, viruses, DNAs, microspheres, nanoparticles, carbon nanotubes, etc.) yield intriguing one or two-dimensional patterns after complete evaporation of solvent. To date, there have been

several impressive studies investigating the use of evaporation to form well-ordered structures rapidly and cheaply over large areas by deliberately controlling the evaporation process.[24, 96, 98-110] Notably, several approaches have been successfully used to generate patterns by confining the evaporating solution in different geometries, such as cylindrical tubes,[111-112] crossed cylindrical mica,[113] "curve-on-flat" geometry and nearly parallel-plate geometry. Here we will only focus on the last two approaches and review the recent progress.

1.4.1 Controlled evaporative self-assembly in a "curve-on-flat" geometry

Controlled evaporative self-assembly in a "curve-on-flat" geometry has been shown as a simple, rational preparation route for the creation of microscopic structures having high fidelity and regularity.[24-25, 114-115] If a droplet of solution is allowed to evaporate in a "curve-on-flat" geometry composed of a curved upper surface situated on a flat substrate (i.e., forming a capillary-held solution), self-assembled structures of high regularity can be generated.[116] Similar to the free evaporation of a droplet on substrate, the evaporation flux also reaches its extremity at the region close to the contact line, leading to highly ordered deposition due to the geometrical restriction.[24-25, 96, 108, 110] In addition to concentric rings of polymers, nanoparticles,[96, 117] carbon nanotubes,[105] graphenes,[118] and other ordered yet complicated structures can also be produced in the "sphere-on-flat" geometry, including spokes,[96] fingers,[107-108] "snake-skin",[119] and serpentines[106] by carefully tuning the experimental parameters such as the concentration and the interaction between solutes and substrates.

Due to the various potential applications of poly[2-methoxy-5-(2-ethylhexyloxy)-1,4-phenylenevinylene] (MEH-PPV) in light emitting diodes (LED), photovoltaic cells (PVCs) and thin-film transistors (TFTs),[120] the synthesis of highly regular concentric rings of MEH-PPV has been investigated by controlled evaporation in a sphere-on-flat

geometry (**Figure 1.9**)[24]. Since the slowly drying front is arrested (pinned) in the geometrical restriction, the evaporation flux reached the extremity at the region close to contact line. During the evaporation of the solution, the contact line was pinned by MEH-PPV deposition (i.e., "stick"), thereby yielding the formation of a MEH-PPV "coffee ring". The contact angle gradually decreased to a critical contact angle, at which point the depinning force overcomes the pinning force leading to the contact line jumping inward to a new position where the initial contact angle is restored (i.e., "slip"). As shown in **Figure 1.9b**, the "slip" distance (i.e., λ_{c-c}) slowly decreased with increasing proximity to the sphere/Si contact center. Notably, theoretical predication of the height of the concentric rings based on the Navier-Stokes equation with lubrication approximation provided a good agreement with the experimental data.[24] In addition, the solution concentration and solvent vapor pressure were also found to have strong influence on λ_{c-c} and the heights of concentric rings.[24] It is also noteworthy that, due to the applications of organometallic polymer in magnetic data storage,[121-123] photonic devices[124-125] and redox-active materials,[126-127] highly ordered concentric rings of organometallic polymers (e.g., poly(ferrocenyldimethylsilane) (PFDMS)) was also obtained by confining PFDMS/toluene solutions in sphere-on-flat geometry.[104, 110] The subsequent pyrolysis of concentric PFDMS rings yielded ferromagnetic ceramics containing α-Fe nanoparticles.[128] Interestingly, once the low concentration PFDMS toluene solution was used for pattern, the PFDMS rings would break into dots due to the surface tension-driven Rayleigh instability at the contact line.[104, 110]

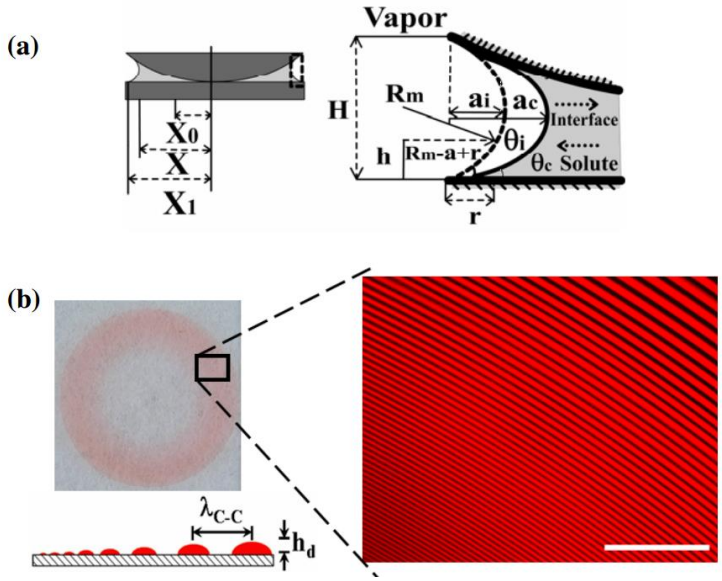

Figure 1.9 a) Upper left: Schematic cross section of a capillary-held solution containing a nonvolatile solute placed in a "sphere-on-flat" geometry. X_1, X, and X_0 are the radii of outermost, intermediate, and innermost rings from the sphere/flat contact center, respectively. Upper right: close-up of the capillary edge marked in the left panel. b) Bottom left: Digital image of entire gradient concentric rings formed by the deposition of MEH-PPV in the geometry shown in (a). Bottom right: A small zone of the fluorescent image of MEH-PPV rings in red is shown. Scale bar=200 mm. As the solution front moves inward, the rings become smaller and the height decreases as illustrated in lower left schematic.[24]

Quantum dots (QDs) are highly emissive nanoparticles[129-131] due to their quantum-confinement property, offering promising opportunities in light emitting diodes (LED),[132-135] photovoltaic cells (PVCs),[136-138] biosensors[139-141] and bio-imaging.[142-143] By passivation of the vacancies and trap sites on CdSe surface with ZnS, the prepared CdSe/ZnS core/shell QDs have bio-applications[144-145] due to their strong photoluminescence.[146-148] To this end, QDs with two sizes (i.e, 4.4 and 5.5nm in diameter) were prepared by passivation with a monolayer of tri-n-octylphosphine oxide (TOPO) to enhance solubility in toluene while retaining the spectroscopic properties and preventing aggregation.[96] Notably, the evaporation-induced self-assembly of larger CdSe/ZnS core shells QDs (i.e., 5.5nm in diameter) yielded concentric rings through the use of sphere-on-flat geometry confinement.[96] It was also found that the presence of

excess surface capping ligand TOPO lead to no concentric ring pattern formation. Whereas concentric rings formed using larger QDs under optimized conditions, spokes were generated exclusively during the drying of the solution when smaller QDs were used (i.e., 4.4nm in diameter) (**Figure 1.10**). The formation of spokes was caused by fingering instabilities at the liquid front. [99, 149-151] The reason for the distinct deposition patterns formed by large and small QDs was attributed to the moving speed of the liquid front during evaporation.[96] The slow moving speed induced fingering instability at the liquid front.[150] However, theoretical model for the stripe-spoke transformation has not been proposed.

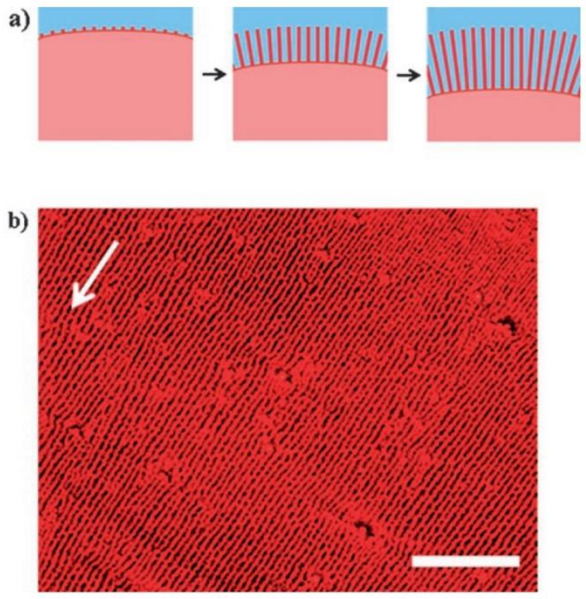

Figure 1.10. a) Formation of spoke patterns upon evaporation from the capillary bridge in the sphere-on-flat geometry. b) Optical micrograph showing the spokes formed by drying 4.4-nm CdSe/ZnS toluene solution (c = 0.25 mgmL^{-1}). The scale bar is 100 mm. The arrow on the upper left indicates the direction of the movement of the solution.[96]

Moreover, gradient concentric rings (i.e., stripes) of asymmetric comb block copolymer (CBCP) were yielded by constraining CBCP toluene solution in a wedge-on-flat geometry during evaporation (**Figure 1.11**).[152] The height of the wedge strongly affected the deposition pattern of CBCP. In general, large wedge height lead to straight

stripes of CBCP while small wedge heights lead to jagged stripes.[152] Intriguingly, hierarchically ordered patterns of CBCP were produced by subsequent solvent vapor annealing, because that solvent vapor induced unfavorable interfacial interaction between CBCP rings and the Si substrate lead to the destabilization of CBCP substrate at the microscopic scale.[152] Moreover, within the microscopic stripes, CBCP phase separation was observed at the nanoscale (i.e., CBCP nanocylinders). The nanocylinders oriented either vertically or horizontally to the substrate, depending on the vapor annealing time.

On the other hand, chemically patterned surfaces consisting of gradient stripes of poly(methyl methacrylate) (PMMA) segments created by a wedge-on-flat geometry can be used for directing hierarchical ordered block copolymer structures.[153] First, PMMA stripes were generated by controlled evaporation in the wedge-on-flat geometry; then PMMA segments (i.e., ultrathin PMMA stripes) chemically adsorbed on the Si substrate were obtained after extensive washing with solvent. Finally, asymmetric diblock copolymer, polystyrene-block-poly(ethylene oxide) (PS-*b*-PEO) thin film was spin-coated on the prepared chemically patterned surfaces. After mixed-solvent vapor annealing, PS-*b*-PEO stripes would segregate on the ultrathin PMMA stripes.[153] Such chemically patterned surfaces may serve as templates for incorporating other functional nanomaterials or studying cell adhesion.[153]

Due to promising applications in photonics, biosensors, electronics and solar cells, conjugated polymers (e.g., poly(3-hexylthiophene) (P3HT) and poly(3-butylthiophene) (P3BT)) have attracted great attention. To this end, stripes of two conjugated homopolymers (P3HT and P3BT) and one all-conjugated diblock copolymer (P3BHT) were crafted by controlled evaporation in a cylinder-on-flat geometry (**Figure 1.12**). Due to the different interfacial interactions between conjugated polymers and substrate, microscopic stripes (straight or wavy) consisting of nanoscale fiber-like or nodule-like domains were formed. Furthermore, the improved crystallinity of all-

conjugated diblock copolymer stripes by vapor annealing could lead to a fourfold increase in electrical conductivity.[154] In addition, hierarchically-assembled structures can be realized such as amphiphilic diblock copolymer (poly(styrene)-blockpoly(4-vinylpyridine) (PS-*b*-P4VP)) stripes produced via controlled evaporation in a cylinder-on-flat geometry. Such stripe structures processed mophology on the microscopic scale as well as self-assembly of PS-*b*-P4VP micelles arrays on the nanometer scale.[155]

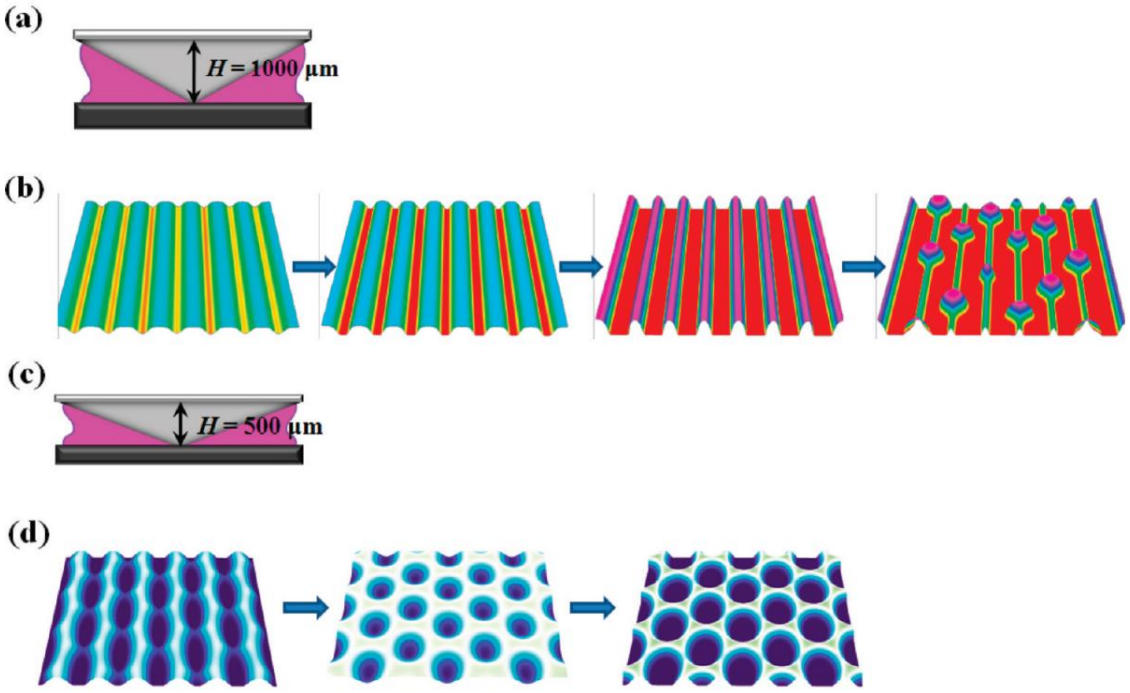

Figure 1.11. (a) Schematic illustration of the wedge-on-flat geometry on a silicon surface. The height of the wedge, H was 1000 µm. (b) Stepwise representation of the morphological evolution of CBCP stripes as a function of solvent vapor annealing: first panel, as-prepared; second panel, annealed for 5 h; third panel, annealed for 10 h; last panel, annealed for 15 h. (c) Schematic illustration of the wedge-on-Si geometry with H of 500 µm. (d) Stepwise representation of the morphological evolution of CBCP stripes as a function of solvent vapor annealing time: left panel, as-prepared; central panel, annealed for 12 h; right panel, annealed for 16 h.[153]

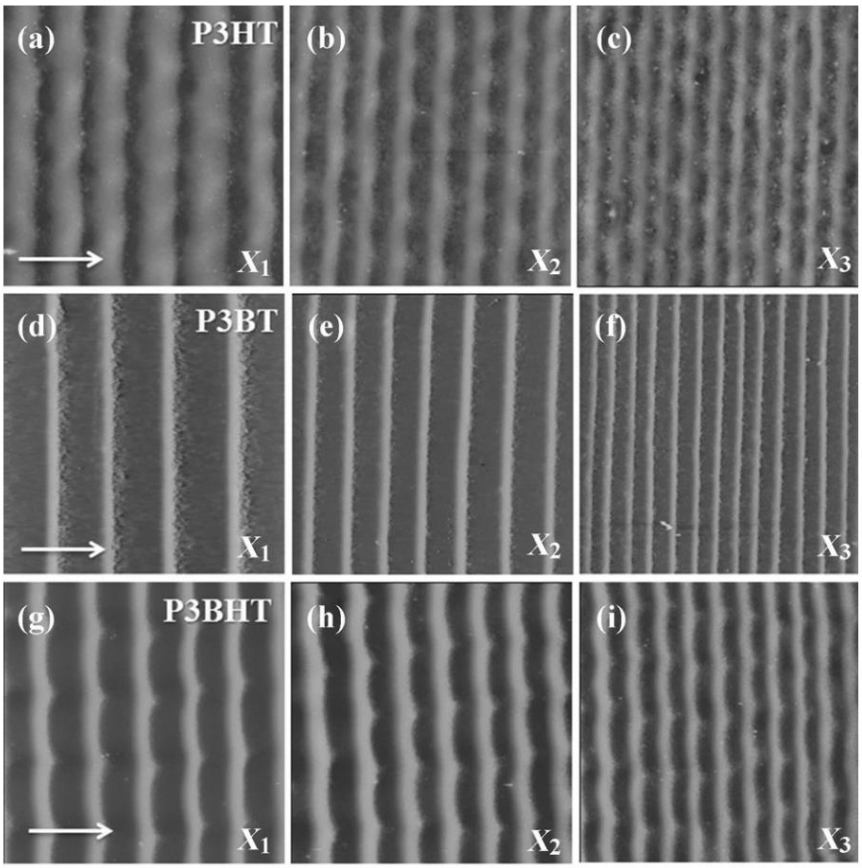

Figure 1.12. Representative AFM height images of conjugated polymer stripes taken in the three different regions (X_1-X_3). (a–c) P3HT; (d–f) P3BT; (g–i) P3BHT. X_1 is the outermost region, X_2 is an intermediate region, and X_3 is the innermost region, where X is the distance away from the cylinder/flat substrate contact. Image size=80×80 μm^2. Z range=400 nm for (a, d, g); 300 nm for (b, e, h); and 200 nm for (c, f, i).[154]

In addition to synthetic polymer structures, highly aligned DNA nanowires (i.e., spokes) were successfully created by confining aqueous DNA solutions to a curve-on-flat geometry (i.e., sphere-on-flat or cylinder-on-flat) during evaporation.[153] Unlike coffee-ring structures(or stripes), DNA nanowires formed perpendicular to the contact line. The extremities of DNA were able to anchor to the hydrophobic substrate under certain range of pH. Thus, analogous to aligning seaweeds on the beach during the ebbing tide, DNA molecules were preferentially accumulated at the fingers of the liquid front and stretched straight by the capillary force exerted on DNA molecules during the recession of contact

line.[153] In addition, it was also found that the pH and temperature of aqueous DNA solutions strongly influenced the formation of DNA nanowires. For example, increasing the pH of the solution lead to a transition from spoke-like patterns to coffee-ring-like patterns.[153]

In general, controlled evaporative self-assembly in a "curve-on-flat" geometry is a simple, rational preparation route for the creation of ordered self-assembled structures having high fidelity and regularity. The confinement of evaporating solutions turns out to be an effective means of achieving regular patterns. However, a restricted geometry always results in regular pattern with gradient parameters (e.g., progressive decrease in center-to-center distance between the deposits ($\lambda_{c\text{-}c}$) as the solution front moves to the center of the restricted geometry). Furthermore, the variables that dictate the formation of regular patterns are limited by the choice of concentration, temperature and solvent at the outset of an experiment.

1.4.2 Flow-enabled self-assembly in two-plate geometry

The concept of flow coating came from "slot coating", which has been widely used in the coating industry since 1960s.[156-160] The thickness of the coated liquid layer is set by the prescribed flow rate fed into the coating die and is independent of other process variables. This makes this method ideal for high-precision coating. Starting in the late 1990s, the National Institute of Standards and Technology (NIST) developed the flow coating technique for producing gradients. Termed "flow coating," it is a modified blade-casting technique.[161-164] In a typical flow coating process a highly concentrated polymer solution (1–5% mass fraction) is injected into the gap between a doctor blade positioned over a flat substrate (e.g., silicon wafer) mounted on a computer-controlled translation stage.[162]

If the concentration is low, rather than thin films dissipative structures (e.g., convection patterns, fingering instabilities, etc.) are produced.[102] Such work was subsequently used to topographically control neurite extension on stripe-patterned polymer films,[165] fabrication of periodic micro-structured honeycomb films having multiple periodicities, and polymer nanoparticles.[166] Large-scale ordering was observed. This was defined by the periodic thickness modulation of a block-copolymer film due to the self-organization of the receding contact line.[167]

For example, hierarchically assembled amphiphilic diblock copolymer (e.g., PS-*b*-P4VP) micelles were successfully produced by subjecting PS-*b*-P4VP micelles solutions to evaporate in between two nearly parallel plates.[97] Unlike the curve-on-flat geometry, the lower substrate was mounted on a programmable motorized linear translational stage. Highly regular and parallel threads of PS-*b*-P4VP micelles were crafted by a "stop-and-move" procedure.[97] First, the lower substrate remains still for a period of time (i.e., "stop") to allow a thread of micelles to form at the contact line. Then the lower substrate is moved (i.e., "move") at high speed to the next position set by computer, allowing for the generation of the next thread. Thus, periodic parallel threads can be created by these repeated "stop-and-move" cycles. In general, longer stopping times lead to larger widths of threads. Larger move distance leads to larger spacing between threads. Importantly, both the stopping time and the move distance can be controlled, thereby yielding programmable deposition patterns on the substrate. Notably, by varying the stop time, monolayer and monolayer/bilayer thickness threads can be crafted.[97] Interestingly, by controlling the formation of threads using the substrate, the jumping distance of a depinned contact line can be measured.[97] In addition, the precisely positioned PS-*b*-P4VP micelles can be converted into Au nanoparticle arrays by exposing PS-*b*-P4VP micelles to Au precursors under oxygen plasma.

An important distinction to be made is that instead of being induced by spontaneous evaporation of solvent, the movement of the contact line will be controlled by the motion of the lower substrate, resulting in a programmable “stick-slip” motion in FESA. Therefore, ordered patterns (e.g., thin films, stripes and spokes) can be readily produced in a controllable manner. Notably, the transition between the different patterns may be observed by gradually tuning each variable individually (e.g., velocity of lower substrate). The influence of each variable on the evaporative self-assembly process can also be scrutinized separately.

In this chapter, an overview of the mechanism of “coffee-ring” formation; including theoretical studies on evaporative flux of a volatile droplet, radial and Marangoni flow inside a droplet, and the pinning and depinning process during evaporation, were provided. In addition, highly ordered structures created by confining evaporation in restricted geometry were reviewed. The ability to craft well-defined, dissipative structures from a variety of materials at low cost opens up avenues to novel advanced functional systems and devices in the near future.

.

.

CHAPTER 2

RESEARCH GOAL, OBJECTIVES AND OVERVIEW

2.1. Goals

The **goal** of the proposed work is to (1) develop simple yet robust, one-step techniques, that is, ***flow-enabled self-assembly (FESA) and controlled evaporative self-assembly (CESA),*** to ***craft ordered structures of nanomaterials*** that process high regularity in a precisely controllable manner, dispensing with the need for lithographic techniques and external fields, and (2) understand the formation mechanism that underpins the well-ordered self-assembled structures.

2.2. Technical Objectives

To realize this goal, the following technical objectives will be pursued.

a. Craft ordered self-assembled structures of various nanomaterials based on the properties of nanomaterials, such as threads of polystyrene-*block*-poly(4-vinylpyridine) PS-*b*-P4VP micelles, highly aligned continuous DNA nanowires and PS latex particle film with uniform microchannels.

b. Optimize and explore the experimental condition such as the concentration solution, temperature, and moving speed and stop time of lower plate for ordered self-assembled structure formation.

c. Theoretically investigate the formation mechanism of the deposition pattern by FESA

d. Control the feature sizes (e.g, width and spacing of threads of PS-*b*-P4VP micelles, spacing between two adjacent micrchannels in PS latex particle film) of formed ordered self-assembled structures of various nanomaterials

e. Develop transfer printing technique for transferring patterned nanomaterials to desired substrate.

f. Convert ordered self-assembled structures of organic nanomaterials into inorganic nanomaterial patterns.

g. Align inorganic nanomaterials (e.g., nanoparticles and nanorods) by using prepared ordered structures as template

h. Synthesis inorganic nanomaterials of novel structures

i. Explore the influence of chemically patterned substrate (i.e., hydrophobic stripes on a hydrophilic substrate) on the formation of ordered structures

2.3. Organization and composition of dissertation

Chapter 1 is a critical review of evaporative induced self-assembly. First, the fundamental theoretical study of a freely evaporating droplet on a substrate was reviewed, including evaporative flux of a volatile droplet, radial and Marangoni flow inside a droplet, and the pinning and depinning processes during evaporation. Second, highly ordered structures created by confining evaporation in restricted geometry were reviewed.

Chapter 2 includes a concise description of the goal, the tasks and the associated technical objectives in this dissertation. Furthermore, it presents a brief overview of the organization of the dissertation, with short descriptions of the contents of each chapter.

Chapter 3 presents the study of hierarchical assemblies of amphiphilic diblock copolymer (i.e., polystyrene-*block*-poly(4-vinylpyridine) (PS-*b*-P4VP)) micelles crafted by flow-enabled self-assembly (FESA) by exploiting two concurrent self-assembly processes occurring at different length scales. The periodic threads comprising a monolayer or a bilayer of PS-*b*-P4VP micelles were precisely positioned and patterned on the microscopic scale. At the same time the PS-*b*-P4VP micelles were self-assembled into ordered arrays within an individual thread on the nanometer scale. Notably, the width of the threads can be easily tailored by simply varying the stop time of the translational stage. A minimum spacing between two adjacent threads λ_{min} was observed. A model was proposed to rationalize the relationship between the thread width of and λ_{min}. In addition, such diblock copolymer micelle threads were utilized as nanoreactors for creating inorganic nanoparticle arrays.

Chapter 4 provides the theoretical study of the formation of stripe pattern of solutes by FESA. In particular, the relationship between the characteristic spacing between adjacent stripes, λ_{c-c} and other experimental parameters such as the stripe width, the stop time and the moving speed of lower substrate were investigated. Moreover, the decrease in λ_{c-c} due to the increase of the moving speed of the lower substrates was rationalized by proposed model.

Chapter 5 reports on the highly aligned parallel DNA nanowires in the forms of nanostructured spokes over a macroscopic area crafted by evaporative self-assembly (CESA) by subjecting DNA aqueous solution to evaporate in a curve-on-flat geometry composed of a spherical on a flat substrate. The effects of pH of DNA aqueous solution

and temperature on the formation of DNA nanowires were systematically explored. A transition from spoke-like patterns to coffee-ring-like deposits was, for the first time, observed as the pH was increased.

Chapter 6 describes the formation of large-scale aligned metallic nanowires templated by highly oriented DNA. By subjecting DNA aqueous solution to dry between two nearly parallel plates composed of a stationary upper plate and a movable lower plate mounted on a programmable translational stage, an array of ultralong, high density, and parallel DNA nanowires on a large scale was successfully created by FESA. The formation of DNA nanowires was strongly influenced by the concentration of DNA solution, temperature, and moving speed of lower plate. A simple yet robust swelling-induced transfer printing (SIT-Printing) technique was developed to transfer ultralong DNA nanowires onto the desirable substrate. Subsequently, the resulting DNA nanowires were exploited as templates to form metallic nanowires by exposing DNA nanowires preloaded with metal salts under oxygen plasma. Moreover, DNA nanowires were also employed as scaffold for aligning metal nanoparticles and nanorods.

Chapter 7 discusses a simple yet effective strategy for CTAB capped water-soluble ultrathin gold nanowires. Surprisingly, rather than commonly obtained Au nanorods, by introducing a small amount of hydrophobic solvent (i.e., toluene or chloroform) into the Au growth solution based on conventional preparative approach for Au nanorods with cylindrical CTAB micelles as template, CTAB-capped ultrathin Au nanowires (i.e., water-soluble ultrathin Au nanowires) were yielded. Notably, a certain range of CTAB concentration was observed, beyond which no ultrathin Au nanowires can be produced. The growth mechanism of such intriguing water-soluble ultrathin Au nanowires, differed from those formed by using oleylamine (i.e., non-water-soluble Au nanowires), was explored.

Chapter 8 reports on engineering colloidal microchannels (i.e., cracks) on a large scale by controlling the drying process of colloidal suspensions via flow-enabled self-assembly (FESA). The thickness of the formed colloidal thin film can be tailored, thereby enabling the control over λ_{c-c} of colloidal microchannels. The influence of chemically patterned substrate (i.e., hydrophobic stripes on a hydrophilic substrate) on the formation of colloidal microchannels was explored. In addition, such colloidal microchannels with tunable λ_{c-c} was exploited as template for aligning inorganic nanoparticles.

Chapter 9 provides general conclusions for the overall work in the dissertation with a specific focus on impact and future directions.

CHAPTER 3

CRAFTING THREADS OF DIBLOCK COPOLYMER MICELLES VIA FLOW-ENABLED SELF-ASSEMBLY

B. Li, W. Han, B. Jiang and Z. Lin, "Crafting threads of diblock copolymer micelles via flow-enabled self-assembly", ***ACS Nano***, **8**, 2936 (2014)

3.1 Introduction

Self-assembly of nanoscale materials to form hierarchically ordered structures has received considerable attention[1-6] as it enables high-density integration of controlled and tunable functionalities of nanoscopic building blocks into optical, electronic, optoelectronic, and magnetic materials and devices.[7-9] In this regard, block copolymers permit versatile access to a variety of nanostructures (spheres, cylinders, double-gyroids, and lamellae) depending on the volume fraction of the components.[154, 168-169] The size of nanostructures is governed by the molecular weight of the polymer, typically in a range of 10 to 100 nm. This imparts a density of 10^{13} nanostructures per square inch, representing an attractive alternative to fabricating nanometer-scale structures.[106] Intriguingly, among various types of block copolymers, amphiphilic block copolymers composed of a hydrophobic domain and a hydrophilic domain are thermodynamically driven to self-assemble into a broad range of aggregate structures such as spherical micelles, wormlike micelles, and polymersomes when placed in selective solvents, depending on the ratio of the hydrophilic to hydrophobic blocks. Owing to their size uniformity and good kinetic stability, amphiphilic block copolymers can be exploited as nanoreactors to produce functional nanoparticles[170-172] and as compartments for nanoparticle loading[173] with applications in light harvesting,[174] laser printing,[175] etc. through simple assembly into closely packed structures.[176] The ability to position and pattern amphiphilic block copolymers micelles at desired positions underpins the

realization of these applications and enables the construction of hierarchical device structures.[10] To date, little work has focused on creating hierarchically assembled micelles using lithographically prepared templates.[11] However, the use of lithographic methods often requires costly, complex and multistep procedures. Clearly, a low-cost strategy for achieving hierarchically structured micelles over large scales is highly desirable.

Evaporative self-assembly of nonvolatile solutes (e.g., polymers, nanoparticles, and biomaterials, among others) from a sessile drop is widely recognized as an extremely simple and non-lithographic route to creating intriguing one- or two-dimensional structures.[16-20] However, the instabilities such as fingering instability and Marangoni flow arising from the evaporation process often lead to the formation of irregular and dissipative structures. To this end, recently, controlled evaporative self-assembly in restricted geometries (e.g., curve-on-flat geometry composed of a curved upper surface situated on a lower flat substrate) was developed to impart control over the drying dynamics and associated flows, thus allowing for the creation of ordered yet complex patterns.[106, 177-178] Subjecting drying droplets to the curve-on-flat geometry renders the minimization or elimination of temperature gradient and the control of the evaporation rate of solution. Gradient rings composed of micelles are successfully formed using the curve-on-flat geometry.[169] We note that the self-assembled structures created in such geometry are not dimensionally periodic. Instead, they possess gradient features.[179] On many occasions, it is highly desirable to produce self-assembled structures in a controllable manner for various applications.

Here, we report on a simple route to crafting hierarchical assemblies of amphiphilic diblock copolymer (i.e., polystyrene-*block*-poly(4-vinylpyridine) (PS-*b*-P4VP)) micelles by exploiting two concurrent self-assembly processes occurring at different length scales. The periodic threads comprising a monolayer or a bilayer of PS-*b*-

P4VP micelles were precisely positioned and patterned by flow-enabled self-assembly (FESA) on the microscopic scale over large areas. At the same time the PS-*b*-P4VP micelles were self-assembled into ordered arrays within an individual thread on the nanometer scale. In the FESA process, a drop of PS-*b*-P4VP micelle toluene solution was allowed to evaporate in a confined geometry consisting of two nearly parallel plates. The upper plate was fixed, and the lower plate was mounted on a computer-controlled translational stage that moved against the upper plate at a fixed distance. The width of the threads can be easily tailored by simply varying the stop time of the translational stage. Intriguingly, a minimum spacing between two adjacent threads λ_{min} was observed. A model was proposed to rationalize the relationship between the thread width of and λ_{min}. Such FESA strategy is simple, remarkably controllable, and easy to implement. It can rapidly and inexpensively produce microscopic threads containing diblock copolymer micelles self-assembled on the nanoscale (i.e., forming hierarchical assemblies) at high yield. By extension, it should be possible to position and pattern nanomaterials other than diblock copolymer micelles to yield advanced hierarchical systems for use in nanoelectronics, optoelectronics, magnetic devices, bionanotechnology, among other areas.

3.2 Results and Discussion

The PS-*b*-P4VP diblock copolymer was first dissolved in toluene, forming polymeric micelles (see *Experimental*) as toluene is a good solvent for PS block yet poor solvent for P4VP block (**Figure 3.1a**). Subsequently, by subjecting a drop of PS-*b*-P4VP micelle toluene solution to dry in a two-nearly-parallel-plate geometry in which the lower Si substrate placed on a motorized linear translational stage programmably moved against the upper stationary plate, the parallel threads composed of PS-*b*-P4VP micelles with high regularity and fidelity can be crafted (**Figure 3.1b**) in a "stop-and-move" mode.

First, the lower movable Si substrate was stationary for a period of time *t* (i.e., "stop"). During this process, the evaporative loss of toluene triggered the PS-*b*-P4VP micelles to migrate to the contact line,[16] forming a thread comprising PS-*b*-P4VP micelles. Subsequently, the lower Si substrate translated laterally by a distance λ in the direction marked in **Figure 3.1b** (i.e., "move"). Due to the movement of Si substrate, the meniscus was stretched and the initial contact angle at the edge of the meniscus decreased to a critical value, at which the depinning force became larger than the pinning force.[180] As a result, the contact line jumped inward to the new position and recovered the initial contact angle, leaving behind a new PS-*b*-P4VP thread. The repetitive computer-controlled "stop-and-move" cycles yielded periodic parallel threads.

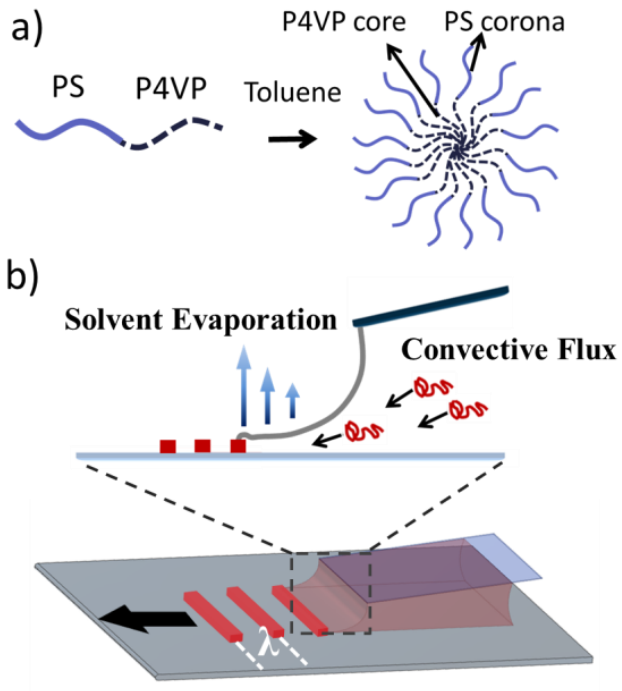

Figure 3.1. (a) Chemical structure of amphiphilic diblock copolymer PS-*b*-P4VP, and scheme of the formation of PS-*b*-P4VP micelles in toluene. (b) Schematic illustration of the formation of periodic threads composed of PS-*b*-P4VP micelles (represented as red chains and red bars).

It is noteworthy that the control of the moving distance λ and the stop time of the lower Si substrate *t* allowed the crafting of uniformly distributed, centimeter-scale (and larger) microscopic PS-*b*-P4VP threads over the entire surface of the Si substrate (**Figure 3.2a**). Close examination by AFM revealed that each individual thread comprised spontaneously self-assembled nanoscopic PS-*b*-P4VP micelles. Clearly, hierarchically assembled PS-*b*-P4VP micelles were obtained, that is, periodic threads formed by FESA on the microscopic scale with the PS-*b*-P4VP micelles self-assembled on the nanoscopic scale within a micro-sized thread. We note that the thread width can be controlled from 800 nm to 1.8 μm by simply changing the stop time *t* (i.e., pinning time) from 0.5s to 3s, respectively, as evidenced by the AFM measurements (**Figures 3.2b-2g**). The transition from a monolayer to a coexisted monolayer/bilayer of PS-*b*-P4VP micelles occurred at the stop time *t* = 1.5s - 2s (**Figures 3.2d and 3.2e**). Remarkably, the formation of PS-*b*-P4VP threads was highly reproducible.

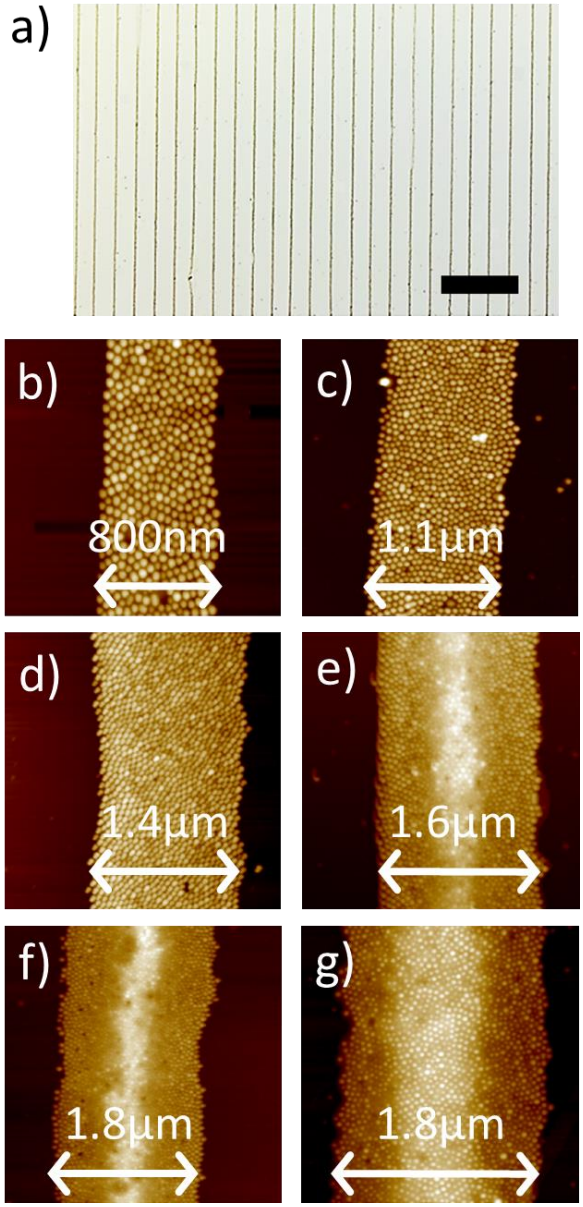

Figure 3.2. (a) Optical micrograph of parallel threads composed of PS-*b*-P4VP micelles with the spacing between two adjacent threads of 50 µm (i.e., λ_{50} = 50 µm). The scale bar = 200 µm. (b-g) AFM height images of a thread containing a monolayer and a coexisted monolayer/bilayer PS-*b*-P4VP micelles obtained at the stop times of (b) 0.5s, (c) 1.0s, (d) 1.5s, (e) 2s, (f) 2.5s, and (g) 3s, respectively.

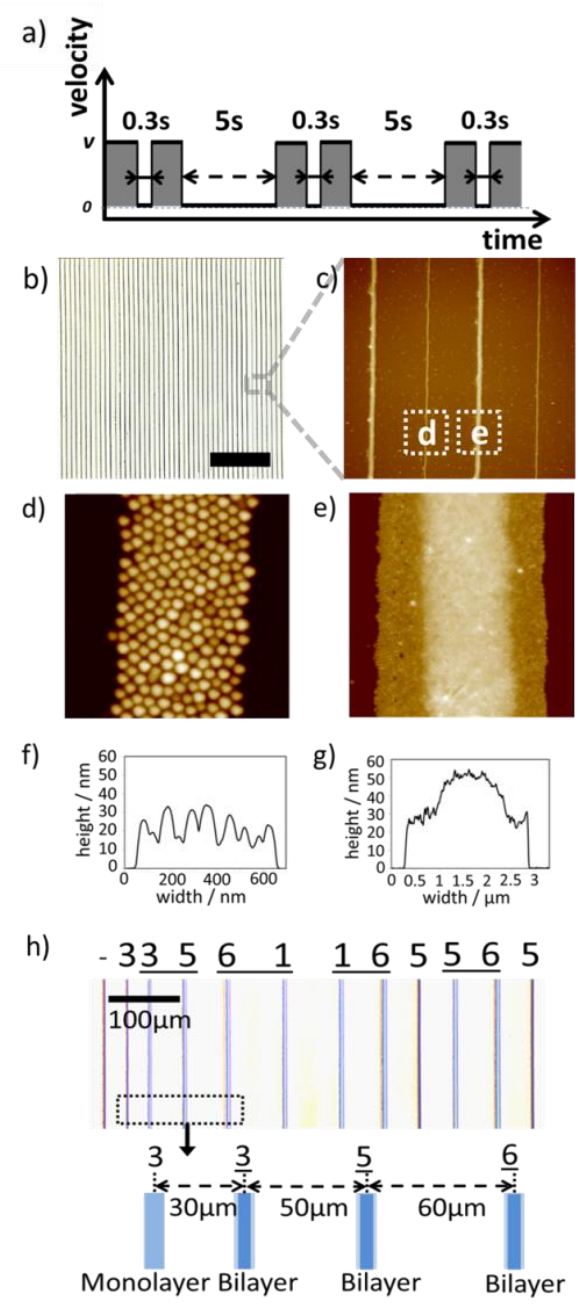

Figure 3.3. (a) Programed movement of the Si substrate mounted on the translational stage, in which the velocity is plotted as function of time. The shaded areas represent each moving distance of 20 µm after the alternative stop of the Si substrate for 0.3s and 5s. (b) Optical micrographs of periodic threads of PS-*b*-P4VP micelles formed on the Si substrate by flow-enabled self-assembly (FESA), in which the Si substrate moved 20 µm, followed by an alternative stop for 0.3s and 5s to yield monolayer- and monolayer/bilayer-thick threads, respectively. The scale bar = 500 µm. (c-e) Representative AFM images of (c) 4 threads (i.e., 2 monolayers and 2 coexisted monolayers/bilayers), (d) single thread containing a monolayer of PS-*b*-P4VP micelles,

and (e) single thread containing a coexisted monolayer/bilayer of PS-*b*-P4VP micelles (i.e., monolayers at both edges with and bilayer in the center). (f-g) Corresponding height profiles of (f) the monolayer-thick thread in (d), and of (g) the monolayer/bilayer-thick thread in (e). (h) Optical micrograph images of the encoded thread pattern on the substrate represented the first sentence of the traditional Chinese song *Jasmine*. The image sizes are 80 μm x 80 μm in (c), 800 nm x 800 nm in (d), and 3 μm x 3 μm in (e), respectively.

To further demonstrate the high level of control over the fabrication of well-ordered PS-*b*-P4VP threads by FESA, alternating threads of a monolayer and a coexisted monolayer/bilayer of self-assembled PS-*b*-P4VP micelles were constructed. First, the Si substrate was moved unidirectionally by a constant distance (i.e., 20 μm in **Figure 3.3a**), and stopped for 0.3s. The substrate was then shifted by another 20 μm and stopped for 5s. As discussed in the above (**Figure 3.2**), a monolayer of PS-*b*-P4VP micelles was found to form with the stop time less than 1.5s (i.e., t = 0.3s in **Figure 3.3a**), while a coexisted monolayer/bilayer of PS-*b*-P4VP micelles was yielded with the stop time longer than 1.5s (i.e., t = 5s in **Figure 3.3a**). Consequently, alternating monolayer-thick and monolayer/bilayer-thick threads with a fixed spacing can be produced by programming the motion of the lower Si substrate (**Figures 3.3b and 3.3c**). It is worth noting that any combination of monolayer and monolayer/bilayers of micelles with varied spacing between the adjacent threads can be readily fabricated by programmable FESA. **Figure 3.3b** shows the optical micrographs of alternating thread that constituted monolayer and monolayer/bilayer of PS-*b*-P4VP micelles over a centimeter scale (only a small zone of the entire centimeter-scale assembly is displayed in **Figure 3.3a**). Further scrutiny of the surface morphologies of two representative adjacent threads by AFM showed that these individual threads, either monolayer- or monolayer/bilayer-thick, were made of arrays of nanometer-sized PS-*b*-P4VP micelles (**Figures 3.3d and 3.3e**).

Quite intriguingly, the threads crafted by FESA can be exploited to encode music. In what follows, we demonstrate the use of threads to encode a famous traditional Chinese song *Jasmine* on the Si substrate (**Figure 3.3h and Figure 3.4**) with the design

rules set as follows: (1) the musical scale was defined by the separation distance between two adjacent threads based on the thread on the left (e.g., *Do* (λ_{10}) = 10 μm, *Re* (λ_{20}) = 20 μm, *Mi* (λ_{30}) = 30 μm, *Fa* (λ_{40}) = 40 μm, *So* (λ_{50}) = 50 μm, *La* (λ_{60}) = 60 μm, *Ti* (λ_{70}) = 70 μm, high *Do* (λ_{80}) = 80 μm); and (2) As tempo of *Jasmine* was four fourths, a crotchet and a quaver were determined by a monolayer and a monolayer/bilayer of PS-*b*-P4VP micelles, respectively. As illustrated in **Figure 3.3h**, the first sentence of numerical notation of musical scale of *Jasmine* is 3 35 61 16 5 56 5. Thus, the corresponding thread pattern is λ_{30}M, λ_{30}MB, λ_{50}MB, λ_{60}MB, λ_{80}MB, λ_{80}MB, λ_{60}MB, λ_{50}M, λ_{50}MB, λ_{60}MB, λ_{50}M, where M and MB represent the monolayer and the coexisted monolayer/bilayer of micelles, respectively. In comparison to the previous work, in which only gradient rings of micelles were formed,[169] a programmed array of PS-*b*-P4VP threads composed of a monolayer or a monolayer/bilayer of micelles can be readily encoded by FESA.

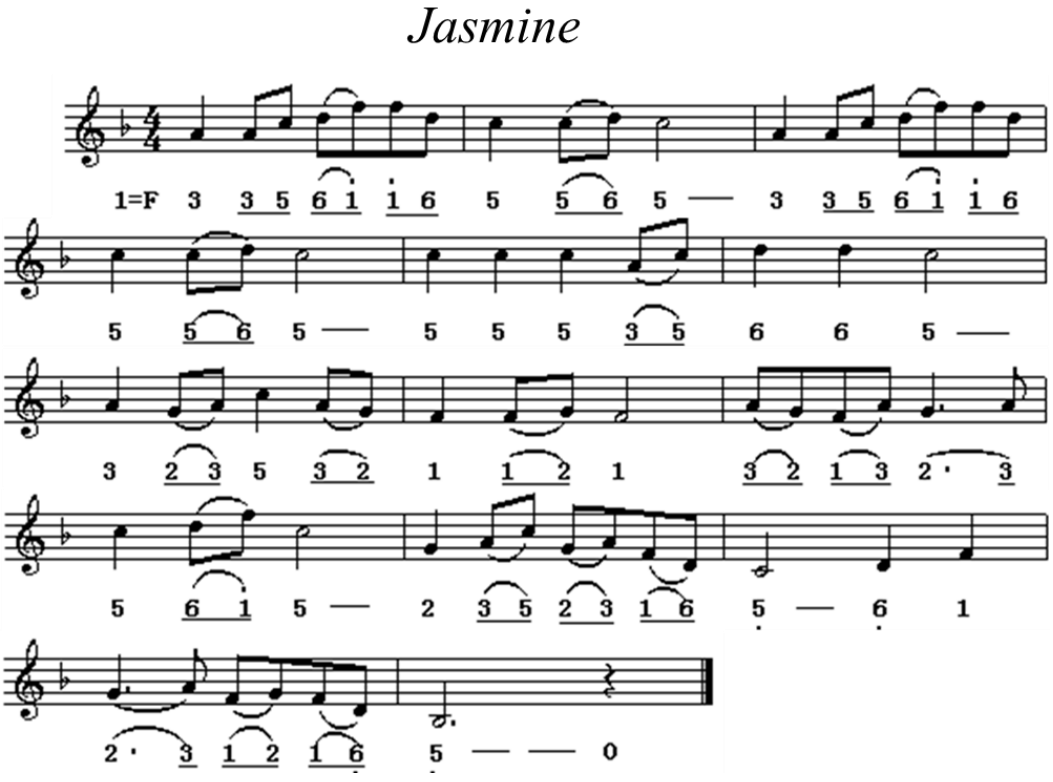

Figure 3.4. Musical score of the traditional Chinese song *Jasmine*.

Interestingly, a minimum spacing between adjacent parallel threads, λ_{min}, was noted in the FESA of PS-*b*-P4VP micelles. It was found that when the moving distance of the Si substrate λ was smaller than λ_{min} (i.e., $\lambda < \lambda_{min}$), a relatively irregular pattern (**Figure 3.5a**) was formed, while a highly ordered pattern was resulted in at $\lambda > \lambda_{min}$ (**Figure 3.5b**). This observation can be rationalized as follows. A critical moving distance was required in order to stretch the meniscus and decrease the contact angle of the meniscus to a critical value, at which the slip of the meniscus pinned at the contact line can be triggered, thereby leading to the formation of a thread of PS-*b*-P4VP micelles. It is not surprising that longer stop times of the Si substrate yielded a larger thread width and thus a larger λ_{min} due to the larger pinning force exerted at the contact line[180] (**Figure 3.5c**) as discussed below.

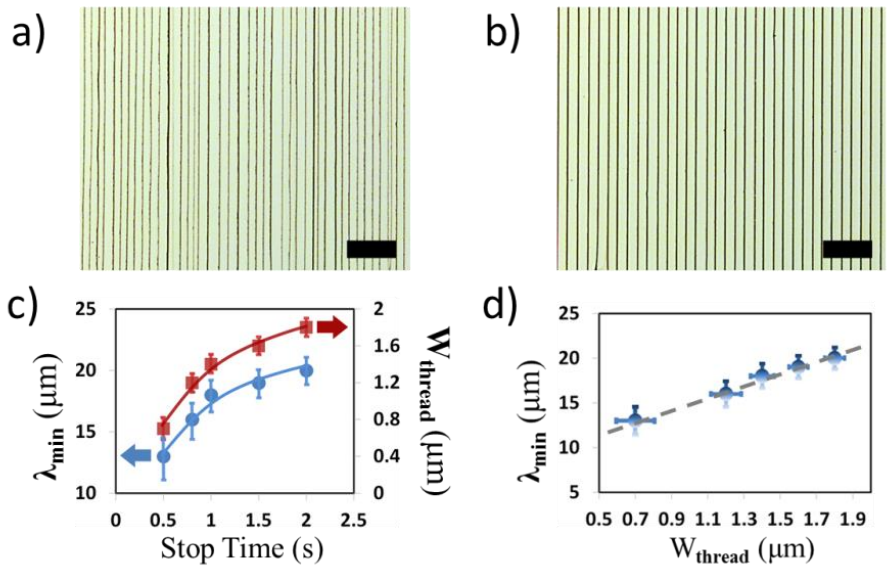

Figure 3.5. Optical micrographs of (a) relatively irregular, and (b) highly regular parallel threads of PS-*b*-P4VP micelles. The scale bar = 100 μm in both (a) and (b). (c)

Relationship between λ_{min} (blue symbols) and the thread width W_{thread} (red symbols) and the stop time of the Si substrate. (d) Relationship between λ_{min} and W_{thread}.

A model was proposed to elucidate the relationship between the thread width and λ_{min}. It is known that the meniscus of a drying droplet depins and jumps to the next position if the pinning force is smaller than the capillary force (i.e., depinning force).[180] The balance between the pinning force and the capillary force can be considered as the equality of the adhesion energy E_{ad} between the deposit and solvent and the increase in surface energy ΔE_{cap} (i.e., the increase in surface energy due to the stretched meniscus).

$$E_{ad} \sim A_{thread} P_{ad} \tag{3.1}$$

$$\Delta E_{cap} \sim (l \times \Delta L_{liq})\gamma \tag{3.2}$$

$$\Delta E_{cap} = E_{ad} \tag{3.3}$$

where A_{stripe} is the surface area of the thread, P_{ad} is adhesion energy per unit area between the deposit and solvent, l is the length of the contact line, ΔL_{liq} is the length increase in the stretched meniscus, and γ is the surface tension of solvent. The area increase for the stretched meniscus is $l \times \Delta L_{liq}$. By combining equations (3.1)-(3.3), we have

$$\Delta L_{liq} = \frac{A_{thread} P_{ad}}{l \gamma} \tag{1.4}$$

The surface area can be calculated based on equation (3.5)

$$A_{thread} = k(l \times L_{thread}) \tag{3.5}$$

where L_{thread} is the thread profile and k is the roughness factor (k = 1.6046, see *Supporting Information*). Since the height of thread (monolayer- or bilayer-micelle thick) is much

smaller than the width of thread W_{thread} (greater than or equal to 1 μm), it follows that $L_{thread} \cong W_{thread}$. As the surface roughness originated from the shape of micelles increases the wettability between the deposit and solvent, the threads composed of PS-*b*-P4VP micelles possess a higher adhesion energy as compared to the smooth threads of the same width. Since the meniscus was stretched due to the movement of the Si substrate during the pinning process (**Figure 3.6**), we have

$$\Delta L_{liq} = \lambda_{min} cos\theta_i \tag{3.6}$$

where θ_i is the initial contact angle of the meniscus. Thus, λ_{min} can be determined by combing equations (3.4) ,(3.5) and (3.6),

$$\lambda_{min} \sim \frac{kW_{thread}P_{ad}}{cos\theta_i \gamma} \tag{3.7}$$

Clearly, λ_{min} of the threads exhibits a linear relationship with the width of threads (i.e., $\lambda_{min} \sim W_{thread}$), which is in good agreement with the experimental results (**Figure 3.5d**). We note that in the present study the effect of the height of threads can be neglected due to much smaller thread height than the thread width.

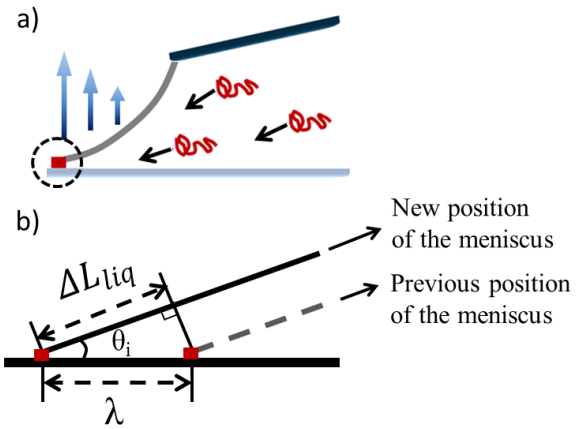

Figure 3.6. (a) Schematic illustration of the flow-enabled self-assembly (side view). (b) The close-up of the meniscus stretched to a new position due to the movement of the Si substrate.

Amphiphilic PS-*b*-P4VP diblock copolymer can self-assemble into nanoscopic spherical micelles with a hydrophilic P4VP core and hydrophobic PS corona when dissolved in toluene. Such diblock copolymers can be utilized as nanoreactors for the synthesis of various nanoparticles.[172] In this context, we have successfully converted the periodic threads composed of the array of PS-*b*-P4VP micelles encapsulated with Au precursors (i.e., forming hierarchically assembled PS-*b*-P4VP/$HAuCl_4$ micelles; **Figure 3.7a**) into the threads of inorganic nanoparticles (i.e., Au nanoparticles) (**Figure 3.7b**). Specifically, Au precursors (i.e., tetrachloroauric acid ($HAuCl_4 \cdot 3H_2O$)) was mixed with PS-*b*-P4VP toluene solution at different molar ratios, yielding PS-*b*-P4VP micelles with Au precursors encapsulated within the P4VP cores (**Figure 3.8**). Similar to the threads of plain PS-*b*-P4VP micelles discussed above, highly ordered, parallel threads constituting the PS-*b*-P4VP/$HAuCl_4$ micelles were crafted by FESA. Subsequently, the sample was exposed to the oxygen plasma to remove the PS-*b*-P4VP templates, leaving behind arrays of Au nanoparticles within the threads (**Figure 3.7 and Figure 3.9**).

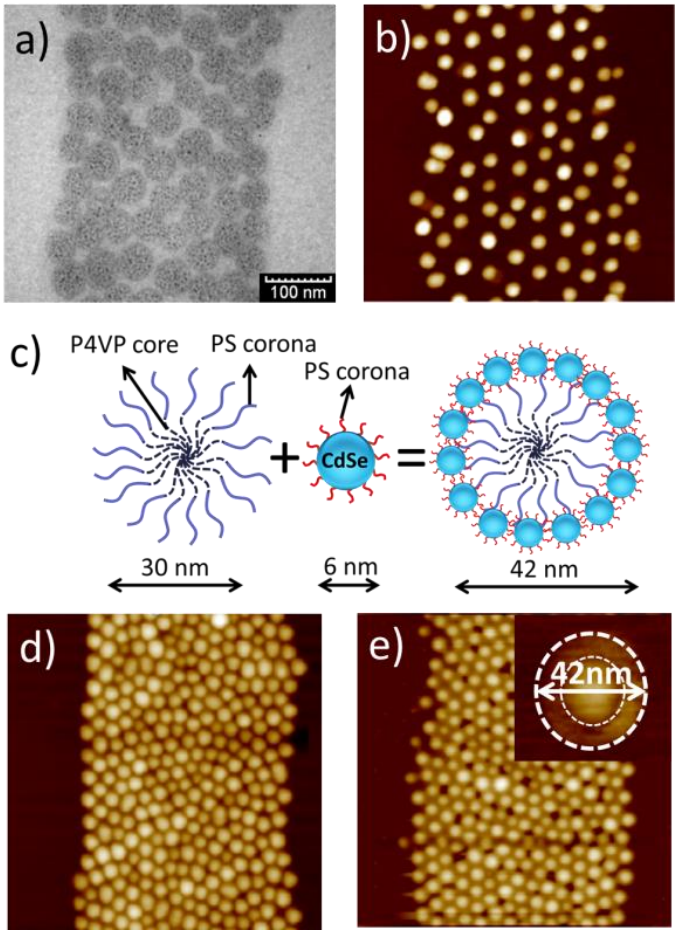

Figure 3.7. (a-b) Representative (a) TEM image of a monolayer-thick thread composed of an array of PS-*b*-P4VP/$HAuCl_4$ micelles (Au^{3+} : P4VP = 110:1) before exposure to oxygen plasma, and (b) corresponding AFM height image after exposure to oxygen plasma. (c) Schematic illustration of the formation of PS-*b*-P4VP micelles surrounded by a ring of PS-capped CdSe nanoparticles. (d-e) AFM height images of a thread composed of (d) plain PS-*b*-P4VP micelles, and (e) hybrid micelles comprising PS-*b*-P4VP micelles decorated with an outer ring of CdSe nanoparticles. A close-up of an individual hybrid micelle is shown as an inset in (e). The image sizes are 600 nm x 600 nm in (b), 1.2 μm x 1.2 μm in (d), and 1.2 μm x 1.2 μm in (e).

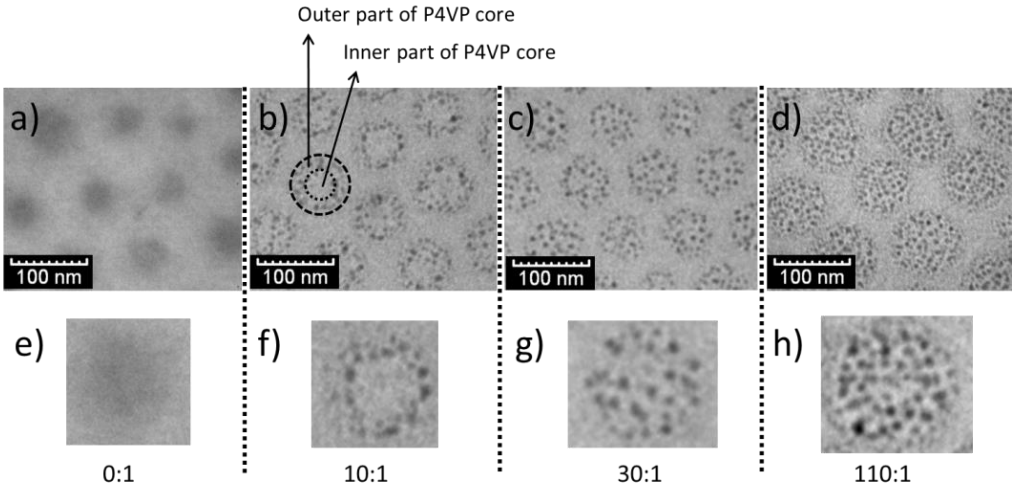

Figure 3.8. TEM images of PS-*b*-P4VP micelles incorporated with Au^{3+} ions within the thread at the Au^{3+} /P4VP ratios of (a) 0:1 (*i.e.*, plain PS-*b*-P4VP micelles), (b) 10:1, (c) 30:1, and (d) 110:1. (e-h) Corresponding TEM images of one single PS-*b*-P4VP micelle with the incorporation of Au^{3+} ions.

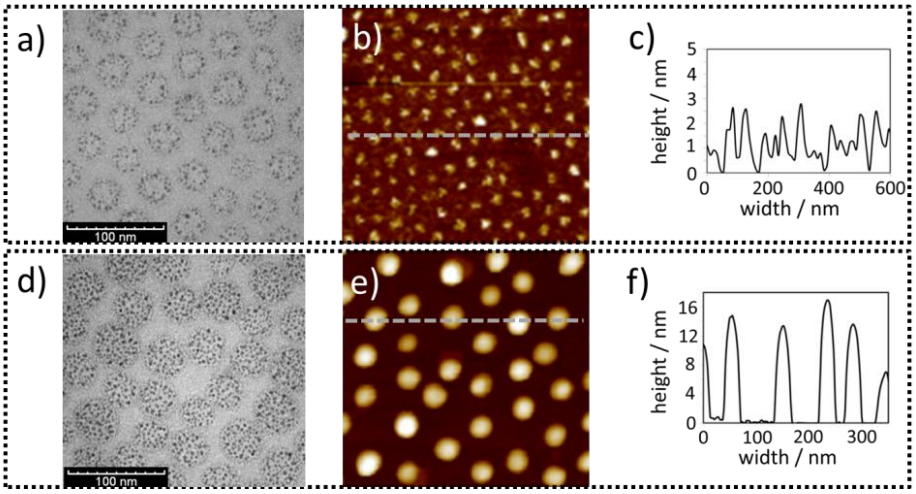

Figure 3.9. (a) and (d) TEM images of PS-*b*-P4VP micelles before the exposure to oxygen plasma. (b) and (e) Corresponding AFM height images, and (c) and (f) corresponding cross sectional analysis of Au nanoparticles obtained from the samples at the Au^{3+} /P4VP ratios of 10:1 and 110:1, respectively, after the exposure to oxygen plasma. The image sizes are 600 nm x 600 nm in (b), and 400 nm x 400 nm in (e).

It is interesting to note that the diameter of Au nanoparticles after the oxygen plasma exposure was dictated by the ratio of Au^{3+} to P4VP chain length during the preparation of PS-*b*-P4VP/$HAuCl_4$ micelles. At the relatively low molar ratio of

Au^{3+}/P4VP (i.e., Au^{3+}/P4VP = 10:1), the Au^{3+} ions preferentially bind to the outer part of the P4VP core via the attachment to the pyridine groups of P4VP by protonating the pyridine units through ionic–polar interaction[181-183] (**Figures 3.8b and 3.10**). In contrast, when the Au^{3+}/P4VP ratio is high enough, the Au^{3+} ions can interact with the entire P4VP core (**Figures 3.8d and 311**). In the present study, the maximum ratio of Au^{3+}/P4VP was found to be 110:1 as higher ratios (> 110:1) would cause Au precursors to precipitate from the micelle toluene solution. We note that the number of 4VP units in one P4VP chain is 220 as the molecular weight of P4VP is 24 kg/mol. This indicates that only half of the 4VP units in a P4VP chain interacted with Au^{3+} ions at the ratio of Au^{3+} : P4VP = 110:1. Intriguingly, the exposure of PS-*b*-P4VP/$HAuCl_4$ micelles with a low Au^{3+}/P4VP ratio (10:1) to the oxygen plasma led to the formation of irregular Au nanodots with approximately 3 nm in height (**Figures 3.9a and 3.9c**). The Au^{3+} ions were reduced to elemental Au,[184] which then merged with one another to form Au nanodots owing to a very small amount of Au^{3+} ions present within one micelle; while the large Au^{3+} /P4VP ratio (110:1) of PS-*b*-P4VP/$HAuCl_4$ micelles yielded spherical Au nanoparticles with a diameter of 16 nm (**Figures 3.9e and 3.9f**) after the oxygen plasma treatment. Compared to the 30-nm plain PS-*b*-P4VP micelle, the diameter of Au nanoparticles produced from the micelle template was smaller (i.e., 16 nm). This is mostly likely due to the condensation of the P4VP core during the oxygen plasma exposure.

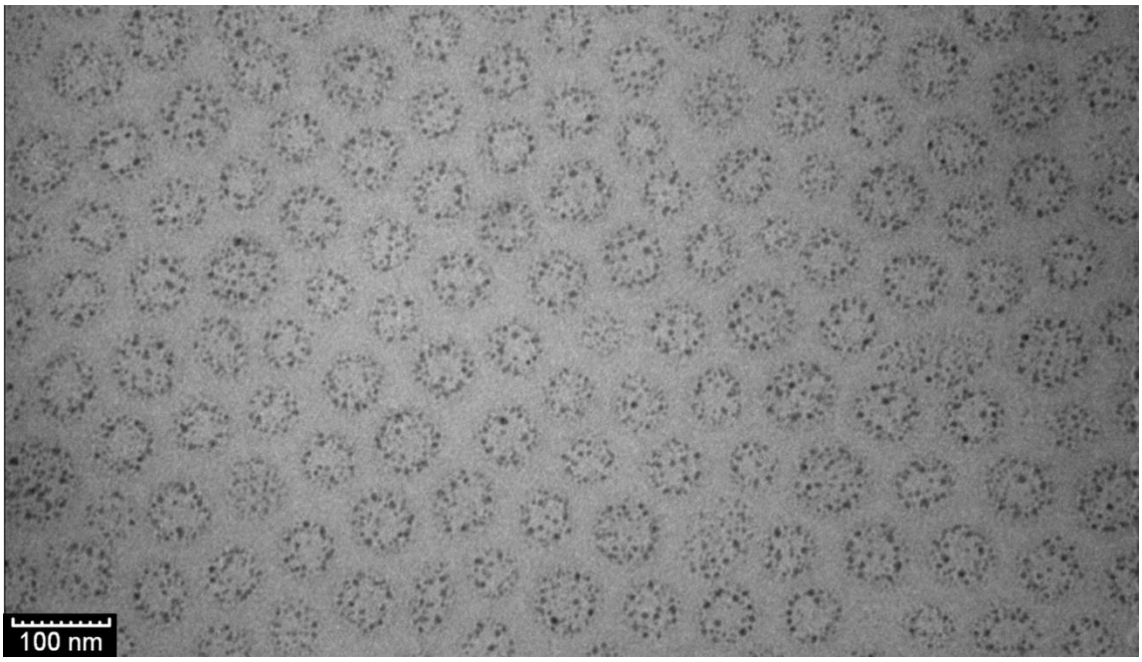

Figure 3.10. TEM image of PS-*b*-P4VP micelles with the incorporation of Au^{3+} at Au^{3+} /P4VP ratio of 10:1. The sample was prepared by spin-coating PS-*b*-P4VP/$HAuCl_4$ micelles at 3000 rpm/min.

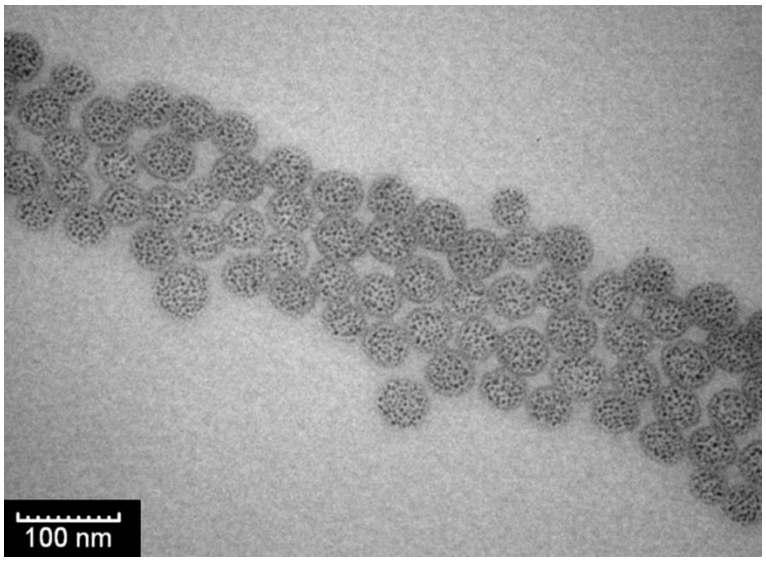

Figure 3.11. TEM image of a thread composed of PS-*b*-P4VP/$HAuCl_4$ micelles at the Au^{3+} /P4VP ratio of 110:1.

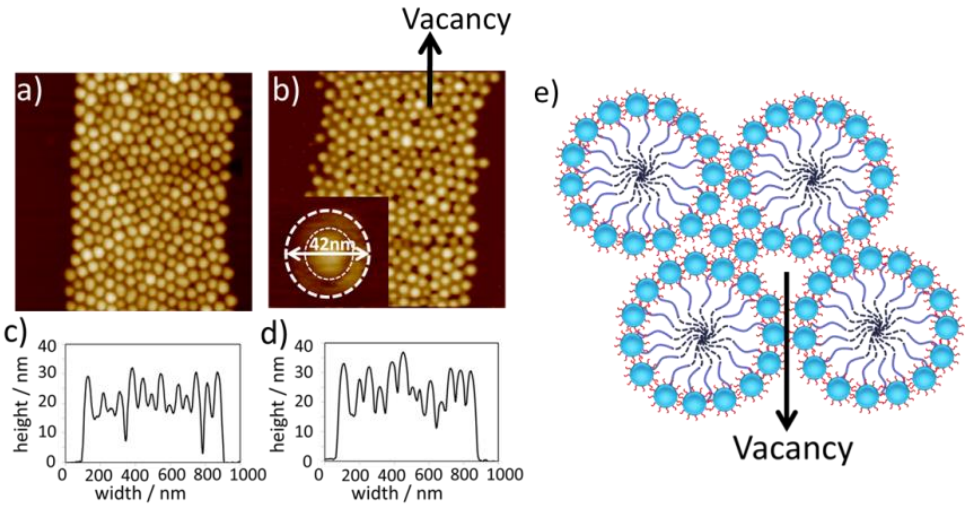

Figure 3.12. (a-b) AFM height images, and (c-d) the corresponding cross sectional analysis of threads composed of plain PS-*b*-P4VP micelles (a and c) and hybrid micelles of PS-*b*-P4VP/CdSe (b and d). (e) Schematic illustration of the formation of PS-*b*-P4VP micelles surrounded by a ring of CdSe nanoparticles with the presence of one vacancy. The image sizes 1.2 μm x 1.2 μm in (a) and (b).

In addition to threads composed of Au nanoparticles, threads of PS-*b*-P4VP micelles surrounded by CdSe nanoparticles were also constructed. Monodisperse CdSe nanoparticles with a diameter of 6 nm *intimately* and *permanently* capped with PS were first synthesized by utilizing a new class of amphiphilic star-like diblock copolymer, poly(acrylic acid)-block-polystyrene (PAA-*b*-PS) as a nanoreactor, prepared by sequential atom transfer radical polymerization (ATRP) of *tert*-butyl acrylate (*t*BA) and styrene (St) based on β-cyclodextrin (β-CD) (i.e., forming poly(tert-butyl acrylate)-block-polystyrene (P*t*BA-*b*-PS)), followed by the hydrolysis of P*t*BA into PAA.[172] Upon mixing PS-capped CdSe nanoparticles with the amphiphilic PS-*b*-P4VP toluene solution, CdSe nanoparticles were selectively incorporated to the PS corona (**Figure 3.7c**). Hierarchically structured assemblies were obtained by FESA of the PS-*b*-P4VP/CdSe nanoparticle toluene solution, namely, highly ordered submicron-wide threads containing monolayer-thick, self-assembled nanoscopic PS-*b*-P4VP micelles surrounded by a ring of self-organizing CdSe nanoparticles (2 x 6-nm CdSe nanoparticles + 30-nm PS-*b*-P4VP

micelles = 42 nm as shown in the inset; **Figure 3.7e**). Interestingly, the height of the hybrid micelles of PS-*b*-P4VP/CdSe was almost the same as that of plain PS-*b*-P4VP micelles (**Figures 3.12c and 3.12d**), suggesting that the PS-*b*-P4VP micelles were decorated by a ring of CdSe nanoparticles (**Figure 3.12e**). [185-186]

3.3 Conclusion

In summary, strictly periodic threads of amphiphilic diblock copolymers and inorganic nanoparticles were exquisitely crafted over large areas by flow-enabled self-assembly in a two-nearly-parallel-plate geometry where the lower substrate was moved against the upper stationary plate in a controlled manner. They can be precisely positioned and patterned at desired locations on the substrate, dispensing with the need for lithography techniques and external fields. These microscopic threads exhibited one-step hierarchical self-organization, that is, parallel threads comprising amphiphilic diblock copolymer micelles and nanoparticles with controllable width on the micrometer scale in conjunction with self-assemblies of PS-*b*-P4VP micelles and inorganic nanoparticles on the nanometer scale. A model was proposed to understand the relationship between the thread width and the minimum spacing between two adjacent threads λ_{min}. The ability to craft hierarchical assemblies rapidly at low cost opens up ways to fabricate novel advanced functional systems and devices for use in nanoelectronics, optoelectronics, and bionanotechnology.

3.4 Experimental

Preparation of PS-b-P4VP micelles: Poly(styrene)-block-poly(4-vinylpyridine) (PS-*b*-P4VP; number average molecular weight of PS = 41.0 kg/mol and P4VP = 24.0 kg/mol; polydispersity index, PDI=1.09; *Polymer Source Inc.*) was dissolved in toluene at a concentration of 2 mg/ml. The PS-*b*-P4VP toluene solution was heated to 70°C and

stirred for 12 hr. The solution was then cooled down slowly. Finally, the PS-*b*-P4VP micelle solution was diluted to 0.2 mg/ml and purified with a 200-nm poly(tetrafluoroethylene) (PTFE) filter.

Flow-enabled self-assemblcy (FESA) of PS-b-P4VP micelles: Parallel threads of PS-*b*-P4VP micelles were formed by subjecting a drop of PS-*b*-P4VP toluene solution to evaporate in a two-nearly-parallel-plate geometry constructed by placing a fixed upper plate slightly angled with respective to the lower movable Si substrate that can be precisely controlled by a motorized linear translational stage (Parker Hannifin Corp, mode: MX80LVixBL2b). The resolution of the translational stage is 100 nm. The translational stage moved at a constant speed of 1mm/s but with different stop times varying from 0.1s to 5s.

Preparation of gold nanoparticles using PS-b-P4VP micelles as nanoreactors: Tetrachloroauric acid ($HAuCl_4 \bullet 3H_2O$) was purchased from Sigma-Aldrich and mixed with PS-*b*-P4VP toluene solution at different molar ratios of Au^{3+}/P4VP. The resulting solution was stirred for 3 days. The periodic threads of PS-*b*-P4VP/$HAuCl_4$ micelles were created by FESA. To yield arrays of Au nanoparticles within the threads, oxygen plasma (Harrick Plasma; PDC-001) operated at 30W and 300 mTorr was applied for 1 hr.

CHAPTER 4

THEORETICAL INVESTIGATION OF THE FORMATION OF THE DEPOSITION PATTERN BY FESA

B. Li and Z. Lin, "Prediction of the smallest dimensions of deposits formed in flow enabled self-assembly ", (manuscript in preparation)

In our study two plates for trapping the drying droplets are composed of an upper fixed plate made from different materials (e.g., glass, polyethylene terephthalate (PET), polydimethylsiloxane (PDMS), etc.) and a lower movable substrate (e.g., Silicon substrate, polymer (hexamethyldisiloxane (HMDS), poly(methyl methacrylate) (PMMA), polystyrene (PS))-coated substrate) (**Figure 4.1a**). The upper fixed plate is slightly angled with respect to the lower moving plate. The motion of the lower substrate can be precisely controlled by a motorized linear translational stage. The use of the programmable translation stage enables the controllable movement of substrate (i.e., stop for a preset stopping time, and then move in either forward or backward direction at a preset velocity). One example of FESA of PMMA parallel lines produced by this method is shown in **Figure 4.1b**.

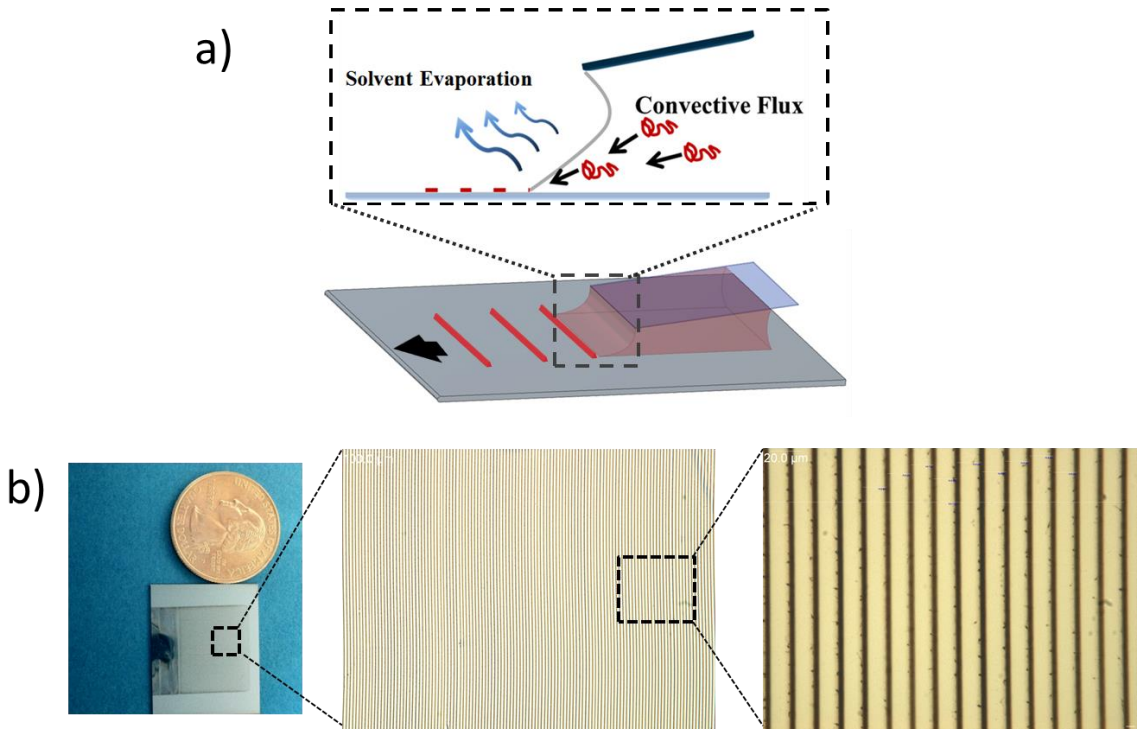

Figure 4.1. (a) Schematic illustration of a home-made apparatus for FESA. (b) One typical result of uniform PMMA parallel stripes formed on Si substrate prepared by FESA of the PMMA toluene solution.

In this chapter, we focus on the theoretical study of the formation of parallel stripes by FESA in terms of the prediction of the smallest dimension of deposits.

4.1 Stripes formed by solvent evaporation with fixed parallel surfaces (i.e., fixed substrate during stripe formation)

In general, the meniscus front is arrested between the upper and lower surfaces for a certain period of time during which a stripe is formed. Then, the meniscus jumps a short distance (λ_{jump}) to the next position where it will be arrested again, and a new stripe is thus deposited.

The meniscus is first pinned at position *I* where the stripe is formed (**Figure 4.2a**). During the solvent evaporation, the contact angle will gradually decrease from the initial contact angle (θ_i) to critical contact angle (θ_c), and the shape of meniscus will change to

position *II*. When it reaches position *II*, with the further evaporation of solvent the meniscus will jump from position *II* to a new position *III*, because the capillary force becomes larger than the pinning force.

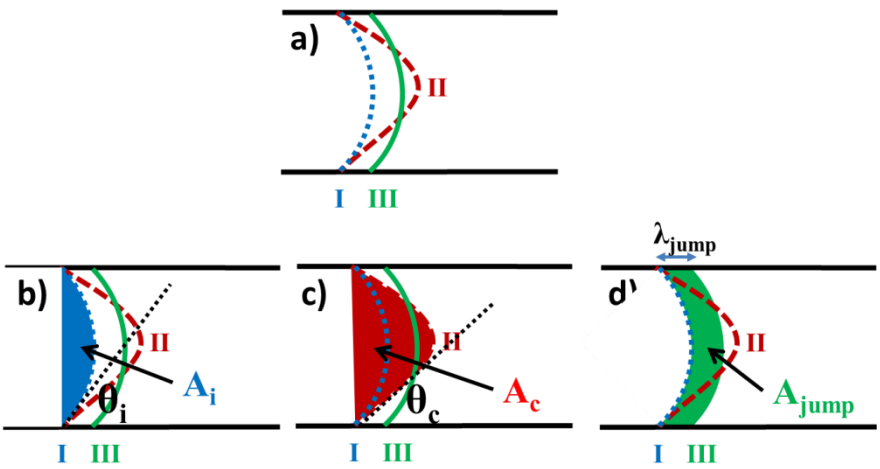

Figure 4.2. Schematic illustration of the stripe formation induced by evaporation.

The total volume before and after the jump of meniscus is the same.

$$A_c - A_i = \Delta A = A_{jump} \tag{4.1}$$

where A_i, A_c is the area of the meniscus at position *I* and position *II* (shown in **Figure 4.2b** and **4.2c**) at contact angle θ_i and θ_c, respectively, A_{jump} is the green area shown in **Figure 4.2d**. The area of the meniscus at position *I* and *II* can be given from the geometry of the meniscus. [180]

$$A_i = \frac{H\left(2H\arctan\frac{2a_i}{H} - H\right) + 2a_i H}{4}$$
$$A_c = \frac{H\left(2H\arctan\frac{2a_c}{H} - H\right) + 2a_c H}{4} \tag{4.2}$$

$$\Delta A = \frac{H}{2}\left[H\left(\arctan\frac{2a_c}{H} - \arctan\frac{2a_i}{H}\right) + \left(a_c - a_i\right)\right] \tag{4.3}$$

where H is the surface separation at the liquid-vapor interface of the solution, and a_i and a_c are the height of meniscus at contact angles θ_i and θ_c, respectively. The volume change between position *I* and position *III* can also be given by

$$\Delta A = \lambda_{jump} H \tag{4.4}$$

Combining Eq. (4.3) and (4.4), λ_{jump} can be given by

$$\lambda_{jump} = \frac{1}{2}\left[H\left(\arctan\frac{2a_c}{H} - \arctan\frac{2a_i}{H} \right) + \left(a_c - a_i \right) \right] \tag{4.5}$$

The height of meniscus at contact angle θ_i can be given from the meniscus geometry, [180]

$$a_i = H\left(1 - \tan\theta_i\right)/2 \tag{4.6}$$

where the initial contact angle θ_i could be measure experimentally. At position *II*, the linear pinning force is balanced by the nonlinear capillary force,

$$\begin{aligned} F_p &= k r_0 \gamma_{dl} \\ F_c &= 4 r_0 \gamma_l \left(\arctan\frac{2a_c}{H} - \arctan\frac{2a_i}{H} \right) \\ F_p &= F_c \end{aligned} \tag{4.7}$$

where γ_{dl} is the surface tension between deposits and solvent and γ_l is the surface tension of the solvent and r_0 is the total length of contact line. The height of meniscus at critical contact angle θ_c at position *II* can be obtained by

$$\arctan\frac{2a_c}{H} - \arctan\frac{2a_i}{H} = \frac{k\gamma_{dl}}{4\gamma_l} \tag{4.8}$$

Combining Eq. (4.5) and (4.8), λ_{jump} can be given by

$$\lambda_{jump} = \frac{1}{2}\left[H\frac{k\gamma_{dl}}{4\gamma_{lv}} + \left(a_c - a_i \right) \right] \tag{4.9}$$

As the height of meniscus at contact angle θ_i and θ_c can be calculated by Eq. (4.6) and (4.8), the distance between two adjacent stripe formed by evaporation of the solvent (i.e., λ_{jump}) can thus be obtained.

4.2 Stripes formation induced by the movement of lower substrate in the "stop-and-move" mode

Different from Section 4.1 discussed above, in which the stripes and the substrate do not move during the stripe formation, in this section, a model will be given based on that the meniscus is stretched by the movement of lower substrate, which is controlled by a translational stage in the experiment.

The meniscus is first pinned (**Figure 4.3a**). Then the contact angle will gradually decrease from the initial contact angle (θ_i) to the critical contact angle (θ_c) due to the substrate moving at a distance λ_{jump} (Note: this λ_{jump} is different from the λ_{jump} in Section 4.1). Moreover, if there is any further movement of the substrate, the capillary force will become larger than the pinning force. Therefore, the meniscus will jump back to the initial position and resumes the initial contact angle θ_i.

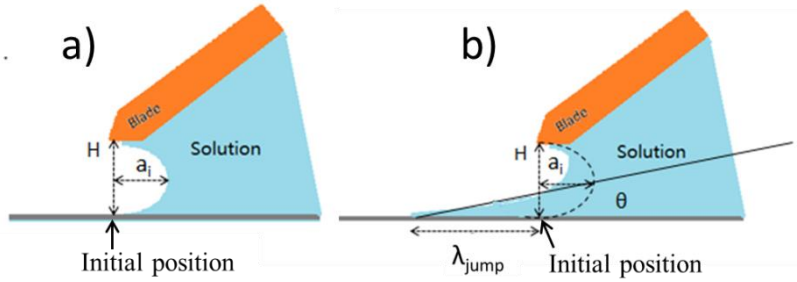

Figure 4.3. Schematic illustration of the stripe formation induced by the movement of lower substrate.

It is assumed that the pinning force is proportional to the viscosity of solvent η, inversely proportional to the velocity of the substrate v. When pinning force is balanced by the depinning force, we have

$$\frac{\mu k}{v} = \gamma_l(\cos\theta_c - \cos\theta_i) \qquad (4.10)$$

$$\theta_c = \arccos\left(\frac{\mu k}{v\gamma_l} + \cos\theta_i\right) \tag{4.11}$$

where μ is viscosity and v is the velocity of subtract, γ_l is the surface tension of the solvent and k is a related constant. From the geometry shown in **Figure 4.3b**, the critical contact angle θ_c can be given by

$$\theta_c = \arctan\left(\frac{H}{2\left(\lambda_{jump} + a_i\right)}\right) \tag{4.12}$$

By substituting Eq. (4.6) into Eq. (4.12), the critical contact angle θ_c is given by

$$\theta_c = \arctan\left(\frac{H}{2\lambda_{jump} + H\left(1 - \tan\theta_i\right)}\right) \tag{4.13}$$

Combining Eq. (4.10) and (4.13), λ_{jump} can be given by

$$\frac{H}{2\lambda_{jump} + H\left(1 - \tan\theta_i\right)} = \tan\left(\arccos\left(\frac{\mu k}{v\gamma_l} + \cos\theta_i\right)\right) \tag{4.14}$$

$$\lambda_{jump} = \frac{H}{2}\left[\frac{1}{\tan\left(\arccos\left(\frac{\mu k}{v\gamma_l} + \cos\theta_i\right)\right)} - 1 + \tan\theta_i\right] \tag{4.15}$$

According to the experiments results (**Figure 4.4**), it is noticed that the λ_{jump} is independent of the velocity of the moving substrate, which is supposed to determine λ_{jump} in Eq. (4.15). However it is dependent on the stopping time of the substrate. Therefore, the model need to be further modified.

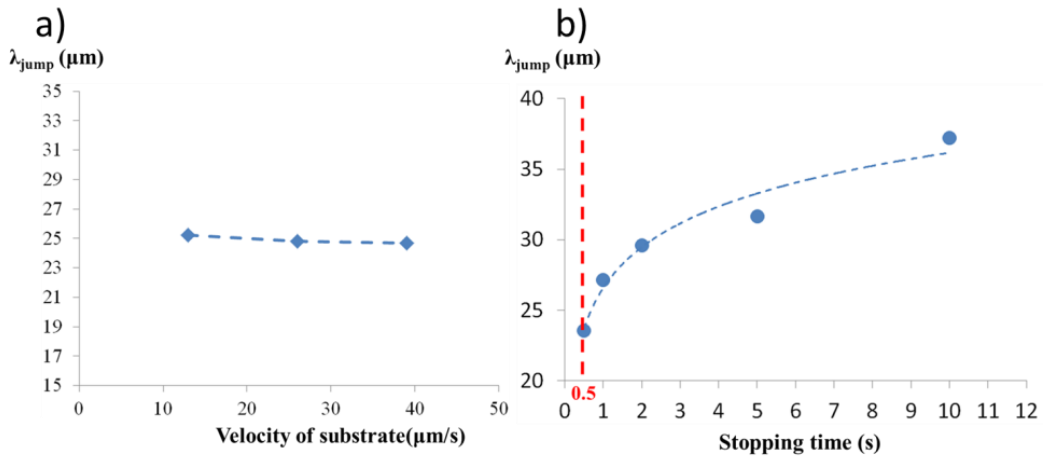

Figure 4.4. Relationships between a) λ_{jump} and velocity of substrate and b) λ_{jump} and stopping time of substrate

It should be noted that on the basis of the experimental observation on the side view of the meniscus of solution confined in between a fixed upper blade and a movable lower substrate (**Figure 4.5**), we found that the schematic illustration depicted in **Figure 4.3** is inaccurate.

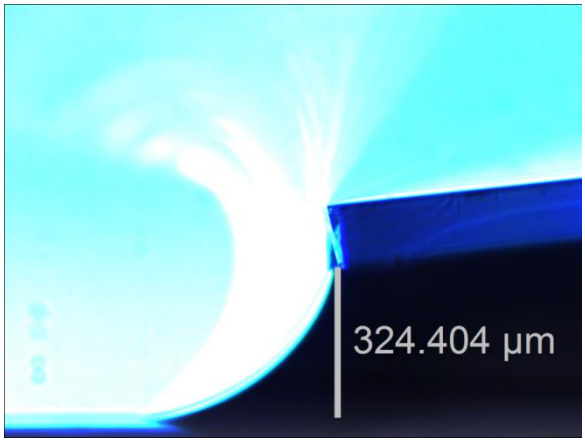

Figure 4.5. Optical microscopic image of the meniscus of solution confined in between a fixed upper blade and a movable lower substrate.

Therefore, we develop an alternative model to account for experimental observations. The balance between the pinning and capillary forces can be considered as

the equality of the pinning energy, E_{pin}, (i.e., the adhesion energy between the deposit and solvent) and the capillary energy, E_{cap} (i.e., the increase in surface tension due to the stretched meniscus interface).

$$E_{pin} = l \times L_{stripe}(\gamma_d + \gamma_l - \gamma_{dl}) \quad (4.16)$$

$$E_{cap} = l \times \Delta L_{liq}\, \gamma_l \quad (4.17)$$

$$E_{cap} = E_{pin} \quad (4.18)$$

$$\Delta L_{liq} = \frac{L_{\text{stripe}}(\gamma_d + \gamma_l - \gamma_{dl})}{\gamma_l} \quad (4.19)$$

where l is the length of the contact line, γ_d and γ_l are the surface tensions of deposit and solvent, respectively, and γ_{dl} is the interfacial tension between the deposit and solvent.

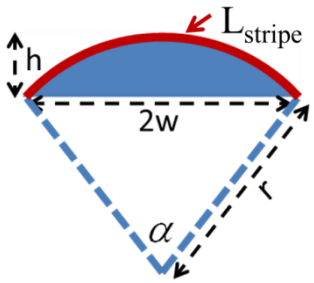

Figure 4.6. Schematic illustration of the profile of one stripe.

The profile of the stripe can be assumed as a circular segment (the blue part shown in **Figure 4.6**), and thus L_{stripe} (i.e., the red line in **Figure 4.6**) is the arc length of the stripe and given by

$$L_{stripe} = \alpha \times r \quad (4.20)$$

$$\alpha = 2\arctan\left(\frac{2wh}{w^2 - h^2}\right) \quad (4.21)$$

$$r = \frac{w^2 + h^2}{2h} \quad (4.22)$$

$$L_{stripe} = \frac{w^2 + h^2}{h}\arctan\left(\frac{2wh}{w^2 - h^2}\right) \quad (4.23)$$

where h is the height of the deposit, $2w$ is the width of the deposit, and α and r are the angle and radius of the circular segment, respectively. We also propose two possible ways for the stretch of the meniscus. The first is as follows (**Figure 4.7**):

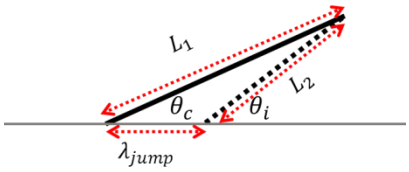

Figure 4.7. Schematic illustration of the first possible way for the stretch of the meniscus.

The substrate moves at a distance λ_{jump}, and the meniscus is stretched from length L_2 to length L_1, while the contact angle decreases from initial contact angle to critical contact angle. Then the increase of the length of the meniscus (ΔL_{liq}) is given by

$$\Delta L_{liq} = L_1 - L_2 \tag{4.24}$$

$$\frac{\sin\theta_i}{L_1} = \frac{\sin\theta_c}{L_2} = \frac{\sin(\theta_i - \theta_c)}{\lambda_{jump}} \tag{4.25}$$

$$\Delta L_{liq} = \lambda_{jump} \frac{sin\theta_i - sin\theta_c}{\sin(\theta_i - \theta_c)} \tag{4.26}$$

The second possible way is that the meniscus is stretched due to the substrate moving at a distance λ_{jump}, but the contact angle keeps constant.

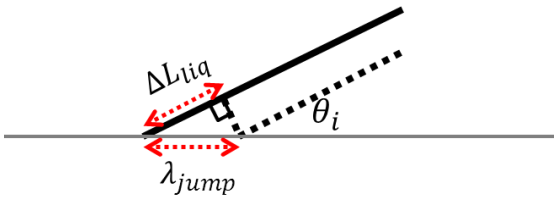

Figure 4.8. Schematic illustration of the second possible way for the stretching of the meniscus.

$$\Delta L_{liq} = \frac{\lambda_{jump}}{cos\theta_i} \tag{4.27}$$

According to Eq. (4.16) and (4.23), E_{pin}~L_{stripe}~h. It is expected that if E_{cap}~λ_{jump}, then there will be a linear relationship between λ_{jump} and h (i.e., λ_{jump} ~h will be satisfied, which was found experimentally (**Figure 4.9**)).

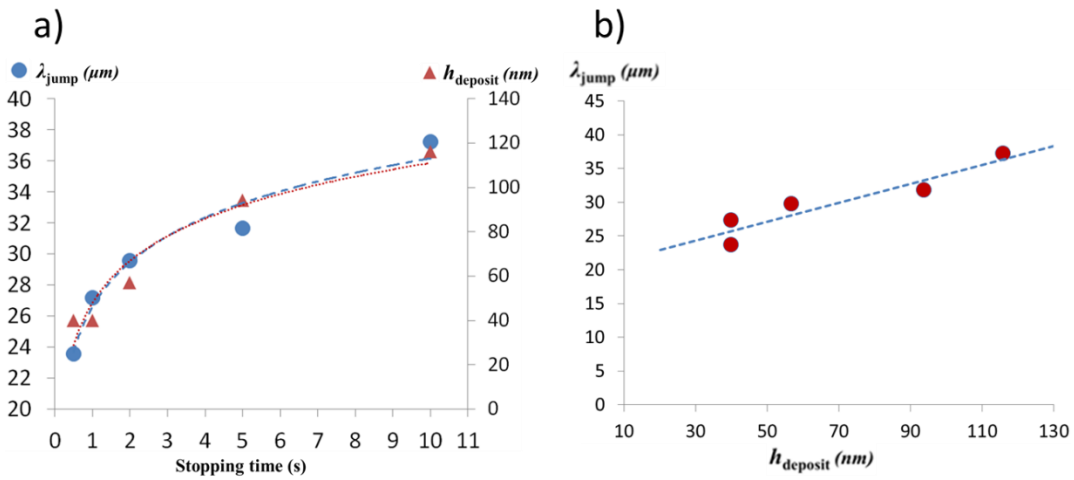

Figure 4.9. a) Relationships between λ_{jump} as well as the height of the deposit, $h_{deposit}$ aas a function of stopping time of substrate. b) linear relationship between λ_{jump} and height of the deposit, $h_{deposit}$.

Therefore, the second possible way seems more valid, as it explains the linear relationship between ΔL_{liq} and λ_{jump} (i.e., E_{cap}~ΔL_{liq}~λ_{jump}). λ_{jump} is thus given by

$$\lambda_{jump} = L_{stripe} \cos\theta_i \frac{\gamma_d + \gamma_l - \gamma_{dl}}{\gamma_l} \qquad (4.28)$$

The interfacial tension can be given as[187]

$$\gamma_{12} = \gamma_1 + \gamma_2 - 4\frac{\gamma_1^d \gamma_2^d}{\gamma_1^p + \gamma_2^p} - 4\frac{\gamma_1^p \gamma_2^p}{\gamma_1^p + \gamma_2^p} \qquad (4.29)$$

where γ_{12} is the interfacial tension between 1 and 2, γ_i (i=1,2) is the surface tension, γ_i^d and γ_i^p are the dispersion and polar components of γ_i, respectively. The dispersion and polar components of solute (i.e., poly(methyl methacrylate) (PMMA); used in my experiment) and solvent (i.e., toluene; used as solvent to dissolve PMMA) and their surface tensions are shown in Table 4.1.[188-189]

	Surface tension (mJ/m^2)	Dispersion (mJ/m^2)	Polar (mJ/m^2)
PMMA	40.2	35.9	4.3
Toluene	29.1	27.8	1.3

Table 4.1 Surface tension of poly(methyl methacrylate) (PMMA) and toluene and their dispersion and polar components.

Combining Eq. (4.28) and (4.29), the relationship between λ_{jump} and L_{stripe} can be calculated: $\lambda_{jump} = 2.354 L_{stripe}$. We note that $\lambda_{jump} = 2.37 L_{stripe} + 14.4$ from the experimental results (**Figure 4.10**). The slopes of both calculated and experimental results fit well. However, a constant value of 14.4 μm was found in experiments, which cannot be explained by the proposed model. The physical meaning of this constant is not clear and needs to be further explored.

Another possible fact is that there is no such a constant (i.e., 14.4 in **Figure 4.10**). All the experimental results fall in the range with the slope between 5.28 and 3.73 (i.e., gray area in **Figure 4.10**). The proposed model is correct. However, the slope (i.e., 2.354) calculated from Eq. (4.28) can be erroneous, due to imprecise measurement of the initial contact angle θ_{i} .

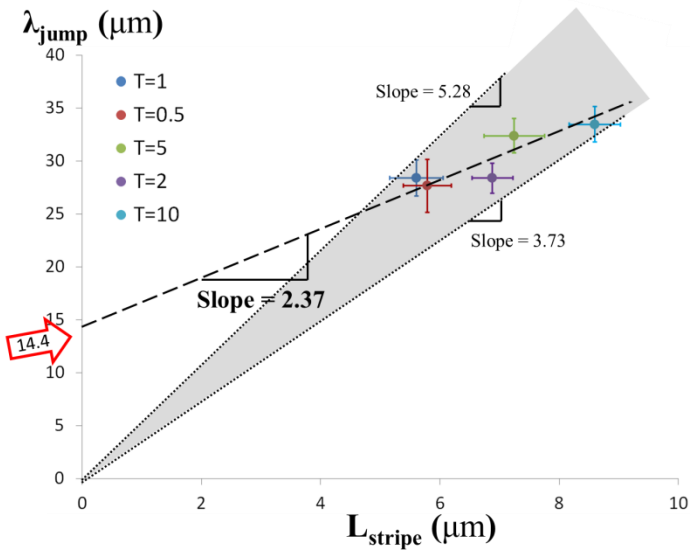

Figure 4.10 Relationships between λ_{jump} and L_{stripe} of the PMMA stripes formed by FESA of PMMA/toluene solution at different stopping time (i.e., t = 0.5, 1, 2, 5, 10s)

4.3 Stripes formation induced by continuous movement of lower substrate

Notably, uniform polymer stripes (**Figure 4.11**) can also be crafted by FESA with the continuous movement of the lower substrate, rather than the "stop-and-move" mode mentioned in Chapter 3 and Section 4.2.The speed of the moving lower substrate which is required to obtain uniform stripes is usually slow (below 100 μm). Interestingly, we found that as the moving speed of the lower substrate increases, the spacing between two adjacent parallel stripes λ_{c-c} will decrease (**Figure 4.12**).

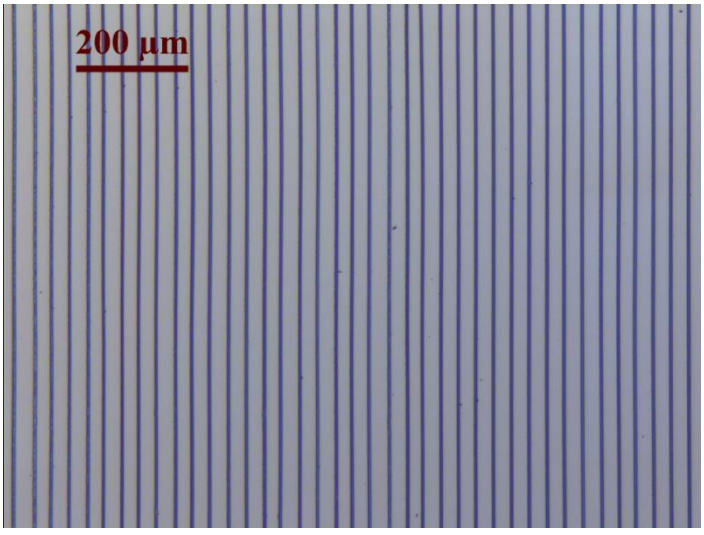

Figure 4.11 Optical microscope image of uniform PMMA stripe pattern formed by FESA with continuous movement of the lower substrate at the speed of 10 μm/s.

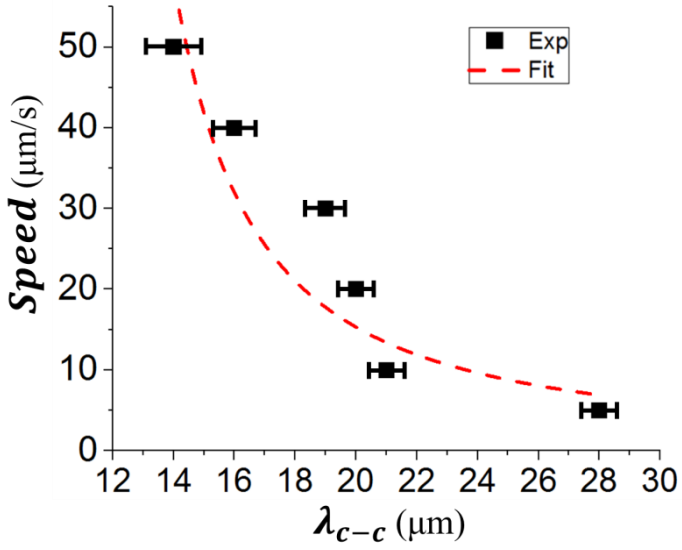

Figure 4.12 The relationship between the spacing of two adjacent parallel stripes and the moving speed of the lower substrate.

The observation can be rationalized as follows. First, for the evaporation rate at the meniscus front, we have [36]

$$\dot{v}(t) = k_e \pi L D (1 - H) C_v \qquad (4.30)$$

where *D* is the diffusivity of the toluene in air, *L* is the length of the meniscus, *H* is the relative humidity, *Cv* is the saturated vapor concentration of the toluene, and *ke* is the evaporation constant. Assuming that the polymer (PMMA) concentration of the solution will not change, then the volume of the stripe, V_{stripe} formed during time period *t* is

$$V_{stripe} = A_{stripe} L = \dot{v}(t) t = k_e \pi L D (1 - Hu) C_v t \qquad (4.31)$$

where A_{stripe} is the cross section area of the stripe, Hu is the humidity. In particular,

$$A_{stripe} = k_e \pi D (1 - Hu) C_v t \qquad (4.32)$$

Moreover, we define that

$$A_{stripe} = k \frac{(W_{stripe})^2}{8} \qquad (4.33)$$

where k is the geometrical constant and $R = \pi$ if we consider the cross section as the half-circle.

Thus we have

$$R\frac{(W_{stripe})^2}{8} = k_e \pi D(1 - Hu)C_v t \qquad (4.34)$$

that is,

$$W_{stripe} = \sqrt{\frac{8k_e \pi D(1-Hu)C_v t}{k}} \qquad (4.35)$$

On the right of the equation, only the time t is variable, that is, $W_{stripe} \sim \sqrt{t}$. After checking with the experimental data, it is clear that the fitted line from eq. (4.35) agreed well with the experimental data (**Figure 4.13**).

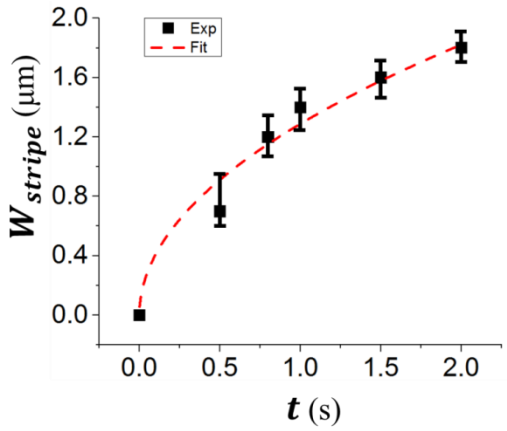

Figure 4.13 The relationship between the width of parallel stripes and the stop time of the lower substrate.

If we consider the stripe formation during the continuous moving of the substrate at speed v, we always have

$$d = vt \qquad (4.36)$$

From the moment the contact line pins (set t = 0), until the moment the contact line depins and jumps to the position of the next stripe, we have

$$\lambda_{c-c} = d = vt \tag{4.37}$$

that is $$t = \frac{\lambda_{c-c}}{v} \tag{4.38}$$

Experimentally, for a stick-slip event, there is a relationship between the slip distance λ_{c-c} and the width of the stripe W_{stripe} , as discussed in Section 4.2.

$$\lambda_{c-c} = A + BW_{stripe} \tag{4.39}$$

By combining eq.(4.38) and (4.39), we get

$$t = \frac{A+BW_{stripe}}{v} \tag{4.40}$$

By subjecting eq. (4.40) into (4.35), we have

$$W_{stripe} = \sqrt{\frac{8k_e\pi D(1-H)C_v(A+BW_{stripe})}{Rv}} \tag{4.41}$$

and

$$\frac{vR}{8}\left(\frac{\lambda_{c-c}-A}{B}\right) = k_e\pi D(1-Hu)C_v\lambda_{c-c} \tag{4.42}$$

Clearly, the fitted line from eq. (4.42) agreed well with the experimental data (**Figure 4.12**).

.

CHAPTER 5

MACROSCOPIC HIGHLY ALIGNED DNA NANOWIRES CREATED BY CONTROLLED EVAPORATIVE SELF-ASSEMBLY

B. Li, W. Han, M. Byun, L. Zhu, Q. Zou, and Z. Lin, "Macroscopic highly aligned DNA nanowires created by controlled evaporative self-assembly", ***ACS Nano***, **7**, 4326 (2013)

5.1 Introduction

DNA is a promising construction material for producing well-defined nanostructures for electronic, magnetic, optoelectronic, and sensory applications. In particular, DNA nanowires produced by stretching DNA permit the physical mapping and diagnosis of diseases,[190] and can also serve as unique template due to their aligned structure and rich chemical functionality[191] for potential use in superconducting nanowires,[192] waveguides,[193] photodetection,[194-195] field-effect transistor,[196] nanophotonic switch,[197] etc. Notably, the prerequisite for most of these applications involving DNA nanowires is to immobilize a large number of DNA molecules on the substrate at the desired position. To date, several methods stemming from simple molecular combing approach,1 including air blowing,[198] electrophoretic stretching,[199] spin-stretching,[200] combing in miscrochannels,[201] and dynamic molecular combing,[202] have been utilized to align and immobilize coiled DNA molecules onto the substrate. Under certain pH and ionic strength, the partial melting of the ends (i.e., extremities) of DNA molecules exposes their hydrophobic core, which adsorbs onto a hydrophobic surface (i.e., specific binding).[201, 203] However, the stretched DNA chains were often randomly distributed. They are not well positioned and ordered over a large area. The length of DNA molecules was also not controlled. Recently, the parallel alignment of DNA arrays has been achieved using a modified molecular combing method combined with soft lithography (i.e., placing a PDMS stamp in contact with the DNA solution)[204-205]; however, the

process was rather complex in terms of the mask preparation and requiring delicate control over the peeling-off speed of PDMS stamp. By utilizing solvent evaporation on a tilted PDMS surface, DNA nanofibers can be fabricated; however, the effects of temperature and pH on the nanofiber formation were still not well understood.[206] Clearly, a low-cost large-scale strategy for highly aligned DNA nanowires is highly desirable and requires a thorough and systematic study.

The use of spontaneous self-assembly as a lithography- and external field-free means to construct highly ordered, often intriguing structures has garnered much attention due to the ease of producing complex, large-scale structures with small feature sizes. In this regard, one extremely simple route to intriguing structures is the drying-mediated self-assembly of nonvolatile solutes (e.g., polymers, nanoparticles and colloids) through the solvent evaporation of a sessile droplet on solid substrate.[207] However, the flow instabilities within drying droplet often result in non-equilibrium and irregular dissipative structures (e.g., randomly organized convection patterns, stochastically distributed multi-rings, and so on). To this end, controlled evaporative self-assembly in a confined geometry has recently emerged as a rational preparation strategy for simple and rapid creation of well-ordered microscopic structures,[207] comprising polymers[25] and particles.[108] The confined geometry imparts a radically distinctive environment for exquisite control over the evaporation process (e.g., evaporative flux, solution concentration, interfacial interaction between the solute and substrate, etc.) to yield complex structures and assemblies with high regularity and fidelity.

Herein, we demonstrate a simple yet robust strategy to yield highly aligned parallel DNA nanowires in the forms of nanostructured spokes and parallel stripes over a macroscopic area (i.e., millimeter scale) by subjecting DNA aqueous solution to evaporate in a curve-on-flat geometry composed of either a spherical lens or a cylindrical

lens situated on a flat substrate. Such confined geometry allowed for the control over the flow within the evaporating solution by eliminating temperature gradient and possible convective instability, thereby leading to the stretching of DNA molecules by the receding meniscus, and in turn forming highly ordered DNA nanowires. The effects of pH of DNA aqueous solution and temperature on the formation of DNA nanowires were systematically explored. A transition from spoke-like patterns to coffee-ring-like deposits was, for the first time, observed as the pH was increased. The optimization of pH and temperature rendered the production of large-scale DNA nanowires aligned parallel to one another.

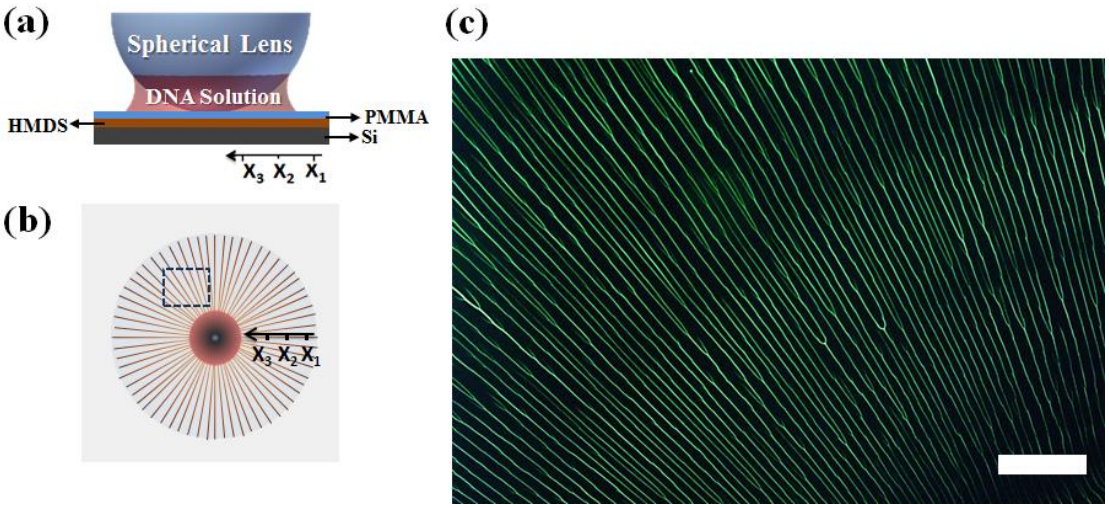

Figure 5.1. (a) Schematic illustration of sphere-on-flat geometry (side view), where a drop of DNA solution is constrained, bridging the gap between the spherical lens and the PMMA-coated Si substrate (i.e., a thin PMMA film was spin-coated on HMDS-coated Si). (b) Schematic illustration of formation of DNA spokes (top view). (c) A small zone of DNA spokes obtained at pH = 6.2, T = 65°C, and the concentration of DNA solution = 8 μg/ml (marked as a dashed box in (b)), emitting green fluorescence. Scale bar = 300 μm.

5.2 Results and Discussion

The DNA spoke-like patterns were formed by allowing a drop of λ-DNA (hereafter referred to as "DNA") aqueous solution to evaporate in sphere-on-flat

geometry constructed by placing a spherical lens on a flat PMMA-coated Si substrate (Figure 5.1.1a; see Experimental Section). The PMMA-coated Si substrate was hydrophobic and facilitated the anchoring of DNA on its extremity. The formation of DNA spokes, analogous to aligning seaweeds on the beach during ebb-tide, can be understood as follows. At the early stage of the drying process, the corrugation of drying front of DNA solution formed, due to fingering instability caused by the long range van deer Waals forces between the liquid and the substrate,24 and DNA molecules preferably accumulated at the "fingers". Over a certain range of pH, the extremity of DNA anchored at the three-phase contact line on the PMMA-coated substrate as a result of the interaction of its extremity with the carboxyl group of PMMA; [190] such anchoring was strong enough to withstand the capillary force (i.e., combing force [24, 208]). The DNA molecules were stretched straight due to the capillary force acting on the rest of DNA molecules by the receding solution front (i.e., air/water interface) during the water evaporation.[209] The anchored DNAs served as nucleation sites and grew into stripes locally that oriented normal to the evaporating front by transporting DNAs from the surrounding solution as the solution front (i.e., meniscus) propagated inward. This resulted in spoke patterns (**Figure 5.1b**).

To scrutinize the surface morphology of the DNA spokes, optical microscopy and AFM measurements were performed. The spacing between two adjacent DNA spokes did not change much from the outermost region (X_1 in **Figure 5.1a-b**) to the innermost region (X_3 in **Figure 5.1a-b**) as the solution front moved toward the sphere/PMMA-coated Si contact center (**Figure 5.1**). This is because as the perimeter of the three-phase contact line dictated by the spherical lens decreased from X_1 to X_3 regions, the spacing between two adjacent DNA spokes is expected to decrease; however, the two adjacent spokes may merge together as one spoke if the distance between them at the drying front was close enough. Locally, the height, h and width, w of DNA spokes were constant.

However, they progressively (but not continuously as will be discussed later) decreased from the outermost region X_1 to the innermost region X_3 as evidenced in three representative AFM height images and the corresponding cross-sectional analysis, namely, from h = 80 nm and w = 400 nm at X_1 = 4200 μm (Figures 5.1.2d and 5.1.2g), to h = 50 nm and w = 200 nm at X_2 = 3400 μm (Figures 5.1.2e and 5.1.2h), and to h = 20 nm and w = 100 nm at X_3 = 2600 μm (Figures 5.1.2f and 5.1.2i); this is not surprising as less DNA molecules were available to be transported to the meniscus as the evaporation proceeded from X_1 to X_3 (Figure 5.1a-5.1b).29 Obviously, the use of sphere-on-flat geometry rendered the production of DNA spokes over a large area (Figures 5.1.1c and 5.1.2a-5.1.2c) with a very long distance (i.e., approximately from X_1 = 2600 μm X_3 = 4200 μm, so a total of 1.6 mm long) (Figure 5.1.1c). On the basis of these observations, it is clear that the dimension of DNA nanowires (i.e., spokes formed in sphere-on-flat geometry) was dictated by not only the concentration of DNA solution, but also the geometry of the upper spherical lens used.

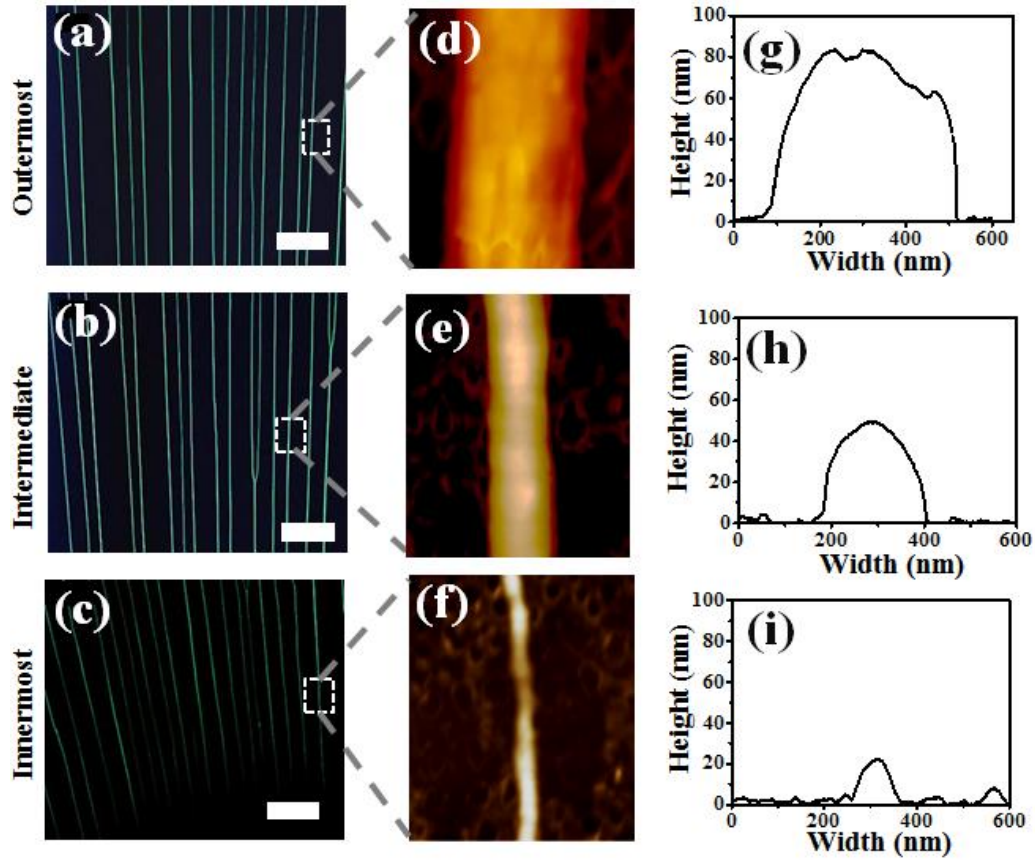

Figure 5.2. (a-c) Representative fluorescence micrographs of DNA spokes formed at different regions (i.e., (a) outermost region, X_1; (b) intermediate region, X_2; and (c) innermost region, X_3) obtained at pH = 6.2, T = 65°C, and the concentration of DNA solution = 8 μg/ml. (d-f) AFM height images of selected areas in (a-c); image size = 600 nm × 600 nm. (g-i) The corresponding cross-sectional analysis of AFM images of DNA spokes in (d-f).

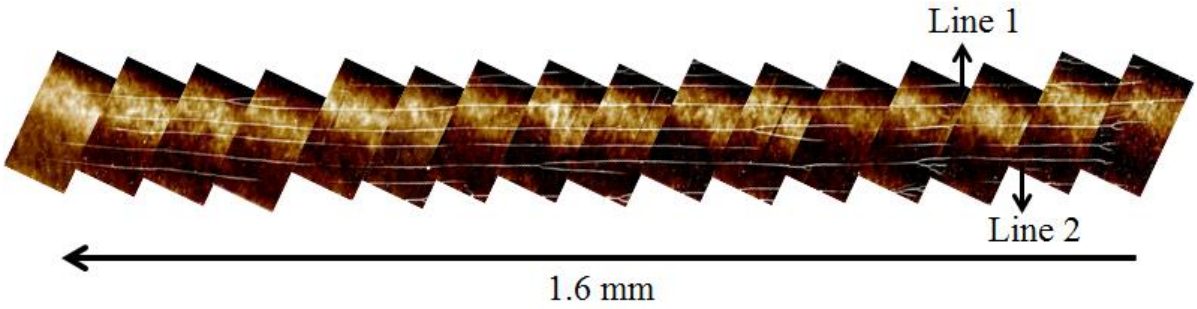

Figure 5.3. Representative AFM image of complete DNA spokes with a total length of 1.6 mm formed at pH = 6.2, T = 65°C, and the concentration of DNA solution = 8 μg/ml. The arrow marked the direction of drying front during the course of water evaporation. The cross-sectional analysis of Line 1 and Line 2 is summarized in Figure 5.4.

As noted above, the length of a complete DNA spoke was approximately 1.6 mm, which was also measured by AFM (**Figure 5.3**). It is noteworthy that the maximum achievable length of DNA spokes is simply limited by the diameter of upper spherical lens used (D = 1 cm in Figure **5.1a**) and the volume of DNA solution loaded. It can be expected that by increasing D and placing a larger amount of DNA solution, much longer DNA spokes with even larger areas can be readily yielded.

Interestingly, although the overall trend of height h of DNA spokes decreased from X1 to X3 as described above, such decrease was not continuous. Instead, a fluctuation in h along a DNA spoke was seen, indicating that during the drying of DNA solution, the three-phase contact line moved toward the sphere/PMMA-coated Si contact center in a "slow-and-fast" manner (**Figure 5.4**). The underlying mechanism for such "slow-and-fast" motion of the meniscus may be rationalized as follows. During the spoke formation process, it was highly possible that the concentration of DNA solution may increase with time due to water evaporation (i.e., the "slow" motion period). As such, the DNA spokes may grow thicker as more DNA were dragged and bundled to the existing DNA nucleation sites, which in turn slowed down the deposition process. The slow move of meniscus further increased the thickness of DNA spokes (i.e., the positive slope in the Height ~ Distance plot in **Figure 5.4**; upward). Subsequently, the "fast" motion was followed. This is because after a certain period of the "slow" motion, the concentration of DNA solution decreased as most of DNA was deposited during this period, leading to the formation of thinner DNA spokes and the increased moving speed of meniscus. The fast moving of drying front resulted in further decrease in the thickness of DNA spokes (i.e., the negative slope in the Height ~ Distance plot in **Figure 5.4**; downward), which led to an increase in the concentration of DNA solution. As the concentration increased, the condition for the "slow" motion was satisfied; the DNA spokes would grow thicker again. Clearly, the repeated "slow-and-fast" motion of drying front resulted in the height

fluctuations along DNA spokes, as also represented in the alternation in fluorescence intensity of green emitting dye-labeled DNA (**Figure 5.1c**).

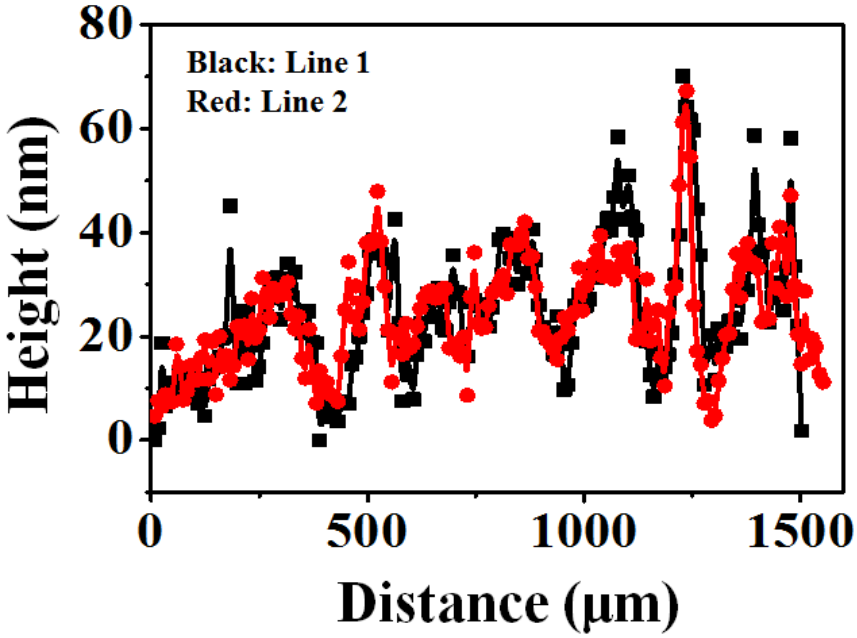

Figure 5.4. The fluctuations in height along two DNA spokes obtained at pH = 6.2, T = 65°C, and the concentration of DNA solution = 8 μg/ml, that is, Line 1 and Line 2, marked in AFM image in Figure 5.1.2, over a distance of 1.6 mm (i.e., the total length of a DNA spoke). We note that the height from the outermost region X_1 (h = 80 nm), to intermediate region X_2 (h = 50 nm), and to innermost region X_3 (h = 20 nm) in Figure 5.4 was slightly different from those in Figure 5.1.4 (i.e., 60 nm, 40 nm, and 20 nm from X_1, to X_2, and to X_3, respectively). This is because that the results in Figure 5.1.4 and Figure 5.1.5 were obtained from two different samples, but under the same experimental condition (pH = 6.2, T = 65°C, and the concentration of DNA solution = 8 μg/ml). It is possible that there may be a slight variation in height between two different samples. However, the trend that there was a decrease in height from the outermost region X_1 to the innermost region X_3 (evidenced in Figure 5.1.4g-i) with the height fluctuation (demonstrated in Figure 5.1.5) was real for all the samples.

The pH value was found to exert a profound influence on the alignment of DNA molecules. The anchoring of DNA on substrate was sensitive to pH, and different pH of DNA solution was responsible for a specific binding mechanism of DNA.[24]For a given temperate T = 65C, at low pH (i.e., pH = 5.5 in **Figure 5.5a**), the DNA molecules were either randomly deposited or aggregated during water evaporation. This was because

DNA molecules underwent intensive protonation, which induced strong nonspecific absorption of DNA on the PMMA surface (i.e., PMMA-coated Si substrate). As the capillary force (i.e., combing force) of drying front was small as compared to the large anchoring force between DNA and the PMMA surface, the meniscus was not able to straightly stretch DNA molecules as it receded. Thus, instead of highly aligned DNA spokes, branches and junctions of DNA spokes were formed. When pH increased to 5.8-6.4 (e.g., optimal pH = 6.2 in **Figure 5.5b**) as in the present study, the denaturation of DNA disappeared and was only restricted to its extremities. Thus, instead of the mid-segment of DNA, DNA molecules were anchored by the end. Subsequently, DNA molecules were aligned (i.e., forming DNA spokes) by the capillary force acting on the rest of DNA molecules as the meniscus receded, as discussed earlier in the above. When pH increased to a higher value (e.g., pH = 7.1 in **Figure 5.5c**), little DNA denaturation was occurred; in other word, the anisotropic property of DNA molecules vanished, and the weak binding between DNA and the PMMA-coated Si substrate cannot fix DNA to the surface. Consequently, DNA can be regarded as a conventional polymer with a large length to diameter aspect ratio. Thus, it is not surprising that concentric ring-like structures were yielded due to "stick-slip" motion of three phase contact line, resembling our previous work on dynamic self-assembly of polymers.[207]Notably, a transition from spoke-like patterns (pH = 6.2) to coffee-ring-like deposits (pH = 7.1) was thus for the first time observed as pH was increased.

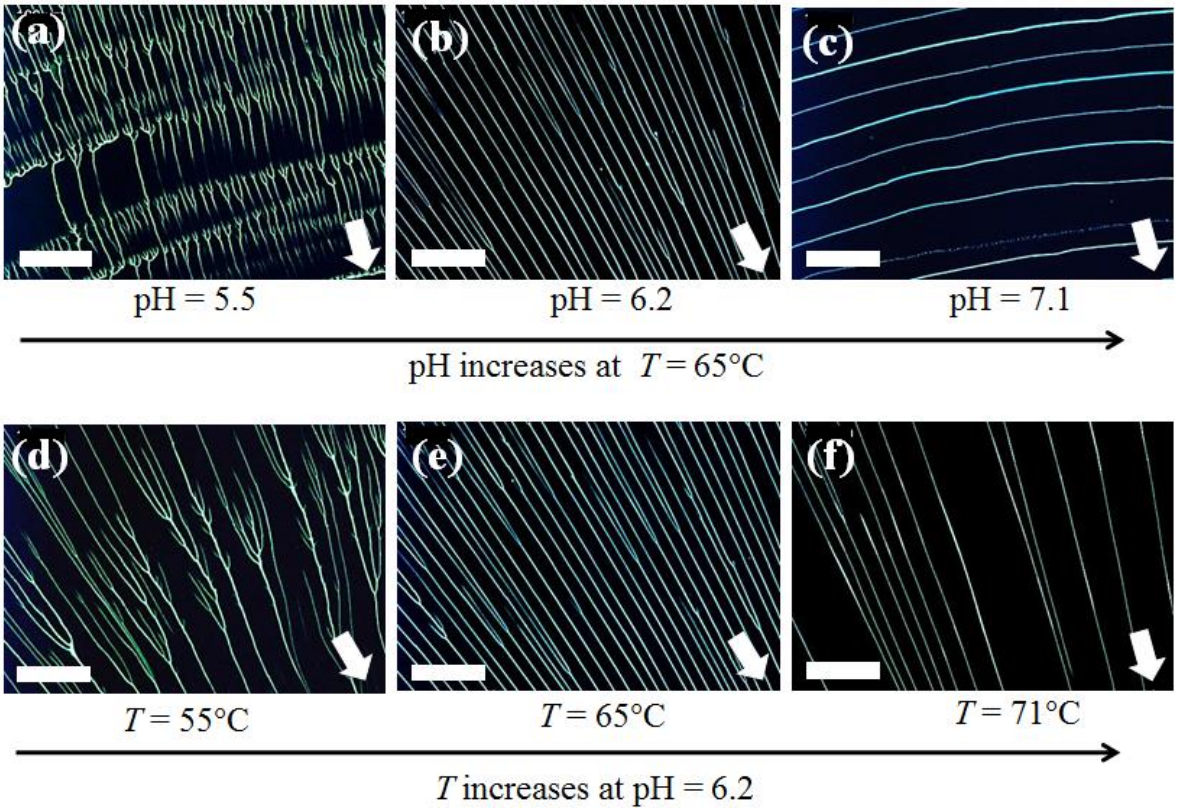

Figure 5.5. Representative fluorescence micrographs of DNA spokes formed in sphere-on-PMMA-coated-Si geometry at the concentration of DNA solution = 8 μg/ml: (a-c) increasing temperature from 55 °C, 65 °C, to 71 °C, respectively, at the constant pH = 6.2; (d-f) increasing pH from 5.5, 6.2, to 7.1, respectively, at constant temperature, T = 65 °C. The white arrows marked the movement of drying front. Scale bar = 200 μm.

In addition to pH, the effect of temperature, which was much less studied in previous molecular combing-based approaches, on the stretching and alignment of DNA was also explored. We note that (a) an increase in temperature would lead to a higher evaporation rate of solvent, and thus faster receding of the three-phase contact line, which in turn promotes the alignment of DNA molecules at the drying front; and (b) on the other hand, the increase in temperature would facilitate the convective flow that carries DNA molecules from the solution inside to the drying front, that is, more DNA would deposit at the three-phase contact line [210-211]. Clearly, based on our observation at the fixed pH = 6.2 as displayed in Figure 5.1.5d-f, the formation of DNA spokes were more likely governed by the former (i.e., (a)). At relatively low temperature (i.e., T ≤ 55°C in

Figure 5.5d), the meniscus moved so slow that DNA molecules not only accumulated at the anchored DNA spoke sites to serve as nucleation sites, but also along the drying front connecting two adjacent spokes. As a result, two spokes were merged together by forming a junction after the meniscus receding. At T = 71 ℃ (**Figure 5.5e**), stretched DNA spokes were obtained, however the regularity of surface pattern in terms of the spacing between two adjacent spokes was reduced due to the increase of fingering instabilities.[210]An optimal temperature, T = 65 ℃ was identified, at which the meniscus receded neither too slow causing two neighboring DNA spokes to merge together, nor too fast so that the regularity of parallel spokes decreased. The ranges of both temperature and pH that rendered the production of highly aligned DNA spokes were summarized in **Figure 5.6**, providing an important piece of information on the proper selection of these two variables to yield well-ordered and positioned DNA that can be used for further research.

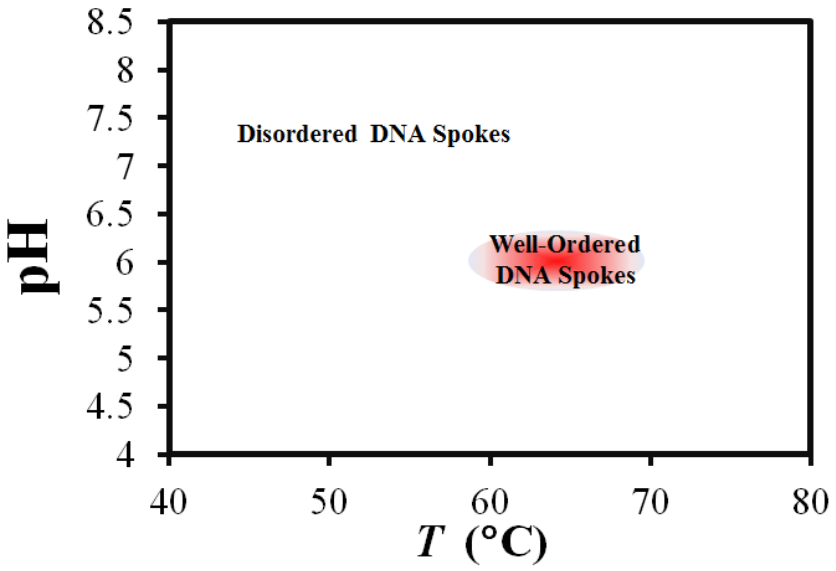

Figure 5.6. Summary of experimental results on the formation of DNA spokes at various pH and temperature *T*. The red area represented the optimum experimental conditions, within which highly aligned DNA spokes can be achieved.

Quite interestingly, rather than spokes yielded from dynamic self-assembly of DNA in sphere-on-flat geometry, a set of parallel stripes were formed by allowing the DNA solution to evaporate in cylinder-on-flat geometry composed of a cylindrical lens situated on a PDMS substrate (Figure 5.1.7). It is worth noting that in comparison to spokes, highly ordered parallel DNA stripes with much fewer junctions over a large area were obtained in cylinder-on-flat geometry (**Figure 5.7c**).

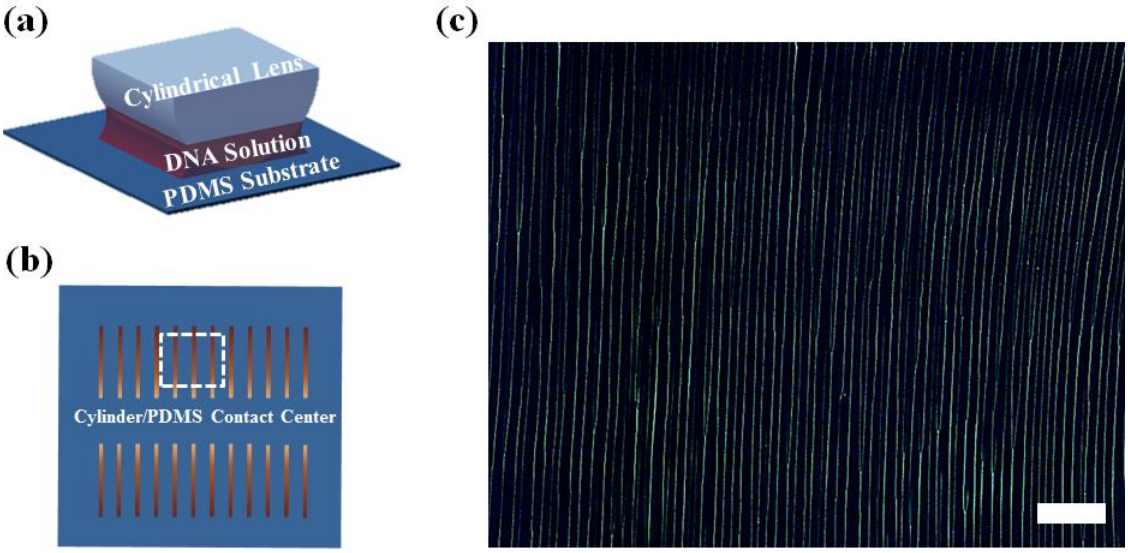

Figure 5.7. (a) Schematic illustration of cylinder-on-flat geometry composed of a cylindrical lens situated on a PDMS substrate (side view). (b) Schematic illustration of formation of parallel DNA stripes on two sides of the cylinder/PDMS contact (marked as "cylinder/PDMS contact center"); similar illustrations are shown in Figure 5.1.8a. (c) A small zone of parallel DNA stripes (marked as white dashed box in (b)) yielded at pH = 6.2, T = 65°C, and the concentration of DNA solution = 8 μg/ml, emitting green fluorescence. Scale bar = 200 μm.

The ability to integrate a large number of one-dimensional DNA stripes into 2D arrays is key to functional DNA-based devices. By performing two orthogonal transfer printing as illustrated in **Figure 5.8a**, 2D arrays of DNA nanowires can be achieved. First, parallel DNA stripes were formed on flat PDMS stamp by evaporative self-assembly of DNA. The use of PDMS substrate rather than PMMA allowed subsequent transfer of stretched DNA to a variety of surfaces through transfer printing (TP) to form

complex patterns. After first TP onto the Si substrate, the second TP was followed by placing DNA stripes in the direction orthogonal to the first TP patterns, thereby yielding 2D arrays of DNA nanowires (**Figure 5.8b**). The AFM measurement showed that the height of two crossed DNA stripes in the overlapped area after two consecutive TPs was approximately 60 μm, and was not the simple sum of the height of stripe 1 (40 μm) and stripe 2 (30 μm), indicating that DNA molecules in each stripe were not tightly bundled (i.e., packed) but with possible spacing among them. Upon the addition of orthogonal DNA stripes on the existing ones, the height decreased. These 2D arrays of DNA nanowires may be used for the construction of functional circuits of DNA-based nanostructures by functionalizing DNA with electronically, magnetically, or chemically active materials;[204] moreover, more complex DNA patterns may be created by multiple TPs. This work is currently underway.

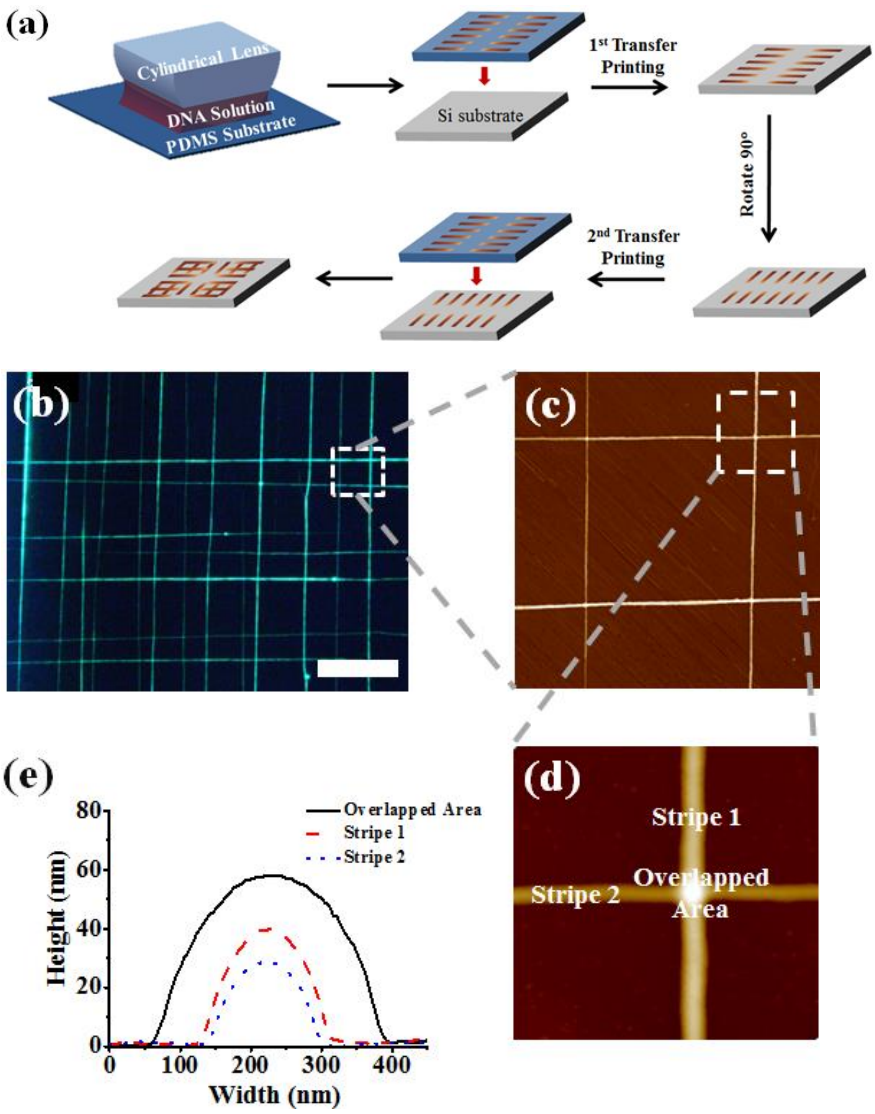

Figure 5.8. (a) Schematic representation of preparation of 2D arrays of DNA nanowires by two consecutive orthogonal transfer-printing using PDMS substrate. The parallel DNA stripes (i.e., a set of lines on the left and right sides in the 2nd and 5th upper panels) were formed on two sides of the cylinder/PDMS contact center. (b) Representative fluorescence micrograph of 2D arrays of DNA nanowires; scale bar = 40 μm. (c) AFM height image of a selected area in (b); image size = 20 μm × 20 μm. (d) The close-up of an overlapped area in (c); image size = 20 μm × 20 μm. (e) The corresponding height profiles of stripe 1, stripe 2, and overlapped area in (d).

5.3.Conclusions

In summary, we demonstrated a simple and low-cost strategy based on controlled evaporative self-assembly in axially symmetric curve-on-flat geometry to yield a high

number density of aligned long DNA nanowires (spokes and parallel stripes) over a macroscopic area (i.e., millimeter scale). The pH of the DNA solution and temperature were found to be important variables that markedly influenced surface patterns of DNA deposits. Such highly oriented DNA nanowires and 2D arrays constructed upon them may open an avenue to realize the full potential of DNA-based nanotechnology for a large scale production of high-density functional nanodevices by capitalizing on these aligned insulating DNA patterns as template.

5.4. Experimental Section

Preparation of PMMA-Coated Si Substrate

A p-type Si wafer (100) was cut into small 1.5–2 cm2 pieces. These pieces were then cleaned with a mixed solution of 18 M sulfuric acid and NoChromix for 12 h. After the acid treatment, Si wafer was then vigorously rinsed with DI water and blow-dried with N2. A layer of hexamtheyldisilazane (HMDS) was spun on Si substrate at 3000 rpm for 60 s, followed by the spin-coating of poly(methylmethacrylate) (PMMA; Polymer Source, Inc.; molecular weight, MWPMMA = 533 kg/mol, PDI = 1.57) toluene solution at a concentration of 4 mg/mL at 2000 rpm for 60 s. The resulting PMMA-coated Si substrates (i.e., thin PMMA film deposited on HMDS-coated Si) were annealed at 120 ℃ for 1 h and allowed to cool to room temperature before use.

Preparation of λ-DNA Buffer Solution

For the preparation of λ-DNA buffer solution, 1 M HCl solution was first prepared by diluting 16.53 mL of 12.1 M HCl stock solution to 200 mL with ultrapure H2O. A total of 0.588 g (0.002 mol) of trisodium citrate dihydrate (TCD) (Fisher Scientific) and 0.5840 g of ethylenediaminetetraacetic acid (EDTA) (FisherBiotech electrophoresis grade, MW = 292.24) were added to 190 mL of ultrapure H2O. By adding HCl solution

to the TCD/EDTA buffer solution, various pH's (i.e., pH = 4.7, 5.1, 5.5, 5.8, 6.2, 6.4, 6.7, and 7.1) were measured and adjusted using a calibrated pH probe. The solution was stirred for 1 h. λ-DNA (New England Biolabs; 48 502 bp; 500 μg/mL in 10 mM Tris·HCl/1 mM EDTA; pH ≈ 8.0) was directly added into the buffer solution described above in a 1.7 mL hinged-cap plastic microvial to yield 8 μg/mL DNA solution. To fluorescently label λ -DNAs at a dye/base-pair ratio of 1:15, YOYO-1 iodide (Life Technologies Corporation, 3 μL) was directly taken from the original solution and added to 8 μg/mL λ -DNA solution (2.4 mL). All procedures were conducted in the dark to prevent the dyes from bleaching. Finally, a green-emitting λ -DNA solution was yielded.

Controlled Evaporative Self-Assembly of DNA Buffer Solution in Curve-on-Flat Geometry

To construct a confined geometry (i.e., curve-on-flat geometry) that was composed of either a spherical lens (i.e., sphere-on-flat) or a cylindrical lens (i.e., cylinder-on-flat) on a flat substrate, a spherical lens made from fused silica and a PMMA-coated Si substrate (for sphere-on-flat), and a cylindrical lens made from fused silica and a PDMS substrate (for cylinder-on-flat) were used. The diameter of spherical lens D was 1 cm (Figure 1a). The diameter and the length of cylindrical lens were 1 and 1 cm, respectively (Figure 4a). The contact of the spherical lens or cylindrical lens with PMMA-coated Si substrate was made using a computer programmable inchworm motor with a step motion on the micrometer scale. Prior to the loading of DNA solution in curve-on-flat geometry, the 1.7 mL microvials containing a specified DNA concentration were submerged in a 37 ℃ water bath for 10–15 min to ensure homogeneity of λ-DNA in solution. The PMMA-coated Si substrate was heated on a Linkam Scientific Precision Temperature Controlled Microscope Stage (Linkam TMS 94 LTS 350) at different temperatures (e.g., 55, 65, and 71 ℃). The humidity was controlled to be the same throughout all experiments. The evaporation took approximately 30 min to complete. Only the patterns formed on the

PMMA-coated Si substrate were evaluated by optical microscope (OM; Olympus BX51) and AFM (Dimension 3100 (Digital Instruments) scanning force microscope in tapping mode).

CHAPTER 6

FLOW-ENABLED SELF-ASSEMBLY OF LARGE-SCALE ALIGNED NANOWIRES

B. Li, C. Zhang, B. Jiang, W. Han and Z. Lin" Flow-Enabled Self-Assembly of Large-Scale Aligned Nanowires ", submitted to ***Angewandte Chemie International Edition***, in press, 2015 (selected as **Very Important Paper (VIP)** paper by Angew. Chem. Int. Ed.) (DOI: 10.1002/ange.201412388)

6.1 Introduction

One dimensional inorganic nanowire enables the realization of fabricating electronic nanodevices as well as for applications in energy conversion and storage. Herein, large-scale aligned DNA nanowires were crafted by flow-enabled self-assembly (FESA). The highly oriented and continuous DNA nanowires were exploited either as templates to form metallic nanowires by exposing DNA nanowires preloaded with metal salts under oxygen plasma or as scaffold to direct the positioning and alignment of metal nanoparticles and nanorods. Such FESA strategy is simple and easy to implement, promising new opportunities in crafting of large-scale one-dimensional nanostructures for nanodevices at low lost.

The past decade has witnessed remarkable progress in chemically synthesized as well as lithographic fabricated nanowires due to their unique size-dependent optical and electronic properties.[212] They have emerged as an important class of nanomaterials as building blocks and interconnects for nanodevices as well as for applications in energy conversion and storage.[213] For example, silicon nanowires are employed as new light harvesting semiconductors for solar energy conversion.[214] In comparison with TiO_2 nanoparticles, the use of an array of densely packed TiO_2 nanowires as photoanode

provides the direct pathway for charge transport from the point of injection to the collection electrode while retaining large surface area for dye loading in DSSCs.[215] It is worth noting that chemically grown nanowires often involve high synthesis costs for industry and exhibit relatively weak adhesion to the substrate. On the other hand, nanowires with controlled size and well-defined growth locations on the substrate can be prepared by lithographic techniques. However, lithographic methods often require an iterative multistep procedure that is time consuming and costly. Clearly, it is of great interest and technological importance to explore nonlithographic strategies to yield long nanowires over large scale at low cost.

In this context, the use of biotemplates (e.g., virus,[216] peptide,[217] and DNA[115, 218]) offers a promising route to one-dimensional nanomaterials.[219] In particular, DNA has been widely recognized as an ideal biotemplate for creating a broad range of metallic nanowires[220-221] due to its remarkably high aspect ratio (i.e., 2 nm in diameter and tens of micrometers in length). However, the dramatic increase in stiffness and significant aggregations of metallized DNA molecules make it difficult to immobilize and precisely position the metallized DNA molecules on solid substrate.[221] Furthermore, the length of metallic nanowires is only on a few tens of micrometer scale. However, long metallic nanowires are highly desirable for practical applications.[222] Obviously, the key to achieving well-ordered and continuous metallic nanowires is to first produce regularly aligned DNA nanowires on the substrate, followed by their subsequent metallization. However, it remains challenging to achieve highly ordered and continuous DNA nanowires on substrate. We note that single flexible DNA molecule can be stretched and aligned using a receding meniscus (a "molecular combing" method).[198] Similar approaches to stretched DNA have also been developed, including microchannel combing,[223] air-blow combing,[224] spin stretching,[225] and electric field assisted combing.[226] Nonetheless, the immobilized individual DNA molecules are often randomly

positioned. The ability of creating long DNA nanowires is very limited in scope.[227] Clearly, the formation of well-positioned, continuous DNA nanowires depends critically on the intricate control over the solvent evaporation during the combing or stretching of DNA molecules. It is worth noting that irregular dissipative patterns composed of nonvolatile solutes (e.g., polymers, colloids, nanoparticles, carbon nanotubes, etc.) are commonly observed from the sessile droplet evaporation due to flow instabilities within the drying droplet.[4, 116, 228] By delicately controlling the evaporation process (e.g., the evaporative flux, the solution concentration, and the interfacial interaction between solute and substrate[108, 229]), for example, by constructing curve-on-flat geometries to constrain and regulate the solvent evaporation and eliminate the temperature gradient, one-dimensional and two-dimensional as well as hierarchical structures and assemblies of polymers[154, 230] and nanoparticles[96] with unprecedented regularity and fidelity can be reproducibly produced.[152-153]

Herein, we report a simple and viable strategy to achieve large-scale aligned nanowires templated by highly oriented DNA crafted by flow-enabled self-assembly (FESA). By subjecting DNA aqueous solution to dry between two nearly parallel plates composed of a stationary upper plate and a movable lower plate mounted on a programmable translational stage (i.e., a FESA process), an array of ultralong, high density, and parallel DNA nanowires on a large scale was successfully created. The positions of DNA nanowire-like deposits were fixed on substrate through the anchoring of its extremity onto the hydrophobic substrate. The formation of DNA nanowires was strongly influenced by the concentration of DNA solution, temperature, and moving speed of lower plate. The length of highly oriented DNA nanowires was simply dictated by the amount of DNA solution used in FESA. A simple yet robust swelling-induced transfer printing (SIT-Printing) technique was developed to transfer ultralong DNA nanowires onto the desirable substrate. Subsequently, the resulting DNA nanowires were

exploited as templates to form metallic nanowires by exposing DNA nanowires preloaded with metal salts under oxygen plasma. Moreover, DNA nanowires were also employed as scaffold for aligning metal nanoparticles and nanorods. The ability of placing DNA into one-dimensional parallel and continuous nanowire arrays over large area, followed by their use as template to yield functional inorganic nanostructures, may render the mass production of integrated nanodevices.

6.2. Results and discussion

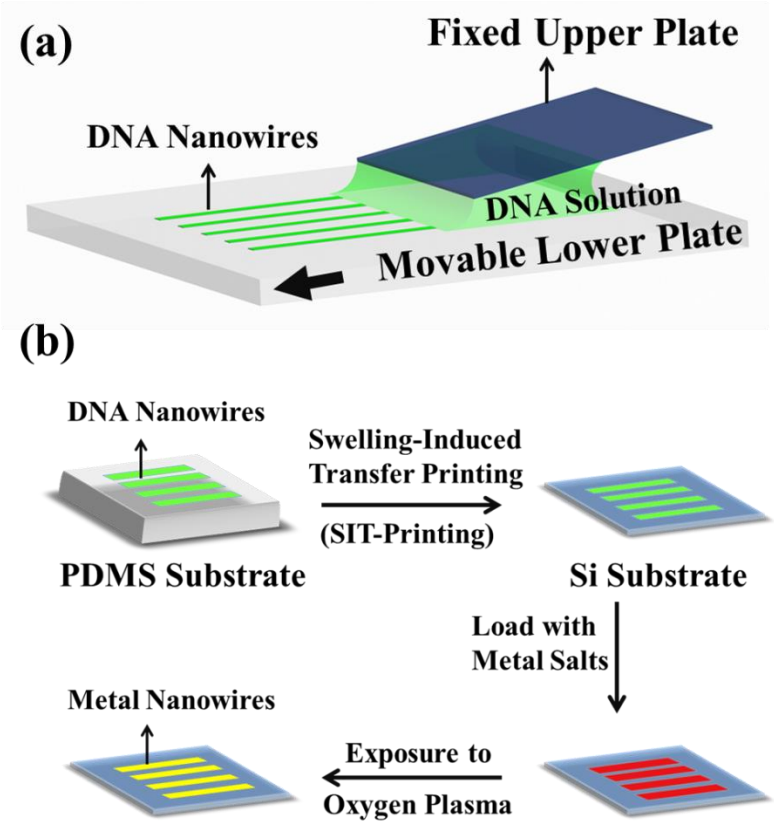

Figure 6.1. a) Schematic illustration of crafting an array of high-density continuous DNA nanowires by flow-enabled self-assembly (FESA). The DNA solution was constrained between two nearly parallel plates with the lower PDMS substrate placed on a translation stage programmably moved against the upper fixed glass plate. b) Schematic representation of swelling-induced transfer printing (SIT-Printing) of DNA nanowires

and the subsequent metallization of DNA nanowires by exposing them preloaded with metal salts to O_2 plasma

A drop of YOYO-1-labeled DNA aqueous solution was loaded in a confined geometry comprising a lower movable PDMS substrate and an upper stationary glass plate with a separation distance of 300 μm between them (**Figure 6.1a**). The lower substrate was mounted on a translational stage programmably controlled by computer (see *Experimental Section*). The DNA molecules were first transported to three-phase contact line (i.e., the air/water/substrate interface; receding meniscus) due to the evaporative loss of water.[180, 228] As the lower PDMS substrate was subsequently moved, fingering instabilities were emerged at the drying front due to the unfavorable interaction between DNA and PDMS (i.e., van der Waals force).[149] It has been reported that, over a certain range of pH, the partial melting of the ends (i.e., extremities) of DNA molecules exposes their hydrophobic core, which adsorbs onto a hydrophobic surface (i.e., specific binding).[204, 223] Such anchoring was strong enough to withstand the dragging force exerted due to the motion of PDMS substrate. Thus, DNA molecules were stretched and aligned along the moving direction of PMDS substrate. The anchored DNA molecules acted as the nucleation sites, at which more DNA molecules were transported and grown along with them, thereby creating continuous DNA nanowires with a length of a centimeter (**Figure 6.1a**). It is noteworthy that much longer DNA nanowires are easily attainable by loading a larger amount of DNA solution (> 60 μL) and increasing the moving distance of the PDMS substrate (> 1 cm) (see *Experimental Section*). It is not surprising that as DNA molecules were stretched perpendicularly with respect to the evaporating front, an array of parallel and continuous DNA nanowires on a centimeter scale were thus readily obtained.

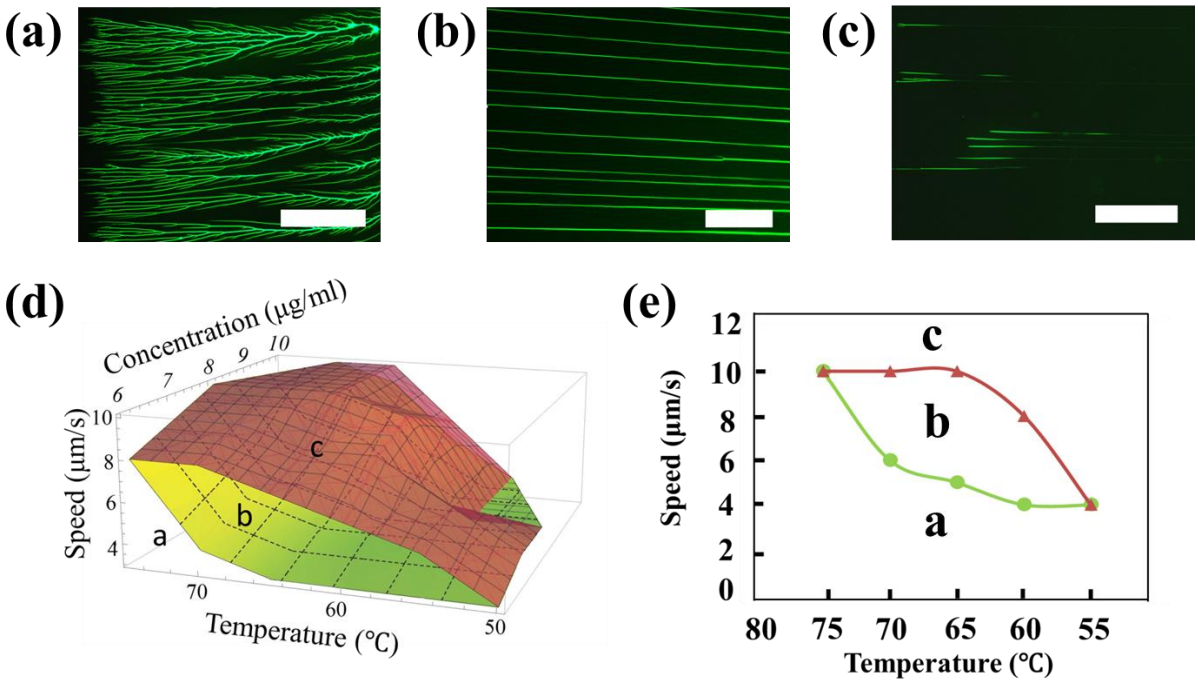

Figure 6.2. Representative fluorescence micrographs of self-assembled YOYO-1-labeled DNA molecules. a) branched DNA bundles, b) continuous DNA nanowires, c) short DNA lines. d) 3D map of the DNA concentration, moving speed of PDMS substrate, and temperature for DNA pattern formation. The label a, b and c correspond to the range. of experimental conditions for yielding DNA nanostructures shown in a), b) and c), respectively. e) 2D map of the moving speed of lower PDMS substrate as a function of temperature for DNA pattern formation at the fixed concentration of 8 μg/ml. Scale bar = 500 μm in a) and c), and 100 μm in b)

Intriguingly, the formation of highly aligned DNA nanowires depended sensitively on the DNA concentration, temperature, and moving speed of PDMS substrate (**Figure 6.2**). Strikingly, there existed an optimal range of the deposition density of DNA molecules for the crafting of long and continuous DNA nanowires (**Figure 6.2b**). However, the higher deposition density led to the formation of branched DNA bundles (**Figure 6.2a**), while the lower deposition density resulted in the production of discontinued DNA lines (i.e., short stripes; **Figure 6.2c**). To tailor the deposition density of DNA, the concentration of DNA solution, temperature, pH of DNA solution, surface chemistry of substrate, and moving speed of substrate can be tuned. To this end, we

systematically varied the concentration, temperature, and moving speed of substrate, while maintaining a constant pH (i.e., pH = 6.2) and PDMS as the substrate. Obviously, a higher DNA solution concentration and a lower moving speed of PDMS substrate would impart a larger deposition. Moreover, an increase in temperature would induce a higher evaporation rate at the receding meniscus, thereby transporting more DNA to deposit at three-phase contact line. The judicious combination of these three variables that led to the formation of long and continuous DNA nanowires was represented by area *b* in **Figure 6.2d**, enveloped by the upper red boundary (above which short DNA lines were formed as marked with *c* in **Figure 6.2d**, corresponding to the optical micrograph in **Figure 6.2c**) and the lower green boundary (below which branched DNA bundles were found as marked with *a,* corresponding to the optical micrograph in **Figure 6.2a**). **Figure 6.2e** shows a representative temperature-moving speed range at the DNA concentration of 8 μg/ml. The temperature-moving speed plots of other concentrations in this work are presented in **Figure 6.3**. Notably, there existed a critical range of DNA concentration (i.e., from 5 μg/ml to 14 μg/ml; not shown in **Figure 6.2d** and **Figure 6.3**). For a higher concentration (i.e., larger than 14 μg/ml), the deposits were either branched DNA bundles or short DNA lines or a mixture of both, depending on the certain combination of the temperature and moving speed of PDMS substrate. With a lower concentration (i.e., smaller than 5 μg/ml), there were few DNA molecules deposited on the substrate, and thus only short DNA lines were seen. It is noteworthy that the FESA of DNA conferred a much wider temperature range to attain continuous DNA nanowires over large scale (55-75 °C; **Figure 6.2e**), compared to the previous work.[230]

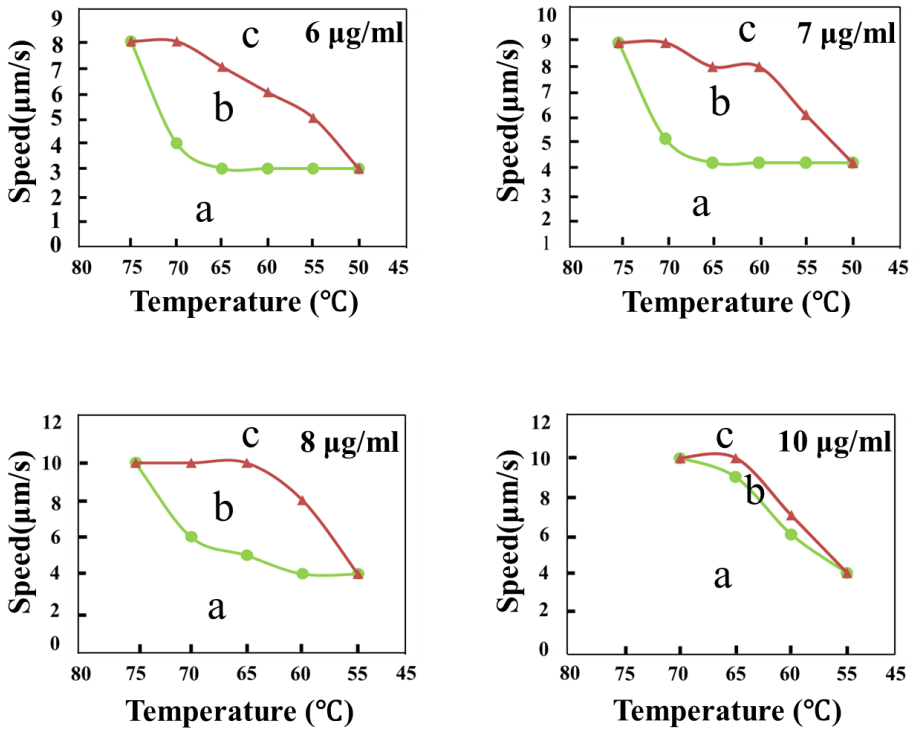

Figure 6.3. Two-dimensional map of the moving speed of lower PDMS substrate as a function of temperature for DNA pattern formation at the concentrations of 6 μg/ml, 7 μg/ml, 8 μg/ml and 10 μg/ml, respectively.

It has been reported that radically aligned DNA nanowires formed by controlled evaporative self-assembly in a curve-on-flat geometry were highly sensitive to the experimental temperature.[230] This was because of the dual roles that the temperature played in the DNA nanowire formation. As the DNA solution was allowed to evaporate in a fixed curve-on-flat geometry, that is, both the upper curved surface and lower flat substrate were kept stationary during the entire evaporation process. Consequently, as the temperature increased, more DNA molecules were transported to three-phase contact line, thus increasing the deposition density of DNA. On the other hand, the temperature increase also simultaneously increased the moving speed of the receding meniscus in the curve-on-flat geometry due to the higher evaporation rate of solvent, which caused the decrease of the deposition density of DNA. Ultimately, the balance of these two competing effects on the deposition density gave rise to a rather narrow range for the

DNA nanowire formation. In stark contrast, for the FESA of DNA in this work, the temperature only determined the transportation of DNA to three-phase contact line. Rather than the temperature, the moving speed of receding meniscus was simply controlled by the programmably moved substrate mounted on a translational stage. Clearly, the FESA of DNA conferred a much wider temperature range to attain continuous DNA nanowires over large scale (55-75 °C; **Figure 6.2e**).

The prerequisite of using DNA as template for creating inorganic nanostructures is to transfer-print DNA nanowires onto the desirable substrates (e.g., from PDMS substrate to Si wafer). In this work, we found that the conventional "contact-and-peel-off" method[231] was not applicable for transfer-printing the as-prepared DNA nanowires from PDMS to Si substrate as only several DNA nanowires were transferred. Moreover, the originally continuous DNA nanowires were segmented after transfer printing. One possible reason may be because the adhesion between DNA nanowires and the PDMS substrate was stronger than that of a single DNA molecule anchored on the PDMS substrate,[231] due to the larger contact area between DNA nanowires and PDMS in the present study. To this end, we developed a facile swelling-induced transfer printing (SIT-Printing) approach to transfer DNA nanowires, as schematically illustrated in **Figure 6.4**. First, the DNA nanowire-deposited PDMS substrate was immediately brought into contact with Si wafer after crafted by FESA. The DNA nanowire-PDMS/Si substrate was then immersed in toluene. As PDMS was swollen in toluene, the PDMS substrate was gradually detached from the Si substrate and floated on the top of toluene. The DNA nanowires were, however, remained and transferred on the Si substrate on the bottom of toluene. The entire SIT-Printing process was completed in 20 mins. It is interesting to note that DNA nanowires transferred on the Si substrate can be preserved in toluene for days as toluene is a non-solvent for DNA. Furthermore, by performing two orthogonal SIT-Printing, 2D meshes of DNA nanowires can be achieved.

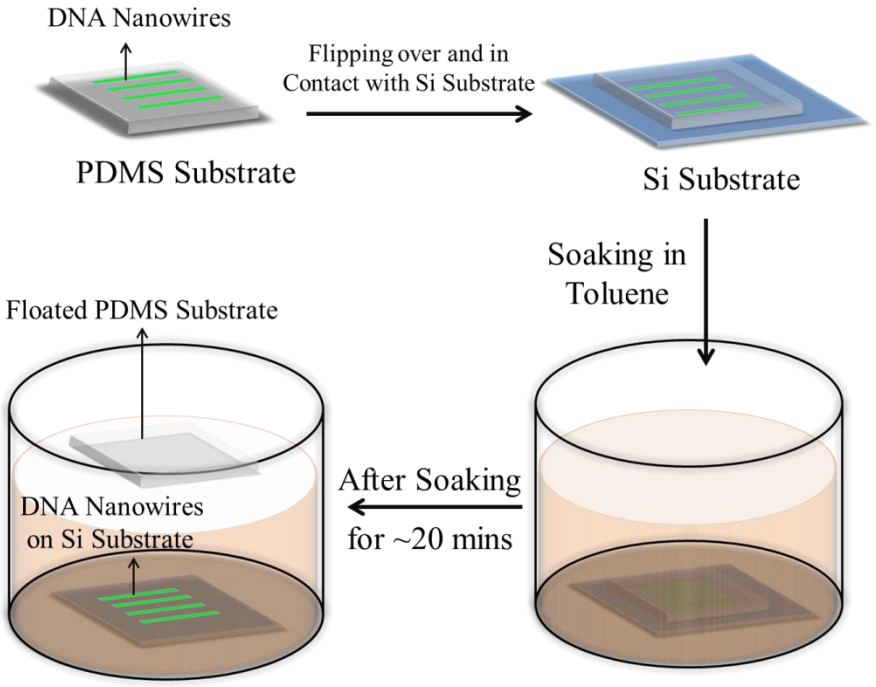

Figure 6.4. Schematic representation of swelling-induced transfer printing (SIT-Printing) of DNA nanowires.

To scrutinize and better understand this intriguing and effective SIT-Printing process, we simply dropped a 20-µl toluene onto the DNA nanowire-coated PDMS substrate noted above. The DNA nanowires were observed to be easily lifted off from the PDMS substrate without destroying the continuity of DNA nanowires (**Figure 6.5**). It is plausible that toluene diffused into the DNA/PDMS interface and PDMS swelled by adsorbing toluene. As DNA is hydrophilic while PDMS is hydrophobic, DNA nanowires were thus delaminate from the swollen PDMS substrate. Similarly, in the SIT-Printing, toluene entered the tightly contacted DNA nanowire-deposited PDMS/Si interface, and facilitated the detachment of DNA nanowires from PDMS and transferred to the Si substrate as both Si and DNA nanowires were hydrophilic. In addition, the swollen

PDMS in toluene may also exert a uniform pressure on the Si substrate to promote the transfer printing.

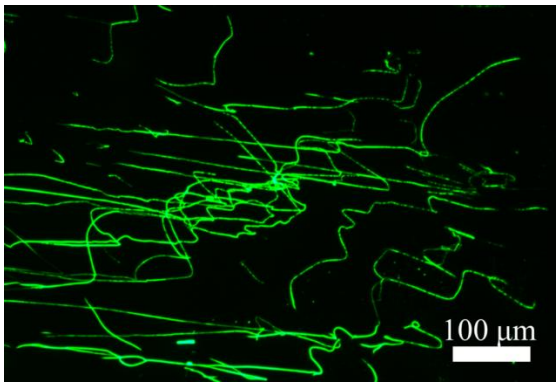

Figure 6.5. Representative fluorescence micrograph of disordered DNA nanowires yielded by casting a drop of toluene on the PDMS substrate.

Subsequently, conductive metal nanowires were produced by exploiting DNA nanowires transferred on the Si substrate by SIT-Printing as template. Despite several studies on metallization of single DNA molecule in solution,[219, 222, 232] the reported methods cannot be extended to metalize continuous DNA nanowires in solid state. This is due likely to the difficulty in metallizing DNA nanowires while retaining self-assembled DNA nanostructures on the substrate. It is easy to understand that as water is used as solvent to prepare the metal precursor solution, and once the precursor water solution is placed on DNA nanowire patterns, the nanowires would be dissolved by water. Thus, in order to load metal salts onto DNA nanowires, a nonsolvent for DNA is needed when preparing the metal precursor solution. In this work, silver precursor solution (i.e., silver nitrate; $AgNO_3$) was prepared using the mixed solvents of dimethylformamide (DMF) and toluene at 1:1 ratio by volume. The DNA nanowire-deposited Si substrate was then immersed into the $AgNO_3$ DMF/toluene solution for 24 hrs. Because of the electrostatic attraction between positively charged Ag^+ and negatively charged DNA backbone, Ag^+

was bonded to DNA. The DNA nanowires preloaded with metal salts were thus produced. Conventionally, silver precursors can be reduced to form Ag nanowires by chemical reduction. However, we found that the reducer needed to be carefully selected. For example, the addition of a strong reducer, such as tetra-n-butylammonium bromide (TBAB), to the soaking solution caused not only the instant formation of Ag nanowires but also the deposition of unwanted Ag nanoparticles all over the substrate (**Figure 6.6a**).

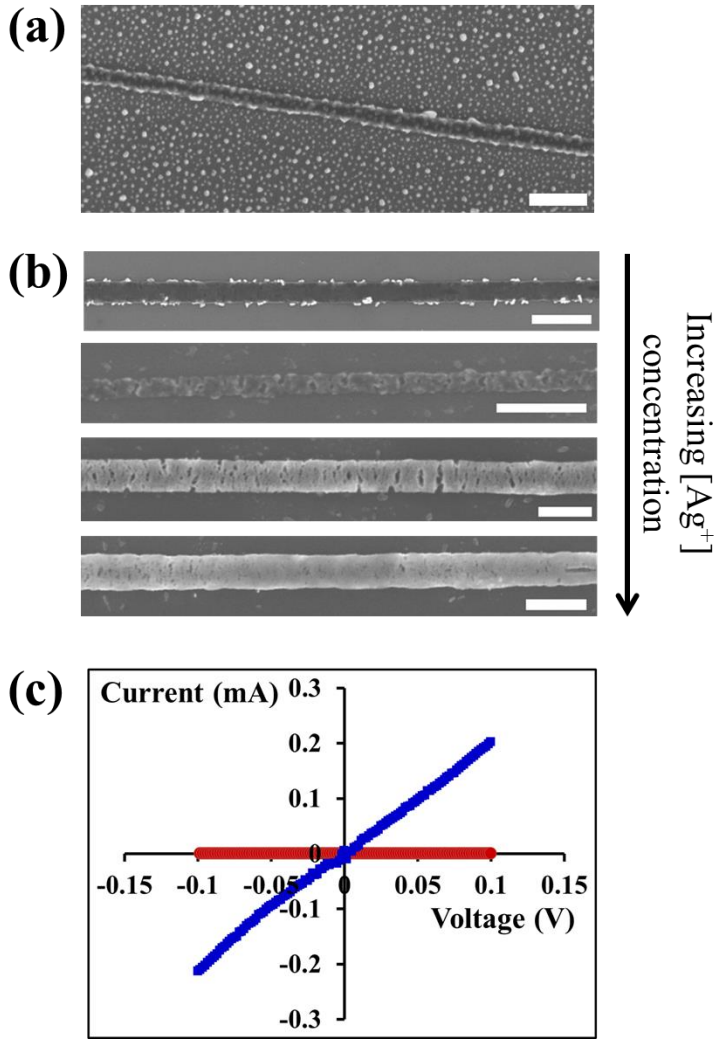

Figure 6.6. Representative SEM images of Ag nanowire formed by (a) chemical reduction with Ag nanoparticles deposited all over the surface, and (b) the reduction induced by oxygen plasma. The morphologies of Ag nanowires with the increased concentrations of $AgNO_3$ (from top to bottom are 0.5mg/ml, 1mg/ml, 10mg/ml, and 50mg/ml, respectively) are shown in (b). (c) Current-voltage (*I*-*V*) characteristics of the resulting Ag nanowires from DNA nanowires preloaded with 50 mg/ml $AgNO_3$ precursors (blue: continuous nanowire; red: discontinued nanowire). Scale bar = 400 nm in both (a) and (b).

Thus, we capitalized on an effective approach to create Ag nanowires by exposing the Ag-precursor-loaded DNA nanowires to oxygen plasma (**Figure 6.6b** and **Figure 6.7**), with which the reduction reaction facilitated by the electrons from oxygen plasma.[97, 155] Moreover, there were no excess Ag nanoparticles deposited on the space between adjacent Ag nanowires on the Si substrate as the substrate was washed by toluene and blow-dried prior to the oxygen plasma treatment. Interestingly, the morphology of the grown Ag nanowire was related to the $AgNO_3$ concentration. A lower $AgNO_3$ concentration (i.e., 0.5 mg/ml) only gave rise to partially metallized DNA nanowires. With a concentration above 10 mg/ml, continuous Ag nanowires were formed. The conductivity of obtained Ag nanowires was then measured (**Figure 6.6c**). The conductivity of continuous Ag nanowires (blue line in **Figure 6.6c**) was much higher than those grown from a single DNA molecule,[218] owing to the larger diameter of DNA nanowires in comparison to single DNA molecule. When the Ag nanowire was cut apart by a razor blade, no current was observed (red line in **Figure 6.6c**).

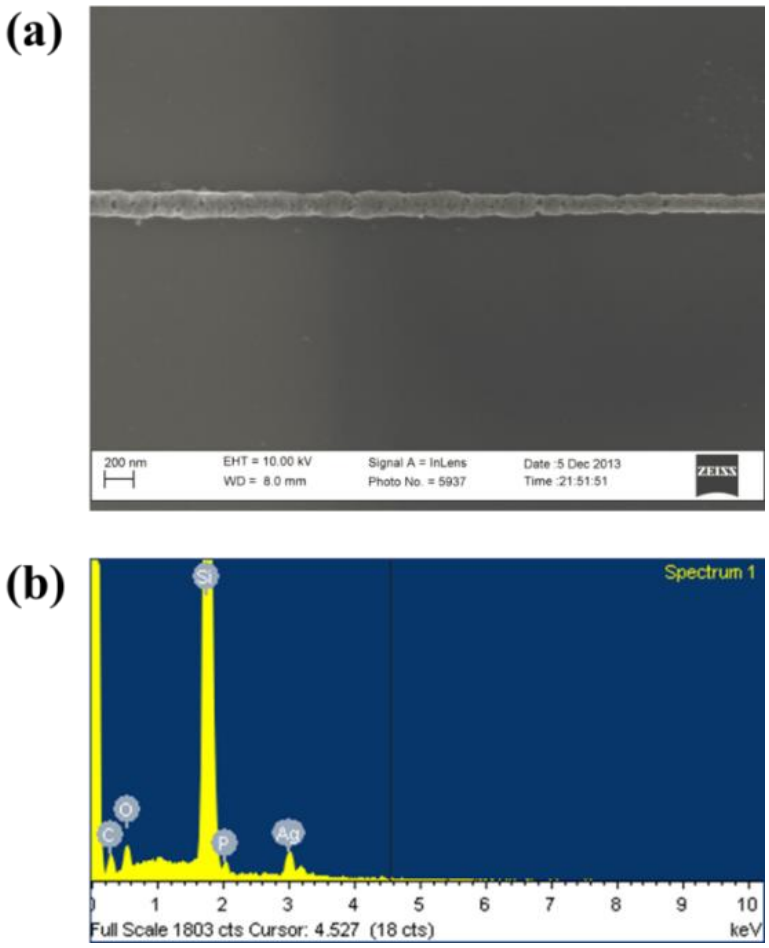

Figure 6.7. Representative SEM image of Ag nanowires and its corresponding EDS spectrum.

In addition to templating for forming metal nanowires, DNA nanowires can also serve as a scaffold for directing the metal nanoparticle assembly. In this regard, two approaches for producing the nanoparticle assembly were developed. The first approach is to grow and align Au nanoparticle along the DNA nanowire by chemical reduction (**Figures 6.8** and **6.9)**. Different from the growth of Ag nanowires, the Au precursor (i.e., chloroauric acid; $HAuCl_4$) bears the negative charge (i.e., $AuCl_4^-$), which is the same as the backbone of DNA nanowire. Thus, after soaking DNA nanowire in the $HAuCl_4$ solution, the electrostatic repulsion prevented $AuCl_4^-$ from binding to the DNA backbone. However, by deliberately adding cetrimonium bromide (CTAB; a ligand capped on the

Au nanoparticle surface), CTAB-functionalized Au nanoparticles were first formed from the precursor solution, and then bonded to DNA nanowires through the electrostatic attraction between positive surface charge on CTAB-functionalized Au nanoparticles and negatively charged DNA backbone. Notably, the Au precursor solution at the concentration of 1 mg/ml was prepared by adding 10 mg $HAuCl_4$ and 0.7289g CTAB (i.e., 0.2M CTAB) into 10ml DMF/methanol mixed solvents (DMF : methanol = 1:1 ratio by volume). Upon the addition of the reducing agent (i.e., sodium citrate), Au nanoparticles were nucleated and grown in solution, and capped with CTAB to prevent Au nanoparticles from aggregation. Interestingly, the size and shape of Au nanoparticles grown and decorated along the DNA nanowire were highly sensitive to the reducing agent (for example, corroded DNA nanowires were seen when sodium borohydride was used as the reducer; **Figure 6.10**), the concentration, and the addition of Ag^+. The size of Au nanoparticles was found to alter from tens of to hundreds of nanometers. The shape of Au nanoparticles was also varied, including spherical (**Figure 6.8**), sea-urchin-like (**Figure 6.9**) and flake-like (**Figure 6.11**) nanoparticles, which may have potential applications in localized surface plasmonic resonance (LSPR) due to their nanometer size and close proximity.[233] All these merit a detailed study, and are currently under investigation.

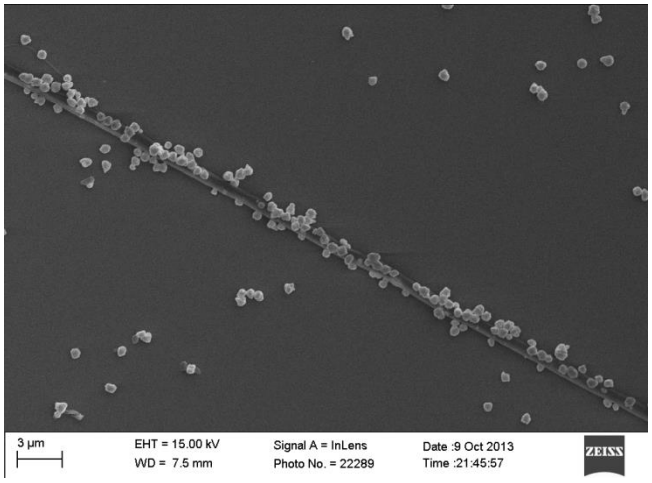

Figure 6.8. SEM image of Au nanoparticles produced by using the DNA nanowire as template.

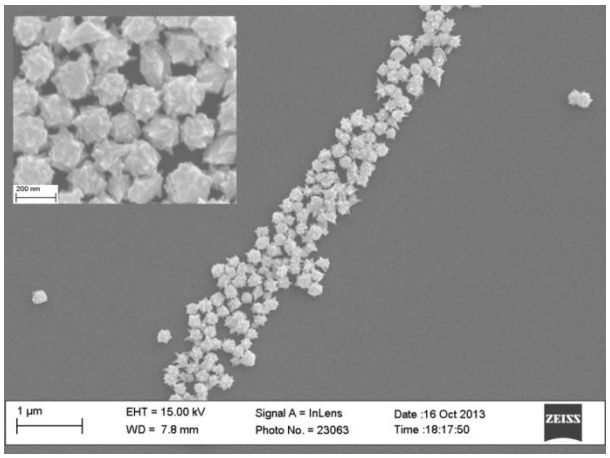

Figure 6.9. Representative SEM image of sea-urchin-like Au nanoparticles using the DNA nanowire as template. The 0.004 M $AgNO_3$ and 0.08 M ascorbic acid (reducer) were added in the Au precursor solution.

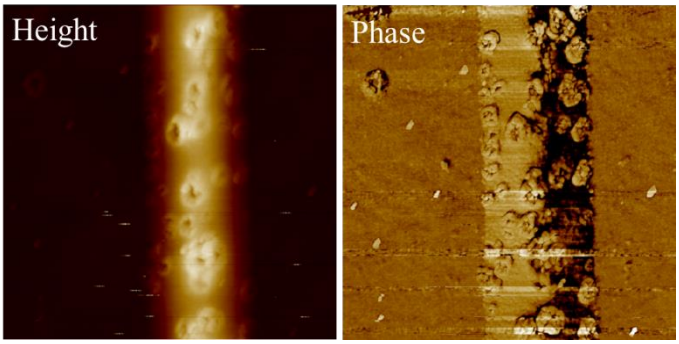

Figure 6.10. AFM height and phase images of corroded DNA nanowire when applying sodium borohydride as the reducer, instead of sodium citrate. Image size = 2 μm × 2 μm.

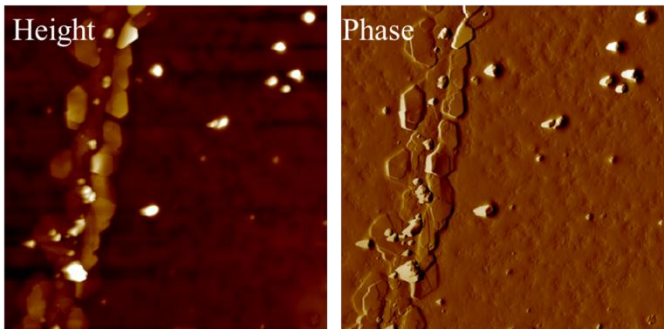

Figure 6.11. AFM height and phase images of Au flakes grown along DNA nanowire when using borane morpholine complex as the reducer, instead of sodium citrate. Image size = 2 μm × 2 μm.

Instead of using the Au precursors as described above, the second approach using DNA nanowire to guide the Au nanocrystal assembly is to employ the premade Au nanoparticle and nanorods. There are two means of patterning pre-synthesized nanocrystals along the DNA nanowire: either mixing DNA and Au nanocrystals first, and then orienting them on the substrate, or patterning DNA nanowire first, followed by aligning Au nanocrystals along the fixed DNA nanowire on the substrate. We found that the first approach did not work as DNA aggregated with Au nanoparticles and precipitated prior to being deposited on the substrate. In contrast, the second approach was successful in achieving Au nanocrystals aligned on DNA nanowires. First, Au

nanoparticles with a diameter of approximately 20 nm were synthesized using sodium citrate as the reducing agent. Subsequently, DNA nanowires were crafted by FESA slowly (e.g., at the moving speed of 6 μm/s on the PDMS substrate). Finally, Au nanoparticles were aligned by the second FESA at a much higher speed (e.g., 100 μm/s) along the direction of preformed DNA nanowires (**Figure 6.12**). A representative TEM image of aligned Au nanoparticles was shown in **Figure 6.12a**. The average height of Au nanoparticle-decorated DNA nanowire was approximately 60 nm (**Figure 6.12b**). In addition to Au nanoparticles, Au nanorods can also be aligned along the DNA nanowire (**Figure 6.13**).

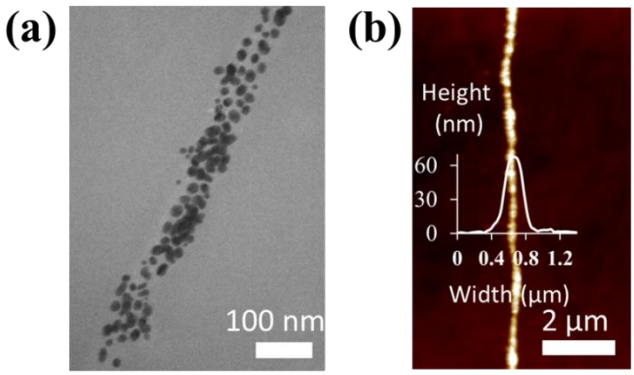

Figure 6.12. (a) Representative TEM image, and (b) 2D AFM height image of direct assembly of premade Au nanoparticles (~16 nm) by employing the DNA nanowire as scaffold.

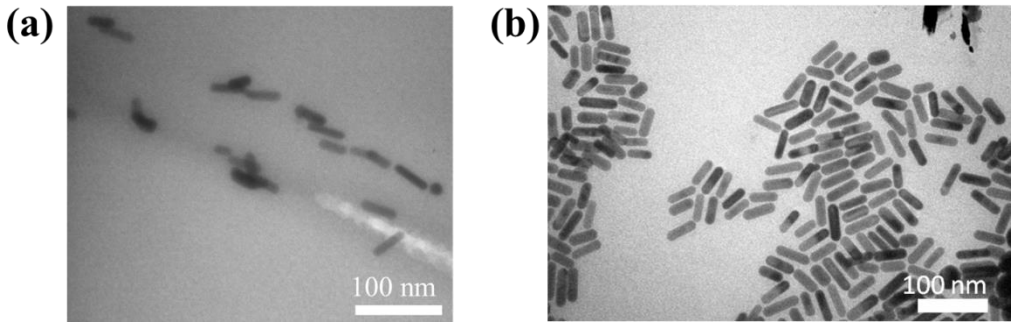

Figure 6.13. (a) Representative TEM image of Au nanorods aligned along the DNA nanowire; (b) TEM image of Au nanorods prepared according to literature.[234]

6.3. Conclusions

In summary, we demonstrated a strikingly simple and robust flow-enabled self-assembly strategy for aligning DNA into an array of high-density long nanowires over large scale. DNA nanowires were then successfully transferred onto desirable substrate via a facile swelling-induced transfer printing (SIT-Printing) technique. Subsequently, these parallel and continuous DNA nanowires were exploited either as template to produce conductive metal nanowires by the oxygen plasma treatment or as scaffold to direct the positioning and alignment of metal nanoparticles and nanorods. Clearly, flow-enabled self-assembly strategy is easy to implement and renders the crafting of large-scale one-dimensional polymer- and biomaterial-based nanostructures at low cost, and their direct exploitation or transformation into useful inorganic nanostructures for effective integration into nanodevices and even the construction of higher hierarchical devices.

6.4. Experimental Section

Preparation of DNA solution. To prepare the DNA solution, 1M HCl solution was firstly prepared by diluting 16.53 mL 12.1M HCl stock solution to 200 mL with ultrapure H2O. 0.588 g (0.002 moles) trisodium citrate dihydrate (TCD) (Fisher Scientific) and 0.5840 g EDTA (FisherBiotech electrophoresis grade, MW = 292.24) was added to 190 ml ultrapure H2O. By adding HCl solution to the TCD/EDTA buffer solution, pH was measured and adjusted using a calibrated pH probe. The as-prepared solution was then mixed with ethanol at volume ratio of 7:3. Subsequently, λ-DNA (New England Biolabs; 48502 bp; 500 μg/mL in 10mM Tris•HCl/1m M ethylenediaminetetraacetic acid (EDTA); pH ≈ 8.0) of different amount was added into the solution noted above, yielding the concentration of 6 μg/ml, 7 μg/ml, 8 μg/ml, and 10 μg/ml. To fluorescently label DNA, green-emitting YOYO-1 iodide (Life Technologies Corporation) was directly added to

the DNA solution at a dye/base-pair ratio of 1:15. The resulting fluorescent DNA solution was stored in dark to prevent the dyes from bleaching. It should be noted that for the metallization of DNA nanowires, no dye was added to DNA solution.

Flow-enabled self-assembly of DNA solution. DNA nanowires were formed by subjecting a drop of DNA solution (60 μl) to evaporate in a two-nearly-parallel-plate geometry comprising a fixed upper glass plate and a lower movable PDMS substrate. The separation distance between the upper glass plate and lower PDMS substrate was approximately 300 μm. The PDMS substrate was mounted on a translational stage ((Parker Hannifin Corp, mode: MX80LVixBL2b) controlled by computer. The resolution of the translational stage is 100 nm. The PDMS substrate was heated on a Linkam Scientific Precision Temperature Controlled Microscope Stage (Linkam TMS 94 LTS 350) at different temperatures and moved over a total distance of 1 cm. The humidity was controlled to be the same throughout all experiments. The evaporation took approximately 30 min to complete. DNA nanowires were evaluated by optical microscope (OM; Olympus BX51) and atomic force microscope in tapping mode (AFM; Dimension 3100, Digital Instruments).

Characterizations. SEM images of Ag nanowires, and Au nanoparticles and nanorods aligned along DNA nanowires were taken by field-emission scanning electron microscope (FE-SEM; FEI Quanta 250) operating at 10kV and 15kV in high vacuum. Electric conductivity of Ag nanowire was measured using a Keithley 2400 multisource meter. To facilitate the conductivity measurement of Ag nanowires, they were first created on the Si substrate by the metallization of as-prepared DNA nanowires. Two Ag electrodes with a 50- μm gap were deposited on the Ag nanowires. The applied voltage increased from -0.1V to 0.1V continuously to measure the current-voltage (I-V) curve. Au nanoparticle (and nanorod)-decorated DNA nanowires were characterized by transmission electron microscopy (TEM) (JEOL 100CX; operated at 100kV). To prepare

TEM sample, Au nanoparticle (and nanorod)-decorated DNA nanowires were first prepared on the PDMS substrate, followed by dropping 10 μl toluene on the top. Au nanoparticle (and nanorod)-decorated DNA nanowires were then detached from the PDMS substrate and floated within the toluene droplet. The TEM grid was placed underneath the droplet for transferring Au nanoparticle (and nanorod)-decorated DNA nanowires. Upon drying, nanoparticle (nanorod)-decorated DNA nanowires were deposited on the TEM grid.

6.5. Theoretical Study of the Formation of Figure-like pattern

Notably, the self-assembly of DNA from its aqueous solution is a complicated system to model, as DNA under a certain range of pH becomes anisotropic molecules (i.e., "sticky" end exposed in solution which allowed the attachment of DNA molecules onto the substrate). Thus, instead of studying the formation mechanism of finger-like DNA nanowires, we begin the theoretical study with the finger-like pattern of PS deposition on Si wafer. It is noteworthy that a PMMA film is stable on a Si substrate as the Hamaker constant (which signifies the interfacial interaction between the solute and substrate) is negative[235-236] for a PMMA film deposited on the Si substrate, yielding stripe patterns (i.e., lines of PMMA deposits parallel to the contact line in FESA); while the Hamaker constant for PS on the Si substrate is positive,[237-238] yielding spoke-like deposition patterns (i.e., lines of PS deposits perpendicular to the contact line in FESA), as shown in **Figure 5.3.1**.

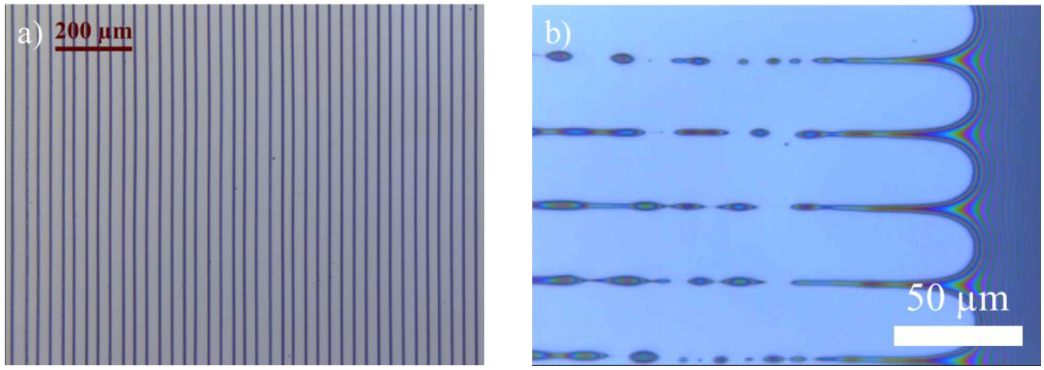

Figure 6.14. a) PMMA stripes formed with the direction parallel to the contact line in FESA. b) PS spokes formed with the direction perpendicular to the contact line in FESA.

The characteristic distance between two adjacent figures in the figuring pattern λ_f can be predicted as follows. A linear stability analysis of a liquid-like thin film (i.e., the capillary edge in) yields the dispersion relation [149]

$$\frac{1}{\tau} = \frac{h^3}{3\eta}\left(-\gamma q^4 + \frac{A}{2\pi h^4} q^2\right) \tag{5.1}$$

where q is the growth mode, $1/\tau$ is the growth rate, r is the surface tension of solute, h is the thickness of the capillary edge, η is the viscosity, and A is Hamaker constant, signifying the interfacial interaction between the solute and substrate.

The condition for equilibrium between a wetting film and a meniscus in a capillary held solution is the equality of the equality of the capillary pressure P_c and the disjoining pressure Π(h) (i.e., van der Waals interaction), [239] yielding

$$P_c = \Pi(h) \Rightarrow \frac{2\gamma_{solvent}}{H} = \frac{|A|}{6\pi h^3} \tag{5.2}$$

Where $\gamma_{solvent}$ is the surface tension of solvent and H is the surface separation at the liquid-vapor interface. The fastest growth mode, corresponding to the maximum in Eq. (5.1)

$$\frac{\partial(1/\tau)}{\partial(q)} = 0 \Rightarrow q_{\max} = \left(\frac{A}{2\pi\gamma h^4}\right)^{\frac{1}{2}} \tag{5.3}$$

Substituting eq. (5.2) into Eq. (5.3), the characteristic distance between adjacent figures, λ_f is thus found from

$$\lambda_f = \frac{2\pi}{q_{\max}} = 2\pi\left(\frac{\gamma hH}{6\gamma_{solvent}}\right)^{\frac{1}{2}} \tag{5.4}$$

In experiments, we found that the molecular weight played a dominate role in the formation of PS finger-like depositions, which is not considered in the model. Thus, the model for calculated λ_f from Eq. (5.4) required further modification, based on the difference between the experimental observations and the theoretical prediction. This work is still undergoing .

.

CHAPTER 7

UNCONVENTIONAL MECHANISM FOR WATER-SOLUBLE ULTRATHIN GOLD NANOWIRE GROWTH

B. Li, B. Jiang, H. Tang and Z. Lin, "Unconventional mechanism for water-soluble ultrathin gold nanowire growth ", submitted to ***Journal of the American Chemical Society***

7.1. Introduction

Controlling the size, shape, composition, and structure of metal nanocrystals is of fundamental and technological importance as the optical, electrical, and catalytic properties of metal nanocrystals depend heavily on these parameters. In this context, due to one-dimensional (1D) confinement of electron transport and high surface area, metallic nanowires possess many intriguing functionalities for use in optical waveguide,[240-241] lasers,[242] sensors,[243-245] and nanoelectronics.[246-248] Among various metal nanocrystals, significant advancement has been made in Au nanocrystals research with good control over their size and shape. Interestingly, ultrathin Au nanowires have been synthesized via an aurophilic reaction by employing oleylamine (OA) as the solvent and reducing agent.[249] They offer a wide range of potential applications[250-251] because of their unique optical properties,[252-253] conductivity,[254] chemical activity,[255] and discrete plasticity.[256] These OA-capped ultrathin Au nanowires, however, are non-water soluble,[257-260] and thus limit their use in biomedical applications.[261] The strong absorption of OA on Au nanowire surface makes it difficult for further ligand-exchanging to yield water-soluble Au nanowires.[262]

Much effort has been concentrated on the creation of 1D Au nanorods based on the commonly used cetyltrimethylammonium bromide (CTAB) template strategy.[263-265] Surprisingly, there has been no report to date on the synthesis of ultrathin Au nanowires by employing the CTAB-templating strategy. The preferential physisorption of CTAB to the {110} and {100} facets facilitates the 1D Au growth along the [110] direction from the prepared Au seeds (i.e., Au nanoparticles).[234, 266] However, such longitudinal growth usually discontinues when the aspect ratio of length to diameter of nanorods reaches 10.[263, 267] The multistep growth allows for the formation Au nanorods with the aspect ratio of 20 or higher.[268-269] However, the diameter of Au nanorods grown from Au seeds is usually larger than 10 nm or even beyond 50 nm,[270] despite the fact that the diameter of Au seeds used for the nanorod growth is of much smaller size (i.e., usually < 3 nm).[263] This may be due to the formation of cylindrical template with a large inner diameter from the self-assembled CTAB molecules in aqueous solution, which makes it difficult to constrain the Au nanorod from growing larger, leading to the production of Au nanorods with a much larger diameter than that of Au nanoparticle seeds. Notably, it is highly desirable to yield ultrathin Au nanowires with a diameter of 2-3 nm for promising applications noted above.[271] To this end, the ability to tune the inner diameter of cylindrical CTAB template offers new opportunities for creating ultrathin Au nanowires. This, however, has yet to be explored.

Herein, we report on a simple yet effective strategy for water-soluble ultrathin Au nanowires. Surprisingly, rather than commonly obtained Au nanorods, by introducing a small amount of hydrophobic solvent (i.e., toluene or chloroform) into the Au growth solution based on conventional preparative approach for Au nanorods with cylindrical CTAB micelles as template, CTAB-capped ultrathin Au nanowires (i.e., water-soluble ultrathin Au nanowires) were yielded. It is interesting to note that there existed a certain range of CTAB concentration, beyond which no ultrathin Au nanowires can be produced.

Moreover, silver ions and Au seeds required for the Au nanorod growth were found to be crucial as well in the formation of CTAB-capped ultrathin Au nanowires. The growth mechanism of such intriguing water-soluble ultrathin Au nanowires, differed from those formed by using oleylamine (i.e., non-water-soluble Au nanowires),[249] was explored.

7.2. Results and Discussion

Figure 7.11a compares the effect of introducing a trace amount of hydrophobic solvent (i.e., toluene) into the Au growth solution. The Au seeds were prepared according to literature.[234] On the other hand, the Au growth solution was prepared as follows:[267] 10 ml 0.1 M CTAB aqueous solution was mixed with 0.5 ml 10 mM $HAuCl_4$ solution and 40 μl 0.1M $AgNO_3$ solution. Subsequently, 0.5 mL 0.1M hydroquinone (as the reducing agent) aqueous solution was added and stirred until the mixed solution became transparent. Without the addition of toluene to the Au growth solution, Au nanorods with high yield were resulted in[267] after adding the Au seed solution[234] (upper panels in **Figure 7.1a**, **Figure 7.1b**, and **Figure 7.2**). However, upon the addition of a trace amount of toluene (100 μl) to the Au growth solution and being mixed well, followed by adding the Au seed solution (see Supporting Information), the final solution remained colorless after a one-day reaction. Surprisingly, from this transparent solution, ultrathin Au nanowires were observed as revealed by the TEM measurement (**Figure 7.1c**). It is noteworthy that in stark contrast to non-water soluble ultrathin Au nanowires synthesized by using oleylamine as in copious past work,[272] which are often self-assembled side-by-side, in this work the resulting CTAB-capped ultrathin Au nanowires laid freely on the TEM grid because of the repulsion between adjacent nanowires due to the presence of positively charged CTAB on the surface of nanowires.

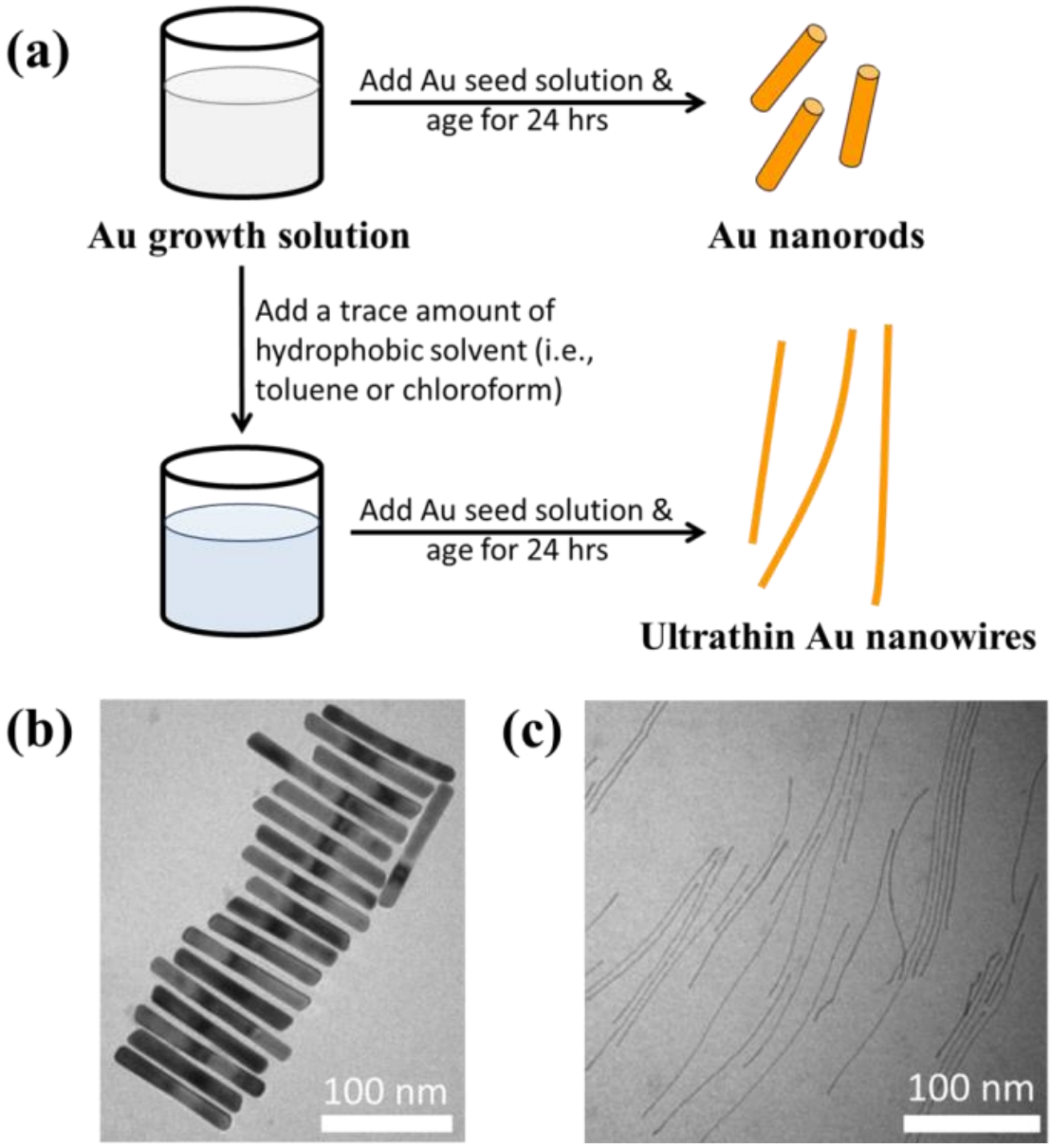

Figure 7.1. (a) Schematic illustration of synthesis of Au nanorods in pure Au growth solution (upper right panel), and of ultrathin Au nanowires with the introduction of a trace amount of hydrophobic solvent (i.e., toluene or chloroform) into the Au growth solution (lower right panel). (b) Au nanorods synthesized without the addition of toluene, corresponding to the upper right panel in (a). (c) Ultrathin Au nanowires formed with the addition of toluene, corresponding to the lower right panel in (a).

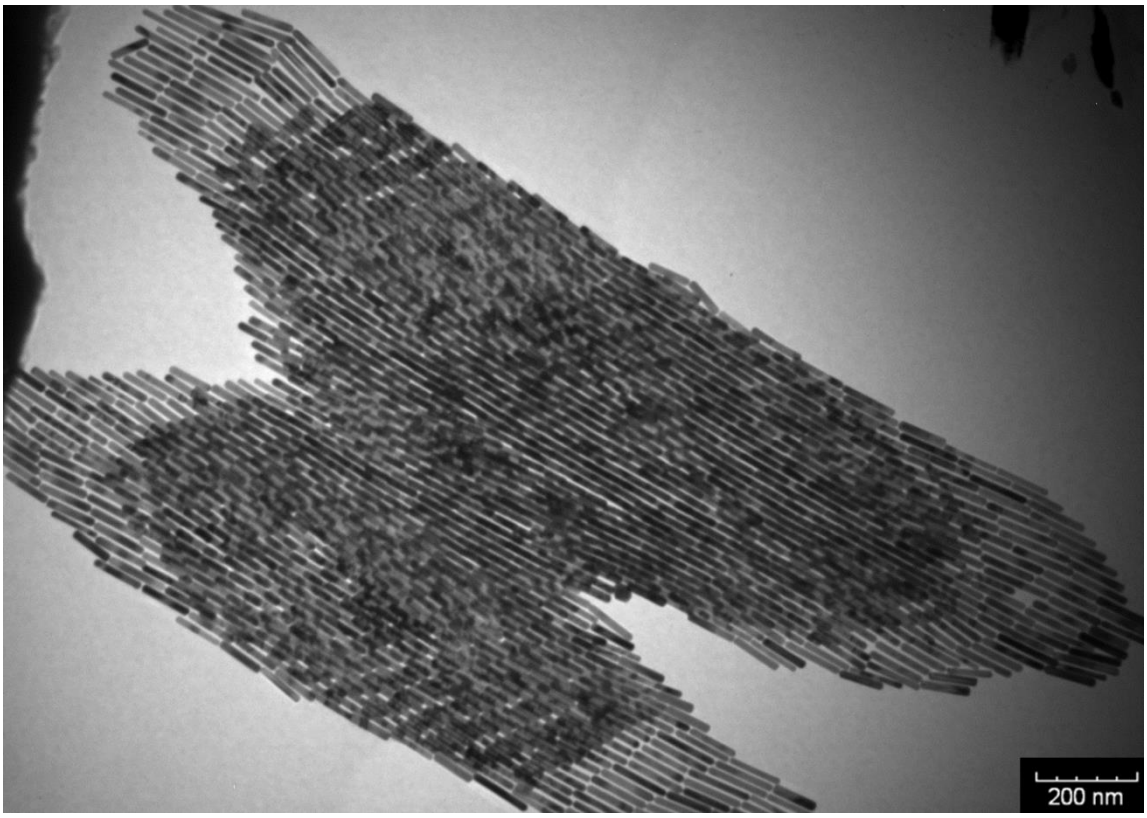

Figure 7.2. TEM image of Au nanorods with nearly 100% yield synthesized without the addition of hydrophobic solvent (i.e., toluene).

To further scrutinize the influence of toluene on the formation of ultrathin Au nanowires, we first prepared the growth solution and mixed it with a varied amount of toluene (i.e., 0 μl, 20 μl, 40 μl, 60 μl, 80 μl, 100 μl, and 120 μl). After that, an 80-μl Au seed solution was introduced to the abovementioned mixed solution and stirred for 2 mins. The solution was then allowed to age for 24 hrs. The digital images of the solutions containing the final products are shown as insets in **Figure 7.3a**. As the amount of toluene added to the growth solution increased, the brownish-red color (i.e., with 0~40 μl toluene added) gradually turned into light pink (i.e., with 60~80 μl toluene added), and eventually became a transparent solution with further addition of toluene (i.e., 100 μl and 120 μl). The color of solutions upon the addition of toluene from 0 μl (i.e., forming Au nanorods) to 40 μl did not have noticeable change. The UV-vis measurements showed

the emergence of two characteristic surface plasmonic resonance peaks, that is, a transverse surface plasmon peak at ~ 520 nm and a longitudinal surface plasmon peak at ~1100_nm, with the 0-μl toluene addition, signifying the formation of Au nanorods.[267] Clearly, the longitudinal absorption peak of Au nanorods slightly blue-shifted with the increase of toluene from 0 μl to 40 μl (**Figure 7.3a**), which is in good agreement with the color change of the solution (inset in **Figure 7.3a**). Nonetheless, this observation suggested the presence of Au nanorods when the amount of added toluene was at 20 μl and 40 μl. Intriguingly, some Au nanorods created by adding a 40 μl toluene showed a tapered ends (marked as dotted circles in **Figure 7.3b**), indicating that the addition of toluene may lead to the shrinking of the cylindrical CTAB micellar template at its ends. In addition, the intensity of longitudinal absorption peak decreased dramatically as the amount of toluene increased from 60 μl to 80 μl and the brownish-red color of the solution gradually disappeared. Further scrutiny by TEM measurement showed the solution containing 80-μl toluene comprised only few Au nanorods together with a small amount of short ultrathin Au nanowires (**Figure 7.4**), indicating that the growth of Au nanorods was strongly suppressed upon the addition of toluene. Notably, further increase in the amount of toluene (e.g., 100 μl) led to the disappearance of longitudinal absorption peak over the entire wavelength range (i.e., 400 nm – 1200 nm), suggesting that almost no Au nanorods were formed in the solution. Instead, ultrathin Au nanowires were obtained (**Figure 7.5**). Recently, it has been reported that the longitudinal absorption peak of oleylamine-capped ultrathin Au nanowires can exceed more than 1200 nm and even up to 10000 nm as a result of its ultrahigh aspect ratio of length to diameter, beyond the measurable wavelength range by UV-vis spectrometer.[252] Thus, in our study the longitudinal absorption peak for ultrathin Au nanowires cannot be detected with the UV-vis spectrometer (**Figure 7.3a**).

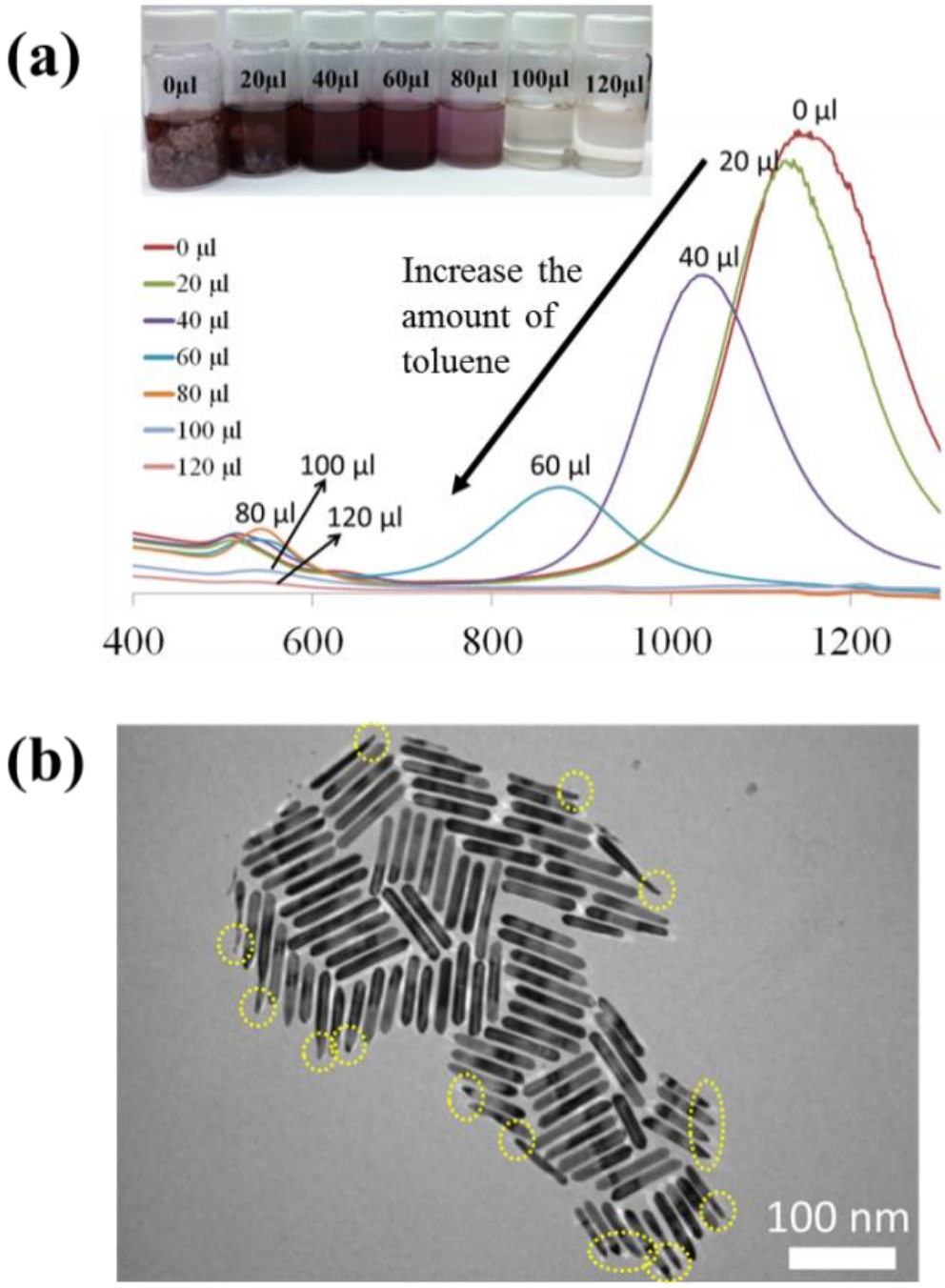

Figure 7.3. (a) UV-vis spectra and the corresponding digital images (insert) of the solutions with the introduction of a varied amount of toluene (i.e., 0 µl, 20 µl, 40 µl, 60 µl, 80 µl, 100 µl and 120 µl). The Au growth solution was prepared by mixing 10 ml 0.1 M CTAB aqueous solution with 0.5 ml 10 mM $HAuCl_4$ solution, 40 µl 0.1 M $AgNO_3$ solution and 0.5 ml 0.1 M hydroquinone aqueous solution. Subsequently, toluene was introduced and well mixed with the growth solution. Finally, 80-µl Au seed solution was added to the abovementioned mixed solution and allowed for a 24-hr reaction to yield the

final solution. (b) Au nanorods obtained from the solution with the introduction of 40-µl toluene. Some of Au nanorods with tapered ends are marked as dotted circles.

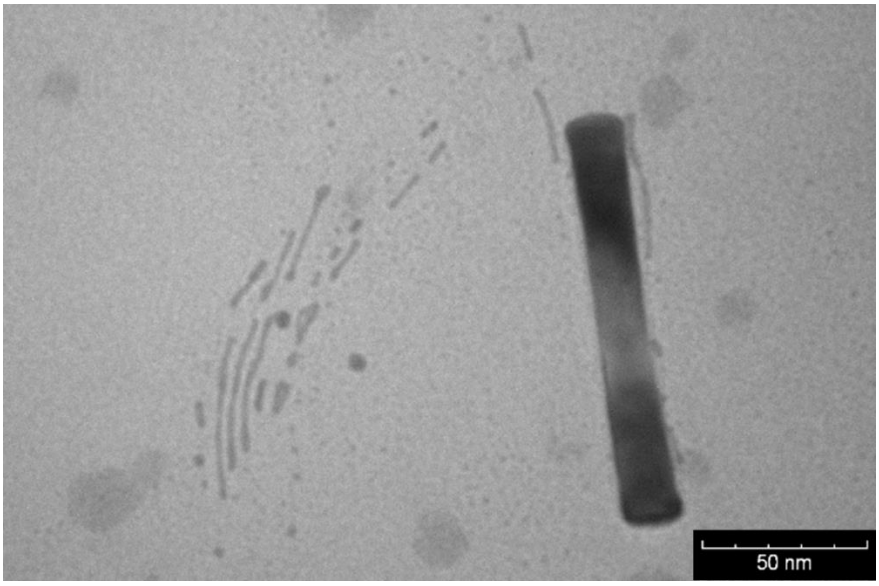

Figure 7.4. TEM image of one Au nanorod together with a small amount of short ultrathin Au nanowires. An 80-µl toluene was added to the Au growth solution and well mixed prior to the addition of the Au seed solution.

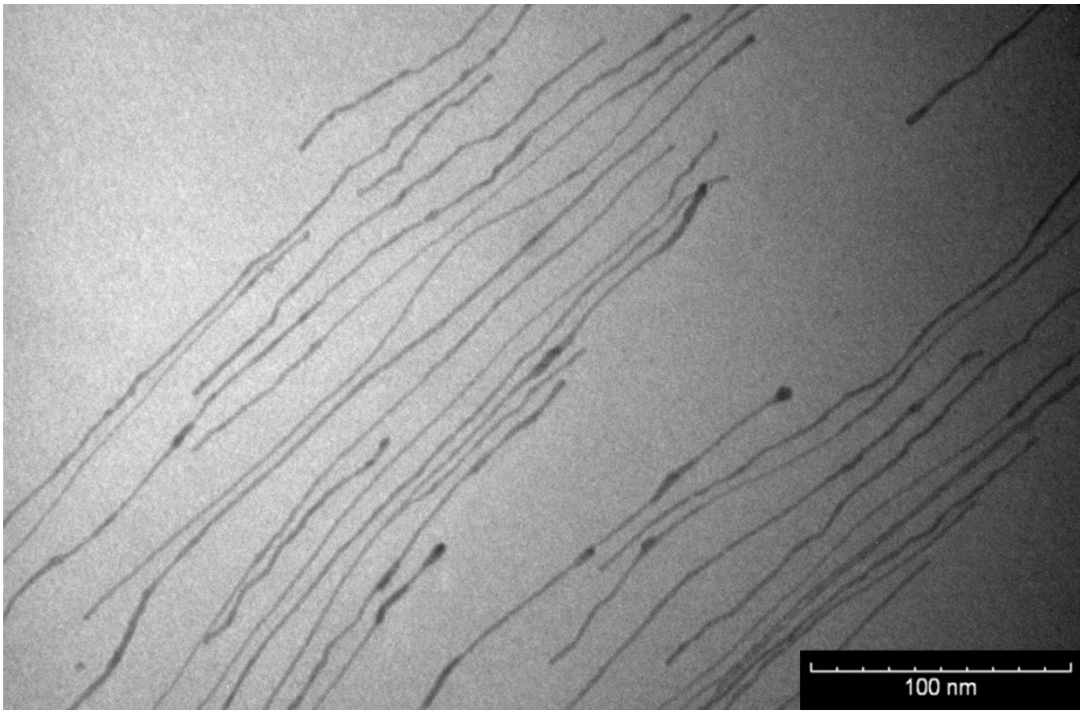

Figure 7.5. TEM image of ultrathin Au nanowire obtained from the solution with the addition of 100-μl toluene to the Au growth solution and well mixed prior to the addition of the Au seed solution.

It is noteworthy that the introduction of a trace amount of toluene into the Au growth solution containing CTAB is the key to the formation of ultrathin Au nanowires in our study. To further explore the synergistic effect of the cylindrical CTAB micellar template and the trace amount of toluene on the creation of ultrathin Au nanowires, the samples with the CTAB concentration ranging from 0.08 M to 0.12 M (i.e., 0.08 M, 0.09 M, 0.10 M, 0.11 M, and 0.12M) were prepared. Interestingly, the critical amount of toluene required for obtaining colorless solution slightly decreased from 120 μl to 90 μl as the concentration of CTAB decreased from 0.12 M to 0.08 M (**Figure 7.6**), respectively. In addition, for the CTAB concentration below 0.08 M, no ultrathin Au nanowires were yielded. For example, Au nanowires with much larger diameter were formed at the CTAB concentration of 0.07M (**Figures 7.7** and **7.8**), and no Au nanowires was observed with a further decrease in the CTAB concentration. Moreover, for low CTAB concentration (i.e., 0.05 M), Au nanorods can still be obtained without the addition of toluene (**Figure 7.9**). When the amount of toluene was introduced to be more than 50 μl, the solution became transparent with no Au nanowires formed in the solution. However, the solution exhibited dark-red color again with the addition of more than 100-μl toluene. The corresponding TEM image clearly showed the formation of Au nanorods; however, both the length and diameter of Au nanorods had a rather wide distribution again (**Figure 7.10**). The formation of such non-uniform Au nanorods merits a detailed study and will be the subject of future study.

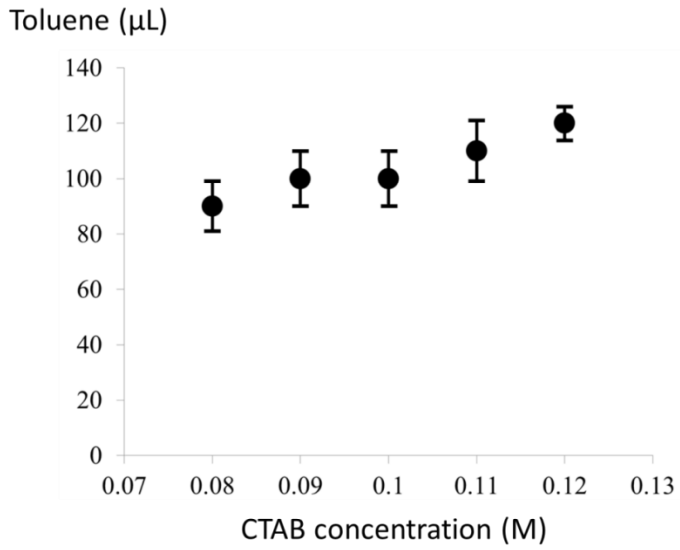

Figure 7.6. Critical amount of toluene required for the formation of ultrathin Au nanowire at different CTAB concentrations.

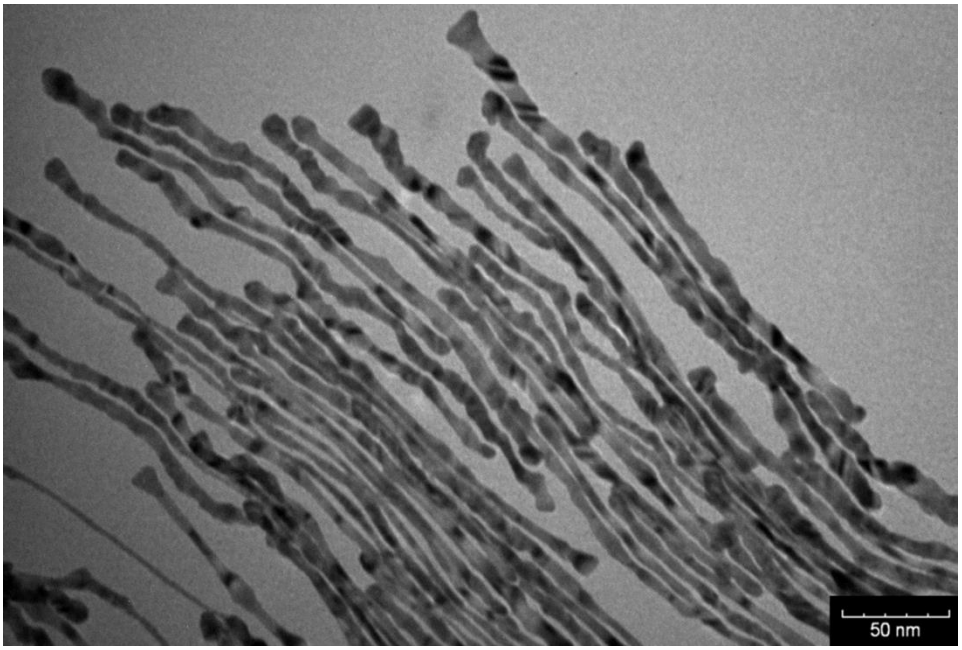

Figure 7.7. TEM image of Au nanowires of larger diameter formed at CTAB concentration of 0.07M with the addition of 100-µl toluene to the Au growth solution prior to the addition of the Au seed solution.

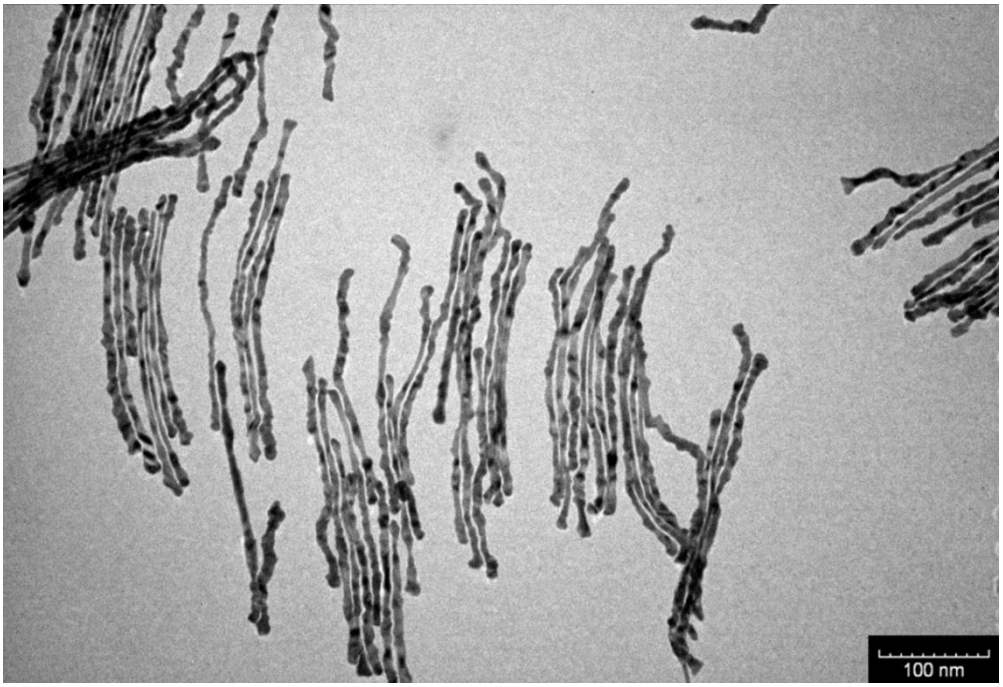

Figure 7.8. TEM image of Au nanowires of larger diameter formed at CTAB concentration of 0.07M with the addition of 100-µl toluene to the Au growth solution prior to the addition of the Au seed solution.

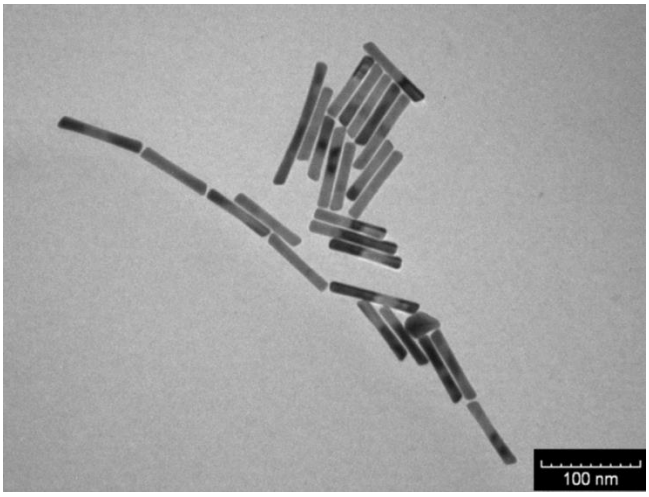

Figure 7.9. TEM image of Au nanorods formed without the addition of toluene at CTAB concentration of 0.05M.

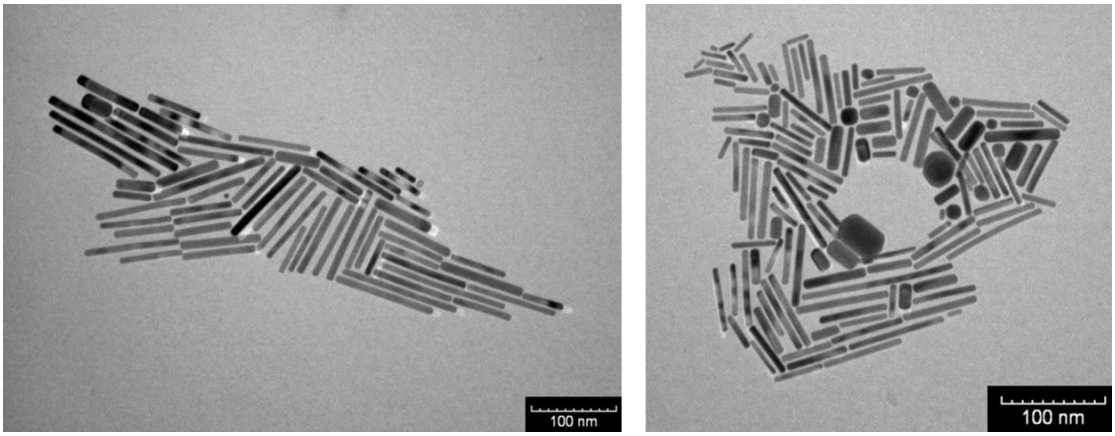

Figure 7.10. TEM image of Au nanorods formed at CTAB concentration of 0.05M with the addition of 100-μl toluene to the Au growth solution prior to the addition of the Au seed solution.

In addition to the CTAB concentration, the effects of the variation in Au seeds and silver ions (Ag^+) while keeping other experimental parameters were also investigated. It is not surprising that without adding Au seeds, no ultrathin Au nanowires were found in the prepared solution, even it was allowed to react for two weeks. Obviously, Au seeds were served as the nucleation sites for the growth of ultrathin Au nanowires in this work. Moreover, Ag^+ has been proved to be critical for the Au nanorod growth[263, 273] by preventing the Au growth at {110} and {100} facets and thus promoting the longitudinal growth.[274] Similarly, we found Ag^+ was also important for the growth of ultrathin Au nanowires. Without the presence of Ag^+, only Au nanoparticles were formed. Furthermore, when the Au growth solution was prepared with Ag^+ at a relatively low concentration (i.e., 0.04 mM by adding 40 μl 0.01M Ag^+ solution to a 10-ml Au growth solution), Au nanostructures with irregular shapes were yielded when a 100-μl toluene was added (**Figures 7.11** and **7.12**). Finally, without the addition of toluene, short Au nanorods were still observed at such low Ag+ concentration (0.04 mM; **Figure 7.13**).

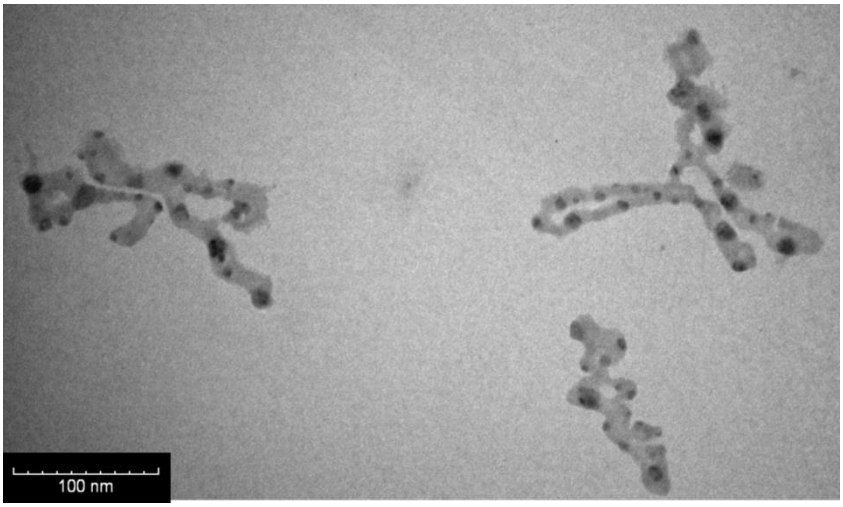

Figure 7.11. TEM image of Au nanostructures with irregular shapes formed at low Ag^+ ion concentration (i.e., 0.04 mM by adding 40-µl 0.01M Ag^+ solution to a 10-ml Au growth solution) with the addition of 100-µl toluene. The concentration of CTAB was 0.1M.

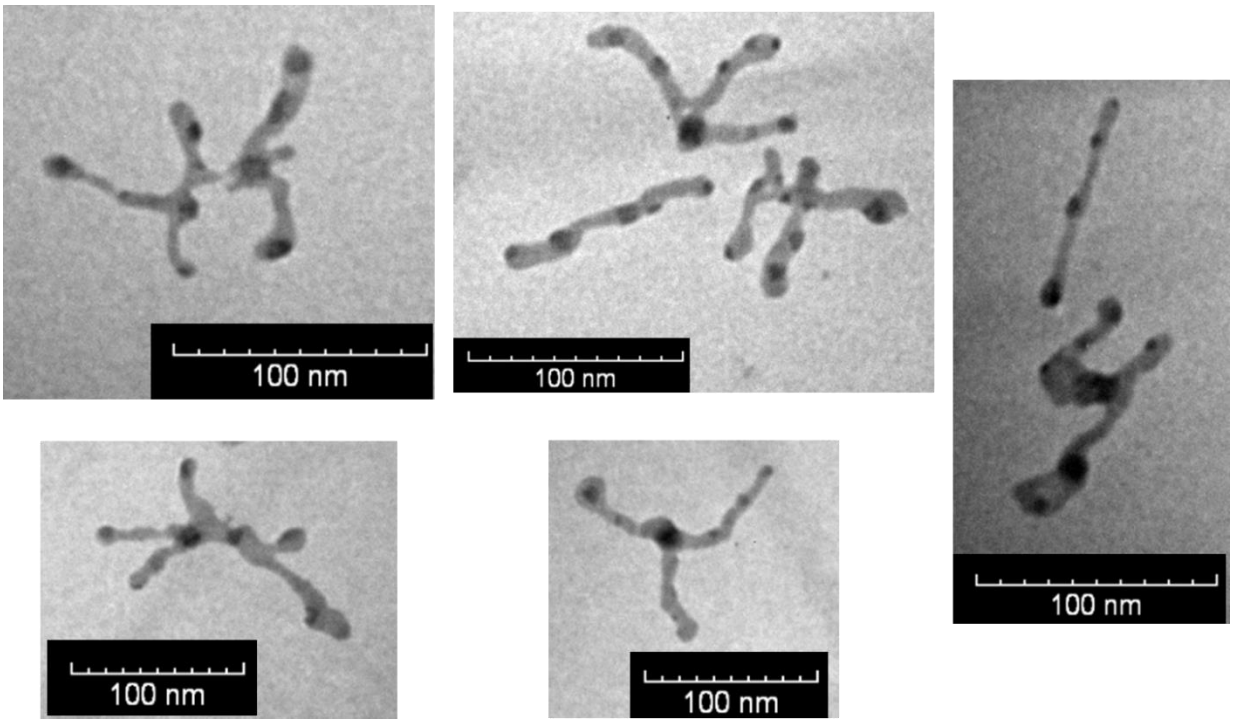

Figure 7.12. TEM image of Au nanostructures with irregular shapes formed at low Ag^+ ion concentration (i.e., 0.04 mM by adding 40-µl 0.01M Ag^+ solution to a 10-ml Au growth solution) with the addition of 100-µl toluene. The concentration of CTAB was 0.1M.

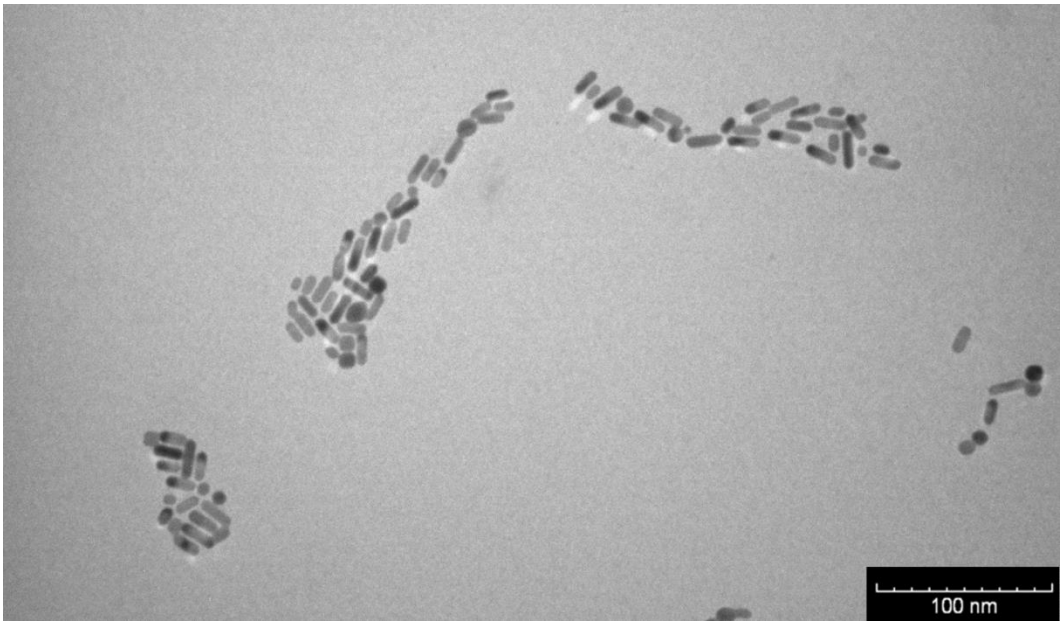

Figure 7.13. TEM image of short Au nanorods formed at the low Ag^+ concentration (i.e., 0.04 mM) without the addition of toluene.

In contrast to the procedure noted above where toluene was well mixed with the Au growth solution prior to the addition of the Au seed solution, remarkably, when toluene was added to the Au growth solution after adding the Au seed solution and the mixed solution was simply gently shaken by hands, the solution formed a layered structure (**Figure 7.14a**) (i.e., dark-red layer on the bottom and a relatively transparent layer on the top). It is worth noting that without the introduction of toluene after adding the Au seed solution, the preparative procedure only led to the formation of Au nanorods. However, with the addition of 100-μl toluene to the Au growth solution, the as-prepared solution displayed two layers after a 24-hr reaction. Interestingly, Au nanorods were formed on the lower layer **(Figure 7.15**), correlated well with the dark-red color observed in the digital image of the solution (inset in **Figure 7.14a**); while the upper layer was primarily composed of ultrathin Au nanowires (**Figure 7.16**), as clearly evidenced by the TEM measurement. The formation of layered solution is a direct consequence of the immiscibility between hydrophobic toluene and water.

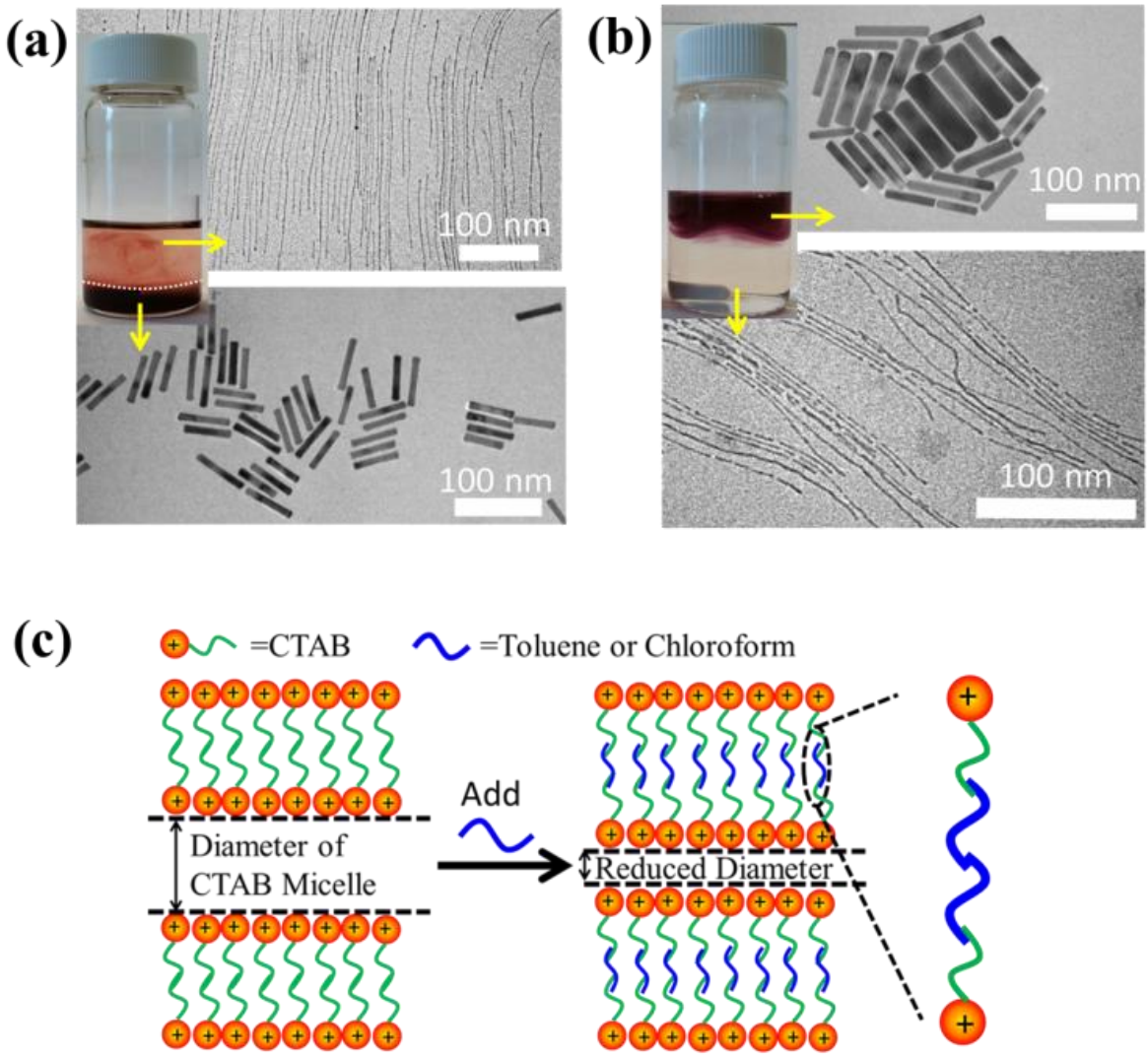

Figure 7.14. Prepared solution with layered structures by mixing either (a) toluene or (b) chloroform with the Au growth solution after adding the Au seed solution and gently shaking the mixed solution. (c) The proposed mechanism for the formation of ultrathin Au nanowires. Hydrophobic molecules (toluene or chloroform) preferably incorporate with the inner hydrophobic chains of the CTAB double layer, thereby leading to a decrease in the inner diameter of self-assembled cylindrical CTAB micelles, which in turn template the growth of ultrathin Au nanowires.

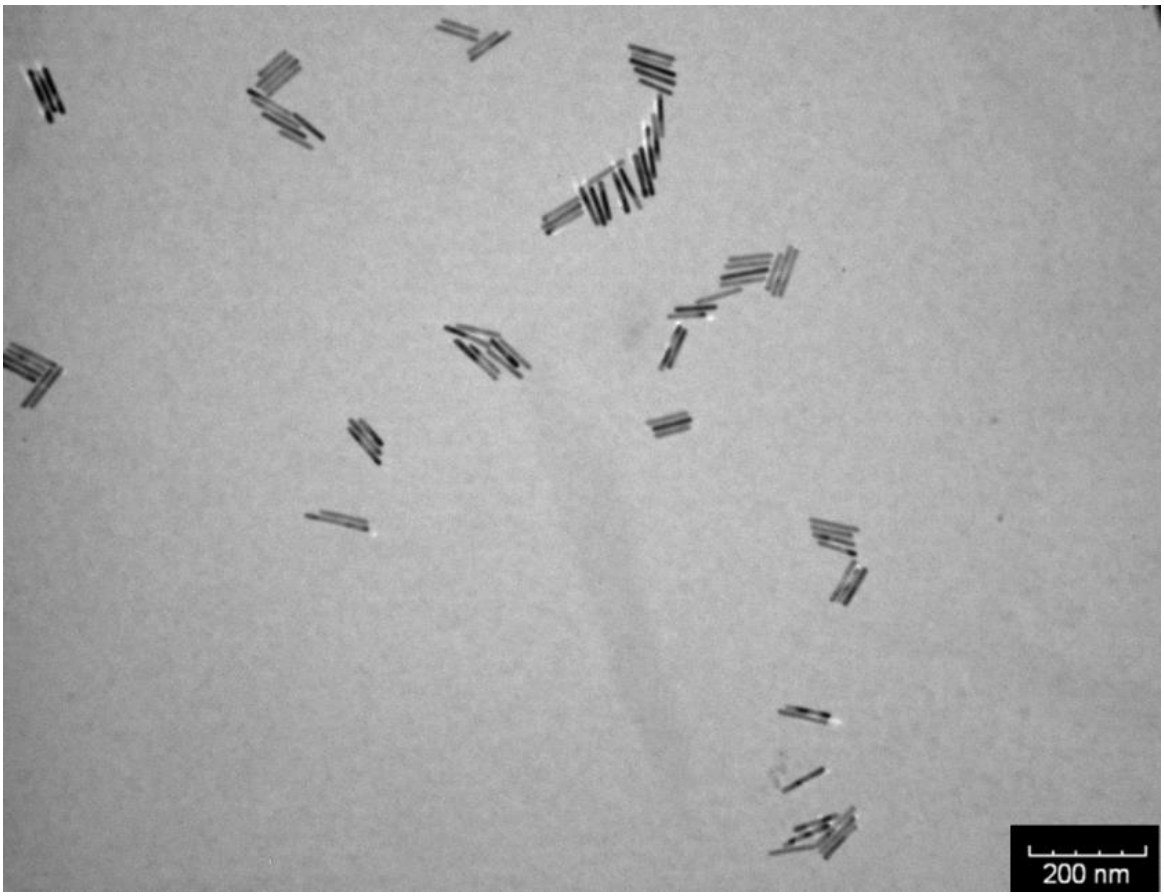

Figure 7.15. TEM image of Au nanorods formed on the bottom layer of solution with the addition of 100 μl toluene to the Au growth solution after adding the Au seed solution. The mixed solution was only gently shaken by hands without stirring. The growth solution was prepared by mixing 10 ml 0.1M CTAB aqueous solution with 0.5 ml 10 mM $HAuCl_4$, 40 μl 0.1 M $AgNO_3$ and 0.5 ml 0.1 M hydroquinone aqueous solution.

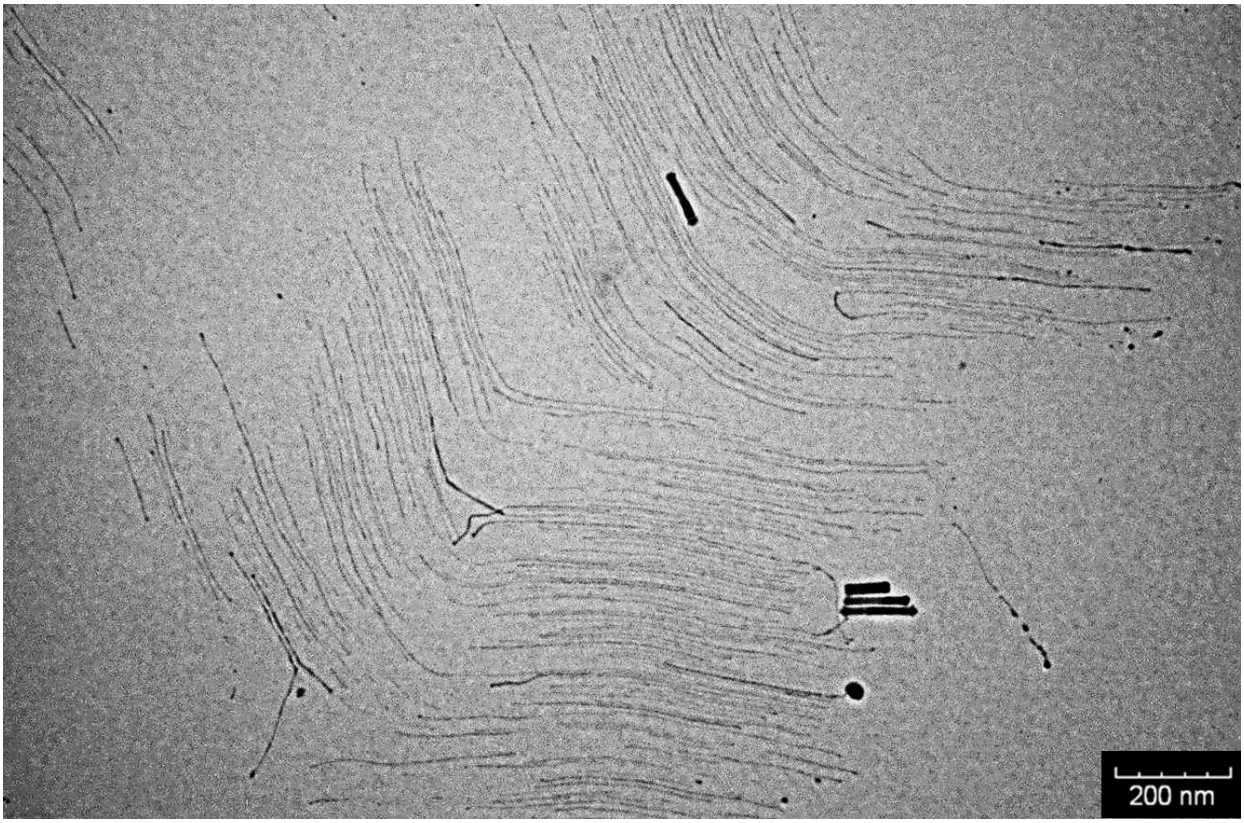

Figure 7.16. TEM image of Au nanorods formed on the upper layer of solution with the addition of 100-μl toluene to the Au growth solution after adding the Au seed solution. The mixed solution was only gently shaken by hands without stirring. The growth solution was prepared by mixing 10 ml 0.1M CTAB aqueous solution with 0.5 ml 10 mM $HAuCl_4$, 40 μl 0.1 M $AgNO_3$ and 0.5 ml 0.1 M hydroquinone aqueous solution.

On the basis of the observed layered solution, the formation mechanism of water-soluble ultrathin Au nanowires may be rationalized as follows (**Figure 7.14**). First, CTAB molecules, which are cationic surfactants, self-assemble into cylindrical micelles in aqueous solution as widely discussed in literature.[274] Such cylindrical micelles comprise the CTAB double layers by exposing the cationic ends with the hydrophobic chains inside.[275] When toluene molecules are mixed with the cylindrical CTAB micelle solution, toluene as a small hydrophobic molecule is preferentially incorporated with the inner hydrophobic chains of the CTAB double layer due to the favorable hydrophobic-hydrophobic interaction.[276] Such an accommodation of toluene molecules within the CTAB double layer increases the total thickness of the double layer, transforming it into

a sandwich-like structure (i.e., toluene molecules situated within the hydrophobic chains of CTAB as depicted in the right panel of **Figure 7.14c**) on each side of double layer. Such sandwich-like CATB/toluene/CTAB structures may lead to the decrease of the inner diameter of self-assembled cylindrical CTAB micelles while retaining the overall original size, thereby rendering the formation of ultrathin Au nanowires template by the shrunk cylindrical micelle (middle panel in **Figure 7.14c**). It is important to note that there were 1×10^{-3} mole CTAB molecules in the as-prepared solution. At the molar ratio of CTAB/toluene = 1:1 for the incorporation of toluene inside the CTAB double layer, the corresponding volume of toluene can be estimated to be 106.3 μl (i.e., $\frac{1\times10^{-3}\ mole\times 92.14 g/mol}{866.90\times10^{-6} g/\mu l} = 106.3\ \mu l$). This correlated well with the critical amount of toluene required for the formation of an ultrathin Au nanowire as described above (i.e., 100 μl). The density of toluene is 0.8669 g/ml, lower than that of water. Taken together, sandwich-like CATB/toluene/CTAB-capped ultrathin Au nanowires were resulted in and dispersed on the upper layer of the two-layer solution (inset in **Figure 7.14a**). Moreover, it is also noteworthy that the thickness of top transparent layer (i.e., the toluene layer) was much larger than the bottom layer (i.e., dark-red layer for the Au nanorod growth), signifying that the majority of CTAB micelles were entered into the upper toluene phase to accommodate toluene molecules inside even with a gentle shaking.

To substantiate the proposed mechanism discussed above, in addition to toluene, chloroform was also employed as the hydrophobic solvent and added to the Au growth solution. Similar to the case of adding toluene, a transparent solution was also observed when the amount of added chloroform was above a certain value (i.e., 80 μl). The TEM measurement showed the formation of ultrathin Au nanowires (**Figure 7.17**). Likewise, as the density and molar moss of chloroform are 1.49 g/ml and 119.38 g/mol, respectively, the corresponding volume of chloroform for incorporating chloroform

within 1×10^{-3} mole CTAB was found to be 80.1 μl (i.e., $\frac{1\times10^{-3}\ mole\times119.38g/mol}{1490\times10^{-6}g/\mu l}=80.1\mu l$), which also agreed well with the critical volume of chloroform required for the formation of an ultrathin Au nanowire (80 μl). Similarly, a layered solution was also seen by mixing chloroform with the Au growth solution after adding the Au seed solution. Intriguingly, the bottom layer of solution was transparent while the upper layer was dark-red (inset in **Figure 7.14b**), which is completely opposite to the layered solution formed by adding toluene (inset in **Figure 7.14a**). The Au nanorods obtained from the upper layer was not uniform (**Figure 7.14b**). In comparison to the case of toluene (i.e., dark-red layer on the top and transparent layer on the bottom), the high density of chloroform (1.48g/ml; larger than that of water) was responsible for the formation of switched layered solution (i.e., colorless layer on the top and dark-red layer on the bottom). Consequently, sandwich-like CATB/chloroform/CTAB-capped ultrathin Au nanowires were produced and dispersed on the lower layer of the two-layer solution (inset in **Figure 7.14b**).

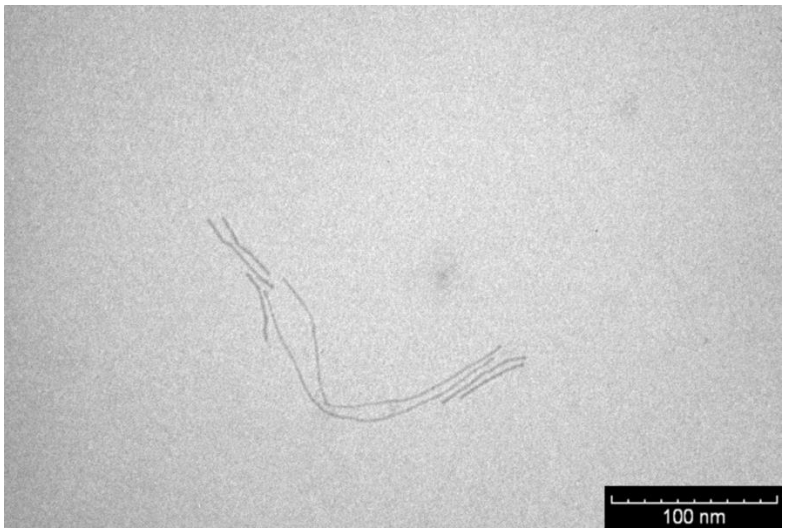

Figure 7.17. TEM image of ultrathin Au nanowires formed by adding a 80-μl chloroform to the Au growth solution after adding the Au seed solution. The growth solution was prepared by mixing 10 ml 0.1M CTAB aqueous solution with 0.5 ml 10 mM $HAuCl_4$, 40 μl 0.1 M $AgNO_3$ and 0.5 ml 0.1 M hydroquinone aqueous solution.

7.3. Conclusions

In summary, we have developed a surprisingly simple yet effective strategy for crafting water-soluble ultrathin Au nanowires by introducing a trace amount of hydrophobic solvent (i.e., toluene or chloroform) to the Au growth solution based on conventional preparative approach for Au nanorods using cylindrical CTAB micelles as template. The influence of introducing these hydrophobic solvents on the self-assembled CTAB micellar template, which led to the formation of ultrathin Au nanowires, was also explored. In principle, such a simple and robust strategy can be extended for the synthesis of a large variety of nanowires that capitalize on CTAB as the surface capping ligands. Furthermore, the ability to create ultrathin Au nanowires may open up exciting opportunities for fundamental studies on their unique physical properties as well as the promising applications in nanoscale photonic, electronic, and optoelectronic devices, sensors, bioimaging, diagnosis, and therapy

7.4. Experimental Section

Preparation of Au seed solution. CTAB solution (10 mL, 0.10 M) was mixed with 0.25 mL of 10 mM $HAuCl_4$. 0.6mL freshly prepared 0.01M $NaBH_4$ aqueous solution was then added, resulting in a brownish yellow solution. Notably, the Au seed solution needs to be prepared freshly each time.

Preparation of Au growth solution. CTAB solution (10 mL, 0.10 M) was mixed with 0.5 mL of 10 mM $HAuCl_4$. 40 μl $AgNO_3$ solution (0.1 M) was then added and well mixed. Hydroquinone aqueous solution (0.5mL, 0.1M) was then added to the solution noted above, and stirred until the solution became colorless and clear. Notably, the time for the solution turning to be colorless depends on the concentration of CTAB. For 0.1 M CTAB, it took around 1 min; and for 0.08M CTAB, it took only several seconds.

However, for the solution with lower CTAB concentration (e.g., 0.01 M), the solution remained turbid after the addition of hydroquinone solution.

Synthesis of ultrathin Au nanowires.

(a) Homogeneous solution: A varied amount of toluene (e.g., 0 μl, 10 μl, 20 μl, 40 μl, 60 μl, 80 μl, 90 μl, 100 μl, 110 μl, 120 μl, 130 μl, 140 μl, 150 μl, 200 μl, 400 μl, and 1000 μl) was added to the Au growth solution and stirred for 10 mins. It is worth noting that for the CTAB solution at concentration of 0.1 M, when the amount of toluene was added at or below 100 μl, the solution became clear after well-mixed. However, the addition of more toluene (e.g., 200 μl, 400 μl, and 1000 μl) led to the turbid solutions even after more than 20 mins. After mixing with toluene, a 80-μl Au seed solution was added. The final solution was allowed to age for 24hrs.

(b) Layered solution: A 80-μl Au seed solution was added to the Au growth solution. A varied amount of toluene (e.g., 0 μl, 10 μl, 20 μl, 40 μl, 60 μl, 80 μl, 90 μl, 100 μl, 110 μl, 120 μl, 130 μl, 140 μl, 150 μl, 200 μl, 400 μl, and 1000 μl) was added to the Au growth solution, and gently shaken by hand. The final solution was allowed to age for 24hrs.

It should be noted that the Au seed solution should be freshly prepared every time as the Au seed solution from a long-time storage may result in large percentage of Au nanoparticles formed in solution.

CHAPTER 8

ENGINEERING COLLOIDAL MICROCHANELS VIA FLOW-ENABLED SELF-ASSEMBLY (FESA)

B. Li, C. Zhang, B. Jiang, W. Han, and Z. Lin, "Engineering Colloidal Microchanels via Flow-Enabled Self-Assembly (FESA)", submitted to ***ACS Nano***

8.1. Introduction

Self-assembly as a bottom-up approach entails the crafting of surface patterns for applications in electronics[277-278] and nanodevices[279] at remarkably low cost, compared to conventional top-down approach (e.g., photolithography, e-beam lithography, soft lithography,[280] dip-pen nanolithography[281]). Among them, controlled evaporative self-assembly of nonvolatile solutes rendered by evaporation of volatile solutes presents a lithography-free and extremely simple yet robust strategy for creating a large variety of surface patterns.

On the other hand, cracks formed upon the drying of thin film are usually undesirable and remain a problematic issue in the inkjet printing industry, whereas a thin film with uniform thickness is desired.[282-283] However, the cracks formed by drying colloidal latex particle thin film may also be beneficial for fabricating surface patterns, by utilizing the cracks as self-assembled template to generate metallic stripes.[114] Notably, even though theoretical models for the mechanism of crack formation has been extensively studied,[284-287] the control over crack formation in a highly ordered manner on a large scale remains a challenge, because of the lack of restriction of the drying of colloidal suspensions.

Herein, we report on a facile strategy for crafting colloidal microchannels (i.e., cracks) with tunable spacing between two adjacent micrchannels λ_{c-c} on a large scale by controlling the drying process of colloidal suspensions via flow-enabled self-assembly (FESA). In a FESA process, a colloidal suspension was allowed to evaporate in a confined geometry composed of a fixed upper blade and a movable lower substrate mounted on a computer-controlled translational stage. By tuning the moving speed of the lower substrate at certain temperature, the thickness of the formed colloidal thin film can be readily tailored, thereby enabling the control over λ_{c-c} of colloidal microchannels. Moreover, the influence of chemically patterned substrate (i.e., hydrophobic stripes on a hydrophilic substrate) on the formation of colloidal microchannels was explored. In addition, colloidal microchannels with tunable λ_{c-c} was exploited as template for aligning inorganic nanoparticles. Such FESA strategy for crafting colloidal microchannels with tunable λ_{c-c} offers new opportunities to craft surfaces patterns and align inorganic nanomaterials over a large scale, and thus holds promising applications in electronics and nanodevices.

8.2. Results and Discussion

By subjecting PS latex particle suspension to a confined geometry consisting of two nearly parallel surfaces (i.e., a fix upper blade and a movable lower substrate), the PS suspension was allowed to dry and solidify along the moving direction of the substrate, which is programmably controlled by a computer (**Figure 8.1** and **Figure 8.2**). The PS latex particle at concentration of 0.5wt% was prepared by diluting 50nm PS latex suspension (purchased from Thermo Schientific) with DI-water at 1:1 volume ratio. First, due to the coffee-ring effect, the loss of water that was maximized at the three-phase contact line resulted in a lateral flow inside the droplet, thereby transporting PS colloidals to the drying front. Subsequently, by continuously moving the lower substrate (Si wafer),

PS latex thin film with highly ordered microchannels (i.e., cracks) all over the surface was formed. The direction of the formed microchannels was parallel to the moving direction of the lower substrate. The moving velocity of the lower substrate was 13 μm/s and the substrate was heated to 50℃ (**Figure 8.1**). Notably, a droplet of 60 μl PS latex particle suspension yielded thin film with uniform microchannels over a surface area of 1×1.5 cm^2 (width × length). The width and length were determined by the width of the upper blade and the volume of the PS latex particle suspension, respectively. Thus, colloidal thin film with uniform microchannels at much larger surface area can be achieved by utilizing a fixed upper blade with a larger width and continuously feeding with PS latex particle suspensions. Moreover, the spacing between two adjacent microchannels (λ_{c-c}) (ranging from 7.8 μm to 38.7 μm) was much smaller than the values reported in literature by freely drying of a droplet of PS latex particle suspensions on a substrate, which are usually above 200 μm.[288-290] Thus, the uniform microchannels produced in this work imparted the creation of surface patterns with much smaller feature sizes.

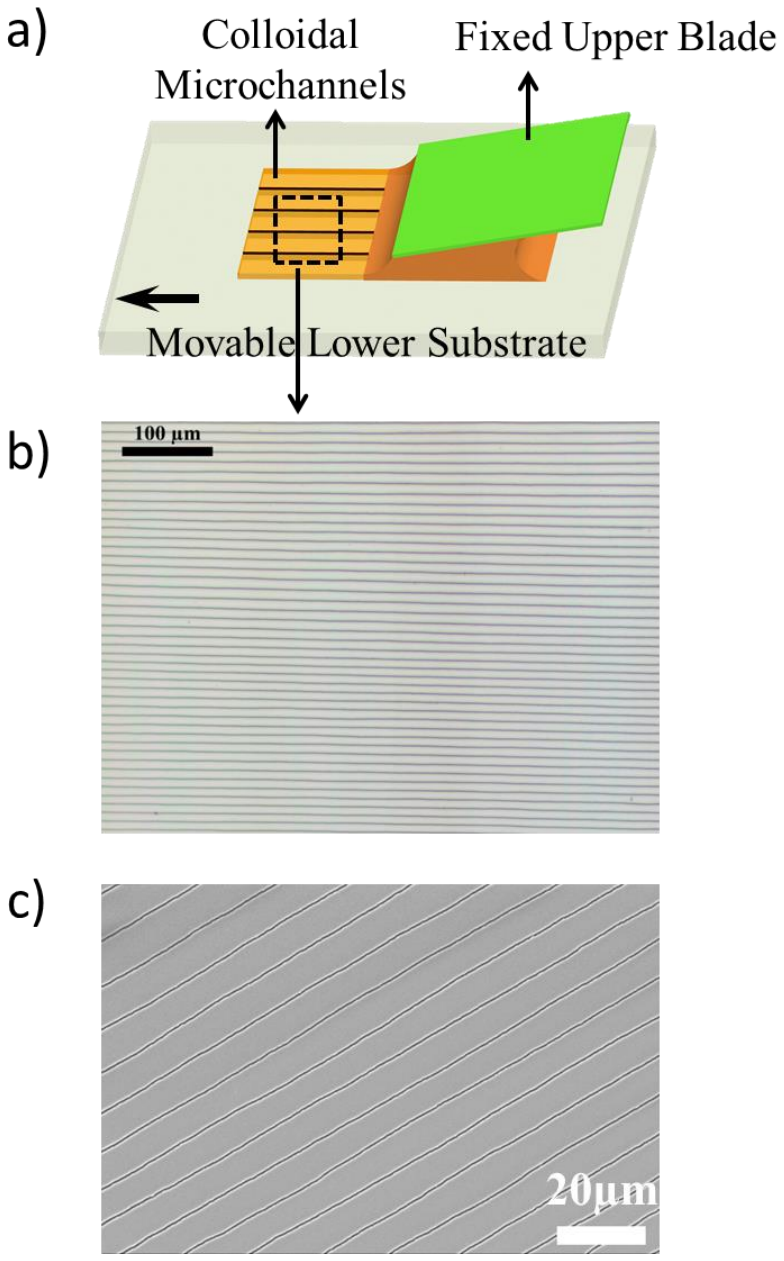

Figure 8.1. a) Schematic illustration of the formation of uniform microchannels over the entire colloidal thin film by FESA, b) optical micrograph of microchannels, and c) SEM image of microchannels. The temperature, the moving velocity of lower substrate, and the solution concentration were 50 ℃, 13 µm/s, and 0.5 wt%, respectively.

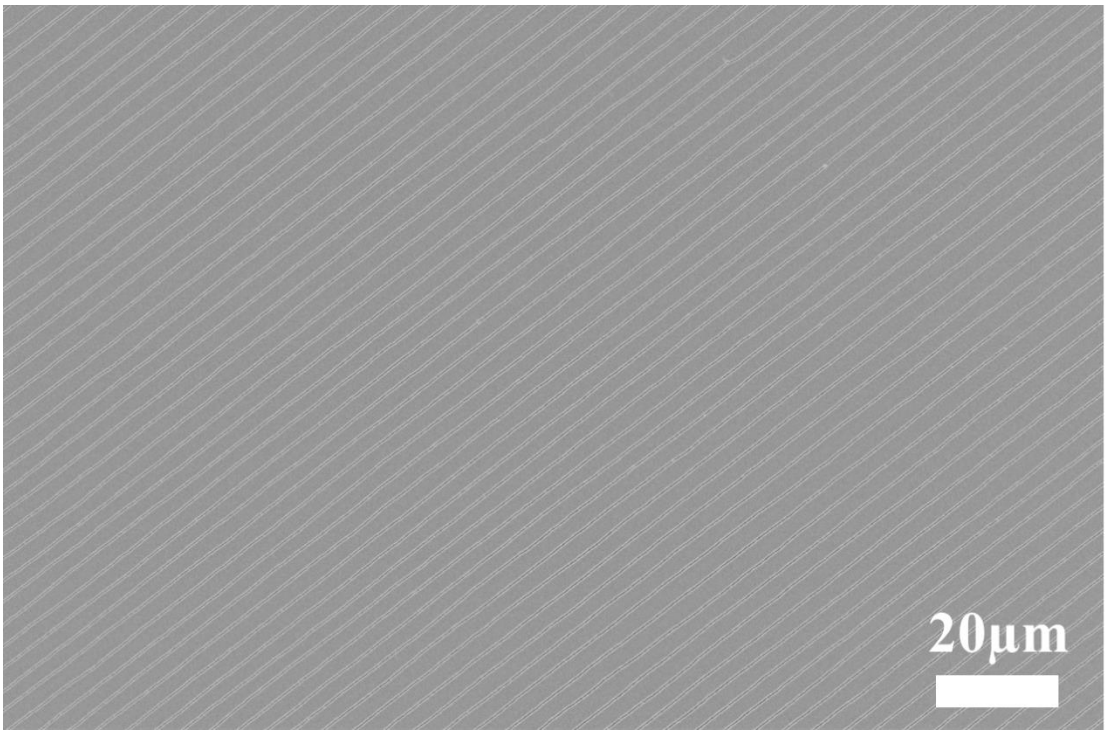

Figure 8.2 SEM image of uniform colloidal microchannels formed by FESA at 50℃, moving velocity of lower substrate of 13μm/s and concentration of 0.5wt%.

Interestingly, λ_{c-c} can be tuned by simply varying the moving velocity of the lower substrate (**Figure 8.3**). In general, the smaller velocity of moving substrate resulted in a larger λ_{c-c} of regular colloidal microchannels (**Figure 8.4a**).

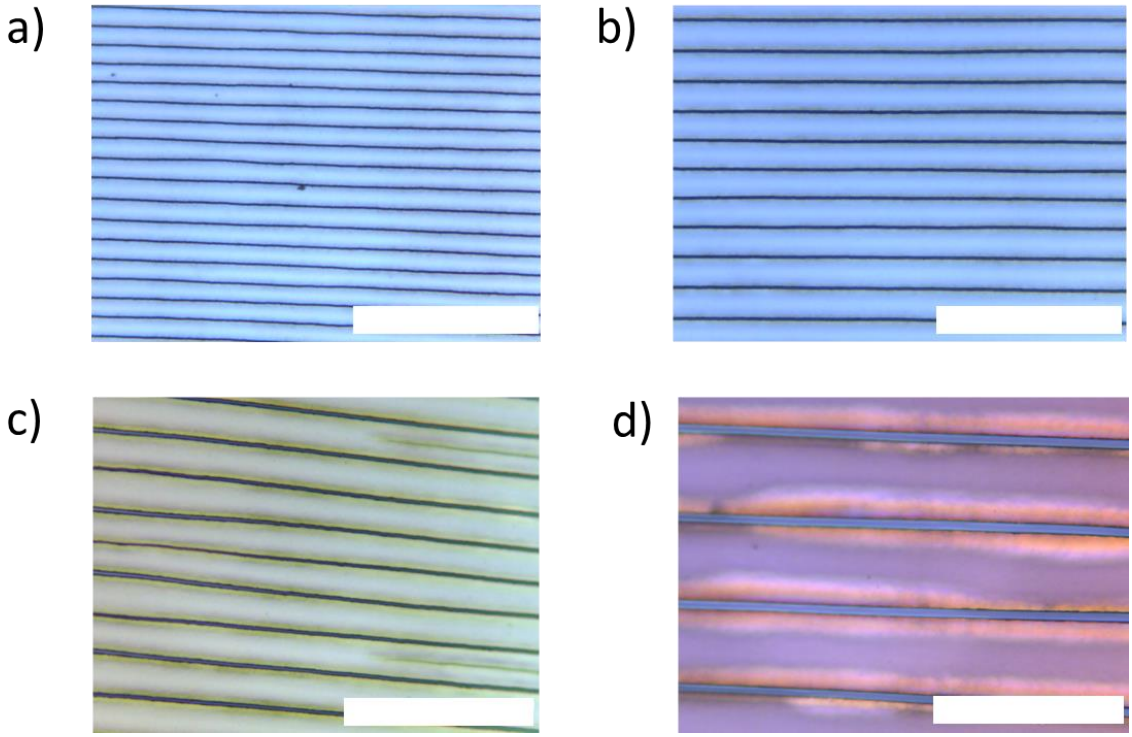

Figure 8.3. Optical micrographs of colloidal microchannels with various spacings, which were crafted by FESA at the different moving velocity of lower substrate of a) 10 μm/s, b) 8 μm/s, c) 5 μm/s, and d) 3 μm/s. All scale bars = 100 μm.

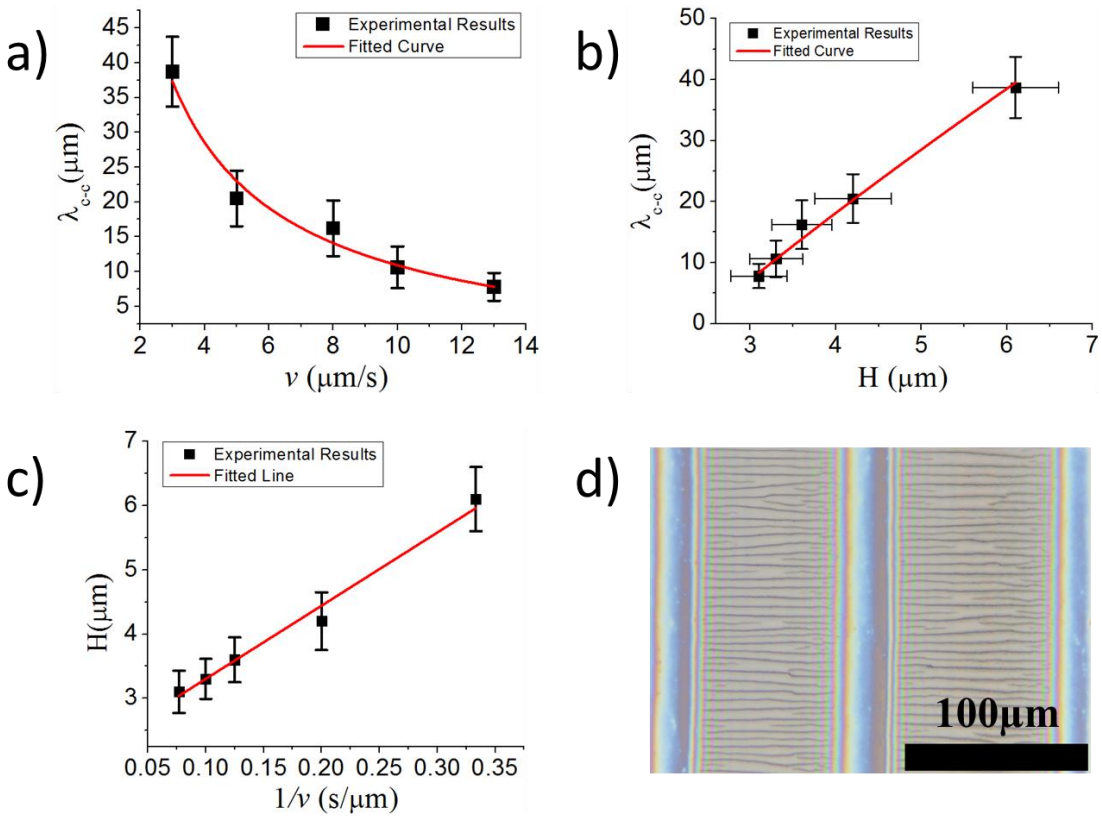

Figure 8.4. Experimental results and theoretical prediction of the relationship of a) the spacing between adjacent microchannels, λ_{c-c} and the moving velocity of the lower substrate v, b) λ_{c-c} and the thickness of the colloidal thin film with microchannels all over the surface H, and c) H and $\frac{1}{v}$. d) optical micrograph of the colloidal thin film of thickness lower than a critical value, in which the microchannels discontinued and microchannel-free region appeared.

The reason for the microchannel formation is the capillary stress generated during the drying of the colloidal thin film.[291] The spacing between two adjacent microchannels λ_{c-c} can be given by[292]

$$\lambda_{c-c} \sim 0.07 \left(\frac{20}{75} \left(\frac{3\gamma\eta_0}{E} \right)^{\frac{1}{2}} \frac{R(1-\phi)^2}{\mu\phi^2 H} \right)^{-0.8} \left(\frac{20R(1-\phi)^2}{75\mu\phi^2} \right) \left(\frac{3\gamma^3\eta_0}{E^3} \right)^{\frac{1}{4}} \quad (9.1)$$

where γ is surface tension of the water, η_0 is the dispersion viscosity of water into colloidal thin films, E is the evaporation rate, R is the radius of colloidal particle, ϕ is the volume fraction of colloidal particle, μ is the viscosity of water, and H is the thickness of the dried film. As we used the same PS latex particle (50nm) and kept the other experimental parameters unchanged (e.g., temperature, concentration and solvent), thus the spacing of microchannels λ_{c-c} was determined by

$$\lambda_{c-c} \sim kH^{0.8} \tag{9.2}$$

where k is the constant, depending on all the other parameters mentioned in eq.(9.1). Notably, the fitting curve using eq.(9.2) agreed well with our experimental results (**Figure 8.4b**), which also agreed with the prediction that λ_{c-c} almost increased linearly with the thickness of dried colloidal thin film H with a slight deviation.[287] The total volume of PS latex particles V deposited by the drying liquid front can be given by

$$V = lHd \sim \frac{4}{3}\pi R^3 nt = \frac{4\pi R^3 nd}{3v} \tag{9.3}$$

where l, H and d is the width, thickness and length of the colloidal thin film, n is the number of PS latex particles deposited at the contact line per unit time, t is the time period of FESA process, and v is the moving velocity of the lower substrate. Clearly, the length of the colloidal thin film equals to the moving distance of substrate at a period time t. Thus, the thickness of the colloidal thin film can be directly correlated with the moving velocity of the lower substrate, $H \sim \frac{4\pi R^3 n}{3vl}$, by cancelling d on both sides of eq. (9.3), and assuming that the deposition rate of PS latex particles n was independent of the moving velocity of the lower substrate. Therefore, the thickness H is inversely proportional to the moving velocity, which was also observed in our experiments (**Figure 8.4c**). To this end, according to eq. (9.2), we have

$$\lambda_{c-c} \sim k\left(\frac{4\pi R^3 n}{3vl}\right)^{0.8} \sim k' v^{-0.8} \quad (4)$$

where $k' = k\left(\frac{4\pi R^3 n}{3l}\right)^{0.8}$. Notably, the fitting curve based on eq. (9.4) and the experimental results agreed well with each other (**Figure 8.4a**). Therefore, the experimental results of the relationship between the spacing of adjacent microchannels and the moving velocity of the lower substrate shown in **Figure 8.4a** can be explained. In addition, it is also reported that there was a critical thickness of microchannel-free thin film, above which colloidal microchannels would form.[293] Importantly, such critical thickness also existed in our work. Notably, by increasing the moving velocity of the lower substrate up to 13 μm/s, the colloidal film with discontinued microchannles (i.e., microchannel-free region) was observed at the thickness below 3.1 μm (**Figure 8.4d**). We note that the thickness of the colloidal thin film that strongly determined the deposition rate of PS latex particles n can be tuned linearly by adjusting the moving velocity v, but also by varying the concentration of the PS latex particle suspensions and the temperature. Thus, colloidal film with microchannel-free region shown in **Figure 8.4d** can also be observed at lower temperature (e.g. 45 ℃, **Figure 8.5a**) or at the lower concentration (e.g., 0.2 wt%, **Figure 8.5b**) while the other parameters remained the same as in **Figure 8.1**.

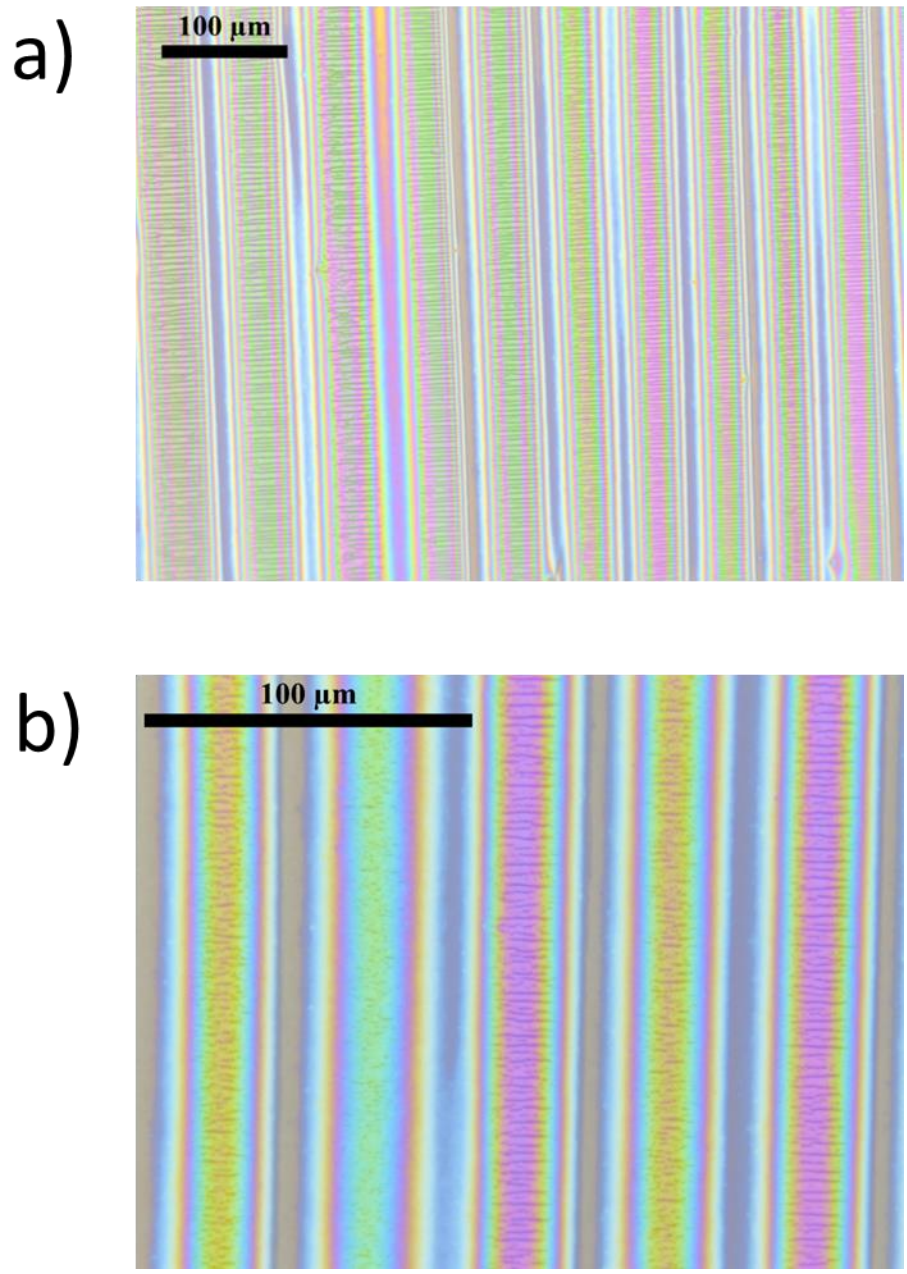

Figure 8.5. Discontinuous microchannels formed at a) lower temperature (e.g. 45 ℃), the concentration of 0.5 wt% and the moving velocity of lower substrate of 13 µm/s; b) at lower concentration (e.g., 0.2 wt%,), the temperature of 50 ℃, and the moving velocity of lower substrate of 13 µm/s.

We also investigated the influence of the microchannel formation on a chemically patterned substrate, that is, a hydrophilic Si wafer patterned with hydrophobic polymer stripes (e.g., PS stripes). The regular PS stripe pattern was crafted by FESA similar to our

previous work.[97] Notably, both the height and the spacing of PS stripes can be precisely tuned by FESA in a "stop-and-move" fashion.[97] First, we set the moving direction of the substrate perpendicular to the PS stripes. Unless otherwise specified, the temperature, the moving velocity of lower substrate and the concentration for the FESA of colloidal suspension on chemically patterned substrate were 50℃, 13 μm/s and 0.5 wt%, respectively. As the PS stripes were of smaller height (~3 μm) and larger spacing (100 μm), colloidal thin film with microchannels can still form (**Figure 8.6**), similar to that formed on the bare Si substrate (**Figure 8.1**). However, the microchannels were blocked at a PS stripe (**Figure 8.6b and 8.6c**) and continued after the PS stripe. Intriguingly, we observed that the PS stripes were cracked by the formation of the adjacent microchannels, but with much smaller width (~100 nm, **Figure 8.6d**). Moreover, subsequent microchannels were formed by the guidance of the formed cracks in PS stripes. Considering the Young's modulus of PS was around 3 GPa,[294] the pressure induced by the microchannel formation was at least one order of magnitude higher than the theoretical prediction in literature.[287] Importantly, such strategy may also be exploited to experimentally evaluate the capillary pressure which caused the microchannel (or crack) formation in colloidal thin films in the future.

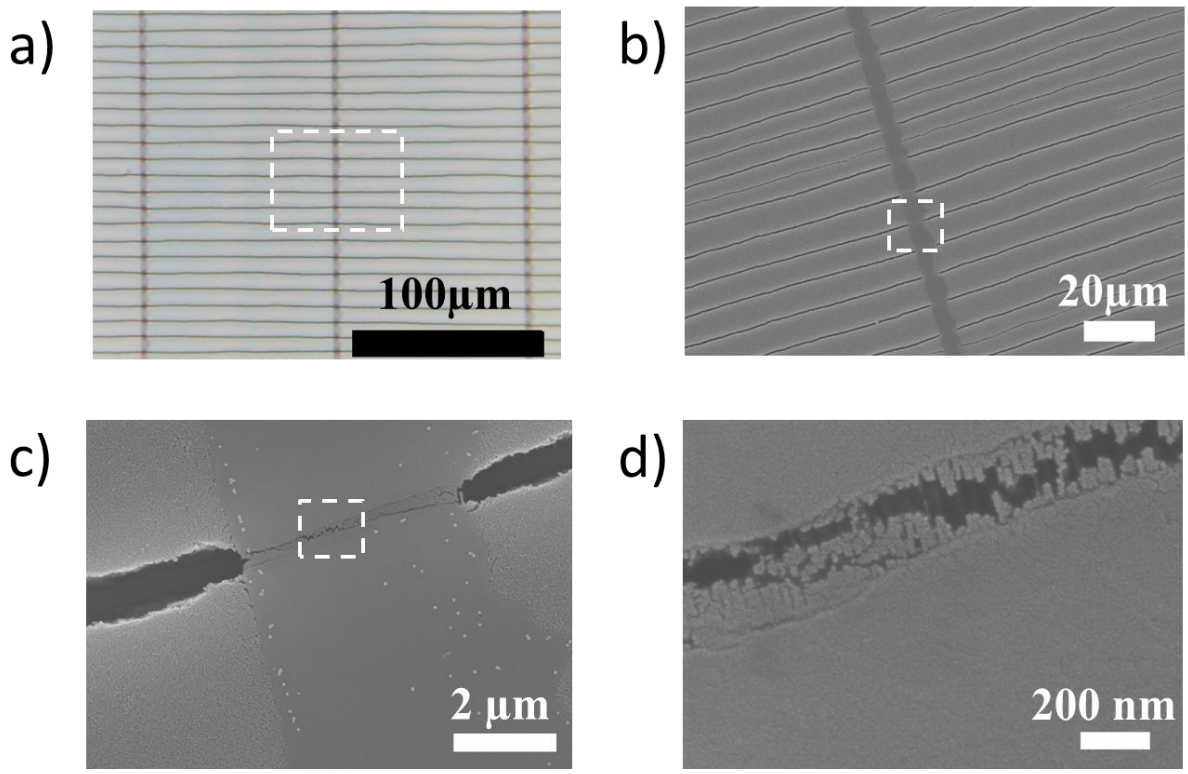

Figure 8.6. a) optical micrograph, and b) and c) SEM images of different magnifications on microchannels formed on chemically patterned substrate by controlled drying of PS latex particle suspension in the direct perpendicular to the PS stripes. The microchannels were formed over the entire substrate except on the top of PS stripes. The spacing between PS stripes is 100 µm. d) SEM image of the crack in a PS stripe induced by a formed microchannel.

In contrast, we found that the colloidal thin film was not formed continuously on chemically patterned substrate consisting of PS stripe of larger height (~5 µm) and smaller spacing (~50 µm) (**Figure 8.7**). The reason is that the contact line moved in a stick-slip motion due to the strong hydrophobicity of the PS stripes, though the lower substrate was moving continuously at a constant velocity. First, once the three-phase contact line was pinned in the middle area between two PS stripes, a ribbon of PS latex particles formed (i.e., stick). As the lower substrate was kept moving, the liquid surface pinned at the contact line was gradually stretched and the contact line decreased to a critical value, at which the depinning force overcame the pinning force exerted at the contact line. As a result, the contact line depinned from the formed ribbon of PS latex

particles and jumped to the middle of the next two PS stripes (i.e., slip), thereby yielding the formation of the second ribbon. Interestingly, microchannels were formed in the ribbons with direction parallel to the moving direction of the lower substrate.

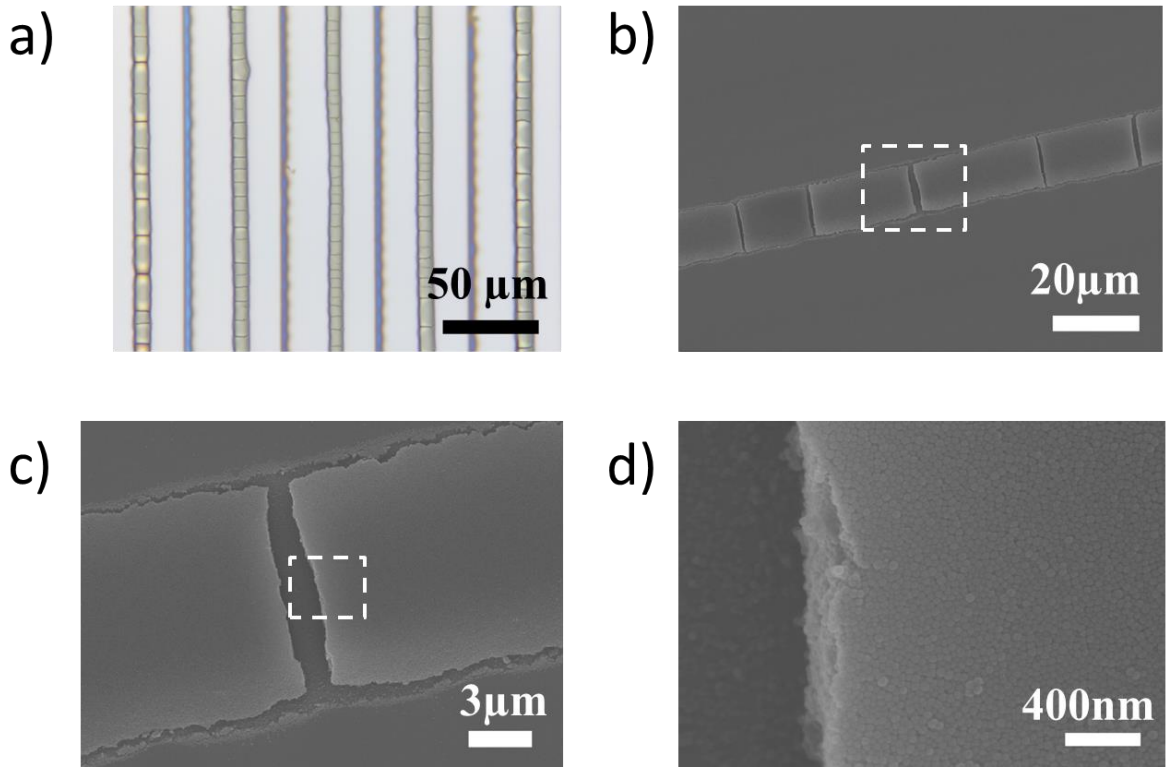

Figure 8.8. a) optical micrograph, and b) and c) SEM images of different magnifications on colloidal ribbons formed on chemically patterned substrate by controlled drying of PS latex particle suspension in the direct perpendicular to the PS stripes. The colloidal ribbons were only formed in the middle region between two PS stripes, due to the stick-slip motion of the contact line. The microchannels were formed inside the colloidal ribbons and the direction of microchannels was parallel to the moving direction of the lower substrate. The spacing between PS stripes is 50 µm.

When the PS stripe pattern was placed parallel to the moving direction of the lower substrate, the liquid front was strongly curved due to the strong hydrophobicity of PS stripes (**Figure 8.8**). Subsequently, intriguing patterns of microchannels were formed between parallel PS stripes (**Figure 8.9**). To rationalize the formation mechanism of such patterns, we first showed that the growth direction of colloidal microchannels was always

perpendicular to the contact line, rather than the moving direction of the substrate. To this end, an upper fixed blade of angled shaped (e.g., 60° and 30° to the moving direction of the lower substrate) was utilized to restrict the contact line of liquid front, thereby yielding the colloidal microchannels exhibiting an angle to the moving direction of lower substrate (**Figure 8.10**). In addition, colloidal microchannels with radially spoke-like structures were formed by utilizing a round-shape upper blade (**Figure 8.11**). Thus, when the PS latex particle solution was dragged along the PS stripes, the liquid front was curved due to the hydrophobicity of the PS stripes. As the colloidal microchannels preferably formed perpendicularly to the liquid front, the intriguing pattern of colloidal microchannels can thus be formed (**Figure 6**).

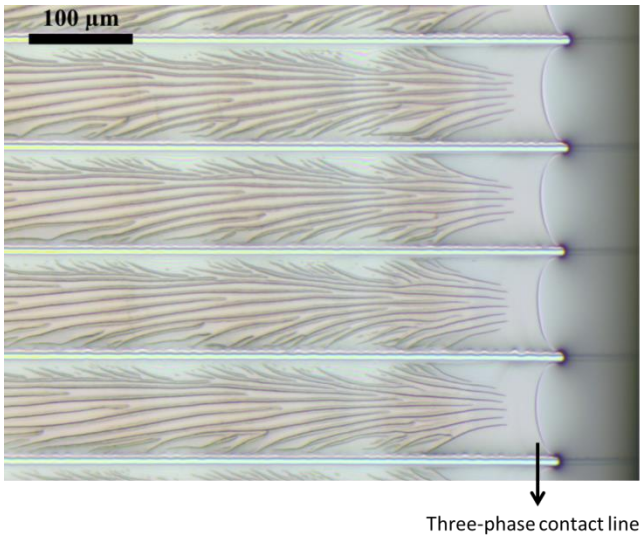

Figure 8.8. Optical micrograph of microchannels formed on chemically patterned substrate by controlled drying of PS latex particle in the direct parallel to the PS stripes at 50 ℃, the moving velocity of lower substrate of 13 μm/s and the concentration of 0.5 wt%. It is noteworthy that the three-phase contact line at the liquid front was strongly curved due to the hydrophobicity of PS stripes, thereby yielding the formation of curved microchannel patterns in between PS stripes.

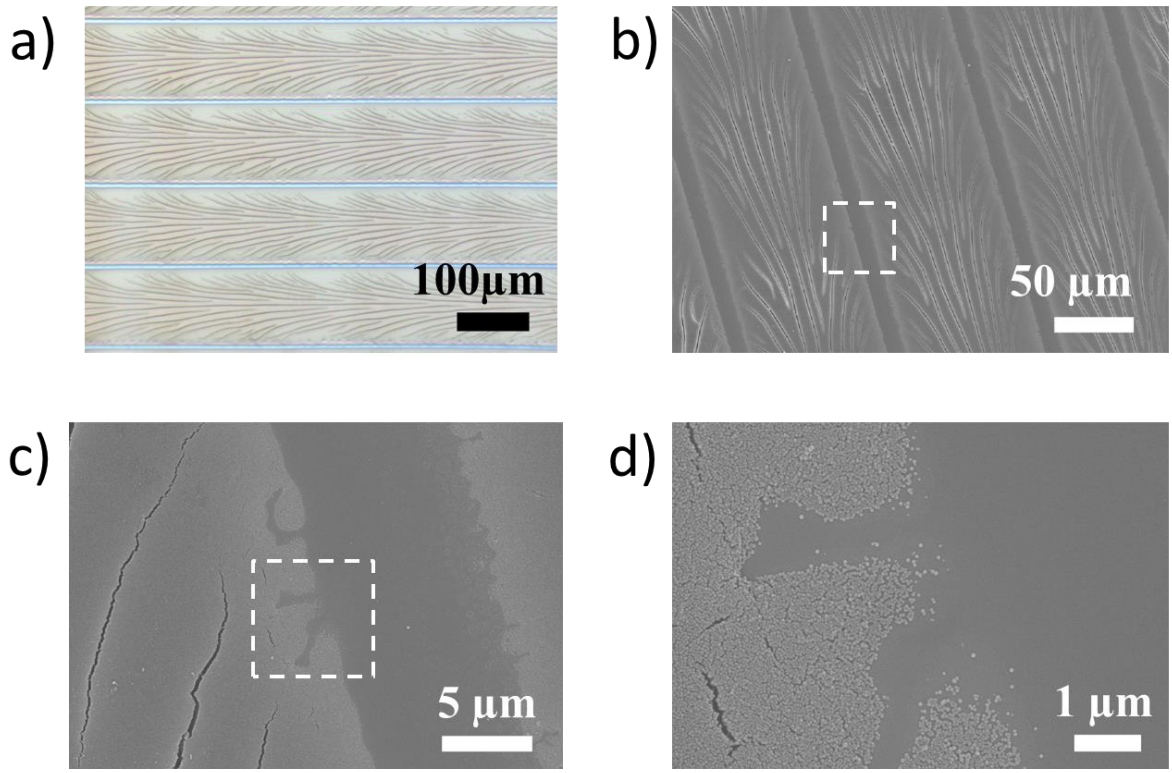

Figure 8.9. a) optical micrograph, and b) and c) SEM images of different magnifications on microchannels formed on chemically patterned substrate by controlled drying of PS latex particle in the direct parallel to the PS stripes. Curved microchannels were formed over the entire substrate except on the top of PS stripes due to the curved liquid water during drying of PS latex particle suspension. The spacing between PS stripes is 100 µm.

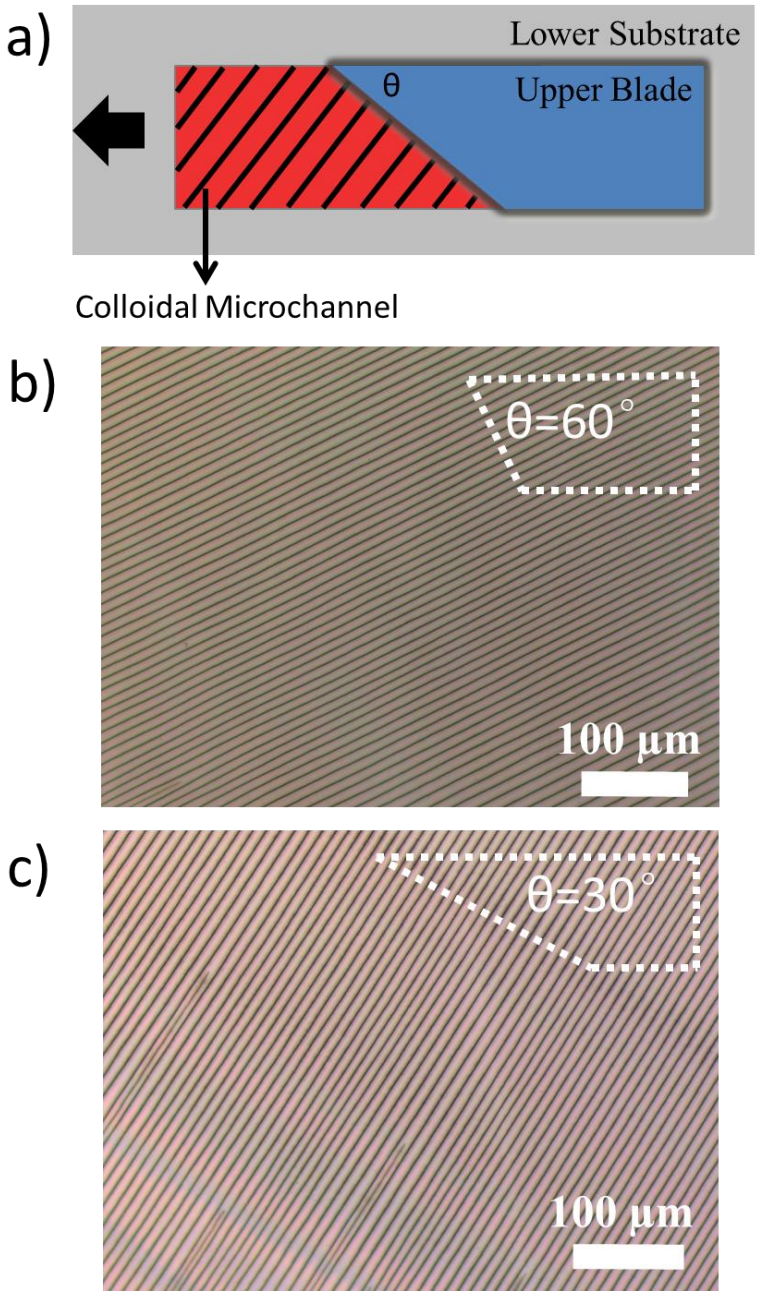

Figure 8.10. a) schematic illustration and optical micrograph of colloidal microchannels formed by the guidance of an angled upper blade of b) 60 ℃ and b) 30 ℃ at 50℃. The moving velocity of lower substrate was 13 μm/s, and the concentration was 0.5 wt%.

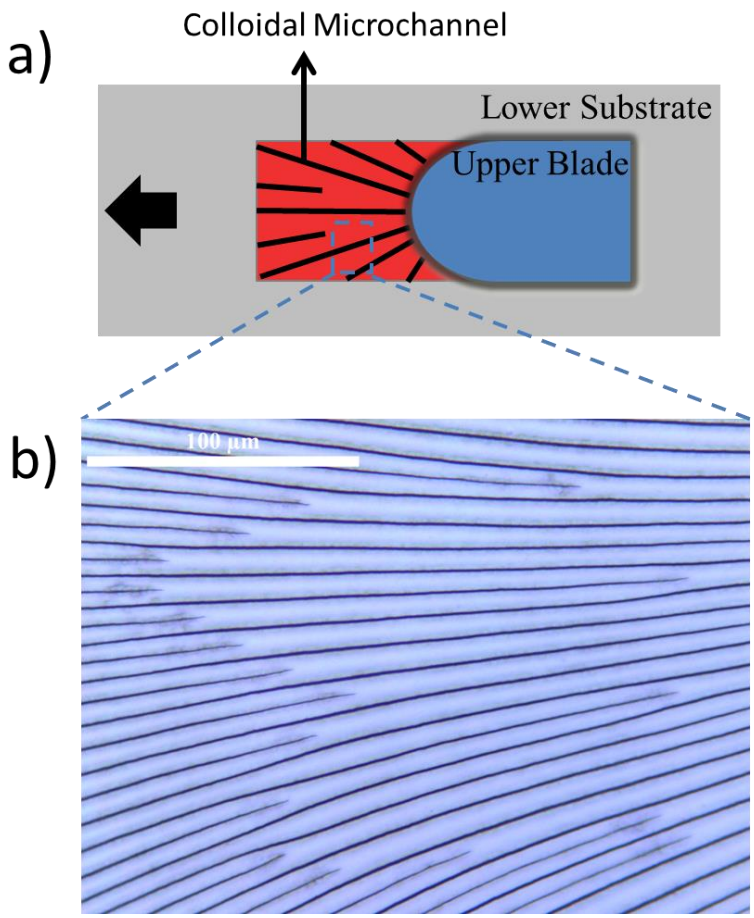

Figure 8.11. a) schematic illustration, and b) optical micrographs of colloidal microchannels formed by the guidance of a round-shape upper blade at 50℃. The moving velocity of lower substrate was 13 μm/s, and the concentration was 0.5 wt%.

By utilizing the prepared colloidal microchannels as template, nanomaterials (e.g., Au nanoparticles) can be guided and patterned accordingly. It is noteworthy that conventional strategy for synthesizing Au nanoparticles (NPs) usually contained extra amount of ligand in solution and the prepared Au NPs were dispersed in aqueous solution. As the PS colloidal microchannels are hydrophobic, Au NPs cannot be transported into the microchannels by water using Au NPs aqueous solution. Thus, we synthesized Au nanoparticles using star-like P4VP-PS copolymer unimicelles as inorganic template, based on our previous work,[295] thereby yielding extra-ligand free Au nanoparticles permanently capped with PS as ligand for dispersion in toluene. Then, by

FESA of Au nanoparticles solution on the prepared colloidal microchannel template, Au NPs were transported by toluene to the bottom of the microchannels (**Figure 8.12a**). Surprisingly, instead of fully covering the bottom of microchannels, Au NPs were deposited in two separated threads within one microchannel. We proposed that during the evaporation of the Au NP toluene solution, toluene gradually dewetted from the Si surface and segregated to the corners at the bottom of microchannels (**Figure 8.12b**). Therefore, Au NPs were deposited at the corners upon drying of the solution, and consequently, two threads of Au NPs were formed in one microchannel. The substrate with Au NP threads was then exposed to oxygen plasma for 1.5h to remove all residual polymers, thereby rendering pure highly-ordered Au NP threads aligned on the substrate.

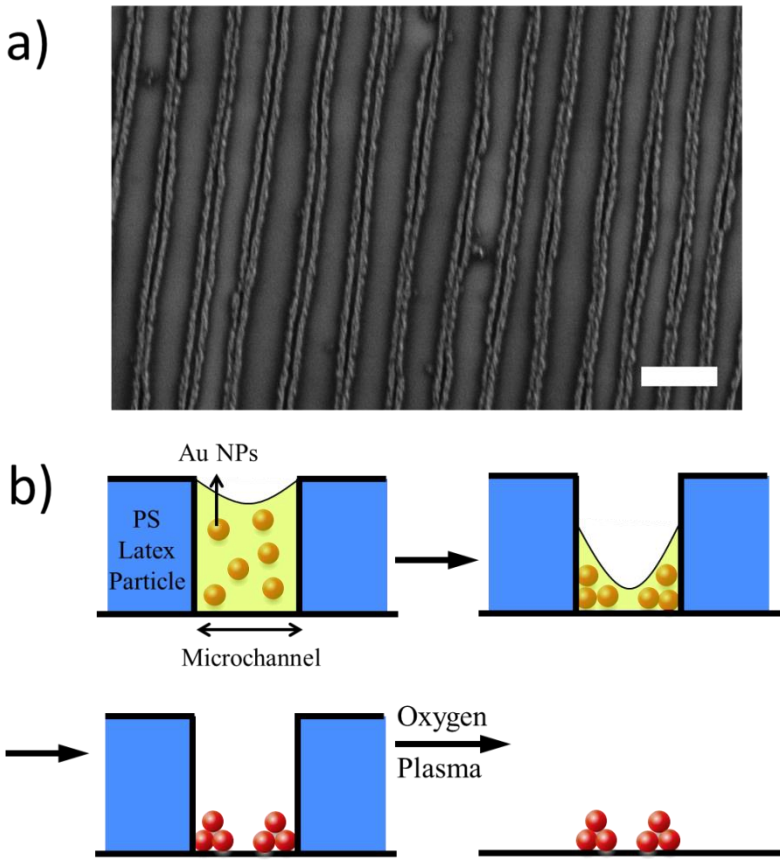

Figure 8.12. a) SEM image of threads of Au NPs aligned by using prepared colloidal microchannels as template. The scale bar is 10 μm. b) schematic illustration of the formation mechanism of two threads of Au NPs in one microchannel.

8.3. Conclusions

In summary, colloidal thin film with strictly ordered microchannels was crafted on a large scale via flow-enabled self-assembly (FESA). The spacing between two adjacent microchannels (i.e., λ_{c-c}) can be readily tuned by varying the moving velocity of the lower substrate. The relationship between λ_{c-c} and v was investigated experimentally and theoretically. In addition, a critical thickness for the formation of microchannels over the entire surface was observed, below which microchannel-free region would appear periodically in the colloidal thin film. Moreover, the influence of the chemically patterned substrate on the formation of colloidal microchannels was explored. The microchannels were found to preferentially grow orthogonally to the three-phase contact line. The prepared colloidal thin film with highly regular microchannels afford a versatile platform for aligning nanomaterials for potential applications in electronics and nanodevices.

CHAPTER 9

GENERAL CONCLUSIONS AND BROADER IMPACT

9.1 General Conclusion and Discussions

The use of spontaneous self-assembly as a lithography free means to construct well-ordered, often intriguing structures has received much attention for its ease of producing complex, centimeter-scale structures with small feature sizes. One extremely simple route to intriguing structures is the evaporative self-assembly of nonvolatile solutes from a sessile droplet on a solid substrate. However, flow instabilities during the evaporation process often result in non-equilibrium and irregular dissipative structures (e.g., randomly organized convection patterns, stochastically distributed multi-rings, etc.). Therefore, for fully controlling the evaporative self-assembly of solutes, two strategies, namely, controlled evaporative self-assembly (CESA) and flow-enabled evaporative-induced self-assembly (FESA) were exploited to create ordered structures of various nanomaterials.

First, hierarchical assemblies of amphiphilic diblock copolymer (i.e., polystyrene-*block*-poly(4-vinylpyridine) (PS-*b*-P4VP)) micelles were crafted by FESA. The periodic threads comprising a monolayer or a bilayer of PS-*b*-P4VP micelles were precisely positioned and patterned over large areas. Notably, the width of the threads can be easily tailored by simply varying the stop time of the translational stage. In addition, such diblock copolymer micelle threads were utilized as nanoreactors for creating inorganic nanoparticle arrays.

Second, highly aligned parallel DNA nanowires in the forms of nanostructured spokes over a macroscopic area were crafted via controlled evaporative self-assembly

(CESA) by subjecting DNA aqueous solution to evaporate in a curve-on-flat geometry composed of a spherical on a flat substrate. The effects of pH of DNA aqueous solution and temperature on the formation of DNA nanowires were systematically explored. A transition from spoke-like patterns to coffee-ring-like deposits was, for the first time, observed as the pH was increased.

Third, large-scale aligned metallic nanowires templated by highly oriented DNA were crafted by flow-enabled self-assembly (FESA). The formation of DNA nanowires was strongly influenced by the concentration of DNA solution, temperature, and moving speed of lower plate. A simple yet robust swelling-induced transfer printing (SIT-Printing) technique was developed to transfer ultralong DNA nanowires onto the desirable substrate. Subsequently, the resulting DNA nanowires were exploited as templates to form metallic nanowires by exposing DNA nanowires preloaded with metal salts under oxygen plasma. Moreover, DNA nanowires were also employed as scaffold for aligning metal nanoparticles and nanorods.

Fourth, colloidal microchannels (i.e., cracks) on a large scale were produced by controlling the drying process of colloidal suspensions via flow-enabled self-assembly (FESA). The thickness of the formed colloidal thin film can be easily tailored, thereby enabling the control over λ_{c-c} of colloidal microchannels. The influence of chemically patterned substrate (i.e., hydrophobic stripes on a hydrophilic substrate) on the formation of colloidal microchannels was explored. In addition, such colloidal microchannels with tunable λ_{c-c} was exploited as template for aligning inorganic nanoparticles.

Importantly, theoretical study of the formation mechanism of parallel stripes of solutes by FESA was evaluated. The relationship between the spacing of adjacent stripes λ_{c-c} and other experimental parameters such as the width of stripe, the stop time and the moving speed of the lower substrate was investigated. Such theoretical modeling would

provide guidance for the precise design and crafting of ordered structures composed of nanomaterials by FESA in the future study.

Interestingly, during the preparation of Au nanorods, the formation of ultrathin gold nanowires were unexpectedly observed. Based on conventional synthetic route to Au nanorods using CTAB as soft-templates, we found that rather than Au nanorods, adding small amount of hydrophobic solvent molecules (e.g., toluene or chloroform) to the Au growth solution triggered the ultrathin Au nanowire formation. The growth mechanism of such intriguing water-soluble ultrathin Au nanowires, differed from those formed by using oleylamine (i.e., non-water-soluble Au nanowires), was explored.

The ability to create highly ordered structures comprising nanomaterials by FESA and CESA open an avenue to organize nanomaterials for potential applications in electronics, optics, optoelectronics, sensors, nanotechnology and biotechnology.

9.2 Significance and Broader Impact

Inorganic nanomaterial synthesized via organic template

Nanocrystals possess a large variety of size- and shape-dependent properties with potential applications in areas such as electronics, catalysis, optics, and .[296-297] Nanoparticle synthesis has gained much attention in the past few years.[298-299] However, due to the nature of the kinetic nanocrystal growth, the procedures often require strict experimental conditions and the shape and size of the nanocrystals are difficult to control. Moreover, in many cases, additives such as ligands and metallic ions are required.[300] For example, the role silver ions play in the longitude growth of gold nanorods is still not clear,[234] even though gold nanorods have been repeatedly and widely produced using

silver ions for more than ten years. Moreover, the role of the additives in many cases is not clear and nanocrystal structure are often highly sensitive to the amount of the additives.[267] To this end, organic templates, which are artificially modified or synthesized, can direct the nucleation and growth of inorganic nanocrystal to achieve the desired shape, size and ultimate properties.

In this work, both 0D inorganic nanoparticle (e.g., Au nanoparticle) and 1D inorganic nanowire (e.g., Ag nanowire) were synthesized via organic template (e.g., block copolymer micelles and DNA nanowires). In addition, the influence of molar ratio of inorganic precursor over organic templates was systematically studied. Moreover, the strategy of removing organic template by using oxygen plasma treatment provides a general route to inorganic nanomaterials from organic templates without the use of reducing agent. Our study can be extended to create patterns of inorganic nanomaterials directly from the prepared patterned organic templates on the substrate.

Ordered structures of nanomaterials crafted by FESA and CESA

Drying droplets containing nonvolatile solutes (polymers, nanospheres, nanoparticles, DNA, etc.) on a solid substrate have been utilized to yield self-assembled structures, possessing dimensions of a few hundred sub-micrometers and beyond. However, these dissipative structures created by evaporation are often irregular and not in equilibrium. Yet for applications in microelectronics, data storage devices and biotechnology, it is highly desirable to achieve surface patterns that have a highly ordered and well controlled spatial arrangement. To date, only a few elegant studies have centered on establishing a means of harnessing the drying process of an evaporating droplet to produce highly regular structures. Among them, flow-enabled evaporative-induced self-assembly (FESA) and controlled evaporative self-assembly (CESA) stand out as extremely simple routes to creating intriguing one- or two- dimensional structures.

For example, in FESA, the nanomaterial solution was allowed to evaporate in a confined geometry consisting of two nearly parallel plates. The upper plate was fixed, and the lower plate was mounted on a computer-controlled translational stage that moved against the upper plate at a fixed distance. By tailoring the interaction between solutes and substrate, highly ordered and self-assembled structure of nanomaterials (e.g., block copolymer micelles and DNA nanowires) were crafted over large areas. The spacing between parallel stripes and the width of stripes can be easily tuned. Furthermore, colloidal microchannels (i.e., cracks) with tunable spacing on a large scale were also yielded by controlling the drying process of colloidal suspensions via FESA. Such colloidal microchannels have been proven to be an ideal template for aligning inorganic nanoparticles, and may render the fabrication of microfluids devices in the future.

Theoretical study of the formation of ordered structure of nanomaterials

Even though the fundamental aspects of a drying droplet with or without solutes have been studied during the past several decades, the theoretical study on the formation of ordered structure of nanomaterials is still lacking. Thus, in this work, theoretical modeling that underpins the FESA process was developed, including the smallest feature size of stripe patterns, the decrease in λ_{c-c} as the moving speed of the lower substrate increases. In addition, the formation of colloidal microchannels was also rationalized with the proposed models. These theoretical studies may offer useful guidance for crafting ordered structures of nanomaterials by FESA in the future.

Dissemination of work

This work has been conveyed to the scientific community by the following publications

1. **B. Li**, C. Zhang, B. Jiang, W. Han and Z. Lin" Flow-Enabled Self-Assembly of Large-Scale Aligned Nanowires ", submitted to ***Angewandte Chemie International Edition***, in press, 2015 (selected as **Very Important Paper (VIP)** paper by Angew. Chem. Int. Ed.) (DOI: 10.1002/ange.201412388)

2. **B. Li**, J. Iocozzia and Z. Lin, "Directing Convection to Pattern Thin Polymer Films: Coffee Rings" chapter in "Instability-Based Methods for Patterning Polymer Surfaces", J. Rodriguez-Hernandez and C. Drummond., Springer Press, in press, 2015 (**book chapter**)

3. **B. Li**, W. Han, B. Jiang and Z. Lin, "Crafting threads of diblock copolymer micelles via flow-enabled self-assembly", ***ACS Nano***, **8**, 2936 (2014).

4. **B. Li**, W. Han, M. Byun, L. Zhu, Q. Zou, and Z. Lin, "Macroscopic highly aligned DNA nanowires created by controlled evaporative self-assembly", ***ACS Nano***, **7**, 4326 (2013).

5. **B. Li**, et. al., "The Rational Design and Implementation of Organic Templates for Inorganic Nanocrystal Growth ", submitted to ***Chemical Reviews***.

6. **B. Li**, et. al., "Unconventional mechanism for ultrathin gold nanowire growth ", submitted to ***Journal of the American Chemical Society***.

7. **B. Li**, et. al., "Engineering Colloidal Microchanels via Flow-Enabled Self-Assembly (FESA)", submitted to ***ACS Nano***.

8. **B. Li**, et. al., "Prediction of the smallest dimensions of deposits formed in flow enabled self-assembly ", in preparation.

9. **B. Li**, et. al., "Coffee-ring effect vs marangoni effect: the solute size matters", in preparation.

10. C. Feng, X. Pang, Y. He, **B. Li**, and Z. Lin, "Crafting unimolecular nanocapsules from photo-crosslinkable core-shell star-like block copolymer", ***Chemistry of Materials***. 26, 6058 (2014).

11. X. Xin, R. Biswas, **B. Li**, J. Jung, and Z. Lin, "Charge transfer at the semiconductor quantum dot/TiO2 interface in quantum dot-sensitized solar cells: ab initio simulation", ***Particle and Particle Systems Characterization***, (2014).

12. J. Ren, Q. Zou, **B. Li** and Z. Lin, " High-speed atomic force microscope imaging: Adaptive multiloop mode", ***Physical Review E***, ***90***, *012405*(2014).

13. W. Han, **B. Li**, and Z. Lin, "Drying-mediated assembly of colloidal nanoparticles into large-scale microchannels", ***ACS Nano*** **7**, 6079 (2013)

14. W. Han, M. He, M. Byun, **B. Li**, and Z. Lin, "Large-scale hierarchically structured conjugated polymer assemblies with enhanced electrical conductivity",

***Angewandte Chemie International Edition*, 52**, 2564 (2013).

15. M. Byun, W. Han, **B. Li**, X. Xin, and Z. Lin, "An unconventional route to hierarchically ordered block copolymer on gradient patterned surface enabled by controlled evaporative self-assembly",***Angewandte Chemie International Edition***, **52**, 1122(2013).

16. W. Han, M. Byun, **B. Li**, X. Pang, and Z. Lin, "A simple route to hierarchically assembled micelles and inorganic nanoparticles", ***Angewandte Chemie International Edition*, 51**, 12588 (2012).

17. M. Byun, W. Han, **B. Li**, S. Hong, J. Cho, Q. Zou, and Z. Lin, "Guided organization of λ-DNA into microring arrays from liquid capillary bridge", ***Small***, **12**, 1641 (2011).

References

1. Park, C.; Yoon, J.; Thomas, E. L., Enabling Nanotechnology with Self Assembled Block Copolymer Patterns, *Polymer*, **2003,** *44*, 6725-6760.

2. Lieber, C. M.; Wang, Z. L., Functional Nanowires, *Mrs Bulletin*, **2007,** *32*, 99-108.

3. Byun, M.; Bowden, N. B.; Lin, Z., Hierarchically Organized Structures Engineered from Controlled Evaporative Self-Assembly, *Nano lett.*, **2010,** *10*, 3111-3117.

4. Khanal, B. P.; Zubarev, E. R., Rings of Nanorods, *Angewandte Chemie International Edition*, **2007,** *46*, 2195-2198.

5. Wild, B.; Cao, L.; Sun, Y.; Khanal, B. P.; Zubarev, E. R.; Gray, S. K.; Scherer, N. F.; Pelton, M., Propagation Lengths and Group Velocities of Plasmons in Chemically Synthesized Gold and Silver Nanowires, *ACS Nano*, **2011,** *6*, 472-482.

6. Zubarev, E. R.; Talroze, R. V.; Yuranova, T. I.; Plate, N. A.; Finkelmann, H., Influence of Network Topology on Polydomain−Monodomain Transition in Side Chain Liquid Crystalline Elastomers with Cyanobiphenyl Mesogens, *Macromolecules*, **1998,** *31*, 3566-3570.

7. Huang, Y.; Duan, X.; Wei, Q.; Lieber, C. M., Directed Assembly of One-Dimensional Nanostructures into Functional Networks, *Science*, **2001,** *291*, 630-633.

8. Cheng, J. Y.; Ross, C. A.; Smith, H. I.; Thomas, E. L., Templated Self-Assembly of Block Copolymers: Top-Down Helps Bottom-Up, *Advanced Materials*, **2006,** *18*, 2505-2521.

9. Song, X.; Gao, L., Facile Synthesis and Hierarchical Assembly of Hollow Nickel Oxide Architectures Bearing Enhanced Photocatalytic Properties, *Journal of Physical Chemistry C*, **2008,** *112*, 15299-15305.

10. Aizawa, M.; Buriak, J. M., Block Copolymer Templated Chemistry for the Formation of Metallic Nanoparticle Arrays on Semiconductor Surfaces, *Chemistry of Materials*, **2007,** *19*, 5090-5101.

11. Park, S.; Kim, B.; Yavuzcetin, O.; Tuominen, M. T.; Russell, T. P., Ordering of PS-b-P4VP on Patterned Silicon Surfaces, *ACS Nano*, **2008,** *2*, 1363-1370.

12. Lin, Y.; Böker, A.; He, J.; Sill, K.; Xiang, H.; Abetz, C.; Li, X.; Wang, J.; Emrick, T.; Long, S., Self-directed self-assembly of nanoparticle/copolymer mixtures, *Nature*, **2005,** *434*, 55-59.

13. Kim, Y.; Han, H.; Kim, Y.; Lee, W.; Alexe, M.; Baik, S.; Kim, J. K., Ultrahigh Density Array of Epitaxial Ferroelectric Nanoislands on Conducting Substrates, *Nano letters,* **2010,** *10,* 2141-2146.

14. Park, S.; Lim, J. H.; Chung, S. W.; Mirkin, C. A., Self-assembly of mesoscopic metal-polymer amphiphiles, *Science*, **2004,** *303*, 348.

15. Whitesides, G. M.; Grzybowski, B., Self-assembly at all scales, *Science*, **2002,** *295*, 2418.

16. Deegan, R. D.; Bakajin, O.; Dupont, T. F.; Huber, G.; Nagel, S. R.; Witten, T. A., Capillary flow as the cause of ring stains from dried liquid drops, *Nature*, **1997,** *389*, 827-829.

17. Deegan, R. D.; Bakajin, O.; Dupont, T. F.; Huber, G.; Nagel, S. R.; Witten, T. A., Contact Line Deposits in an Evaporating Drop, *Physical Review E*, **2000,** *62*, 756-765.

18. Farcau, C.; Moreira, H.; Viallet, B. t.; Grisolia, J. r. m.; Ressier, L., Tunable Conductive Nanoparticle Wire Arrays Fabricated by Convective Self-Assembly on Nonpatterned Substrates, *ACS Nano*, **2010,** *4*, 7275-7282.

19. Han, W.; Lin, Z., Learning from "Coffee Rings": Ordered Structures Enabled by Controlled Evaporative Self-Assembly, *Angewandte Chemie International Edition*, **2011,** 1534-1546.

20. Kim, H. S.; Lee, C. H.; Sudeep, P. K.; Emrick, T.; Crosby, A. J., Nanoparticle Stripes, Grids, and Ribbons Produced by Flow Coating, *Advanced Materials*, **2010,** *22*, 4600-4604.

21. Pauliac-Vaujour, E.; Stannard, A.; Martin, C. P.; Blunt, M. O.; Notingher, I.; Moriarty, P. J.; Vancea, I.; Thiele, U., Fingering instabilities in dewetting nanofluids, *Physical Review Letters*, **2008,** *100*, -.

22. Nguyen, V. X.; Stebe, K. J., Patterning of small particles by a surfactant-enhanced Marangoni-Benard instability, *Physical Review Letters*, **2002,** *88*, -.

23. Deegan, R. D., Pattern formation in drying drops, *Physical Review E*, **2000,** *61*, 475.

24. Xu, J.; Xia, J. F.; Hong, S. W.; Lin, Z. Q.; Qiu, F.; Yang, Y. L., Self-assembly of gradient concentric rings via solvent evaporation from a capillary bridge, *Physical Review Letters*, **2006,** *96*, -.

25. Byun, M.; Bowden, N. B.; Lin, Z. Q., Hierarchically Organized Structures Engineered from Controlled Evaporative Self-Assembly, *Nano letters*, **2010,** *10*, 3111-3117.

26. Langmuir, I., The Evaporation of Small Spheres, *Physical Review*, **1918,** *12*, 368-370.

27. Poulard, C.; Guéna, G.; Cazabat, A. M., Diffusion-driven evaporation of sessile drops, *Journal of Physics-Condensed Matter*, **2005,** *17*, S4213.

28. Fuchs, N. A., *Evaporation and droplet growth in gaseous media*. Elsevier: 2013.

29. Houghton, H. G., A Study of the Evaporation of Small Water Drops, *Journal of Applied Physics*, **1933,** *4*, 419-424.

30. Knacke, O.; Stranski, I. N., The mechanism of evaporation, *Progress in Metal Physics*, **1956,** *6*, 181-235.

31. Cazabat, A.-M.; Guena, G., Evaporation of macroscopic sessile droplets, *Soft Matter*, **2010,** *6*, 2591-2612.

32. Prosperetti, A.; Plesset, M. S., The stability of an evaporating liquid surface, *Physics of Fluids*, **1984,** *27*, 1590-1602.

33. Burelbach, J. P.; Bankoff, S. G.; Davis, S. H., Nonlinear stability of evaporating/condensing liquid films, *Journal of Fluid Mechanics*, **1988,** *195*, 463-494.

34. Marek, R.; Straub, J., Analysis of the evaporation coefficient and the condensation coefficient of water, *International Journal of Heat and Mass Transfer*, **2001,** *44*, 39-53.

35. Frohn, A.; Roth, N., *Dynamics of droplets*. Springer: 2000.

36. Hu, H.; Larson, R. G., Evaporation of a Sessile Droplet on a Substrate, *Journal of Physical Chemistry B*, **2002,** *106*, 1334-1344.

37. Semenov, S.; Starov, V. M.; Rubio, R. G.; Velarde, M. G., Instantaneous distribution of fluxes in the course of evaporation of sessile liquid droplets: Computer simulations, *Colloids and Surfaces A-Physicochemical and Engineering Aspects*, **2010,** *372*, 127-134.

38. Nguyen, T. A. H.; Nguyen, A. V.; Hampton, M. A.; Xu, Z. P.; Huang, L.; Rudolph, V., Theoretical and experimental analysis of droplet evaporation on solid surfaces, *Chemical Engineering Science*, **2012,** *69*, 522-529.

39. Anderson, D. M.; Davis, S. H., The spreading of volatile liquid droplets on heated surfaces, *Physics of Fluids*, **1995,** *7*, 248-265.

40. SHAHIDZADEH-BONN, N.; RAFAÏ, S.; AZOUNI, A.; BONN, D., Evaporating droplets, *Journal of Fluid Mechanics*, **2006,** *549*, 307-313.

41. Birdi, K. S.; Vu, D. T.; Winter, A., A study of the evaporation rates of small water drops placed on a solid surface, *The Journal of Physical Chemistry*, **1989,** *93*, 3702-3703.

42. Dettre, R. H.; Johnson, R. E., Contact Angle Hysteresis. IV. Contact Angle Measurements on Heterogeneous Surfaces1, *The Journal of Physical Chemistry*, **1965,** *69*, 1507-1515.

43. Snoeijer, J. H.; Andreotti, B., Moving Contact Lines: Scales, Regimes, and Dynamical Transitions, *Annual Review of Fluid Mechanics*, **2013,** *45*, 269-292.

44. Rowan, S. M.; Newton, M. I.; McHale, G., Evaporation of Microdroplets and the Wetting of Solid Surfaces, *The Journal of Physical Chemistry*, **1995,** *99*, 13268-13271.

45. Picknett, R. G.; Bexon, R., The evaporation of sessile or pendant drops in still air, *Journal of Colloid and Interface Science*, **1977,** *61*, 336-350.

46. DUNN, G. J.; WILSON, S. K.; DUFFY, B. R.; DAVID, S.; SEFIANE, K., The strong influence of substrate conductivity on droplet evaporation, *Journal of Fluid Mechanics*, **2009,** *623*, 329-351.

47. Oron, A.; Davis, S. H.; Bankoff, S. G., Long-scale evolution of thin liquid films, *Reviews of Modern Physics*, **1997,** *69*, 931-980.

48. Clausius, R., Ueber die bewegende Kraft der Wärme und die Gesetze, welche sich daraus für die Wärmelehre selbst ableiten lassen, *Annalen der Physik*, **1850,** *155*, 368-397.

49. MURISIC, N.; KONDIC, L., On evaporation of sessile drops with moving contact lines, *Journal of Fluid Mechanics*, **2011,** *679*, 219-246.

50. Siregar, D. P.; Kuerten, J. G. M.; van der Geld, C. W. M., Numerical simulation of the drying of inkjet-printed droplets, *Journal of Colloid and Interface Science*, **2013,** *392*, 388-395.

51. Berteloot, G.; Pham, C. T.; Daerr, A.; Lequeux, F.; Limat, L., Evaporation-induced flow near a contact line: Consequences on coating and contact angle, *Europhysics Letters*, **2008,** *83*, 14003.

52. Cachile, M.; Bénichou, O.; Cazabat, A. M., Evaporating Droplets of Completely Wetting Liquids, *Langmuir*, **2002,** *18*, 7985-7990.

53. Guéna, G.; Poulard, C.; Voué, M.; De Coninck, J.; Cazabat, A. M., Evaporation of sessile liquid droplets, *Colloids and Surfaces A-Physicochemical and Engineering Aspects*, **2006,** *291*, 191-196.

54. Joshi, A.; Sun, Y., Wetting dynamics and particle deposition for an evaporating colloidal drop: A lattice Boltzmann study, *Physical Review E*, **2010,** *82*, 041401.

55. Janeček, V.; Nikolayev, V. S., Contact line singularity at partial wetting during evaporation driven by substrate heating, *Europhysics Letters*, **2012,** *100*, 14003.

56. Doumenc, F.; Guerrier, B., Drying of a Solution in a Meniscus: A Model Coupling the Liquid and the Gas Phases, *Langmuir*, **2010,** *26*, 13959-13967.

57. Eggers, J.; Pismen, L. M., Nonlocal description of evaporating drops, *Physics of Fluids*, **2010,** *22*, -.

58. Hołyst, R.; Litniewski, M.; Jakubczyk, D.; Kolwas, K.; Kolwas, M.; Kowalski, K.; Migacz, S.; Palesa, S.; Zientara, M., Evaporation of freely suspended single droplets: experimental, theoretical and computational simulations, *Reports on Progress in Physics*, **2013,** *76*, 034601.

59. Crafton, E. F.; Black, W. Z., Heat transfer and evaporation rates of small liquid droplets on heated horizontal surfaces, *International Journal of Heat and Mass Transfer*, **2004,** *47*, 1187-1200.

60. Cioulachtjian, S.; Launay, S.; Boddaert, S.; Lallemand, M., Experimental investigation of water drop evaporation under moist air or saturated vapour conditions, *International Journal of Thermal Sciences*, **2010,** *49*, 859-866.

61. Chini, S. F.; Amirfazli, A., Understanding the evaporation of spherical drops in quiescent environment, *Colloids and Surfaces A-Physicochemical and Engineering Aspects*, **2013,** *432*, 82-88.

62. Briones, A. M.; Ervin, J. S.; Putnam, S. A.; Byrd, L. W.; Jones, J. G., A novel kinetically-controlled de-pinning model for evaporating water microdroplets, *International Communications in Heat and Mass Transfer*, **2012,** *39*, 1311-1319.

63. Gelderblom, H.; Bloemen, O.; Snoeijer, J. H., Stokes flow near the contact line of an evaporating drop, *Journal of Fluid Mechanics*, **2012,** *709*, 69-84.

64. Weon, B. M.; Je, J. H.; Poulard, C., Convection-enhanced water evaporation, *AIP Advances*, **2011,** *1*, -.

65. Dehaeck, S.; Rednikov, A.; Colinet, P., Vapor-Based Interferometric Measurement of Local Evaporation Rate and Interfacial Temperature of Evaporating Droplets, *Langmuir*, **2014,** *30*, 2002-2008.

66. Fischer, B. J., Particle Convection in an Evaporating Colloidal Droplet, *Langmuir*, **2001,** *18*, 60-67.

67. Popov, Y., Evaporative deposition patterns: Spatial dimensions of the deposit, *Physical Review E*, **2005,** *71*, 036313.

68. Hamamoto, Y.; Christy, J.; Sefiane, K., Order-of-magnitude increase in flow velocity driven by mass conservation during the evaporation of sessile drops, *Physical Review E*, **2011,** *83*, 051602.

69. Bodiguel, H.; Leng, J., Imaging the drying of a colloidal suspension: Velocity field, *Chemical Engineering and Processing*, **2013,** *68*, 60-63.

70. Maki, K. L.; Kumar, S., Fast Evaporation of Spreading Droplets of Colloidal Suspensions, *Langmuir*, **2011,** *27*, 11347-11363.

71. Scriven, L.; Sternling, C., The marangoni effects, **1960**.

72. Hu, H.; Larson, R. G., Analysis of the Effects of Marangoni Stresses on the Microflow in an Evaporating Sessile Droplet, *Langmuir*, **2005,** *21*, 3972-3980.

73. Hu, H.; Larson, R. G., Marangoni Effect Reverses Coffee-Ring Depositions, *Journal of Physical Chemistry B*, **2006,** *110*, 7090-7094.

74. Nguyen, V. X.; Stebe, K. J., Patterning of Small Particles by a Surfactant-Enhanced Marangoni-B\'enard Instability, *Physical Review Letters*, **2002,** *88*, 164501.

75. Assenheimer, M.; Steinberg, V., Observation of Coexisting Upflow and Downflow Hexagons in Boussinesq Rayleigh-B\'enard Convection, *Physical Review Letters*, **1996,** *76*, 756-759.

76. Morris, S. W.; Bodenschatz, E.; Cannell, D. S.; Ahlers, G., Spiral defect chaos in large aspect ratio Rayleigh-B\'enard convection, *Physical Review Letters*, **1993,** *71*, 2026-2029.

77. Block, M. J., Surface Tension as the Cause of Benard Cells and Surface Deformation in a Liquid Film, *Nature*, **1956,** *178*, 650-651.

78. Buffone, C.; Sefiane, K., Investigation of thermocapillary convective patterns and their role in the enhancement of evaporation from pores, *International Journal of Multiphase Flow*, **2004,** *30*, 1071-1091.

79. Buffone, C.; Sefiane, K.; Christy, J. R. E., Experimental investigation of self-induced thermocapillary convection for an evaporating meniscus in capillary tubes using micro–particle image velocimetry, *Physics of Fluids*, **2005,** *17*, -.

80. Buffone, C.; Sefiane, K., IR measurements of interfacial temperature during phase change in a confined environment, *Experimental Thermal and Fluid Science*, **2004,** *29*, 65-74.

81. Pearson, J. R. A., On convection cells induced by surface tension, *Journal of Fluid Mechanics*, **1958,** *4*, 489-500.

82. Nield, D. A., Surface tension and buoyancy effects in cellular convection, *Journal of Fluid Mechanics*, **1964,** *19*, 341-352.

83. Barmi, M. R.; Meinhart, C. D., Convective Flows in Evaporating Sessile Droplets, *Journal of Physical Chemistry B*, **2014,** *118*, 2414-2421.

84. Hu, Y.-C.; Zhou, Q.; Ye, H.-M.; Wang, Y.-F.; Cui, L.-S., Peculiar surface profile of poly(ethylene oxide) film with ring-like nucleation distribution induced by Marangoni flow effect, *Colloids and Surfaces A-Physicochemical and Engineering Aspects*, **2013,** *428*, 39-46.

85. Barash, L.; Bigioni, T.; Vinokur, V.; Shchur, L., Evaporation and fluid dynamics of a sessile drop of capillary size, *Physical Review E*, **2009,** *79*, 046301.

86. Xu, X.; Luo, J.; Guo, D., Criterion for Reversal of Thermal Marangoni Flow in Drying Drops, *Langmuir*, **2009,** *26*, 1918-1922.

87. Thompson, I.; Duan, F.; Ward, C., Absence of Marangoni convection at Marangoni numbers above 27,000 during water evaporation, *Physical Review E*, **2009,** *80*, 056308.

88. Hu, H.; Larson, R. G., Analysis of the Microfluid Flow in an Evaporating Sessile Droplet, *Langmuir*, **2005,** *21*, 3963-3971.

89. Savino, R.; Paterna, D.; Favaloro, N., Buoyancy and Marangoni Effects in an Evaporating Drop, *Journal of Thermophysics and Heat Transfer*, **2002,** *16*, 562-574.

90. Steinchen, A.; Sefiane, K., Self-organised Marangoni motion at evaporating drops or in capillary menisci–thermohydrodynamical model, *Journal of Non-Equilibrium Thermodynamics*, **2005,** *30*, 39-51.

91. Kang, K. H.; Lim, H. C.; Lee, H. W.; Lee, S. J., Evaporation-induced saline Rayleigh convection inside a colloidal droplet, *Physics of Fluids*, **2013,** *25*, -.

92. Yunker, P. J.; Still, T.; Lohr, M. A.; Yodh, A. G., Suppression of the coffee-ring effect by shape-dependent capillary interactions, *Nature*, **2011,** *476*, 308-311.

93. Larson, R. G., Re-Shaping the Coffee Ring, *Angewandte Chemie International Edition*, **2012,** *51*, 2546-2548.

94. Bhardwaj, R.; Fang, X.; Somasundaran, P.; Attinger, D., Self-Assembly of Colloidal Particles from Evaporating Droplets: Role of DLVO Interactions and Proposition of a Phase Diagram, *Langmuir*, **2010,** *26*, 7833-7842.

95. Anyfantakis, M.; Baigl, D., Dynamic Photocontrol of the Coffee-Ring Effect with Optically Tunable Particle Stickiness, *Angewandte Chemie International Edition*, **2014,** *126*, 14301-14305.

96. Xu, J.; Xia, J.; Lin, Z., Evaporation-Induced Self-Assembly of Nanoparticles from a Sphere-on-Flat Geometry, *Angewandte Chemie International Edition*, **2007,** *119*, 1892-1895.

97. Li, B.; Han, W.; Jiang, B.; Lin, Z., Crafting Threads of Diblock Copolymer Micelles via Flow-Enabled Self-Assembly, *ACS Nano*, **2014,** *8*, 2936-2942.

98. Harris, D. J.; Hu, H.; Conrad, J. C.; Lewis, J. A., Patterning colloidal films via evaporative lithography, *Physical Review Letters*, **2007,** *98*, -.

99. Gleiche, M.; Chi, L. F.; Fuchs, H., Nanoscopic channel lattices with controlled anisotropic wetting, *Nature*, **2000,** *403*, 173-175.

100. Chi, L. F.; Rakers, S.; Hartig, M.; Gleiche, M.; Fuchs, H.; Schmid, G., Monolayers of nanosized Au-55-clusters: preparation and characterization, *Colloids and Surfaces a-Physicochemical and Engineering Aspects*, **2000,** *171*, 241-248.

101. Prevo, B. G.; Velev, O. D., Controlled, rapid deposition of structured coatings from micro- and nanoparticle suspensions, *Langmuir*, **2004,** *20*, 2099-2107.

102. Yabu, H.; Shimomura, M., Preparation of Self-Organized Mesoscale Polymer Patterns on a Solid Substrate: Continuous Pattern Formation from a Receding Meniscus, *Advanced Functional Materials*, **2005,** *15*, 575-581.

103. Hong, S. W.; Byun, M.; Lin, Z. Q., Robust Self-Assembly of Highly Ordered Complex Structures by Controlled Evaporation of Confined Microfluids, *Angewandte Chemie International Edition*, **2009,** *48*, 512-516.

104. Hong, S. W.; Giri, S.; Lin, V. S. Y.; Lin, Z. Q., Simple route to gradient concentric metal and metal oxide rings, *Chemistry of Materials*, **2006,** *18*, 5164-5166.

105. Hong, S. W.; Jeong, W.; Ko, H.; Kessler, M. R.; Tsukruk, V. V.; Lin, Z. Q., Directed self-assembly of gradient concentric carbon nanotube rings, *Advanced Functional Materials*, **2008,** *18*, 2114-2122.

106. Hong, S. W.; Wang, J.; Lin, Z. Q., Evolution of Ordered Block Copolymer Serpentines into a Macroscopic, Hierarchically Ordered Web, *Angewandte Chemie International Edition*, **2009,** *48*, 8356-8360.

107. Hong, S. W.; Xia, J. F.; Byun, M.; Zou, Q. Z.; Lin, Z. Q., Mesoscale patterns formed by evaporation of a polymer solution in the proximity of a sphere on a smooth substrate: Molecular weight and curvature effects, *Macromolecules*, **2007,** *40*, 2831-2836.

108. Hong, S. W.; Xia, J.; Lin, Z., Spontaneous Formation of Mesoscale Polymer Patterns in an Evaporating Bound Solution, *Advanced Materials*, **2007,** *19*, 1413-1417.

109. Hong, S. W.; Xu, J.; Lin, Z. Q., Template-assisted formation of gradient concentric gold rings, *Nano letters*, **2006,** *6*, 2949-2954.

110. Hong, S. W.; Xu, J.; Xia, J. F.; Lin, Z. Q.; Qiu, F.; Yang, Y. L., Drying mediated pattern formation in a capillary-held organometallic polymer solution, *Chemistry of Materials*, **2005,** *17*, 6223-6226.

111. Abkarian, M.; Nunes, J.; Stone, H. A., Colloidal Crystallization and Banding in a Cylindrical Geometry, *Journal of the American Chemical Society*, **2004,** *126*, 5978-5979.

112. Wang, H.; li, X.; Nakamura, H.; Miyazaki, M.; Maeda, H., Continuous Particle Self-Arrangement in a Long Microcapillary, *Advanced Materials*, **2002,** *14*, 1662-1666.

113. Lin, Z.; Granick, S., Patterns Formed by Droplet Evaporation from a Restricted Geometry, *Journal of the American Chemical Society*, **2005,** *127*, 2816-2817.

114. Han, W.; Li, B.; Lin, Z., Drying-Mediated Assembly of Colloidal Nanoparticles into Large-Scale Microchannels, *ACS Nano*, **2013,** *7*, 6079-6085.

115. Byun, M.; Han, W.; Li, B.; Hong, S. W.; Cho, J. W.; Zou, Q.; Lin, Z., Guided Organization of λ-DNA into Microring Arrays from Liquid Capillary Bridges, *Small*, **2011,** *7*, 1641-1646.

116. Han, W.; Lin, Z., Learning from "Coffee Rings": Ordered Structures Enabled by Controlled Evaporative Self-Assembly, *Angewandte Chemie International Edition*, **2012,** *51*, 1534-1546.

117. Myunghwan, B.; Jun, W.; Zhiqun, L., Massively ordered microstructures composed of magnetic nanoparticles, *Journal of Physics-Condensed Matter*, **2009,** *21*, 264014.

118. Kim, T. Y.; Kwon, S. W.; Park, S. J.; Yoon, D. H.; Suh, K. S.; Yang, W. S., Self-Organized Graphene Patterns, *Advanced Materials*, **2011,** *23*, 2734-2738.

119. Byun, M.; Laskowski, R. L.; He, M.; Qiu, F.; Jeffries-El, M.; Lin, Z., Controlled evaporative self-assembly of hierarchically structured regioregular conjugated polymers, *Soft Matter*, **2009,** *5*, 1583-1586.

120. Schwartz, B. J., Conjugated Polymers as Molecular Materials: How Chain Conformation and Film Morphology Influence Energy Transfer and Interchain Interactions, *Annual Review of Physical Chemistry*, **2003,** *54*, 141-172.

121. Berenbaum, A.; Ginzburg-Margau, M.; Coombs, N.; Lough, A. J.; Safa-Sefat, A.; Greedan, J. E.; Ozin, G. A.; Manners, I., Ceramics Containing Magnetic Co–Fe Alloy Nanoparticles from the Pyrolysis of a Highly Metallized Organometallic Polymer Precursor, *Advanced Materials*, **2003,** *15*, 51-55.

122. Clendenning, S. B.; Aouba, S.; Rayat, M. S.; Grozea, D.; Sorge, J. B.; Brodersen, P. M.; Sodhi, R. N. S.; Lu, Z. H.; Yip, C. M.; Freeman, M. R.; Ruda, H. E.; Manners, I., Direct Writing of Patterned Ceramics Using Electron-Beam Lithography and Metallopolymer Resists, *Advanced Materials*, **2004,** *16*, 215-219.

123. Clendenning, S. B.; Fournier-Bidoz, S.; Pietrangelo, A.; Yang, G.; Han, S.; Brodersen, P. M.; Yip, C. M.; Lu, Z.-H.; Ozin, G. A.; Manners, I., Ordered 2D arrays of ferromagnetic Fe/Co nanoparticle rings from a highly metallized metallopolymer precursor, *Journal of Materials Chemistry*, **2004,** *14*, 1686-1690.

124. MacLachlan, M. J.; Ginzburg, M.; Coombs, N.; Coyle, T. W.; Raju, N. P.; Greedan, J. E.; Ozin, G. A.; Manners, I., Shaped ceramics with tunable magnetic properties from metal-containing polymers, *Science*, **2000,** *287*, 1460-1463.

125. Paquet, C.; Cyr, P. W.; Kumacheva, E.; Manners, I., Polyferrocenes: metallopolymers with tunable and high refractive indices, *Chemical Communications*, **2004,** 234-235.

126. Whittell, G. R.; Manners, I., Metallopolymers: New Multifunctional Materials, *Advanced Materials*, **2007,** *19*, 3439-3468.

127. Manners, I., Poly(ferrocenylsilanes): novel organometallic plastics, *Chemical Communications*, **1999,** 857-865.

128. Ginzburg, M.; MacLachlan, M. J.; Yang, S. M.; Coombs, N.; Coyle, T. W.; Raju, N. P.; Greedan, J. E.; Herber, R. H.; Ozin, G. A.; Manners, I., Genesis of Nanostructured, Magnetically Tunable Ceramics from the Pyrolysis of Cross-Linked Polyferrocenylsilane Networks and Formation of Shaped Macroscopic Objects and Micron Scale Patterns by Micromolding Inside Silicon Wafers, *Journal of the American Chemical Society*, **2002,** *124*, 2625-2639.

129. Leutwyler, W. K.; Bürgi, S. L.; Burgl, H., Semiconductor clusters, nanocrystals, and quantum dots, *Science*, **1996,** *271*, 933-937.

130. Peng, X.; Schlamp, M. C.; Kadavanich, A. V.; Alivisatos, A. P., Epitaxial Growth of Highly Luminescent CdSe/CdS Core/Shell Nanocrystals with Photostability and Electronic Accessibility, *Journal of the American Chemical Society*, **1997,** *119*, 7019-7029.

131. Murray, C. B.; Norris, D. J.; Bawendi, M. G., Synthesis and characterization of nearly monodisperse CdE (E = sulfur, selenium, tellurium) semiconductor nanocrystallites, *Journal of the American Chemical Society*, **1993,** *115*, 8706-8715.

132. Coe, S.; Woo, W.-K.; Bawendi, M.; Bulovic, V., Electroluminescence from single monolayers of nanocrystals in molecular organic devices, *Nature*, **2002,** *420*, 800-803.

133. Colvin, V.; Schlamp, M.; Alivisatos, A., Light-emitting diodes made from cadmium selenide nanocrystals and a semiconducting polymer, *Nature*, **1994,** *370*, 354-357.

134. Dabbousi, B. O.; Bawendi, M. G.; Onitsuka, O.; Rubner, M. F., Electroluminescence from CdSe quantum-dot/polymer composites, *Applied Physics Letters*, **1995,** *66*, 1316-1318.

135. Gao, M.; Richter, B.; Kirstein, S., White-light electroluminescence from self-assembled Q-CdSe/PPV multilayer structures, *Advanced Materials*, **1997,** *9*, 802-805.

136. Greenham, N. C.; Peng, X.; Alivisatos, A. P., Charge separation and transport in conjugated-polymer/semiconductor-nanocrystal composites studied by photoluminescence quenching and photoconductivity, *Physical Review B*, **1996,** *54*, 17628-17637.

137. Huynh, W. U.; Dittmer, J. J.; Alivisatos, A. P., Hybrid nanorod-polymer solar cells, *science*, **2002,** *295*, 2425-2427.

138. Milliron, D. J.; Gur, I.; Alivisatos, A. P., Hybrid Organic–Nanocrystal Solar Cells, *MRS Bulletin*, **2005,** *30*, 41-44.

139. Chan, W. C. W.; Nie, S., Quantum Dot Bioconjugates for Ultrasensitive Nonisotopic Detection, *Science*, **1998,** *281*, 2016-2018.

140. Ishii, D.; Kinbara, K.; Ishida, Y.; Ishii, N.; Okochi, M.; Yohda, M.; Aida, T., Chaperonin-mediated stabilization and ATP-triggered release of semiconductor nanoparticles, *Nature*, **2003,** *423*, 628-632.

141. Mattoussi, H.; Mauro, J. M.; Goldman, E. R.; Anderson, G. P.; Sundar, V. C.; Mikulec, F. V.; Bawendi, M. G., Self-Assembly of CdSe−ZnS Quantum Dot Bioconjugates Using an Engineered Recombinant Protein, *Journal of the American Chemical Society*, **2000,** *122*, 12142-12150.

142. Medintz, I. L.; Uyeda, H. T.; Goldman, E. R.; Mattoussi, H., Quantum dot bioconjugates for imaging, labelling and sensing, *Nat Mater*, **2005,** *4*, 435-446.

143. Alivisatos, P., The use of nanocrystals in biological detection, *Nat Biotech*, **2004,** *22*, 47-52.

144. Larson, D. R.; Zipfel, W. R.; Williams, R. M.; Clark, S. W.; Bruchez, M. P.; Wise, F. W.; Webb, W. W., Water-Soluble Quantum Dots for Multiphoton Fluorescence Imaging in Vivo, *Science*, **2003,** *300*, 1434-1436.

145. Santra, S.; Yang, H.; Holloway, P. H.; Stanley, J. T.; Mericle, R. A., Synthesis of Water-Dispersible Fluorescent, Radio-Opaque, and Paramagnetic CdS:Mn/ZnS Quantum Dots: A Multifunctional Probe for Bioimaging, *Journal of the American Chemical Society*, **2005,** *127*, 1656-1657.

146. Dabbousi, B. O.; Rodriguez-Viejo, J.; Mikulec, F. V.; Heine, J. R.; Mattoussi, H.; Ober, R.; Jensen, K. F.; Bawendi, M. G., (CdSe)ZnS Core−Shell Quantum Dots: Synthesis and Characterization of a Size Series of Highly Luminescent Nanocrystallites, *Journal of Physical Chemistry B*, **1997,** *101*, 9463-9475.

147. Hines, M. A.; Guyot-Sionnest, P., Synthesis and Characterization of Strongly Luminescing ZnS-Capped CdSe Nanocrystals, *The Journal of Physical Chemistry*, **1996,** *100*, 468-471.

148. Kortan, A. R.; Hull, R.; Opila, R. L.; Bawendi, M. G.; Steigerwald, M. L.; Carroll, P. J.; Brus, L. E., Nucleation and growth of cadmium selendie on zinc sulfide quantum crystallite seeds, and vice versa, in inverse micelle media, *Journal of the American Chemical Society*, **1990,** *112*, 1327-1332.

149. Leizerson, I.; Lipson, S. G.; Lyushnin, A. V., Finger Instability in Wetting−Dewetting Phenomena, *Langmuir*, **2003,** *20*, 291-294.

150. Lyushnin, A. V.; Golovin, A. A.; Pismen, L. M., Fingering instability of thin evaporating liquid films, *Physical Review E*, **2002,** *65*, 021602.

151. Cazabat, A.; Heslot, F.; Troian, S.; Carles, P., Fingering instability of thin spreading films driven by temperature gradients, *Nature*, **1990,** *346*, 824-826.

152. Byun, M.; Bowden, N. B.; Lin, Z., Hierarchically Organized Structures Engineered from Controlled Evaporative Self-Assembly, *Nano Lett.*, **2010,** *10*, 3111-3117.

153. Byun, M.; Han, W.; Li, B.; Xin, X.; Lin, Z., An Unconventional Route to Hierarchically Ordered Block Copolymers on a Gradient Patterned Surface through Controlled Evaporative Self-Assembly, *Angewandte Chemie International Edition*, **2013,** *52*, 1122-1127.

154. Han, W.; He, M.; Byun, M.; Li, B.; Lin, Z., Large-Scale Hierarchically Structured Conjugated Polymer Assemblies with Enhanced Electrical Conductivity, *Angewandte Chemie International Edition*, **2013,** *52*, 2564-2568.

155. Han, W.; Byun, M.; Li, B.; Pang, X.; Lin, Z., A Simple Route to Hierarchically Assembled Micelles and Inorganic Nanoparticles, *Angewandte Chemie International Edition*, **2012,** *124*, 12756-12760.

156. Carvalho, M. S.; Kheshgi, H. S., Low-flow limit in slot coating: Theory and experiments, *AIChE Journal*, **2000,** *46*, 1907-1917.

157. Higgins, B. G.; Scriven, L. E., Capillary pressure and viscous pressure drop set bounds on coating bead operability, *Chemical Engineering Science*, **1980,** *35*, 673-682.

158. Kenneth J, R., Limiting flow in a pre-metered coating device, *Chemical Engineering Science*, **1976,** *31*, 1057-1060.

159. Lee, K.-Y.; Liu, L.-D.; Ta-Jo, L., Minimum wet thickness in extrusion slot coating, *Chemical Engineering Science*, **1992,** *47*, 1703-1713.

160. Sartor, L. Slot Coating: Fluid Mechanics and Die Design. Univ. of Minnesota, Minneapolis, 1990.

161. Fasolka, M.; Stafford, C.; Beers, K., Gradient and Microfluidic Library Approaches to Polymer Interfaces Polymer Libraries. Meier, M. A. R.; Webster, D. C., Eds. Springer Berlin / Heidelberg: 2009; Vol. 225, pp 63-105.

162. Stafford, C. M.; Roskov, K. E.; Epps, T. H.; Iii; Fasolka, M. J., Generating thickness gradients of thin polymer films via flow coating, *Review of Scientific Instruments*, **2006,** *77*, 023908-7.

163. Meredith, J. C.; Karim, A.; Amis, E. J., High-Throughput Measurement of Polymer Blend Phase Behavior, *Macromolecules*, **2000,** *33*, 5760-5762.

164. J. Carson Meredith, A. K. a. E. J. A., Combinatorial Methods for Investigations in Polymer Materials Science., *MRS Bulletin*, **2002,** *27*, 330-335.

165. Tsuruma, A.; Tanaka, M.; Yamamoto, S.; Fukushima, N.; Yabu, H.; Shimomura, M., Topographical control of neurite extension on stripe-patterned polymer films, *Colloids and Surfaces A-Physicochemical and Engineering Aspects*, **2006,** *284–285*, 470-474.

166. Yabu, H.; Inoue, K.; Shimomura, M., Multiple-periodic structures of self-organized honeycomb-patterned films and polymer nanoparticles hybrids, *Colloids and Surfaces A-Physicochemical and Engineering Aspects*, **2006,** *284–285*, 301-304.

167. Kim, B. H.; Shin, D. O.; Jeong, S.-J.; Koo, C. M.; Jeon, S. C.; Hwang, W. J.; Lee, S.; Lee, M. G.; Kim, S. O., Hierarchical Self-Assembly of Block Copolymers for Lithography-Free Nanopatterning, *Advanced Materials*, **2008,** *20*, 2303-2307.

168. Hawker, C. J.; Russell, T. P., Block Copolymer Lithography: Merging "Bottom-up" with "Top-down" Processes, *MRS bulletin*, **2005,** *30*, 952-966.

169. Han, W.; Byun, M.; Li, B.; Pang, X.; Lin, Z., A Simple Route to Hierarchically Assembled Micelles and Inorganic Nanoparticles, *Angew. Chem., Int. Ed.*, **2012,** *51*, 12588-12592.

170. Li, J.; Shi, L.; An, Y.; Li, Y.; Chen, X.; Dong, H., Reverse Micelles of Star-Block Copolymer as Nanoreactors for Preparation of Gold Nanoparticles, *Polymer*, **2006,** *47*, 8480-8487.

171. Cho, H.; Park, H.; Park, S.; Choi, H.; Huang, H.; Chang, T., Development of Various PS-b-P4VP Micellar Morphologies: Fabrication of Inorganic Nanostructures from Micellar Templates, *Journal of Colloid and Interface Science*, **2011,** *356*, 1-7.

172. Pang, X.; Zhao, L.; Han, W.; Xin, X.; Lin, Z., A General and Robust Strategy for the Synthesis of Nearly Monodisperse Colloidal Nanocrystals, *Nature Nanotechnology*, **2013,** *8*, 426-431.

173. Li, W.; Liu, S.; Deng, R.; Wang, J.; Nie, Z.; Zhu, J., A Simple Route To Improve Inorganic Nanoparticles Loading Efficiency in Block Copolymer Micelles, *Macromolecules*, **2013,** *46*, 2282-2291.

174. Wang, M.; Kumar, S.; Lee, A.; Felorzabihi, N.; Shen, L.; Zhao, F.; Froimowicz, P.; Scholes, G. D.; Winnik, M. A., Nanoscale Co-organization of Quantum Dots and Conjugated Polymers Using Polymeric Micelles As Templates, *Journal of the American Chemical Society*, **2008,** *130*, 9481-9491.

175. Acharya, H.; Yoon, B.; Park, Y. J.; Bae, I.; Park, C., Block Copolymer Micelles with Near Infrared Metal Phthalocyanine Dyes for Laser Induced Writing, *Macromolecular Rapid Communications*, **2010,** *31*, 1071-1077.

176. Riess, G., Micellization of Block Copolymers, *Progress in Polymer Science*, **2003,** *28*, 1107-1170.

177. Xu, J.; Xia, J.; Lin, Z., Evaporation-Induced Self-Assembly of Nanoparticles from a Sphere-on-Flat Geometry, *Angew. Chem., Int. Ed.*, **2007,** *46*, 1860-1863.

178. Hong, S. W.; Xia, J. F.; Lin, Z. Q., Spontaneous Formation of Mesoscale Polymer Patterns in an Evaporating Bound Solution, *Advanced Materials*, **2007,** *19*, 1413-1417.

179. Hong, S. W.; Byun, M.; Lin, Z., Robust Self-Assembly of Highly Ordered Complex Structures by Controlled Evaporation of Confined Microfluids, *Angewandte Chemie International Edition*, **2009,** *48*, 512-516.

180. Xu, J.; Xia, J.; Hong, S. W.; Lin, Z.; Qiu, F.; Yang, Y., Self-Assembly of Gradient Concentric Rings via Solvent Evaporation from a Capillary Bridge, *Physical Review Letters*, **2006,** *96*, 066104.

181. Leong, W. L.; Lee, P. S.; Lohani, A.; Lam, Y. M.; Chen, T.; Zhang, S.; Dodabalapur, A.; G. Mhaisalkar, S., Non-Volatile Organic Memory Applications Enabled by In Situ Synthesis of Gold Nanoparticles in a Self-Assembled Block Copolymer, *Advanced Materials*, **2008,** *20*, 2325-2331.

182. Yoo, S. I.; Sohn, B.-H.; Zin, W.-C.; An, S.-J.; Yi, G.-C., Self-Assembled Arrays of Zinc Oxide Nanoparticles from Monolayer Films of Diblock Copolymer Micelles, *Chemical Communications*, **2004,** 2850-2851.

183. Antonietti, M.; Wenz, E.; Bronstein, L.; Seregina, M., Synthesis and Characterization of Noble Metal Colloids in Block Copolymer Micelles, *Advanced Materials*, **1995,** *7*, 1000-1005.

184. Yoo, S. I.; Kwon, J.-H.; Sohn, B.-H., Single Layers of Diblock Copolymer Micelles for the Fabrication of Arrays of Nanoparticles, *Journal of Materials Chemistry*, **2007,** *17*, 2969-2975.

185. Sohn, B.-H.; Choi, J.-M.; Yoo, S. I.; Yun, S.-H.; Zin, W.-C.; Jung, J. C.; Kanehara, M.; Hirata, T.; Teranishi, T., Directed Self-Assembly of Two Kinds of Nanoparticles Utilizing Monolayer Films of Diblock Copolymer Micelles, *Journal of the American Chemical Society*, **2003,** *125*, 6368-6369.

186. Sohn, B.-H.; Yoo, S.-I.; Seo, B.-W.; Yun, S.-H.; Park, S.-M., Nanopatterns by Free-Standing Monolayer Films of Diblock Copolymer Micelles with in Situ Core−Corona Inversion, *Journal of the American Chemical Society*, **2001,** *123*, 12734-12735.

187. Wu, S., Calculation of interfacial tension in polymer systems, *Journal of Polymer Science Part C: Polymer Symposia*, **1971,** *34*, 19-30.

188. Owens, D. K.; Wendt, R. C., Estimation of the surface free energy of polymers, *Journal of Applied Polymer Science*, **1969,** *13*, 1741-1747.

189. Binks, B. P.; Clint, J. H., Solid Wettability from Surface Energy Components: Relevance to Pickering Emulsions, *Langmuir*, **2002,** *18*, 1270-1273.

190. Guan, J.; Lee, L. J., Generating highly ordered DNA nanostrand arrays *Proc. Nati. Acad. Sci. U.S.A.*, **2005,** *102*, 18321.

191. Becerril, H. A.; Woolley, A. T., DNA-templated nanofabrication, *Chem. Soc. Rev.*, **2009,** *38*, 329-337.

192. Hopkins, D. S.; Pekker, D.; Goldbart, P. M.; Bezryadin, A., Quantum Interference Device Made by DNA Templating of Superconducting Nanowires, *Science*, **2005,** *308*, 1762-1765.

193. O'Carroll, D.; Lieberwirth, I.; Redmond, G., Microcavity effects and optically pumped lasing in single conjugated polymer nanowires, *Nat Nano*, **2007,** *2*, 180-184.

194. Hu, M.-S.; Chen, H.-L.; Shen, C.-H.; Hong, L.-S.; Huang, B.-R.; Chen, K.-H.; Chen, L.-C., Photosensitive gold-nanoparticle-embedded dielectric nanowires, *Nat Mater*, **2006,** *5*, 102-106.

195. Wang, J.; Gudiksen, M. S.; Duan, X.; Cui, Y.; Lieber, C. M., Highly Polarized Photoluminescence and Photodetection from Single Indium Phosphide Nanowires, *Science*, **2001,** *293*, 1455-1457.

196. Keren, K.; Berman, R. S.; Buchstab, E.; Sivan, U.; Braun, E., DNA-templated carbon nanotube field-effect transistor, *Science*, **2003,** *302*, 1380.

197. Hsieh, C.-H.; Chou, L.-J.; Lin, G.-R.; Bando, Y.; Golberg, D., Nanophotonic Switch: Gold-in-Ga2O3 Peapod Nanowires, *Nano Lett.*, **2008,** *8*, 3081-3085.

198. Bensimon, A.; Simon, A.; Chiffaudel, A.; Croquette, V.; Heslot, F.; Bensimon, D., Alignment and sensitive detection of DNA by a moving interface, *Science*, **1994,** *265*, 2096-2098.

199. Deng, Z.; Mao, C., DNA-Templated Fabrication of 1D Parallel and 2D Crossed Metallic Nanowire Arrays, *Nano Lett.*, **2003,** *3*, 1545-1548.

200. Dewarrat, F.; Calame, M.; Schönenberger, C., Orientation and Positioning of DNA Molecules with an Electric Field Technique, *Single Mol.*, **2002,** *3*, 189-193.

201. Yokota, H.; Sunwoo, J.; Sarikaya, M.; van den Engh, G.; Aebersold, R., Spin-Stretching of DNA and Protein Molecules for Detection by Fluorescence and Atomic Force Microscopy, *Anal. Chem.*, **1999,** *71*, 4418-4422.

202. Petit, C. A. P.; Carbeck, J. D., Combing of Molecules in Microchannels (COMMIC): A Method for Micropatterning and Orienting Stretched Molecules of DNA on a Surface *Nano Lett.*, **2003,** *3*, 1141.

203. Michalet, X.; Ekong, R.; Fougerousse, F.; Rousseaux, S.; Schurra, C.; Hornigold, N.; Slegtenhorst, M. v.; Wolfe, J.; Povey, S.; Beckmann, J. S.; Bensimon, A., Dynamic

Molecular Combing: Stretching the Whole Human Genome for High-Resolution Studies, *Science*, **1997,** *277*, 1518-1523.

204. Allemand, J. F.; Bensimon, D.; Jullien, L.; Bensimon, A.; Croquette, V., PH-dependent specific binding and combing of DNA, *Biophys. J.*, **1997,** *73*, 2064.

205. Guan, J.; Yu, B.; Lee, L. J., Forming Highly Ordered Arrays of Functionalized Polymer Nanowires by Dewetting on Micropillars, *Adv. Mater.*, **2007,** *19*, 1212-1217.

206. Nakao, H.; Taguchi, T.; Shiigi, H.; Miki, K., Simple one-step growth and parallel alignment of DNA nanofibers via solvent vapor-induced buildup, *Chem. Comm.*, **2009,** 1858-1860.

207. Han, W.; Lin, Z., Learning from "Coffee Rings": Ordered Structures Enabled by Controlled Evaporative Self-Assembly, *Angew. Chem. Int. Ed.*, **2012,** *51*, 1534-1546.

208. Zhang, J.; Ma, Y.; Stachura, S.; He, H., Assembly of highly aligned DNA strands onto Si chips, *Langmuir*, **2005,** *21*, 4180.

209. Kim, J. H.; Shi, W.-X.; Larson, R. G., Methods of stretching DNA molecules using flow fields *Langmuir*, **2007,** *23*, 755.

210. Huang, J.; Kim, F.; Tao, A. R.; Connor, S.; Yang, P. D., Spontaneous formation of nanoparticle stripe patterns through dewetting, *Nature Mater.*, **2005,** *4*, 896.

211. Herrick, J.; Bensimon, A., Invited Review. Imaging of Single DNA Molecule: Applications to High-Resolution Genomic Studies, *Chromosome Res.*, **1999,** *7*, 409-423.

212. Yan, R.; Gargas, D.; Yang, P., Nanowire photonics, *Nature Photonics*, **2009,** *3*, 569-576.

213. Yuan, J.; Xu, Y.; Walther, A.; Bolisetty, S.; Schumacher, M.; Schmalz, H.; Ballauff, M.; Muller, A. H. E., Water-soluble organo-silica hybrid nanowires, *Nature Materials*, **2008,** *7*, 718-722.

214. Hochbaum, A. I.; Chen, R.; Delgado, R. D.; Liang, W.; Garnett, E. C.; Najarian, M.; Majumdar, A.; Yang, P., Enhanced thermoelectric performance of rough silicon nanowires, *Nature*, **2008,** *451*, 163-167.

215. Feng, X.; Shankar, K.; Paulose, M.; Grimes, C. A., Tantalum-Doped Titanium Dioxide Nanowire Arrays for Dye-Sensitized Solar Cells with High Open-Circuit Voltage, *Angewandte Chemie international Edition*, **2009,** *121*, 8239-8242.

216. Nam, K. T.; Kim, D.-W.; Yoo, P. J.; Chiang, C.-Y.; Meethong, N.; Hammond, P. T.; Chiang, Y.-M.; Belcher, A. M., Virus-Enabled Synthesis and Assembly of Nanowires for Lithium Ion Battery Electrodes, *Science*, **2006,** *312*, 885-888.

217. Chen, C.-L.; Rosi, N. L., Peptide-Based Methods for the Preparation of Nanostructured Inorganic Materials, *Angewandte Chemie International Edition*, **2010,** *49*, 1924-1942.

218. Braun, E.; Eichen, Y.; Sivan, U.; Ben-Yoseph, G., DNA-templated assembly and electrode attachment of a conducting silver wire, *Nature*, **1998,** *391*, 775-778.

219. Zinchenko, A., Templating of inorganic nanomaterials by biomacromolecules and their assemblies, *Polymer Science Series C*, **2012,** *54*, 80-87.

220. Mertig, M.; Colombi Ciacchi, L.; Seidel, R.; Pompe, W.; De Vita, A., DNA as a Selective Metallization Template, *Nano Letters*, **2002,** *2*, 841-844.

221. Richter, J.; Seidel, R.; Kirsch, R.; Mertig, M.; Pompe, W.; Plaschke, J.; Schackert, H. K., Nanoscale Palladium Metallization of DNA, *Advanced Materials*, **2000,** *12*, 507-510.

222. Becerril, H. A.; Woolley, A. T., DNA-templated nanofabrication, *Chem. Soc. Rev.*, **2009,** *38*, 329-337.

223. Petit, C. A. P.; Carbeck, J. D., Combing of Molecules in Microchannels (COMMIC): A Method for Micropatterning and Orienting Stretched Molecules of DNA on a Surface, *Nano Letters*, **2003,** *3*, 1141-1146.

224. Deng, Z.; Mao, C., DNA-Templated Fabrication of 1D Parallel and 2D Crossed Metallic Nanowire Arrays, *Nano Lett.*, **2003,** *3*, 1545-1548.

225. Yokota, H.; Sunwoo, J.; Sarikaya, M.; van den Engh, G.; Aebersold, R., Spin-Stretching of DNA and Protein Molecules for Detection by Fluorescence and Atomic Force Microscopy, *Anal. Chem.*, **1999,** *71*, 4418-4422.

226. Dewarrat, F.; Calame, M.; Schönenberger, C., Orientation and Positioning of DNA Molecules with an Electric Field Technique, *Single Molecules*, **2002,** *3*, 189-193.

227. Nakao, H.; Taguchi, T.; Shiigi, H.; Miki, K., Simple one-step growth and parallel alignment of DNA nanofibers viasolvent vapor-induced buildup, *Chem. Commun.*, **2009,** 1858-1860.

228. Deegan, R. D., Pattern formation in drying drops, *Phys. Rev. E*, **2000,** *61*, 475-485.

229. Hong, S. W.; Wang, J.; Lin, Z., Evolution of Ordered Block Copolymer Serpentines into a Macroscopic, Hierarchically Ordered Web, *Angewandte Chemie International Edition*, **2009,** *48*, 8356-8360.

230. Li, B.; Han, W.; Byun, M.; Zhu, L.; Zou, Q.; Lin, Z., Macroscopic Highly Aligned DNA Nanowires Created by Controlled Evaporative Self-Assembly, *ACS Nano*, **2013,** *7*, 4326-4333.

231. Nakao, H.; Gad, M.; Sugiyama, S.; Otobe, K.; Ohtani, T., Transfer-Printing of Highly Aligned DNA Nanowires, *Journal of the American Chemical Society*, **2003,** *125*, 7162-7163.

232. Qun, G.; Chuanding, C.; Ravikanth, G.; Shivashankar, S.; Sathish, A.; Kun, D.; Donald, T. H., DNA nanowire fabrication, *Nanotechnology*, **2006,** *17*, R14.

233. Halas, N. J.; Lal, S.; Chang, W.-S.; Link, S.; Nordlander, P., Plasmons in Strongly Coupled Metallic Nanostructures, *Chemical Reviews*, **2011,** *111*, 3913-3961.

234. Nikoobakht, B.; El-Sayed, M. A., Preparation and Growth Mechanism of Gold Nanorods (NRs) Using Seed-Mediated Growth Method, *Chemistry of Materials*, **2003,** *15*, 1957-1962.

235. Morariu, M. D.; Schäffer, E.; Steiner, U., Molecular Forces Caused by the Confinement of Thermal Noise, *Physical Review Letters*, **2004,** *92*, 156102.

236. Lin, Z.; Kerle, T.; Russell, T. P.; Schäffer, E.; Steiner, U., Electric Field Induced Dewetting at Polymer/Polymer Interfaces, *Macromolecules*, **2002,** *35*, 6255-6262.

237. Reiter, G., Dewetting of thin polymer films, *Physical Review Letters*, **1992,** *68*, 75-78.

238. Xie, R.; Karim, A.; Douglas, J. F.; Han, C. C.; Weiss, R. A., Spinodal Dewetting of Thin Polymer Films, *Physical Review Letters*, **1998,** *81*, 1251-1254.

239. Churaev, N. V.; Galwey, A., *Liquid and vapor flows in porous bodies: surface phenomena*. Taylor & Francis: 2000; Vol. 13.

240. Tong, L.; Gattass, R. R.; Ashcom, J. B.; He, S.; Lou, J.; Shen, M.; Maxwell, I.; Mazur, E., Subwavelength-diameter silica wires for low-loss optical wave guiding, *Nature*, **2003,** *426*, 816-819.

241. Law, M.; Sirbuly, D. J.; Johnson, J. C.; Goldberger, J.; Saykally, R. J.; Yang, P., Nanoribbon Waveguides for Subwavelength Photonics Integration, *Science*, **2004,** *305*, 1269-1273.

242. Johnson, J. C.; Choi, H.-J.; Knutsen, K. P.; Schaller, R. D.; Yang, P.; Saykally, R. J., Single gallium nitride nanowire lasers, *Nat Mater*, **2002,** *1*, 106-110.

243. McAlpine, M. C.; Ahmad, H.; Wang, D.; Heath, J. R., Highly ordered nanowire arrays on plastic substrates for ultrasensitive flexible chemical sensors, *Nat Mater*, **2007,** *6*, 379-384.

244. Zheng, G.; Patolsky, F.; Cui, Y.; Wang, W. U.; Lieber, C. M., Multiplexed electrical detection of cancer markers with nanowire sensor arrays, *Nat Biotech*, **2005,** *23*, 1294-1301.

245. Gong, S.; Schwalb, W.; Wang, Y.; Chen, Y.; Tang, Y.; Si, J.; Shirinzadeh, B.; Cheng, W., A wearable and highly sensitive pressure sensor with ultrathin gold nanowires, *Nat Commun*, **2014,** *5*.

246. Melosh, N. A.; Boukai, A.; Diana, F.; Gerardot, B.; Badolato, A.; Petroff, P. M.; Heath, J. R., Ultrahigh-Density Nanowire Lattices and Circuits, *Science*, **2003,** *300*, 112-115.

247. Wang, Z. L.; Song, J., Piezoelectric Nanogenerators Based on Zinc Oxide Nanowire Arrays, *Science*, **2006,** *312*, 242-246.

248. Barrelet, C. J.; Greytak, A. B.; Lieber, C. M., Nanowire Photonic Circuit Elements, *Nano Letters*, **2004,** *4*, 1981-1985.

249. Wang, C.; Sun, S., Facile Synthesis of Ultrathin and Single-Crystalline Au Nanowires, *Chem Asian J*, **2009,** *4*, 1028-1034.

250. Cui, H.; Hong, C.; Ying, A.; Yang, X.; Ren, S., Ultrathin Gold Nanowire-Functionalized Carbon Nanotubes for Hybrid Molecular Sensing, *ACS Nano*, **2013,** *7*, 7805-7811.

251. Sánchez-Iglesias, A.; Rivas-Murias, B.; Grzelczak, M.; Pérez-Juste, J.; Liz-Marzán, L. M.; Rivadulla, F.; Correa-Duarte, M. A., Highly Transparent and Conductive Films of Densely Aligned Ultrathin Au Nanowire Monolayers, *Nano Letters*, **2012,** *12*, 6066-6070.

252. Takahata, R.; Yamazoe, S.; Koyasu, K.; Tsukuda, T., Surface Plasmon Resonance in Gold Ultrathin Nanorods and Nanowires, *Journal of the American Chemical Society*, **2014,** *136*, 8489-8491.

253. Chen, Y.; Ouyang, Z.; Gu, M.; Cheng, W., Mechanically Strong, Optically Transparent, Giant Metal Superlattice Nanomembranes From Ultrathin Gold Nanowires, *Advanced Materials*, **2013,** *25*, 80-85.

254. Chandni, U.; Kundu, P.; Kundu, S.; Ravishankar, N.; Ghosh, A., Tunability of Electronic States in Ultrathin Gold Nanowires, *Advanced Materials*, **2013,** *25*, 2486-2491.

255. Yang, L.; Zhang, Y.; Chu, M.; Deng, W.; Tan, Y.; Ma, M.; Su, X.; Xie, Q.; Yao, S., Facile fabrication of network film electrodes with ultrathin Au nanowires for nonenzymatic glucose sensing and glucose/O-2 fuel cell, *Biosensors & Bioelectronics*, **2014,** *52*, 105-110.

256. Zheng, H.; Cao, A.; Weinberger, C. R.; Huang, J. Y.; Du, K.; Wang, J.; Ma, Y.; Xia, Y.; Mao, S. X., Discrete plasticity in sub-10-nm-sized gold crystals, *Nat Commun*, **2010,** *1*, 144.

257. Pazos-Pérez, N.; Baranov, D.; Irsen, S.; Hilgendorff, M.; Liz-Marzán, L. M.; Giersig, M., Synthesis of Flexible, Ultrathin Gold Nanowires in Organic Media, *Langmuir*, **2008,** *24*, 9855-9860.

258. Lu, X.; Yavuz, M. S.; Tuan, H.-Y.; Korgel, B. A.; Xia, Y., Ultrathin Gold Nanowires Can Be Obtained by Reducing Polymeric Strands of Oleylamine−AuCl Complexes Formed via Aurophilic Interaction, *Journal of the American Chemical Society*, **2008,** *130*, 8900-8901.

259. Huo, Z.; Tsung, C.-k.; Huang, W.; Zhang, X.; Yang, P., Sub-Two Nanometer Single Crystal Au Nanowires, *Nano Letters*, **2008,** *8*, 2041-2044.

260. Halder, A.; Ravishankar, N., Ultrafine Single-Crystalline Gold Nanowire Arrays by Oriented Attachment, *Advanced Materials*, **2007,** *19*, 1854-1858.

261. Mourdikoudis, S.; Liz-Marzán, L. M., Oleylamine in Nanoparticle Synthesis, *Chemistry of Materials*, **2013,** *25*, 1465-1476.

262. Li, C. C.; Chen, L. B.; Li, Q. H.; Wang, T. H., Seed-free, aqueous synthesis of gold nanowires, *CrystEngComm*, **2012,** *14*, 7549-7551.

263. Lohse, S. E.; Murphy, C. J., The Quest for Shape Control: A History of Gold Nanorod Synthesis, *Chemistry of Materials*, **2013,** *25*, 1250-1261.

264. Vigderman, L.; Khanal, B. P.; Zubarev, E. R., Functional Gold Nanorods: Synthesis, Self-Assembly, and Sensing Applications, *Advanced Materials*, **2012,** *24*, 4811-4841.

265. Khanal, B. P.; Zubarev, E. R., Purification of High Aspect Ratio Gold Nanorods: Complete Removal of Platelets, *Journal of the American Chemical Society*, **2008,** *130*, 12634-12635.

266. Liu; Guyot-Sionnest, P., Mechanism of Silver(I)-Assisted Growth of Gold Nanorods and Bipyramids, *Journal of Physical Chemistry B*, **2005,** *109*, 22192-22200.

267. Vigderman, L.; Zubarev, E. R., High-Yield Synthesis of Gold Nanorods with Longitudinal SPR Peak Greater than 1200 nm Using Hydroquinone as a Reducing Agent, *Chemistry of Materials*, **2013,** *25*, 1450-1457.

268. Busbee, B. D.; Obare, S. O.; Murphy, C. J., An Improved Synthesis of High-Aspect-Ratio Gold Nanorods, *Advanced Materials*, **2003,** *15*, 414-416.

269. Wang, Y.-N.; Wei, W.-T.; Yang, C.-W.; Huang, M. H., Seed-Mediated Growth of Ultra long Gold Nanorods and Nanowires with a Wide Range of Length Tunability, *Langmuir*, **2013,** *29*, 10491-10497.

270. Kim, F.; Sohn, K.; Wu, J.; Huang, J., Chemical Synthesis of Gold Nanowires in Acidic Solutions, *Journal of the American Chemical Society*, **2008,** *130*, 14442-14443.

271. Cademartiri, L.; Ozin, G. A., Ultrathin Nanowires—A Materials Chemistry Perspective, *Advanced Materials*, **2009,** *21*, 1013-1020.

272. Loubat, A.; Impéror-Clerc, M.; Pansu, B.; Meneau, F.; Raquet, B.; Viau, G.; Lacroix, L.-M., Growth and Self-Assembly of Ultrathin Au Nanowires into Expanded Hexagonal Superlattice Studied by in Situ SAXS, *Langmuir*, **2014,** *30*, 4005-4012.

273. Murphy, C. J.; Thompson, L. B.; Alkilany, A. M.; Sisco, P. N.; Boulos, S. P.; Sivapalan, S. T.; Yang, J. A.; Chernak, D. J.; Huang, J., The Many Faces of Gold Nanorods, *Journal of Physical Chemistry Letters*, **2010,** *1*, 2867-2875.

274. Grzelczak, M.; Perez-Juste, J.; Mulvaney, P.; Liz-Marzan, L. M., Shape control in gold nanoparticle synthesis, *Chemical Society Reviews*, **2008,** *37*, 1783-1791.

275. Ortiz, N.; Skrabalak, S. E., On the Dual Roles of Ligands in the Synthesis of Colloidal Metal Nanostructures, *Langmuir*, **2014,** *30*, 6649-6659.

276. Klostranec, J. M.; Chan, W. C. W., Quantum Dots in Biological and Biomedical Research: Recent Progress and Present Challenges, *Advanced Materials*, **2006,** *18*, 1953-1964.

277. Jacobs, H. O.; Whitesides, G. M., Submicrometer Patterning of Charge in Thin-Film Electrets, *Science*, **2001,** *291*, 1763-1766.

278. Erdogan, B.; Song, L.; Wilson, J. N.; Park, J. O.; Srinivasarao, M.; Bunz, U. H. F., Permanent Bubble Arrays from a Cross-Linked Poly(para-phenyleneethynylene): Picoliter Holes without Microfabrication, *Journal of the American Chemical Society*, **2004,** *126*, 3678-3679.

279. McDonald, J. C.; Whitesides, G. M., Poly(dimethylsiloxane) as a Material for Fabricating Microfluidic Devices, *Accounts of Chemical Research*, **2002,** *35*, 491-499.

280. Xia, Y.; Whitesides, G. M., Soft Lithography, *Angewandte Chemie International Edition*, **1998,** *37*, 550-575.

281. Piner, R. D.; Zhu, J.; Xu, F.; Hong, S.; Mirkin, C. A., "Dip-Pen" Nanolithography, *Science*, **1999,** *283*, 661-663.

282. Jang, Y.; Jo, J.; Kim, D.-S., Control of doctor-blade coated poly (3,4-ethylenedioxythiophene)/poly(styrenesulfonate) electrodes shape on prepatterned substrates via microflow control in a drying droplet, *Journal of Polymer Science Part B: Polymer Physics*, **2011,** *49*, 1590-1596.

283. Alexander, F. R., Drying of thin colloidal films, *Reports on Progress in Physics*, **2013,** *76*, 046603.

284. Lidon, P.; Salmon, J.-B., Dynamics of unidirectional drying of colloidal dispersions, *Soft Matter*, **2014,** *10*, 4151-4161.

285. Tirumkudulu, M. S.; Russel, W. B., Cracking in Drying Latex Films, *Langmuir*, **2005,** *21*, 4938-4948.

286. Jagla, E. A., Stable propagation of an ordered array of cracks during directional drying, *Physical Review E*, **2002,** *65*, 046147.

287. Allain, C.; Limat, L., Regular Patterns of Cracks Formed by Directional Drying of a Collodial Suspension, *Physical Review Letters*, **1995,** *74*, 2981-2984.

288. Dufresne, E. R.; Corwin, E. I.; Greenblatt, N. A.; Ashmore, J.; Wang, D. Y.; Dinsmore, A. D.; Cheng, J. X.; Xie, X. S.; Hutchinson, J. W.; Weitz, D. A., Flow and Fracture in Drying Nanoparticle Suspensions, *Physical Review Letters*, **2003,** *91*, 224501.

289. Dufresne, E. R.; Stark, D. J.; Greenblatt, N. A.; Cheng, J. X.; Hutchinson, J. W.; Mahadevan, L.; Weitz, D. A., Dynamics of Fracture in Drying Suspensions, *Langmuir*, **2006,** *22*, 7144-7147.

290. Ma, J.; Jing, G., Possible origin of the crack pattern in deposition films formed from a drying colloidal suspension, *Physical Review E*, **2012,** *86*, 061406.

291. Routh, A. F.; Russel, W. B., A Process Model for Latex Film Formation: Limiting Regimes for Individual Driving Forces, *Langmuir*, **1999,** *15*, 7762-7773.

292. Lee, W. P.; Routh, A. F., Why Do Drying Films Crack?, *Langmuir*, **2004,** *20*, 9885-9888.

293. Singh, K. B.; Tirumkudulu, M. S., Cracking in Drying Colloidal Films, *Physical Review Letters*, **2007,** *98*, 218302.

294. Prasad, M.; Kopycinska, M.; Rabe, U.; Arnold, W., Measurement of Young's modulus of clay minerals using atomic force acoustic microscopy, *Geophysical Research Letters*, **2002,** *29*, 13-1-13-4.

295. Pang, X.; Zhao, L.; Han, W.; Xin, X.; Lin, Z., A general and robust strategy for the synthesis of nearly monodisperse colloidal nanocrystals, *Nat Nano*, **2013,** *8*, 426-431.

296. Wang, X.; Zhuang, J.; Peng, Q.; Li, Y., A general strategy for nanocrystal synthesis, *Nature*, **2005,** *437*, 121-124.

297. Sun, S.; Murray, C. B.; Weller, D.; Folks, L.; Moser, A., Monodisperse FePt Nanoparticles and Ferromagnetic FePt Nanocrystal Superlattices, *Science*, **2000,** *287*, 1989-1992.

298. Peng, X.; Manna, L.; Yang, W.; Wickham, J.; Scher, E.; Kadavanich, A.; Alivisatos, A. P., Shape control of CdSe nanocrystals, *Nature*, **2000,** *404*, 59-61.

299. Yang, P.; Zhao, D.; Margolese, D. I.; Chmelka, B. F.; Stucky, G. D., Generalized syntheses of large-pore mesoporous metal oxides with semicrystalline frameworks, *Nature*, **1998,** *396*, 152-155.

300. Xia, Y.; Xiong, Y.; Lim, B.; Skrabalak, S. E., Shape-Controlled Synthesis of Metal Nanocrystals: Simple Chemistry Meets Complex Physics?, *Angewandte Chemie International Edition*, **2009,** *48*, 60-103.

VITA

BO LI

Bo Li was born in Shijiazhuang, Hebei in China on May 25th, 1986. He attended Shijiazhuang No. 41 middle school and Shijiazhuang No. 2 high school in Shijiazhuang, Hebei. He earned his Bachelor and Master degree in Materials Science and Engineering (MSE) at Xi'an Jiaotong University in 2008 and 2010 respectively. He pursured a Ph.D. in Materials Science and Engineering (MSE) at Georgia Institute of Technology with Professor Zhiqun Lin.